Doctoral Dissertation

Doctoral Program in Mechanical Engineering (32^{th} cycle)

Aerodynamics of a squareback road vehicle with active flow control

Experimental analysis of the drag reduction and fuel consumption through flow control and platooning of vehicles

By

Juan José Cerutti

******

Supervisors

Prof. Gaetano Iuso, Supervisor
Prof. Gioacchino Cafiero, Co-supervisor

Doctoral Examination Committee:

Prof. Giuseppe Gibertini, Politecnico di Milano.
Prof. Alberto Guardone, Politecnico di Milano.

Politecnico di Torino
July 2020

I hereby declare that, the contents and organization of this dissertation constitute my own original work and does not compromise in any way the rights of third parties, including those relating to the security of personal data.

Juan José Cerutti
Turin, 2020

Summary

In the present thesis a wind tunnel investigation over a 1:10 scaled van model was performed in order to evaluate two different techniques for drag reduction: active flow control (AFC) and platooning of vehicles. The AFC consist in four cylindrical actuators along the trailing edges, with longitudinal slots blowing tangentially to the actuator surface and angled in 65° regarding the model's base. For the platooning evaluation, three replicas of the model were built and then configured in different arrangements to emulate the various positions of a two, three and four vehicle convoy PIV and Stereo PIV techniques were used to the reconstruct the architecture of the flowfield on the model's rear part. The model mounts 64 pressure taps in order to measure the mean pressure in the whole model's surface and 16 microphones on the rear part for pressure fluctuations. Drag measurements were performed through a drag balance mounted on the top of the test chamber and connected to the model by a hollowed beam, that houses the electric lines of the sensors and the tubing for the AFC.
The baseline (non controlled case, isolated model) presents a drag coefficient of $C_D = 0.45$ at $Re = 2.5 \times 10^5$, typical for this kind of vehicles. The pressure distribution evidence the presence of the A-pillar vortex on the side part and an almost constant pressure distribution on the rear, showing a slight growing tendency towards the bottom. The pressure fluctuations on the rear base were analyzed in the frequency domain highlighting a dominant peak of energy at a Strouhal number of $St = 0.12$, agreeing with the typical vortex shedding frequencies of this kind of vehicles. The mean flow PIV confirm the classic wake structure for squareback bluff bodies, composed by a recirculating flow zone on the near wake and two streamwise counter-rotating vortexes that trail away from the model.
The AFC was first analyzed by using steady blowing. The drag characterization of the individual jets demonstrated that the bottom and lateral jets produce drag reduction, while the top one produces drag increasing. This undesirable effect might be produced by the increased wake asymmetry due to the top blowing. Combined blowing using the lateral and bottom jets further reduces the drag regarding the singe blowing. Varying the blowing speeds of both lateral and bottom jets two main configurations were found: A maximum drag reduction (Max DR) performing $\Delta C_D = -10.6\%$ and a best compromise (BC) given by the maximum values of the ratio between the drag variation and the blowing coefficient $\Delta C_D/C_\mu$, performing a drag variation of $\Delta C_D = -5\%$. A successive energy budget analysis was performed by calculating the efficiency ratio (ξ) given by the power gained by the drag reduction versus the power consumed by the blowing jets, that demonstrates that the BC recovers through the drag reduction five times the power consumed by the jets ($\xi = 5$) while in the Max DR the power spent overcomes the power gain ($\xi = 0.8$). The pressure distributions demonstrate that the AFC only modifies the pressure distribution on the rear part and the drag reduction is a consequence of the increasing base pressure, that grows with the increasing blowing.

The PIV and Stereo PIV of the wake for the BC and Max DR cases display a reduction of the recirculation bubble and a reduction of the counter rotating streamwise vortexes. For the Max DR the wake severally changes, further reducing the recirculating bubble and canceling the streamwise vortexes.
The AFC unsteady actuation was analyzed by using a squared waveform and changing the frequency, duty cycle, minimum and maximum velocities of blowing. In a first stage the pulsed blowing was studied, performing a zero minimum velocity and a maximum equal to the freestream speed. No significant values of drag reduction where found for frequencies ranging between 1 and $50Hz$ and different duty cycles. Only the bottom jets evidence three drag reduction peaks reaching near the steady blowing values, around the $St = 0.12$ frequency and the two consecutive harmonics for a duty cycle of 30%. This might evidence a response of the wake to the dynamic actuation, but not strong enough to obtain high values of drag reduction. These peaks are not observed when blowing from the lateral or combined jets. Actually, for the lateral jets some peaks of drag increasing were observed. A second study was performed involving the fluctuation of the blowing velocity around the freestream speed, with different ranges of velocities, frequencies and duty cycles. As in the pulsed blowing, the drag results show no improvement regarding the steady blowing.
Lastly, the platooning test were performed using the model replicas. The two-model configuration was extensively analyzed, presenting high values of drag reduction for both vehicles. The increasing of the base pressure of the front vehicle due to the approaching of the following produces a maximum drag reduction of $\Delta C_D = -30\%$ for half model length of distance ($d/L = 0.5$). The rear vehicle sees a drop of the front pressure distribution product of the front vehicle's wake, reaching $\Delta C_D = -42\%$ for the same distance. For convoys of three and four models three characteristic positions were discovered: front, middle and rear models. Independent from the number of components of the platoon, these positions present the same drag variations regarding the distance between models, allowing to extrapolate the platoon to a virtually infinite number of vehicles. The extrapolation show an asymptotic tendency of the average drag reduction of the platoon for all different d/L distances studied, reaching 90% of this maximum value when the convoy exceeds 18 models.

Acknowledgements

I would like to thanks the personnel of the aerodynamic lab, Marco Grivet and Ing. Marco Cannata for the invaluable help during my three years of research. To Gioacchino Cafiero for the support during the test campaigns and to my friend and colleague Costantino Sardu. Lastly, to my tutor Professor Gaetano Iuso for the guidance during the PhD cycle.

Quisiera también agradecer a mi familia y amigos por su paciencia y apoyo incondicional en estos años, y muy especialmente a mi Madre, por haberme siempre ayudado a desarrollar mis pasiones.

Dedicado a la memoria de mi abuelo "Pepe" y a mi Madre,

A. Lis Garcia Suarez.

Prologue

The greenhouse effect is the most important and harmful product of the technological development of mankind. It generates global warming, climate change, melting of the ices and a series of successive implications that could lead to an ecologic crisis in the mid or short term. This phenomenon is produced by the enclosing of the sun's energy on the earth's atmosphere. In a normal situation the light radiated by the sun warm the surface of the earth and part of this energy is reflected to the space. The greenhouse gases block this reflection, keeping the energy inside the atmosphere and consequently rising the earth's temperature. The main element that produces this effect is the *Carbon dioxide* (CO_2). This gas is present in the atmosphere in natural way, product of the digestion of animals and the volcano activity. The *Methane* and *Nitrous Oxide* have the same effect and the same sources, but they are produced in smaller quantities and therefore the impact is weaker. *Fluorinated gases*, product of artificial processes, have an impact 23000 times greater that CO_2. Nevertheless, the intense control of these gases' discharges make its impact negligible.
Nowadays the CO_2 emissions are the most critical due to the high levels of concentration in atmosphere, mainly prompted by burning fossil fuels, cutting down rainforests and farming livestock. The trends of CO_2 emissions since 1990 are shown in figure 1, where the emission reference is settled on the starting point. As seen, all different sources of CO_2 have been decreasing except for the *Transport*.

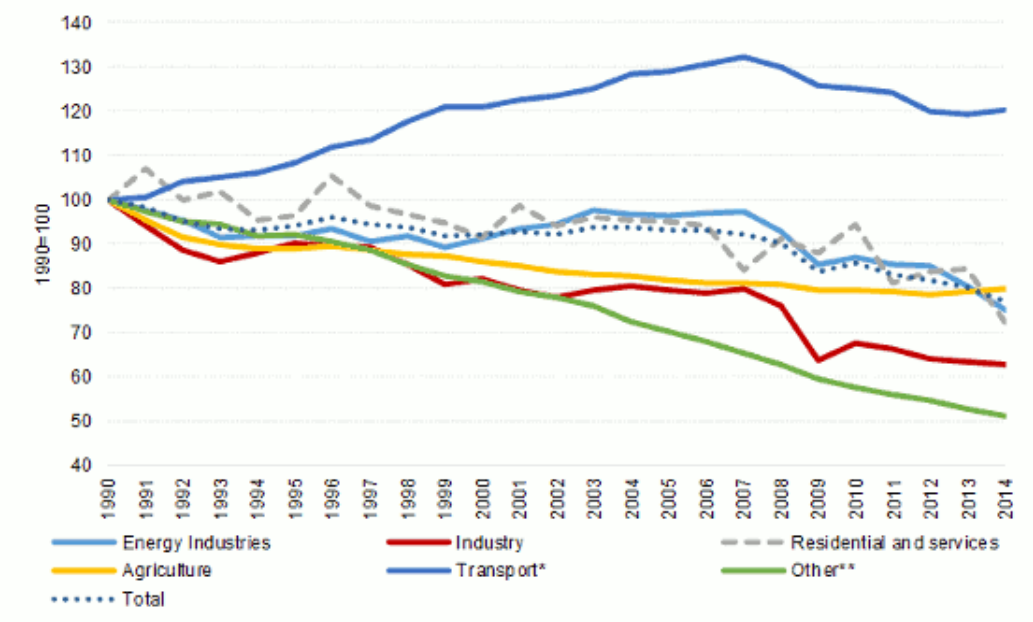

Figure 1: Percentage of CO_2 emissions through the years from different sources, taking 1990 as a reference. Taken from *https* : *//ec.europa.eu/clima/ policies/transport _en*.

The *Transport* source follows the economic development of the society, since is linked to the commercial mobility. This is an opposite behavior regarding the ecologic point of view, and the main reason why reducing the *Transport* emissions is such a challenge. If further analyzed, this source can be divided in shares corresponding to the different modes of Transport. For the year 2014, the shares are shown in figure 2 for two different modes' classification. Transport modes as Aviation, Navigation and Railways are some of the less influencing factors, while the road transport reaches near 73% of the total *Transport* emissions. Actually, in 2016 the road transport represented the 21% of the overall CO_2 emissions in Europe. By the examination of this results is easy to conclude that the Transport's CO_2 emissions are highly sensitive to the Road transport variations and acting over these category is the most effective way to reduce them.

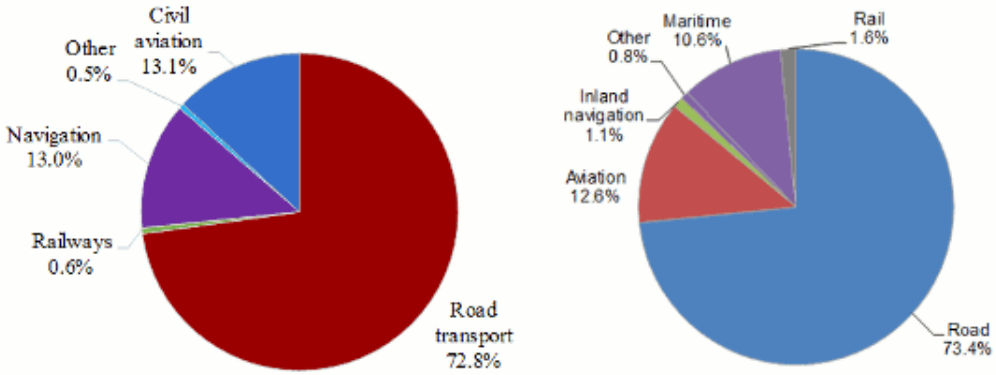

Figure 2: Shares of CO_2 emissions or the *Transport* source in 2014. Taken from *https* : *//ec.europa.eu/clima/policies/transport_en*.

Within the road transport CO_2 share of figure 2 are present the *light-duty vehicles*, including cars and vans, representing the 15% of the overall CO_2 emissions on 2016. Moreover, *heavy-duty vehicles* as trucks and buses account for near 5% of the overall CO_2 emissions in the same year. This means that the main emission source of this share are the commercial vehicles.
In order to reduce the CO_2 emissions trends of figure 1 and control the greenhouse effect, the *European Union* (EU) set a series of target reductions for the near future and for the different sources. In particular, a target of 60% reduction to meet by 2050 has been settled for the road transport emissions (Regulations EU-2019/631 [48] for cars and light-duty vehicles and EU-2019/1242 [47] for heavy-duty vehicles). This plan includes a set of incremental reductions resumed in table 1 for different type of vehicles. The table shows significant reductions for the oncoming years that the manufacturers must meet for vehicles built after 2020. In order to push the market, penalties will be applied for vehicles above those targets and prices for vehicles below. In addition, a regulation for heavy-duty vehicles will be applied for the firs time from year 2020.

The commercial vehicles (light and heavy-duty) represent a double challenge on the emission reduction: as claimed in the precedent paragraphs the mobility means economic development, hence reducing the activity of these vehicles is not an option. If considered the state of the art of electric-driven vehicles, there is no technological solution that reaches the same efficiency level of *Internal Combustion Engine*(ICE). The main problem of this technology is the lack of range, charge stations and the

Vehicle type	Current value	Target 2020	Target 2030
Cars	130	95	−30%(*)
Light-duty vehicles	175	147	−30%(*)
Heavy-duty vehicles	-	−15%(**)	−30%(**)

Table 1: Emission targets for different type of vehicles in $GrCO_2/km$. (* Reduction regarding the 2020 emissions results; ** Reduction regarding the period between 1 July 2019 and 30 June 2020).

charging periods. Therefore, electrifying these vehicles is not a conceivable solution and the only viable powertrain that does not compromise the economic development is the ICE.
The remaining way to reduce the emissions is to diminish the aerodynamic drag, and this presents another challenge: the shape of these vehicles is given by the maximization of the internal volume and the accessibility, being these the reasons why they have all the same box shape with a squareback rear part. Such a geometry has a very low aerodynamic performance producing high drag and therefore high fuel consumption. Reducing the aerodynamic drag will consequently reduce the consumption, thus reducing the emissions. Furthermore, if in the future the electric technology reaches the ICE efficiency level, this aerodynamic enrichment could improve the range and battery life. This makes commercial vehicles an optimum candidate for improving the emissions through the aerodynamic enhancement without compromising his utilization, which is the main objective of this work.

Thesis objectives and outline

The present thesis presents two methods to reduce the aerodynamic drag of commercial vehicles (vans and lorries) consisting in Active flow control and Platooning of vehicles. The main goal behind the aerodynamic enhancement produced by these methods is the increasing of the vehicle's efficiency, which can be traduced in a direct reduction of emissions for ICE-driven vehicles or improved energy utilization for electric-driven ones.

The thesis is organized as follows:

- Chapter 1: Introduction. A bibliographic survey covering the most important aspects of the problem, from the most basic shapes until the different models typically used for wind tunnel testing.

- Chapter 2: Experimental setup and Data Processing. Complete description of the hardware and software used during the tests and the mathematical tools available to post-process the raw data.

- Chapter 3: Wind tunnel methodology. Description of the experimental methodology used for the wind tunnel assessment and testing.

- Chapter 4: The non-controlled case: baseline. Aerodynamic characteristics of the isolated model.

- Chapter 5: The stationary controlled case. Flow control using steady blowing on the rear of the vehicle.
- Chapter 6: The non-stationary controlled case. Flow control using unsteady blowing on the rear of the vehicle.
- Chapter 7: Platooning. Analysis of the benefits of a platoon of two, three and four vehicles.
- Conclusions.

Contents

List of Figures

List of Tables

Chapter 1: Introduction

The aerodynamics of bluff bodies will be described in the time and frequency domains starting from the most basic geometries until the Ahmed body, which is the benchmark for vehicle's aerodynamics. A brief overview of some of the most popular models with different geometries and theirs features will be also presented. The drag reduction through passive and active flow control techniques will be exposed with pros and cons, as well as some examples of feedback active flow control. In addition, the concept of platoon driving and its vantages on the aerodynamics will be presented, together with the control challenges. The fuel consumption and emissions will be estimated through a series of relations that legates them with the vehicle's drag.

1.1 Bluff bodies' aerodynamics

If considered a passenger vehicle as a car or a van, their shape respond to practical issues like internal space and utility. Only sport cars consider aerodynamics as a main design principle. This makes nowadays vehicles, specially vans and lorries, bluff-shaped bodies with low aerodynamic efficiency. In order to fully comprehend the general characteristics of the flow surrounding this bodies we begin analyzing from the most simple three dimensional bluff shapes until reaching the *Ahmed body*, which is the actual benchmark for vehicle's aerodynamics.

The main aerodynamic characteristic of bluff bodies is a large separated-flow region on the aft, the near wake. This is responsible for a low pressure region behind the body, being one of the main aerodynamic drag components. The drag coefficient represents the adimensional force over the body in the streamwise direction and is defined in equation 1.1, where D is the measured aerodynamic drag, ρ is the air density, V_∞ is the free stream speed and S is the reference area. Since the wake is one of the major components of bluff bodies' drag, this coefficient is an accurate indicator of the wake behavior.

$$C_D = \frac{D}{\frac{1}{2}\rho V_\infty^2 S} \tag{1.1}$$

If consider a disk facing the flow, the separation is present in almost all Reynolds range, being Reynolds defined as $Re_L = \rho V_\infty L/\mu$ with L the reference length and μ the flow viscosity. From the research of Morel and Bohn [84] presented in figure 1.1a, on the left image is observable the flow surrounding a facing-flow disk. Is clearly visible how the sharp edges instigate the separation, generating a constant recirculating

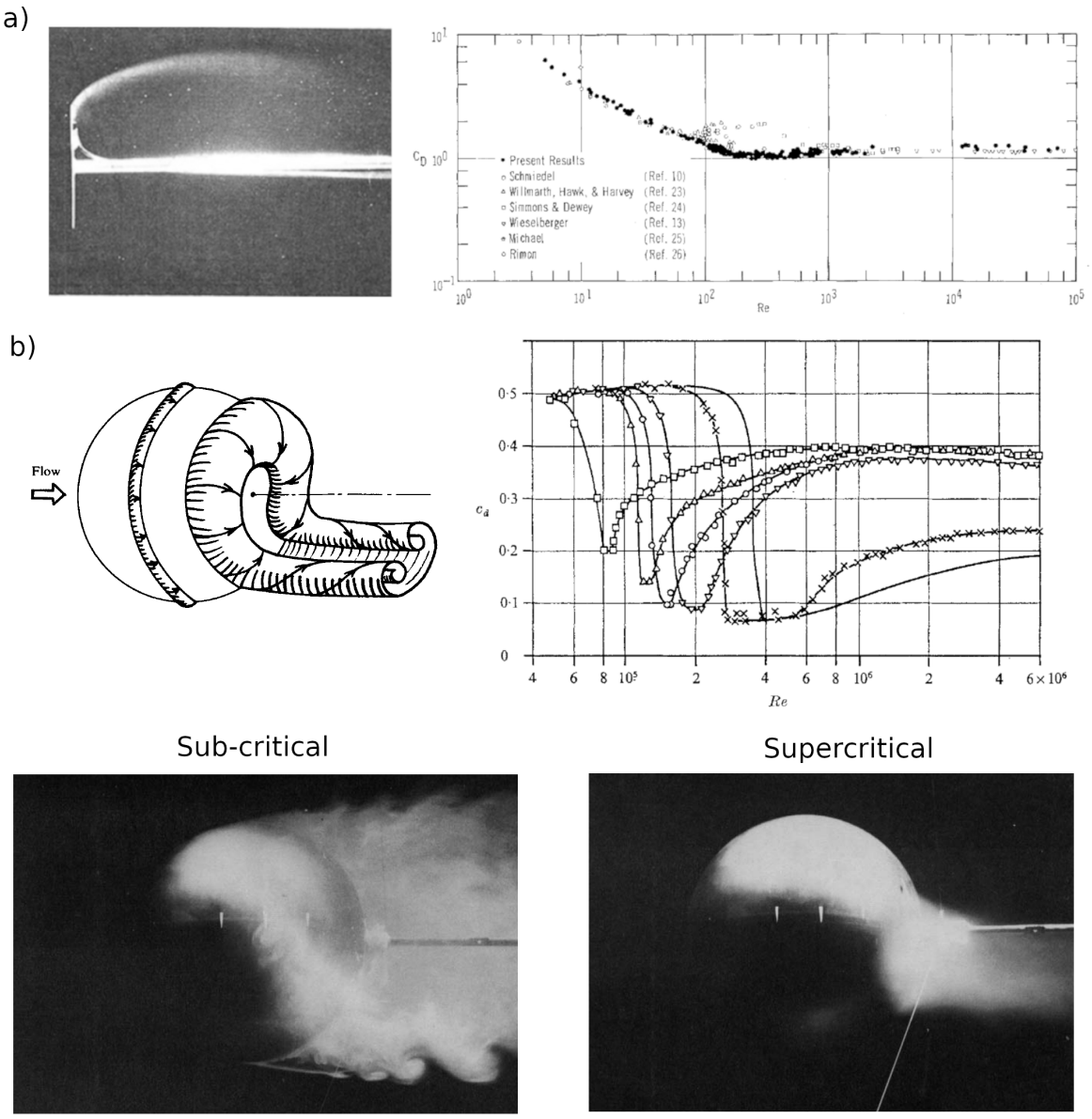

Figure 1.1: Mean wake and C_D vs Reynolds of a disk facing the flow(a). Mean wake of a sphere, C_D vs Reynolds for different roughness and the subcritical and supercritical flow conditions(b). Taken from [84], [96] and [1].

bubble that does not change with the increasing of the speed. This wake stabilization is traduced in an almost constant C_D values above $Re = 2 \times 10^2$, as seen on the right chart. The C_D values below this stabilization evidence dependency with Reynolds, given by the wake's early formation on the viscous-dominant (low Reynolds) flow range. Similar results are obtained for three dimensional cubes facing the flow, as demonstrated by Raul and Bernard [93]. The reason behind this similar C_D trend is, again, the separation induced by the sharp edges of the geometry. In fact, the wake structure for these two bluff bodies is quite similar despite the differences between the models. The flow over a sphere is slightly more complex that the facing-flow disk or cube. An instantaneous image of the wake is shown in the left part of figure 1.1b, evidencing the recirculating near wake and a couple of streamwise vortexes. Instead of a complete stabilization of the C_D above the viscous-dominant range, the circular shape induces a particular condition known as critical or transitional in which the C_D values shown a drop to lower levels at a certain critical Reynolds number (Re_c), as seen on the chart of figure 1.1b. It is known that for smooth spheres the drag crisis occurs near $Re_c = 4 \times 10^5$, but the increasing roughness of the sphere's surface and the increasing flow turbulence reduce this value, as demonstrated by Achenbach [1] and Clamen and Gauvin [37]. This is due to the energizing of the boundary layer surrounding the sphere prompting the flow attachment and delaying the separation, therefore reducing the drag. The sub-critical and supercritical conditions of the sphere's near wake can be observed in figure 1.1c and a complete description of these states was given in Taneda [110] and Taneda [111]. The previous results shown the time-averaged aerodynamic behavior over the sphere, but within the wake there are instabilities given by the irregular flow separation. Achenbach [2] and Calvert [28] evidence the wake unsteadiness of a sphere through the Strouhal number, expressed in equation 1.2.

$$St = \frac{f \cdot L}{V_\infty} \tag{1.2}$$

Where f is the frequency of fluctuation and L is the reference length, which in the sphere is typically the diameter. In the Achenbach [2] study, the oscillations of the wake were measured with a hot-wire anemometer on the $400 < Re_D < 5 \times 10^6$ range, and expressed in Strouhal number versus Reynolds (figure 1.2b). This study evidence a sinusoidal fluctuation of the wake indicating a regular vortex shedding between the $Re_D = 6 \times 10^3$ and $Re_D = 3 \times 10^5$. For Reynolds above critical, the periodicity of the signal disappears. A representation of the wake configuration on regular vortex shedding is presented in figure 1.2a. These last results were confirmed by Calvert [28], that found for Reynolds numbers above $Re_D = 10^4$ a Strouhal number of $St = 0.19$ through hot-wire anemometry.
The drag crisis and shedding phenomena are also present in two dimensional cylinders, as demonstrated by Barbi et al. [12], Bearman [16], Williamson [124], Szepessy and Bearman [109] and many others; and they present the same dynamic characteristics but in this case with a bi-dimensional behavior. Actually, the Strouhal values for cylinders below critical Reynolds ($Re_c = 4 \times 10^5$) reach $St = 0.2$ (Rodríguez et al. [94]), remarkably similar to the precedent values. For higher Reynolds the Strouhal tend to double this initial value. The Strouhal number of the cylinder versus Reynolds from different studies and the regular vortex shedding sketch are reported in figure 1.2b.

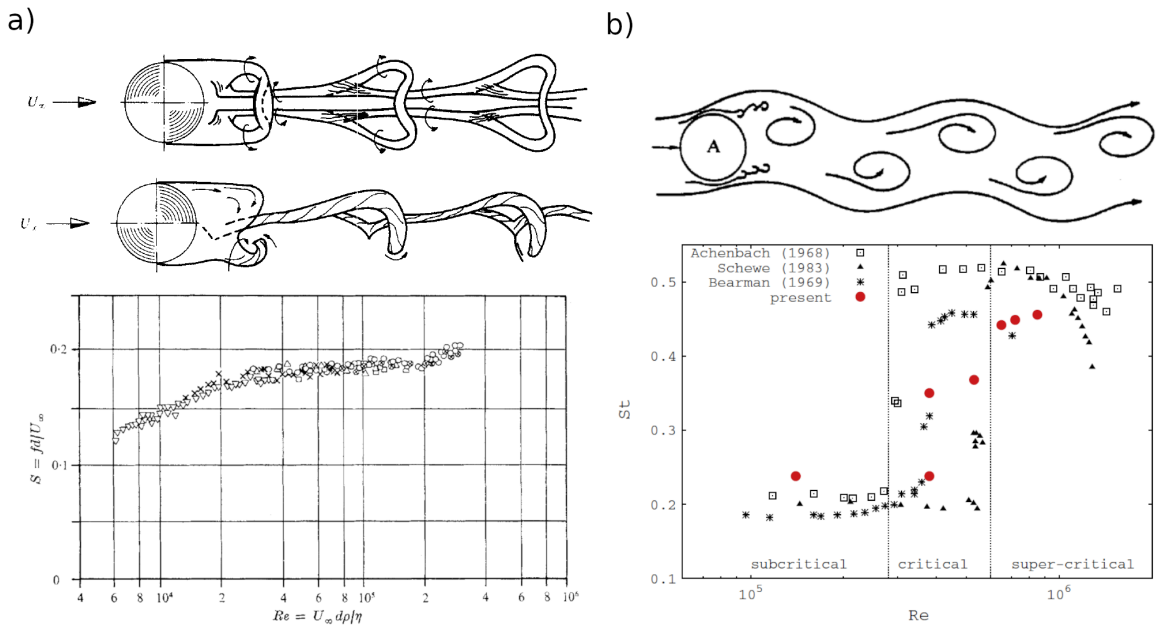

Figure 1.2: Regular vortex shedding and Strouhal vs. Reynolds for a sphere(a) and a two-dimensions cylinder(b). Taken from [2], [12],[97],[94].

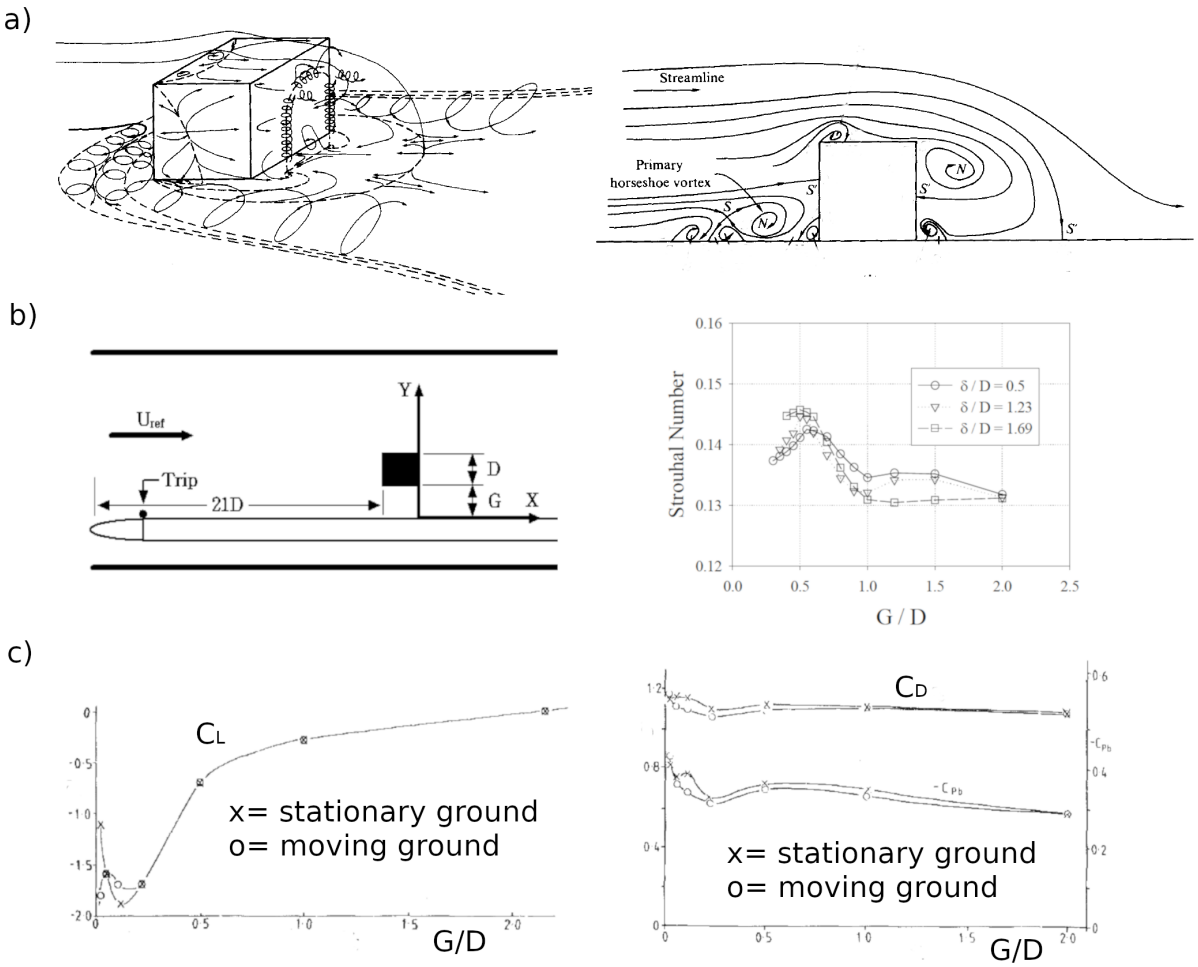

Figure 1.3: Near-ground bluff bodies' flow. Taken from [66] and [71]

Once the main aerodynamic characteristics of the bluff bodies were defined, a key border condition of the vehicle simulation problem needs to be settled: the ground. The presence of the floor restrain the vertical symmetry of the flow field and set off the under-body flow, both generating non-symmetric pressure distributions regarding the horizontal plane. Product of this, the wake of near-ground bluff bodies and their dynamics are strongly modified.
Early studies of Hunt et al. [66] depicts the flow field around a cube settled on the floor, identifying the primary structures generated by the body-ground interaction. In the left image of figure 1.3a is shown a cube on the ground with the horseshoe vortex structures ahead and the recirculating structures behind. In the right image there is a vertical cut of the symmetry plane, where can be identified the main average structures of the wake. A recirculating bubble is observed on the wake of the body composed by two counter rotating vortexes, being the top the dominant. Even if the body is far from a vehicle model the aerodynamic structures shown certain characteristics that correspond with it, as will be further detailed in the successive paragraphs. Nevertheless, this study has a major problem regarding the simulation of a vehicle, there is no underflow. To address this issue, Kim et al. [71] and Hwang and Yao [67] performed experimental and computational studies of cubes near to the ground with a certain gap, as shown in figure 1.3b. They both find the Strouhal number of the cube far from the ground around $St = 0.13$, and the closeness to the ground produces different effects on this value. The Strouhal number tend to grow when the boundary layer have the order of magnitude of the gap, and to reduce when the boundary layer is above the cube. Still, the variations are small and the Strouhal number remains at the same order of magnitude.
Furthermore, Bearman [17] analyzed the effect of still and moving floor on the pressure distribution over the cube with a certain clearance G. Their results are shown in figure 1.3c. They highlight that the pressure distribution surrounding the body is more affected by the presence of the ground than its relative movement. Moreover, the moving ground has more impact on the lift of the body than the drag, showing for the latter almost no changes. This modifications on the lift happen for ground clearances below $G/D = 0.25$.

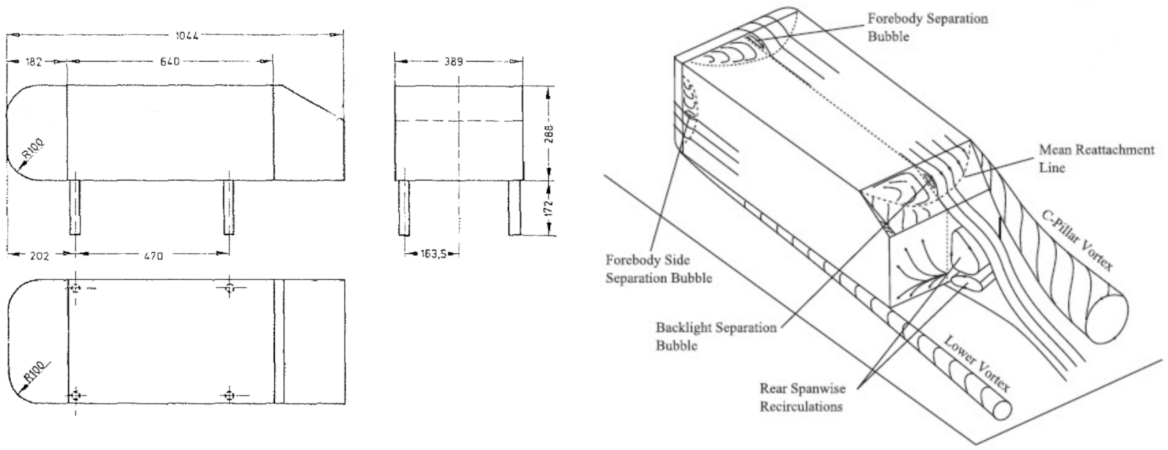

Figure 1.4: Ahmed body geometry and wake flow field for $\varphi = 25°$. Taken from [3], [106].

As seen, all bluff bodies respond to merely the same wake configuration compose

by a predominantly separated and recirculating aft flow that sheds with a predictable frequency for mid and high Reynolds numbers. However, none of this bodies represents a real vehicle. In early wind tunnel testing of vehicles, the models were made in order to replicate a certain vehicle geometry. In this way each model respond to the necessity of the vehicle that was represented, being unique on their shape and dimensions. For example, Romberg et al. [95] used models of *Dodge Charger*, *Dodge Coronet*, and *Plymouth Road Runner* at 3/8 scale; while Hucho et al. [64] tested a *VW 1600 Notchback* and a *Porsche 914*. From a more academic point of view some simplified models were developed, as resumed in Le Good and Garry [73]. This wide variety of models quickly became a problem, since there was not an unique geometric reference for the aerodynamic representation and comparison of vehicles and flow control devices. The first model that became a benchmark on the automotive field was the *Ahmed body*, represented in figure 1.4. It was developed by S. R. Ahmed and first introduced in Ahmed et al. [3]. This model represent the main characteristics of a near-ground vehicle: bluff shape, length bigger that the height and width, small ground clearance regarding the height and a rear part that can be converted from a "Hatchback" to a square back vehicle by only changing the top trailing edge's drop angle. In his research, [3] evaluated the C_D trend with varying the top trailing edge slant angle, φ, and found that the drag reaches a minimum around 12°. For higher angles the values of the C_D grow until reaching a maximum near 30° where the values drop to the initial condition. The C_D in function of the slant angle φ are presented in figure 1.5.

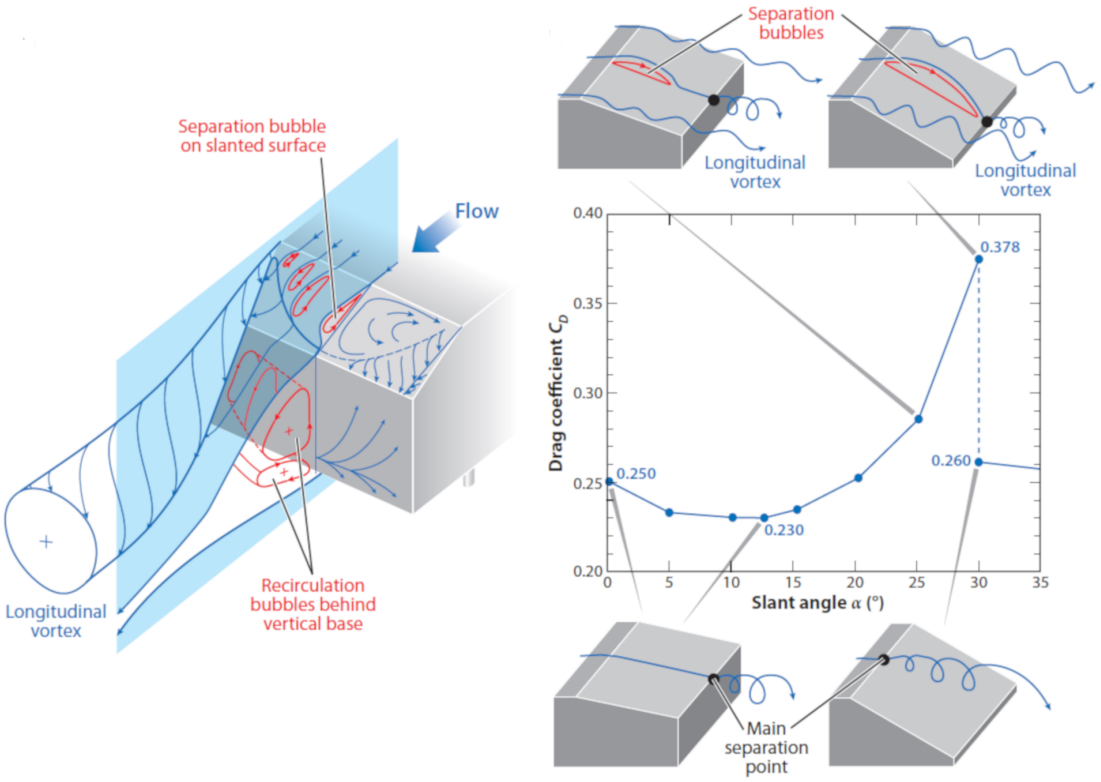

Figure 1.5: Ahmed body drag trends with the slant angle φ. Taken from [36]

Maybe the less accurate representation is the vehicle's front part since the model has a rounded front, like an ogive. It is clear that there is no vehicle with such a front shape. Actually, real vehicles have (in majority) a slanted front. The lack of

this geometry on the *Ahmed body's* fore presents two important problems: The fist is the absence of a vertical component on the aerodynamic forces due to the front shape, and the second is the loss of the "A-pillar" vortex. The latter is a vortical structure generated by the impact on the incoming flow with the slanted front, that grows towards the upper part following the front edge. Near the top this structure changes direction to the free stream flow's and trails away from the model (see Watanabe et al. [119], Paul and LaFond [88], Levy and Brancher [76]). This generates a set of two counter rotating vortexes, one for each side of the vehicle. Nevertheless this deviation from the real cases, several studies from numerical to experimental use this model to represent the flow field around a vehicle. In fact, many trucks and lorries may be well represented by this model due to theirs square fore.
The flow surrounding the *Ahmed body* presents the following average structure, represented in the right image of figure 1.4: In the front part and due to the ogive shape the flow is fully attached to the surface except for the external edges where a small separation bubble is present. The ground-body interaction generates a small horseshoe vortex similar that the one observed in figure 1.3 for the cube on the ground, that travels downstream and remains attached to the floor. The high pressure zone on the nose performs a $C_p \approx 1$, that decrease towards the outside. The C_p is defined in equation 1.3:

$$C_p = \frac{p_i - p_\infty}{q_\infty} \tag{1.3}$$

On the sides of the body the pressure stabilizes to a value $C_p \approx -0.1$. In the rear part, instead, there is a large separated flow region with a recirculating bubble composed by a toroidal vortex parallel to the rear base and a couple of streamwise vortexes that trails away from the top slanted trailing edge. This two characteristic structures can be observed in figure 1.4 and 1.5. In the slanted top part a small separation bubble may appear for angles above 10°. The pressure on the rear base presents an almost uniform distribution of $C_p \approx -0.2$. Observing the wake's midplane flow (figure 1.5) the recirculating vortexes are not symmetric, being the top part bigger in size and therefore presenting a stagnation point near the bottom of the model's rear base. A saddle point is present at approximately one height of distance from the rear base and at merely the same height that the previous one, where the near wake ends. Lastly, the streamwise counter-rotating vortexes on the top are generated by the interaction of the incoming flow with the slanted top, in an opposite configuration than the previously cited "A-pillar" vortexes, and when this angle is zero these are not present.
Now that the average flow field surrounding the body is fully defined, it is interesting to evaluate the drag produced by each one of these flow structures. Hucho and Sovran [63] proposes two ways of analyzing it: from the vehicle's and from the stream's perspective. The vehicle's perspective is not practical since is the integral of all drag components over the body's surface. The stream's point of view considers the momentum of the flow over a control volume containing the model, and the resultant force that represents the drag is given in equation 1.4.

$$D = \int\int_A (p_{t,\infty} - p_t)dA + \frac{\rho}{2}\int\int_A (U^2 - u^2)dA + \frac{\rho}{2}\int\int_A (v^2 + w^2)dA \tag{1.4}$$

This equation was developed considering the main three phenomena involving the stream: the first part represents the defect of stagnation pressure, the second the defects on the dynamic pressure and lastly the streamwise vortex drag, being all these three components strongly influenced by the shape of the model inside the volume.

For example, in the case of the *Ahmed body*, a slanted rear reduce the wake dimension and therefore the static and dynamic pressure defects, but also increment the vortex drag components.
An interesting conclusion that [63] reach is that the most important part for this kind of subsonic vehicles (road vehicles including cars, vans and trucks) is the rear part, due to the complex separated structures generated. This concept is in complete agreement with all bluff bodies analyzed previously, since they present a complex and unsteady wake. This also give us a hint about the control of the flow: if the target is modifying the drag of a bluff body, the actions should be taken on the rear part which is the most sensible to drag changes.

1.2 Squareback bodies' aerodynamics

A growing interest concerning the near-ground squareback models have been developed in the last years, prompted by the necessity of improving the aerodynamic of heavy-vehicles. These vehicles travel for long distances at relative high speeds, so an improvement on theirs aerodynamics could be traduced in an important reduction of the total energy consumed. A deep investigation on this issue was performed on Choi et al. [36], where a general overview of the time-averaged heavy vehicle aerodynamics is given with a set of different flow control techniques in order to reduce the drag.

1.2.1 Squareback Ahmed body

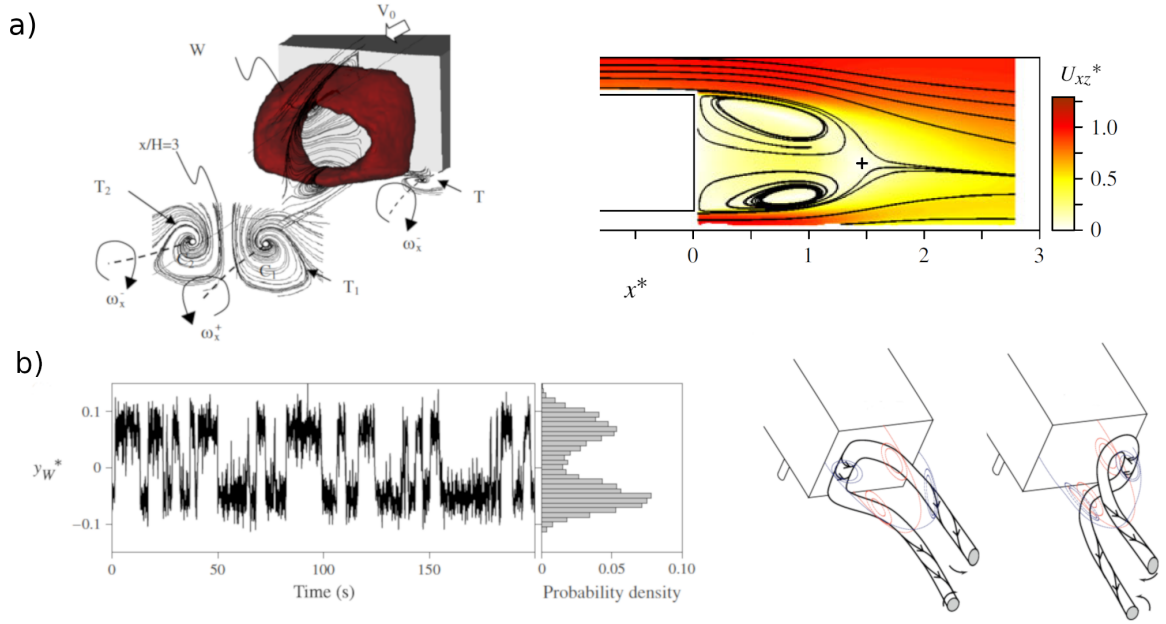

Figure 1.6: Squared-back Ahmed body wake characteristics. Average wake flow: Recirculation toroidal structure,streamwise counter-rotating vortexes and symmetry plane flow (a). Random switching between two symmetric positions of the rear's pressure center on the horizontal axis, namely bi-stability (b). Taken from [98], [58] and [49].

Grandemange et al. [58] studied a squared-back *Ahmed body* model at $Re = 9.2 \times 10^4$ mounting several pressure taps distributed on the body and in particular on the rear base. The high density of pressure taps together with the high sampling frequencies and hot wire measurements allowed a complete characterization of the near wake dynamics, and PIV (Particle Image Velocimetry) measurements helped understand the mean characteristics. In this study the fore-body presents the same flow architecture than the previous example, presenting the same pressure distribution. The differences are present in the rear part, as will by successively explained.
The wake's average behavior is represented in the left image of figure 1.6a, showing a recirculating toroidal structure and two counter-rotating vortexes that trail away from the model. This particular image was taken from the studies of Rouméas et al. [98] for a squareback body. It represents the same average wake of [58], and was used due to the clarity of the representation. The flowfield on the symmetry plane is recontructed from PIV measurements in the right image, evidencing the counter-rotating vortex structure and theirs relative dimensions, as well the saddle point where the near wake ends ($1.5x^* = x/W$). The underflow on the mid plane presents a speed higher than the freestream flow, an expected effect since the flow accelerates due to the reduction of the passage section below the model.
Once the average structure is defined, the time domain characteristics were analyzed. For a long time scale ($T = 10^3 H/V_\infty$) the authors found a phenomenon that consist in the random switching of the pressure center on the rear base between two horizontal symmetric positions. This Reynolds-independent phenomenon is also known as bi-stability of the wake and can be observed in figure 1.6b, on the instantaneous pressure coefficient position on the horizontal axis (y_w^*) and a sketch of the two possible instantaneous wake structures performed by Evrard et al. [49]. For a short time scale ($T = 5H/V_\infty$) the shedding phenomena was observed with coherent oscillations on the vertical and horizontal plane, presenting a peak of energy near $St = 0.17$ and $St = 0.13$ respectively.
A different study performed by Volpe et al. [117] for the same model found for $Re_H > 5 \times 10^5$ the same random bi-stable behavior at long-time scales. In addition, the sensibility of the bi-stability was evaluated regarding to the yaw angle evidencing that it locks itself in one of the two positions when the yaw angles are above $\pm 1°$. The spectra of pressure fluctuations on the rear and hot-wire measurements on the wake feature a dominant energy at $St = 0.13$ and $St = 0.19$ corresponding with the vortex shedding of the trailing edges. Furthermore, another peak of energy near $St = 0.08$ was found. This peak was not identified by [58], and corresponds with the streamwise fluctuation of the near wake. This phenomena was also addressed by Duell and George [45] and Khalighi et al. [70] at $St = 0.07$ and is known as bubble pumping.
The pressure distribution on the rear base was decomposed by POD, evidencing four main modes containing almost 80% of the whole signal energy. The first mode (50% of the energy) is a horizontal symmetry breaking mode (HSB), coherent with the bi-stability and the horizontal vortex shedding. The spectra of the reconstructed first mode's signals evidence a peak at $St = 0.13$, supporting the representation of the vortex shedding. The second mode (30% of the energy) evidences a symmetric distribution with maximum values on the vertical center line. The Strouhal peak of this mode is present at $St = 0.08$, evidencing the bubble pumping. The third and fourth modes (10% of energy each) represents a similar bubble pumping mode and a vertical symmetry breaking mode (VSB) respectively. The spectra of the last mode evidence a peak near $St = 0.19$, linking this mode to the vertical vortex shedding.

Evrard et al. [49] also found the bi-stability phenomenon on this same model and highlights also the sensibility to the yaw angle, at $Re = 4 \times 10^5$. Actually, they manage to correct the geometric yaw angle regarding the aerodynamic one by tracing the bi-stability.
Brackston et al. [26] confirms all previous findings for Reynolds between 2.3×10^5 and 4.4×10^5, with vortex shedding at $St = 0.2$. Moreover, achieves a model of the bi-stability from which creates a law control in order to modify the wake's topology through lateral moving flaps.
Bonnavion and Cadot [22] studied the sensibility to yaw and pitch angle. The yaw results shown agreement with the previous ones and similar sensibilities were found for the pitch angle. The representation of the bi-stability is expressed as defined by [58], in function of the pressure coefficient gradients (equation 1.5)

$$g_y^* = \frac{dC_{p_y}}{dy}; g_z^* = \frac{dC_{p_z}}{dz} \tag{1.5}$$

The figure 1.7 show the maps of g_y^* (horizontal) and g_z^* (vertical) on the rear base for the changing angles. As previously demonstrated, the bi-stability is presented on the horizontal plane (y) as shown in figure 1.7 for 0°.

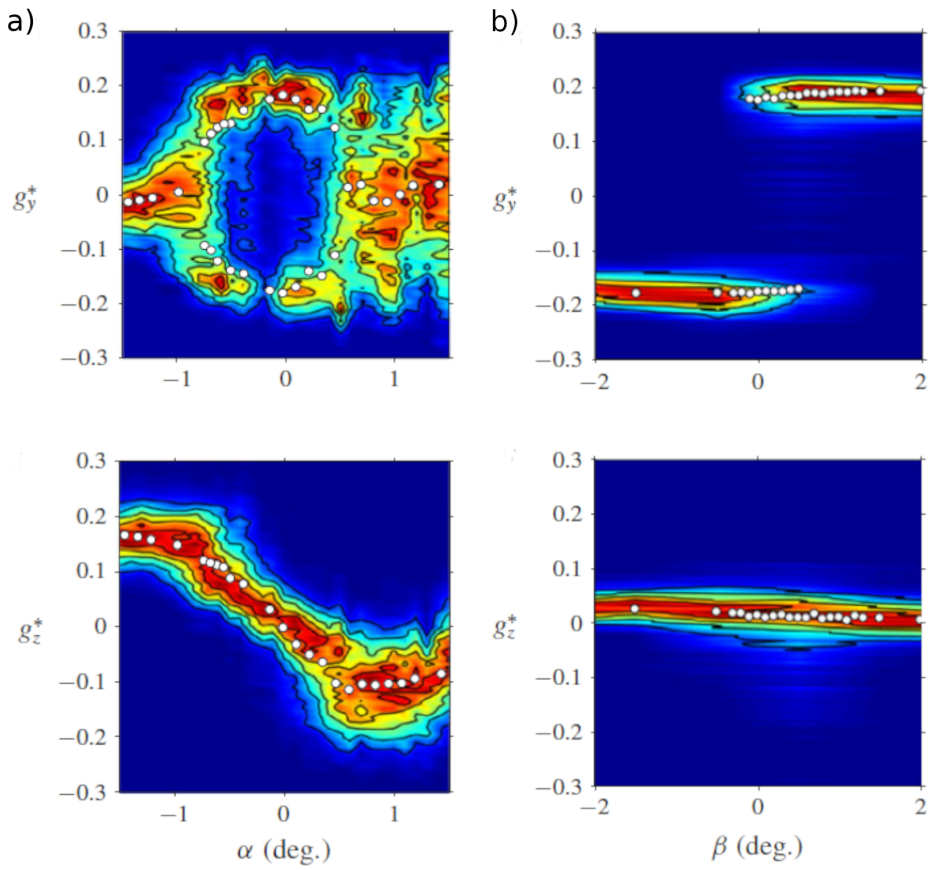

Figure 1.7: Sensibility of the bi-stability to the Pitch (α) and Yaw (β) angles. Taken from [22].

With the changing of the pitch angle (α) there is a ±0.5 range from the aligned position in which te bi-stability is present and there is no pressure gradient on the vertical axis. above this limits the lateral bi-stability disappear and the vertical gradients grow linearly. The latter shows a stabilization for angles above 0.8° that could

be associated to the effect of the ground. It seems that above ± 0.5 the wake tend to a stable position near the top or bottom instead of a lateral state. When changing the yaw angle (β) the bi-stability disappears in the same range cited before and the wake locks in one of the symmetric states, but in this case without changes on the vertical gradient regarding the aligned case.
Similar results were found by Evstafyeva et al. [50] at numerical low-Reynolds calculations ($Re_H \approx 400$). They further evidenced the bi-stability and also three states within: unsteady symmetric, steady asymmetric and unsteady asymmetric, that change with the growing Reynolds. In this study was also evidenced the importance of the underflow, showing that the dominant interaction on the top and bottom shear layers (unsteady asymmetric state) is only possible when the underflow is sufficiently intense. Also numerically but at $Re \approx 4 \times 10^5$, Lucas et al. [78] studied the same squareback model evidencing the lateral bi-stability. In this particular case and due to the short simulation, a fully recreation of this phenomenon was not possible. Nevertheless, the switching of the wake in two lateral mirror modes was observed and the structure proposed by Grandemange et al. [58] of the vortex shedding modes was confirmed, as well as the correspondent Strouhal numbers. The ground effect over the bi-stability was not analyzed, but was evidenced that the presence of the ground may lock it in a top or bottom position, being only possible the lateral instability.
It can be concluded that the squareback *Ahmed body* wake presents the main following dynamic characteristics: 1. Bubble pumping at $St \approx 0.07$, 2. Vortex Shedding mode at $St \approx 0.17$, 3. Lateral bi-stability of the wake for Reynolds numbers above 400 and occurring laterally at a time scale of $T = 10^3 H/V_\infty$. These attributes are common for all bodies presenting a squareback rear part but some differences may appear for different geometries. In the next section an overview of some of the most salient variations regarding the squareback *Ahmed body* will be exposed and analyzed considering the wake's behavior and their dynamics.

1.2.2 Other squareback bodies

Even if the *Ahmed body* is a nice representation of a road vehicle, it has been demonstrated that has a lot of room for improvements. In order to overcome the model's limitations some researchers have developed models that fit better the aerodynamics of certain types of vehicles, with more or less accuracy. The most salient ones are resumed in Le Good and Garry [73] with theirs main aerodynamic characteristics. The first noticeable difference of the squareback *Ahmed body* with a real vehicle, in particular a van or a lorry, is the aspect ratio ($AR = Height/Width$), being those higher than wider. Williams et al. [123] studied the aspect ratio of 8 rounded rectangular bodies with the same frontal area, showing that the drag coefficient reduces with the increasing of the height. Unfortunately, no information of the flow field is given. Venning et al. [116] also studied the effect of the AR but on a $\varphi = 25°$ slanted *Ahmed body*, with improved results respect to the previous study. Besides the difference with the squareback model, a couple salient observations can be made: the average near-wake structure retains the original toroidal shape, but in this case the down-wash grows with the AR. The test was performed at $Re = 3 \times 10^4$ using as a length reference the square root of the frontal area of the original *Ahmed body*. Moreover, Grandemange et al. [59] evaluate the bi-stability of the squareback *Ahmed body* in function of the $AR = H^*$ and the ground clearance $C^* = C/H$. It exposes that the bi-stability tend

to switch between two symmetric positions over the longer axis as shown in figure 1.8a. The ground proximity evidence the same effect of the underflow proposed by Evstafyeva et al. [50]: the ground clearance need to be at least 0.09 times the model's height in order to settle the bi-stability, as shown in figure 1.8a. Interestingly, these two conclusions are the same independently from the very different Reynolds numbers of each study.

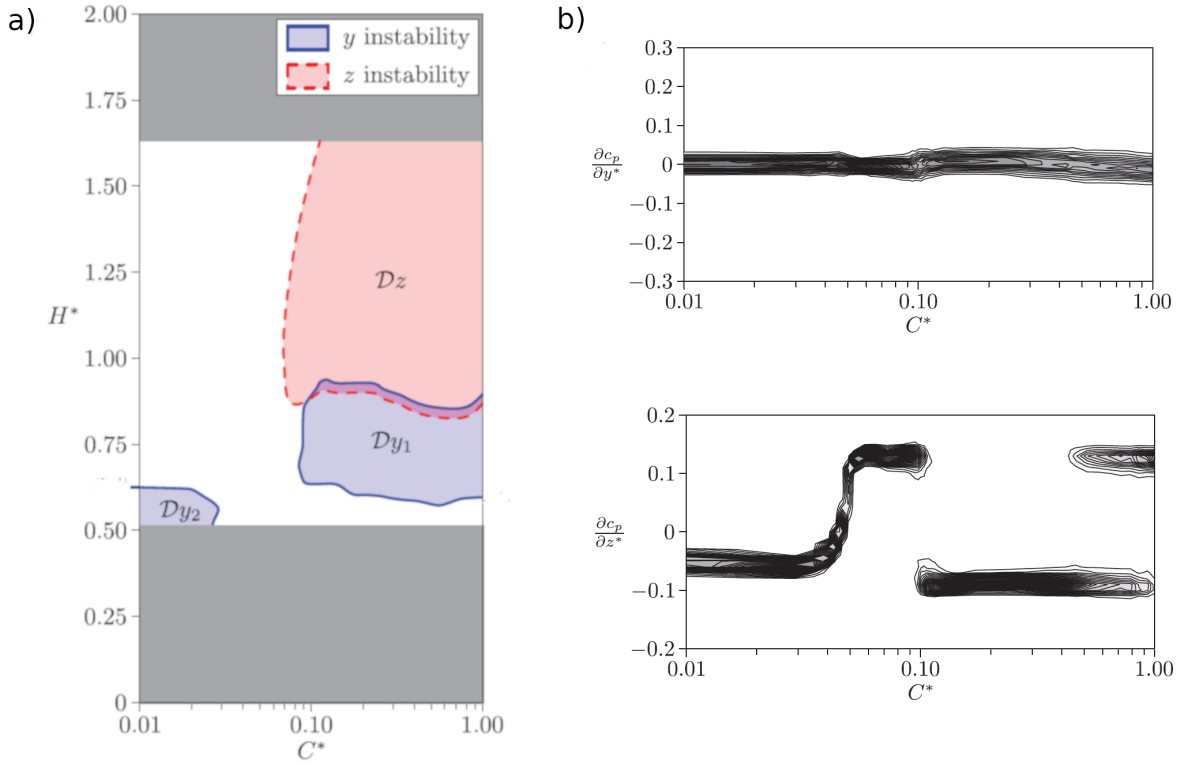

Figure 1.8: Variation of the bi-stability with the aspect ratio and ground clearance (a) and sensibility to the ground clearance for $H/W = H^* > 1$ (b). Taken from [59]

In particular for the top-bottom bi-stability (when $H/W > 1$) there is a marked sensibility to the ground clearance, showing the bi-stability only for $C^* = C/H \approx 0.1$ and $C^* > 0.5$ (see figure 1.8b). For the other conditions, the wake locks in one of the stable positions without switching.
Additionally, Dalla Longa et al. [42] compared the results of a squareback *Ahmed body* with a simplified lorry of $AR = 1.15$ (see European lorry model in figure 1.9). The relation of the bi-stability with the AR and ground clearance defined in figure 1.8 is verified, reaching top-bottom bi-stability for $AR > 1$ and right-left for $AR < 1$. The pressure fluctuations on the lorry model's rear are analyzed, showing two peaks of energy at $St \approx 0.08$ for the bubble pumping and a $St \approx 0.18$ for the vortex shedding.

Considering cars and commercial vans, the lack of the slanted front angle of the *Ahmed body* is another disadvantage on the representation of these vehicles. Littlewood and Passmore [77] use the *Windsor model* presented in figure 1.9. This features a slanted front which generates the A-pillar vortex, reaching a more realistic aerodynamic configuration. Perry et al. [91] and Pavia et al. [89] evidence that the lateral bi-stability is present for the *Windsor model* as in the squareback *Ahmed body*. This

further evidences the bi-stability as a phenomena characterizing squareback bluff bodies, independent from the rest of the geometry. Regarding the wake dynamics, [89] found a Strouhal number of $St = 0.07$ for the bubble pumping and $St = 0.13$ for the vortex shedding.

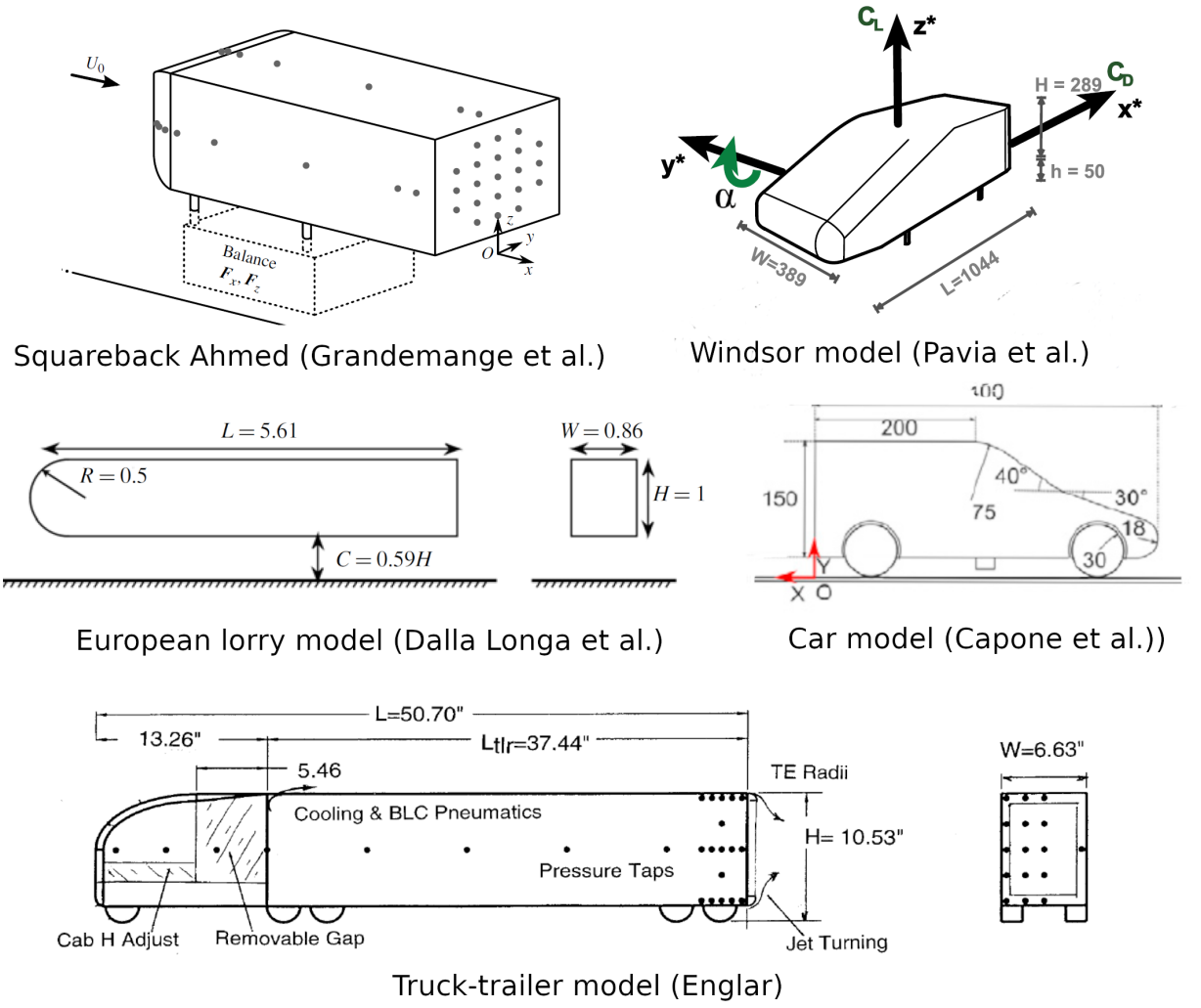

Figure 1.9: Resume of some of the different squareback models. Taken from [58],[89], [42], [46],[31].

Even if this last model approaches a real van/car case, the front angle is not realistic. In addition, a key component of all vehicles has not cover by any of the precedent studies: the wheels. In order to address these absences on the models, Sardu et al. [104] and Cerutti et al. [35] used a realistic van model, also called *GM Model*. This model respond to the geometry of a commercial van scaled 1 : 10 and performing a realistic slanted front angle and wheels, and will be used in this research. Further information will be given in section 2.1. A similar model was used by Capone and Romano [31], with merely the same scale and a more complex frontal shape performing a double slant angle. The profile of the model is shown in figure 1.9. Unfortunately, no dynamic information of the near wake is given.
There are also further models representing other characteristic shapes, as trucks and tractor-trailer trucks. For example, Englar [46] (figure 1.9) analyzed a fully tractor-

trailer configuration while Minelli et al. [83] only the front (cabin). Manosalvas-Kjono et al. [79] and Rao et al. [92] perform computational analysis of a long body with $AR > 1$ and a curved top front part, and Van Raemdonck and van Tooren [114] studied experimentally a rectangular-sectioned body with square front and rear.
Finally, the apex of geometric similarity is the vehicle itself. In some cases this is the only way of obtaining an accurate analysis, as for example in racing cars. Porsche and Volvo wind tunnels [21] or the Pininfarina wind tunnel [39] have enough size to test full-scale models. Recently, Bonnavion et al. [24] performed a dynamic analysis of minivans in a full-scale configuration where the wake dynamics was explored. The bi-stability present of squareback models was also observed on the minivans, with the same characteristic parameters found for the models.

From the studies considered regarding the squareback geometry it can be concluded that the average and frequency-resolved wake presents similar characteristics for all the different geometries evidenced. Actually, the mean toroidal recirculating zone remains unchanged and the Strouhal values regarding the bubble pumping and vortex shedding modes have the same order of magnitude. The bi-stability is also present with the same characteristic times. This highlights the independence of the wake characteristics in relation to the geometry, and the fact that this average and dynamic features are observed also for a real-case scenario demonstrates the high level of similarity of the squareback models. In table 1.1 are presented the wake's main characteristics for the most relevant models previously cited.

Model	Reynolds	Bi-stability	Wake pumping	Vortex shedding
Sphere [2]	$\times 10^5$	-	-	St=0.18
Box [71]	18×10^3	-	-	St=0.13
Squareback Ahmed Body [58]	9.2×10^4	Horizontal	-	St=0.13;0.17
Squareback Ahmed Body [42]	3.3×10^4	Horizontal	St=0.04	St=0.08-0.2
European lorry model [42]	2×10^4	Vertical	St=0.08	St=0.18
Windsor body [89]	7.7×10^5	Horizontal	St=0.07	St=0.13
Berlingo (Full-scale) [24]	5.13×10^6	Vertical	-	-
Partner (Full-scale) [24]	5.76×10^6	Vertical	-	-

Table 1.1: Resume of the main dynamic wake characteristics of some models and full-scale vehicles.

1.3 Drag reduction methodology

One of the main goals of the aerodynamics of vehicles is the drag reduction , and this could be achieved by various means. This thesis is focused in a flow control technique and platooning of vehicles for the drag reduction, that will be exposed next.

1.3.1 Passive and active flow control

Regarding the flow control, there are two techniques available: **passive flow control** (PFC) and **active flow control** (AFC). Both of them modify the flow field surround-

ing the initial geometry but with a significant difference: in order to perform, the AFC uses external energy while the PFC uses the energy of the flow itself.

PFC devices like wings, spoilers, flaps and boat tails are used mainly in motorsport and some particular street vehicles. The main restriction for this kind of appendices is the homologation, since they may become a potential harm in case of accidents or interfere with the driver's field of view. Another important disadvantage is the vehicle's utilization, since the settling of aerodynamic devices may compromise its operation. Finally, a passive device cannot adapt itself to different flow conditions, and this lack of flexibility leads to efficiency loses. In the following section some of the most salient PFC devices will be exposed.

The effect of a **splitter plate** on the rear part of a squareback *Ahmed body* (see figure 1.10a, left image) at $Re \approx 1 \times 10^6$ is studied by Gilliéron and Kourta [57]. The drag of the model evidence a reduction while the plate moves away from the model, reaching a minimum of 12% when the distance is $0.5x/H$. The drag reduction is product of the trapping and stabilization of the counter rotating near wake.

The **base cavity** is shown in center image of figure 1.10a. Balkanyi et al. [11] and Evrard et al. [49] studied this technique experimentally, Lucas et al. [78] numerically and Khalighi et al. [70] numerically and experimentally. Khalighi et al. [70] uses a squareback body with four plates mounted on the rear forming a cavity of $0.5H$ depth with $0.08H$ offset regarding the laterals, top and bottom model surfaces. The experimental results of the base cavity shown an increasing on the base pressure, and consequently a reduction of the mean drag in 20% regarding the baseline. Furthermore, the $St = 0.07$ (bubble pumping) energy peak is reduced, together with the wake's turbulence. The numerical result of the unsteady RANS shown good fit with the precedent results, validating the algorithm. Balkanyi et al. [11] studied the same cavity configuration, in this case founding a $St = 0.107$ peak of energy for the baseline, corresponding with the vortex shedding. Again, the cavity performs an increasing of the base pressure and a reduction of the overall base-pressure fluctuations. Furthermore, the vortex shedding peak is suppressed. Evrard et al. [49] demonstrates that when the base cavity reach a certain critical dimension ($0.24H$) the bi-stability is suppressed and the wake becomes toroidal (symmetric) and the overall turbulence is reduced. The same response of the bi-stability is found by Lucas et al. [78], but for values slightly higher of the cavity depth. The latter study also highlights a reduction of the energy intensity around the vortex shedding mode, found at $St = 0.16$. No evidence of a reduction on the turbulence is observable as the previous study suggest, but may be legate to the lack of frequency resolution of this numerical case.

The **boat tailing** passive technique is shown in the right image of figure 1.10a. Bonnavion and Cadot [23] and Perry et al. [91] analyzed the effects of boat tailing only on the top and bottom trailing edges of both squareback *Ahmed body* and *Windsor body*. Particularly, these two experiments evidence the same trend of the drag reduction with the boat-tail angle, and with similar values regarding figure 1.5. Both authors claim a weakening the bi-stability phenomena with the increasing taper angle, almost disappearing when both angles coincide in 12°. This is also the lowest drag condition, that manifest the minimum size of the wake.

Alamaan et al. [7] numerically tested different **flaps** with different angles on the top trailing edge of a squareback model, reaching drag reductions above 10%. Unfortunately there is no data about the wake dynamics. Furthermore, Capone and Romano [31] (figure 1.10b) experimentally studied the effects of flaps on the top and vertical

trailing edges of a squareback van-like model, reaching 6% of drag reduction and damping the flow oscillations. Schmidt et al. [105] experimentally tested the effect of four flaps in the rear part of a *General European Transport System* (GETS) body, similar to the *European lorry model* shown in figure 1.9. It was evidence that the flaps were effective until 15°, angle from which the wake behaves as a squareback body. A drag reduction of 17% was achieved for 15° of flaps deflection together with a reduction of the near wake's recirculating region and an attenuation of the bi-stability and vortex shedding.

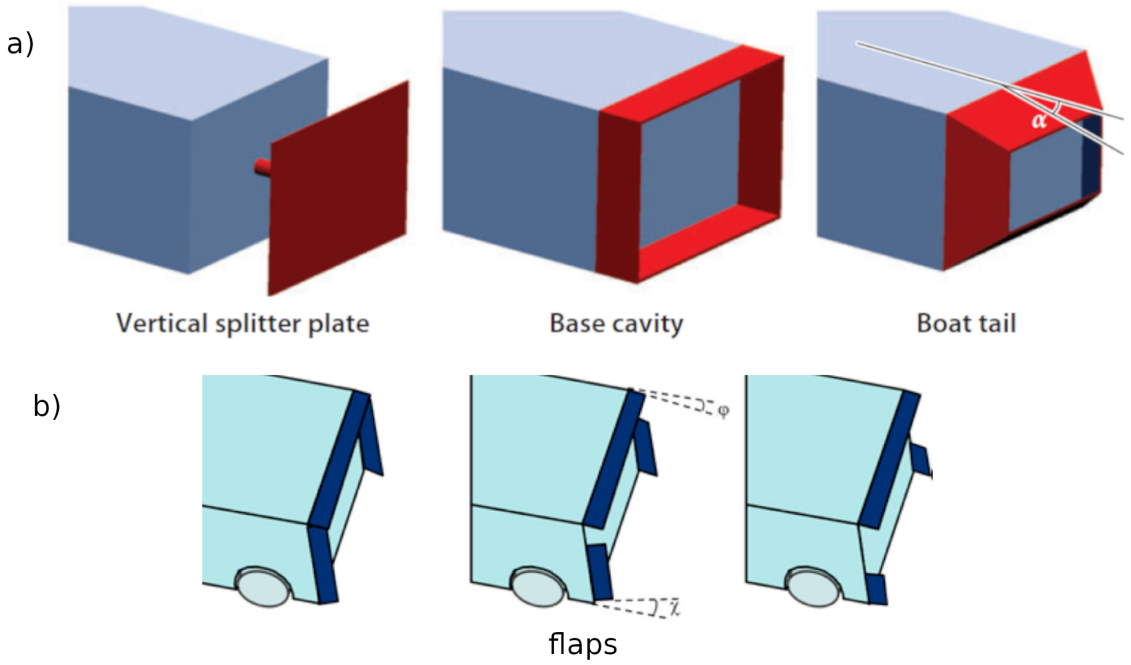

Figure 1.10: Passive flow control examples: Splitter plate, base cavity, boat tailing (a) and flaps (b). taken from [36], [31].

Also experimentally Brackston et al. [26] studied the behavior of flaps in the lateral trailing edges of a squareback *Ahmed body*. It shows that only 1° of angle of the flaps, in on direction or the other, produce the stabilization of the wake in one of the bi-stable positions. Is highlighted also the growth of the PDF's skewness of the center of pressure, certainly due to the loss of average symmetry of the wake.

As explained before, the **AFC devices** need energy to perform. This energy feed the actuators, which are the devices that act over the flow. An efficiency parameter is commonly used, expressed by the ratio of the power gain versus the power consumed defined in equation 1.6. This parameter is useful to analyze the overall cost/benefit of the control system: values above one characterize an efficient control, meaning that the energy gain given by the flow control is higher than the energy consumed by the AFC.

$$\xi = \frac{P_g}{P_c} \tag{1.6}$$

AFC is most likely applicable to aeronautics, being use to achieve higher lift coefficients, noise reduction and more, as explained by Bower and Kibens [25]. Some of the most popular actuators are flaps, suction slots, blowing jets, fluidic oscillators and synthetic jets. A review of some these actuators with theirs characteristics can be

found on Cattafesta and Sheplak [32]. However, many of this devices emigrated from the aeronautics to different fields as, in this case, the automotive. Next, a brief description of the most relevant AFC techniques will be presented with the main effects produced.

Brackston et al. studied the effect of **oscillating flaps** on the rear part of a square-back *Ahmed body*, positioned on the lateral ([26]) and top-bottom ([27]) trailing edges. Figure 1.11a shows the lateral flaps used in [26]. In order to analyze the response of the drag to the flapping, a frequency-domain test was performed by oscillating the flaps from $St = 0.005$ to $St = 0.5$. The results showed, for both lateral and top-bottom flaps, an increasing of the drag when the flapping frequency approach $St = 0.2$. Evidently this technique is not useful to reduce the drag of the vehicle, but it could be profitable from other purposes as changing the lift or drag increasing on breaking.

The **suction slots** are commonly used in separation and boundary-layer control, specially on high-lift devices and wind-tunnel boundary layer reduction. The effect of suction slots on the rear end of an $\varphi = 25°$ sloped box model was evaluated by Rouméas et al. [99]. The configuration used is depicted in figure 1.11b. Through the suction, the flow manages to follow the rear geometry of the body avoiding the separation bubble observed in figure 1.5 for $\varphi > 30°$. This technique is efficient on reattaching the flow to a surface when the pressure gradients produce the separation, thus reducing the form drag. In this study drag reductions of 17% were obtained with an efficiency of $\xi = 14$. But in a squareback body the separation is triggered by the sharp trailing edges, an the reattachment of the flow is not possible. This constricts the applications of this technique to boundary layer control.

An interesting actuator is the **synthetic-jet**, that alternates suction and blowing through the same slot. The net mass flux of this jet is zero, but through the generation of toroidal vortexes a momentum is induced that produces thrust. Evstafyeva et al. [50] perform a numerical simulation of synthetic jets on the edges of a square-back *Ahmed body* through feedback control, using the base pressure as a sensor and the energy of the synthetic jets as control parameter. The model used is shown in figure 1.11d. The open-loop results were tested for Strouhal values between 0.02 and 1, showing a stable rear-pressure zone until $St = 0.1$ and then growing when further increasing the forcing frequency. Since this study was focused on the FAFC, the open-loop results are expressed in gain of the system regarding the forcing frequency with no direct values of the relative increase of the base pressure or the drag reduction. Nevertheless the result evidence a favorable behavior of the synthetic jets considering that the base pressure grows with actuation frequencies above $St = 0.1$. Experimentally and numerically Minelli et al. [83] uses synthetic jets to control the separation over a truck cabin, in particular on the front pillars. Is found that the synthetic blowing at the characteristic frequencies of the flow energizes the boundary layer, promoting the reattachment of the flow to the lateral wall and reaching a drag reduction of 50%. In this study is also described the architecture of couple of vortexes produced by a normal-to-flow synthetic actuator, highlighting its capability of generating two pairs of counter rotating structures that trail away from the actuator in absence of vorticity stratification in a phase-averaged analysis

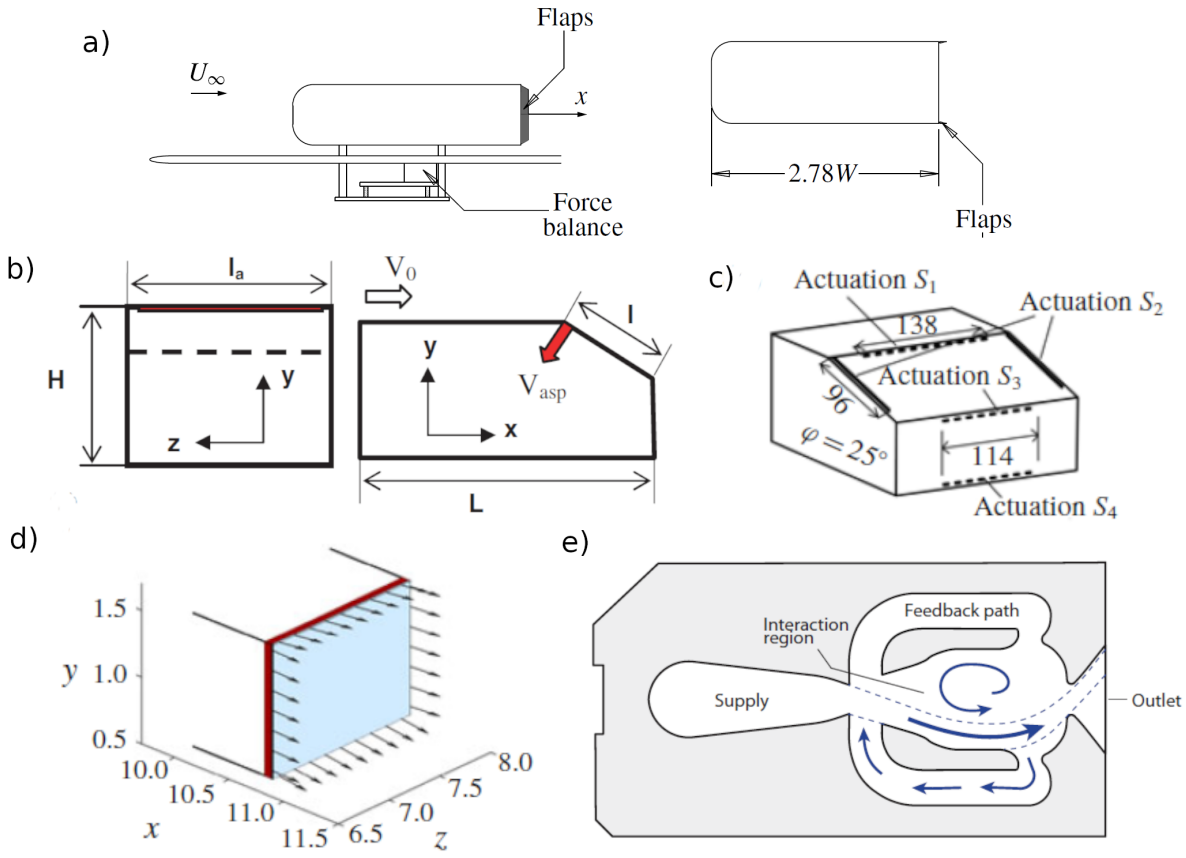

Figure 1.11: Active flow control examples: Suction, blowing, synthetic, fluidic oscillators, microjets. taken from [99],[127] [50], [32], [81]

The **pulsed jets** have the same nature of the synthetic ones but in this case also introduce a pulsating momentum. These jets oscillates between two non-negative output speeds (in most cases the lower is zero) and the frequency of actuation might be targeted to some physical phenomenon or respond to a certain control input. Barros et al. [13] studied pulsed jets on the trailing edges of a squareback *Ahmed body*. The actuation frequency was ranged through values below and above the shedding ($St = 0.13$). Was demonstrated that the natural fluctuations of the wake, namely the baseline vortex shedding frequencies, changed with the introduction of forcing. In fact, the wake's fluctuation frequency responds to the forcing frequency with a growing linear relationship. This was explained by the enhancement of the vortex shedding antisymmetry due to the forcing. When the forcing frequency reaches 2.25 times the natural one ($St \approx 0.45$), the fluctuations do not respond anymore to the forcing and recover theirs original baseline values. The base pressure evidences an increasing regarding the baseline case for all frequencies, reaching more than 25% when the forcing frequency duplicates the natural one. The fluctuation energy of the wake was increased with the growing actuation frequency, reaching a maximum when the forcing is performed at twice the shedding frequency and supporting the hypothesis of the increased vortex shedding antisymmetry. In [14], Barros et al. extended the research to to higher frequency values, reaching a $St = 14$ forcing. The base pressure showed and increase with the Strouhal achieving a maximum for $St = 0.4$, equal to the precedent research. Above $St = 1$ the base pressure achieved begins to reduce, reaching the baseline values for $St = 4$ actuation and further decreasing with the increasing frequency.
The **microjets** are mainly used to control the separation. Sandrine et al. [101] used a

distribution of $0.4mm$ drilled holes with a separation of $5mm$ on the "rear window" of a 25° slanted *Ahmed body*. These jets blown constantly at different speeds for Reynolds between 1×10^6 and 2×10^6, reaching a maximum drag reduction of near 14% and a maximum efficiency of $\xi = 18$. Also McNally et al. [81] tested microjets in the same *Ahmed body*, but in this case with a wider distribution of the actuators. The maximum drag reduction reached is 12.8%, using actuators on the upper part of the "rear window" and on the top part of the rear base simultaneously.
As in the suction slot case, this technique works well when the control performs over boundary layer or small separation due to unfavorable pressure gradients. But in the case of blunt-surface separation the effect is reduced, discarding this technique as an effective one on squareback flow separation.
An interesting actuator that produces a continuous output of flow but with oscillating direction is the **fluidic oscillator** or **fluidic actuator**, described in Cattafesta and Sheplak [32]. These use the Coandă principle ([38]) and tuned tubes to generate an instability on the flow direction, meaning that no external e energy is needed for the fluctuation. Nevertheless, the oscillation frequency is fixed by the geometric parameters. A sketch of the fluidic actuator is shown in figure 1.11e, with the flowing settled in one of the two states. When the flow is settled, part of it flows through the feedback channel switching the flow to the other state. By tuning this feedback paths the oscillation frequency is changed. In the study of Schmidt et al. [105] was analyzed the effect of these actuators tuned at $St = 17$ and 24 over a *GETS body*. In particular, this study used the fluidic actuators in order to enhance the effect of flaps on the rear. It was demonstrated that the actuation cancels the bi-stability and suppress the vortex shedding, but has no effect over the bubble pumping.
Maybe the most popular active technique because of its simplicity is the **continuous-blowing jet**. This basically introduce energy on the flow in form of momentum and they could be easily fitted in different geometries and conditions. Rouméas et al. [98] evaluated the blowing of four jets on the edges of a squareback model blowing at $1.5V_\infty$ towards the center of the base with angles between 30° and 90° (freestream direction) in a numerical study. A maximum drag reduction of 28.9% was achieved for a blowing angle of 45° with a symmetric wake on the vertical plane, and a maximum efficiency of $\xi \approx 7$ with a drag reduction of 20%. Also numerically, Zhang et al. [127] evaluated continuous blowing jets on the slanted rear part of the *Ahmed body* reaching, as in the precedent case, a maximum drag reduction of 29% for a combination of five slot actuators in the rear. The model used is shown in 1.11c with a description of the actuators' geometry. Differently from [98], the efficiency raised exponentially with the decreasing of blowing. In this case, drag reductions up to 25% were reached for $\xi > 1$. The pressure fluctuations on the near wake evidences a peak of energy that is reduced with the actuation, but this peak is present at $St \approx 0.6$, way above the typical vortex shedding frequency that was expected. In any case, the reduction of the rear base's pressure fluctuations is associated to the control effect.
Wassen and Thiele [118] used a 25° *Ahmed body* with streamwise blowing on the whole rear periphery on a numerical LES study. The results showed a maximum reduction of 6.4% on the drag when blowing at the same speed that the freestream flow. Furthermore, is demonstrated that the efficiency of the control (ξ) is slightly above one for this condition.
Geropp and Odenthal [56] studied a bi-dimensional *Windsor body* with continuous blowing on the top and bottom trailing edges enhanced by Coănda effect. The system absorb the air of the rear base in order to inject it trough the slots. A drag reduction of

10% is reached when blowing at twice the freestream speed, evidencing also a favorable energy budget ($\xi > 1$).
Sardu et al. [104] numerically and Cerutti et al. [34] experimentally used the previous cited *GM Model*, with four blowing slots on the rear part. For the experimental case a blowing angle of 65° was used since was the most efficient of the numerical survey. A drag reduction of 12% was found using the lateral and bottom jets at $V_j/V_\infty \approx 1.2$. The drag reductions obtained in this case are lower than the precedent ones, but this may be explained by the model's geometry: in the rear part there is a boat tail that already establish drag reduction, explaining the smaller effect of the control. The drag reduction is accompanied by a decreasing of the fluctuating energy around $St = 0.13$, corresponding with the vortex shedding.

As seen, both PFC and AFC techniques produce a relevant reduction of the drag, and the choosing of one or the other is dictated by the requirements of each case. But as already resumed, the PFC devices have the drawback of penalize the homologation and have to be designed for working in a determinate condition. This lack of flexibility also penalize the performance, since the ideal working condition is only a concept and is hardly reached in a real-case scenario. The AFC instead, seems to better fit the necessities of aerodynamic enhancement without significantly modifying the vehicle. In particular the continuous blowing show promising results and high reliability as well simplicity.

1.3.2 Feedback active flow control

The next step of flow control is the modulation of the forcing in function of a certain input parameter. This is called the **feedback active flow control** (FAFC) and involves the actuators, sensors and a criteria that correlates both, also called control law. There are different types of FAFC depending on the necessities of each particular case and some of them are classified in figure 1.12 in function of the robustness and the time of stabilization, as defined by Pastoor et al. [87]. The chart evidences three main types of control. The extremum/slope seeking FAFC is an automatic control that seeks for a minimum or maximum of a certain parameter. They have the characteristic of being robust, but the stabilization time is high. The next level of complexity is given by the adaptive black-box based controller and the black-box-based controllers, that are algorithms that stabilize the working point of the system on a desired value. They are noticeably faster than the precedent ones but may have reduced robustness. Finally, the physically motivated controllers are the most efficient ones because they aim to control a physical phenomena. The robustness of this control may vary depending on the phenomena that needs to be controlled. For example, the vortex shedding is a very regular phenomena of bluff bodies, making this an optimal phenomenon to perform a high-robustness control.

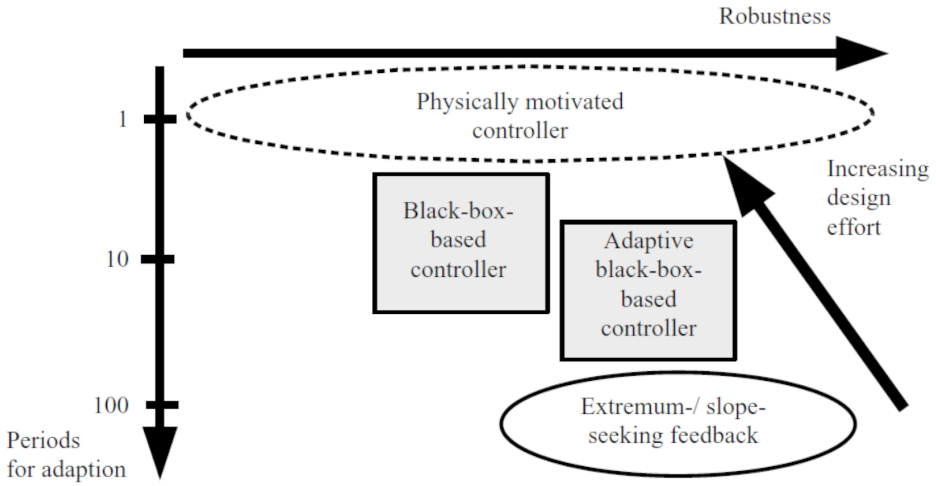

Figure 1.12: Classification of the different types of control in function of the periods of adaptation and robustness. Taken from [87].

In figure 1.13 are schematized two demonstrative diagrams for open-loop and closed-loop AFC. $G(s)$ is the plant's transfer function in the complex coordinate s and $H(s)$ and $K(s)$ are the transfer functions of the external noise and feedback respectively. The difference of the FAFC diagram is the feedback of plant's output signal $(K(s)Y(s))$. Full description of these systems and theirs response for impact, step and ramp inputs can be found in *Modern control engineering* [85].

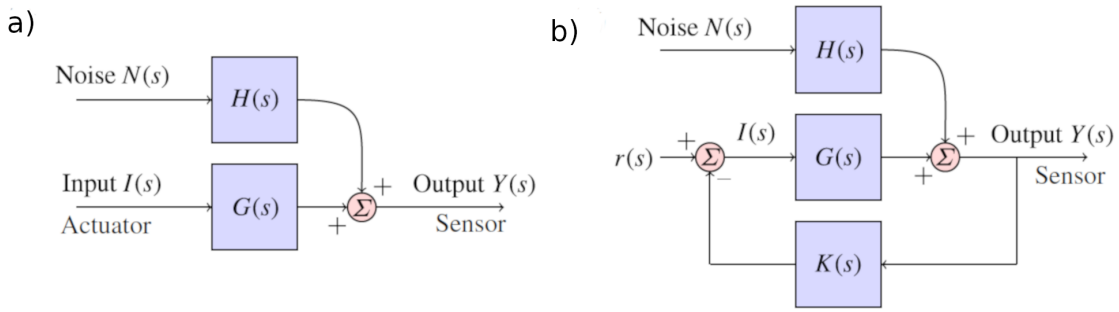

Figure 1.13: Open-loop (a) closed-loop (b) control diagrams. Taken from [40].

The most interesting property of this kind of control is the system adaptation at each particular flow condition in the long or short term. From low frequency/occurrence phenomena like a change on the vehicle speed or the wake's bi-stability, until the reduction of the bubble pumping or the vortex shedding could be controlled.
Most of the authors dedicate the FAFC to the drag control. A backward-facing step was numerically analyzed by Dahan et al. [40] at low Reynolds number, comparing the response of two synthetic actuators with different positions on the back. Open-loop control demonstrates the potentiality of the actuators in reducing the dominant fluctuating instability, specially when forcing frequency is below it. The closed-loop control shows the same level of improvement on the drag reduction, but in this case the main different is in the actuation: there is a transition time since the control is turned on in which the actuation is high, but once the system is stabilized the actuation is reduced to a minimum way below the open-loop levels. The configuration of the blowing and

the results are observed in figure 1.14a, where the continuous line represents the *actuator 1* (top) and the dashed the *actuator 2* (bottom). The actuation starts at 50s. Early experimental studies of Pastoor et al. [87] around a bi-dimensional D-shaped body at Reynolds regarding the height (Re_H) ranging from 23000 to 70000 demonstrates the capability of different types of FAFC. The control was performed through two blowing slots settled in the trailing edges of the body and nine pressure taps on the rear base were the control input. A slope-seeking control was used to determine the characteristics of the model, and the results are shown in figure 1.14b. As seen the actuation oscillates in order to trace the response of the pressure coefficient, successively increasing the mean actuation value until reaching 15% of drag reduction. Another approach of control in this study was the physically motivated, aimed to reduce the vortex shedding through blowing in the same Strouhal frequency but in counter-phase with synthetic actuation. Using only one actuator, this control law reaches 15% of drag reduction as in the precedent control type, but in this case using only 56% of the energy.

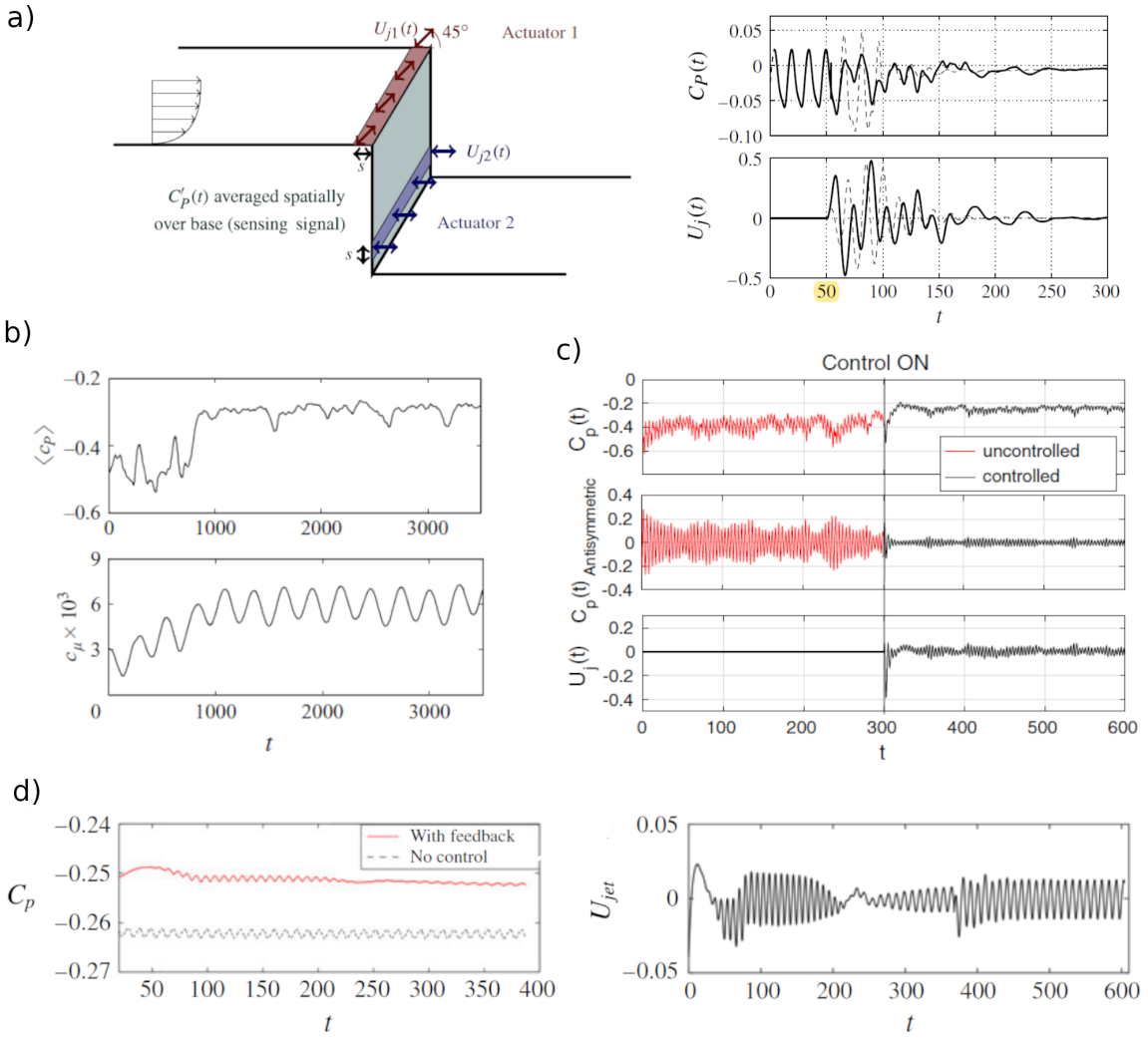

Figure 1.14: Effect of the feedback control over a backward-facing step: position of the actuators and results in function of the pressure coefficient on the rear base. The control starts at 50s (a). Control over a D-shaped bluff body in experimental (b) and numerical (c) studies. Control over a squareback *Ahmed body* on experimental testing (d). Taken from [40], [41], [87], [50]

A similar body was used by Dalla Longa et al. [41] but in a numerical study and with Reynolds numbers slightly lower ($Re_H = 10000$). The control law was targeted to reduce the base pressure asymmetry produced by the vortex shedding, and the results of figure 1.14c evidence strong similarity with the precedent ones on the controlled and non-controlled stable pressure coefficient. In this case an increase of 38% of the base pressure is reached, with an evident attenuation of the pressure fluctuations. It is interesting to highlight that both numerical and experimental studies present very similar pressure coefficient values in the rear even in different Reynolds numbers.
Evstafyeva et al. [50] uses synthetic blowing on the four trailing edges of an *Ahmed body* at low Reynolds numbers, where demonstrates the capacity of this control to reduce the pressure fluctuations with a consequent increasing of the base pressure of 5% when the control is performing stable. The results are shown in figure 1.14d in terms of pressure coefficient on the rear base an velocity of the jets on time scale. The fact that the Reynolds number on this test is low (≈ 400) may introduce some doubts about the results of this control technique at higher Reynolds. Still, the precedent citations demonstrate the effects of synthetic jets for higher Reynolds values.
From the previous examples seems that the blowing actuators are well fitted for the flow control. However, different kinds of actuators can be used, as demonstated by Brackston et al. in [26] and [27]. In these experimental studies, two flaps are settled in the lateral ([26]) and in the top and bottom ([27]) trailing edges of a squareback *Ahmed body*, in order to control the bi-stability and vortex shedding respectively. In both cases is evidenced the possibility of modifying the dynamic characteristics of the wake through this actuator: the control was demonstrated very positive in suppressing the bi-stability and consequently reducing the drag. For the vortex shedding control, the fluctuation energy at the Strouhal frequency is reduced. Still, no drag reduction was achieved since the degradation of energy at a certain Strouhal was compensated by the enlargement of energy on a different one. Maybe the most positive characteristic of this technique is the capability of setting the most profitable angle for each flow condition, working as a quasi-passive device as already explained in the PFC devices of section 1.3.1

Finally, the FAFC enhance the capabilities of the simple AFC by identifying the most profitable condition and performing only when the plant requires, thus reducing the energy used by the system. Nowadays few vehicles have this kind of systems. Even though, the promising results in the experimental and numerical fields confirms the potentiality of FAFC in the automotive enviroment and evidence the possible application in the near future.

1.3.3 Platooning

Besides the flow control techniques, there is a very interesting way of driving that enhances the aerodynamics. It is call the platooning and consist in a group of vehicles traveling at constant speed one behind the other maintaining theirs in-between distance, as shown in figure 1.15. This driving configuration involves two main aspects: the aerodynamics and position control.

Figure 1.15: Three trucks in platoon configuration. Taken from [6]

It is evident that several vehicles traveling at close distance represent a high-risk condition, therefore the main challenge behind the control is to maintain the distance between vehicles avoiding risky situations. The problem of position controlling has several solutions: autonomous vehicles with distance control using optics, radars or an intercommunicating system between vehicles through $5G$ connection are some of them. Even human-controlled distance is considered, which might be the most simple solution. But the results presented by Summala [108] are not promising, since the breaking reaction time of an unalerted driver is from 1 to 1.3 seconds. This means that if a vehicle is traveling at $100km/h$ and there is an unexpected situation the vehicle travels at least 28 meters until the braking begins. For this reason automatic controls are considered for distance control.
Maybe one of the first studies that treated the autonomous control of vehicles was Gage and Pletta [54]. In this study was investigated the possibility of a control of the distance in between vehicles, aiming to an autonomous driving. This study was targeted to the safety and reduction of manpower, but not to the fuel consumption improvement. Was demonstrated that a control system might be capable of controlling a convoy of vehicles, but also evidences the tight error margin involved in using this kind of control in a public road. Alam et al. [5] evaluated a control system of the individual position of a vehicle regarding a leading one, and claims that a heavy-duty vehicle can drive safely behind another with a minimum distance of 2 meters, considering until $500ms$ of delay in the system response. Gehring and Fritz [55] proposes a double-loop control, considering a controller for the whole platoon (outer control) and an acceleration control for each vehicle (inner control). The concept was tested on a real case and the results were successful, evidencing the capability of the control to follow a leading vehicle with until 7 vehicles behind. Alam et al. [6] analyzed the viability of a commercial control system for a platoon of trucks in sloped roads, evidencing the fuel-consumption benefit of 14% in downhill and a 0.7% in uphill condition. Yu et al. [125] present a complex control system for hybrid electric vehicles and tested through *Matlab/Simulink*®different conditions of the road. Bergenhem et al. [19] exposes a Vehicle-to-Vehicle communication system in order to control the platoon in a real road condition. This article's study is part of the *SARTRE project* (www.sartre-project.eu), an European project that prompt the development of platooning on heavy vehicles without modifications on the roads and looking for the interaction with different kind of vehicles. The results evidence a preliminary stage of the positioning control, but in this case the test were performed at a distance around 50 meters, far beyond the expected for an efficient fuel-consumption reduction.

However, this technology is still in development and the remarkable aspect is that the test performed respond well to the position control. Another interesting project regarding the platoon of vehicles is the *KONVOI project*, from the Aachen University (https://www.ika.rwth-aachen.de/en/research/projects/automated-driving/1636-konvoi.html). The project also concentrates in the Vehicle-to-Vehicle communication but with different protocols. In this case they reach distances about 10 meters between heavy vehicles, which represent a more suitable condition for platooning.

All previous studies focus on the control aspects of the problem without a deep understanding of the aerodynamic phenomena. The next studies meet this second issue, in agreement with the containt of this thesis. Early wind tunnel studies of Romberg et al. [95] began identifying the effect of close-driving on passing maneuvers during car racing. The results showed a benefit on both leading and approaching cars on the average resultant forces, evidencing an aerodynamic enhance of both vehicles. Later, Fletcher and Stewart [53] evidenced similar results but in this case for two buses in tandem configuration. Also different geometries were tested, showing similar results. The average visualizations on the midplane between the vehicles evidenced the presence of a trapped vortex, that may be the cause of the aerodynamic benefits. A more detailed study was performed by Zabat et al. [126], where a 1/8 scaled minivan model was wind tunnel tested in two, three and four vehicles platoons. The results highlight the benefits of the platooning driving, reaching 50% of overall drag reduction (mean value of the drag reduction of each individual model). Moreover, for more than 2 vehicles in the convoy, the middle vehicles evidenced the most beneficial effects, followed by the tail and finally the front. In figure 1.16a are shown the results for 2, 3, 4 and virtually infinite models. It is clearly seen how the overall drag of the platoon reduces while approaching and with the increasing number of vehicles. An important conclusion from these results is that the major effects on the drag reduction were achieved when the distance between the models was less than one length, in correspondence with the presence of the near wake of the leading model.
Tsuei and Savas [113] investigated the effect of a car passing a convoy of four cars on a wind tunnel test. This study was part of the *California Partners for Advanced Transit and Highways* (PATH), a collaboration between government, academic institutions and industry of the United States of America (https://path.berkeley.edu/). Here was evidenced the lateral forces involving the side-by-side configuration produced by the passing car, and the importance of the passing vehicle's shape: a bluff-shaped vehicle produces higher side load than an streamlined shape. On road testing, Michaelian and Browand [82] also demonstrates the platooning capabilities but in this case on the fuel consumption, using real vehicles. As in the precedent case the benefits of the convoy can be separated in three groups: front, middle and tail, where the higher benefits are for the middle ones as shown in figure 1.16b. Similar results are found by Davila et al. [44] in real case testing, but using different vehicles (combination of cars and trucks). These results supports all previous ones, evidencing a decreasing fuel consumption on each vehicle when approaching. In this study a CFD survey is performed conferring some information of the possible flowfield involving the platoon: the leading vehicle's wake produces a deficit on the downstream dynamic pressure, thus reducing the aerodynamic force on the following vehicles.

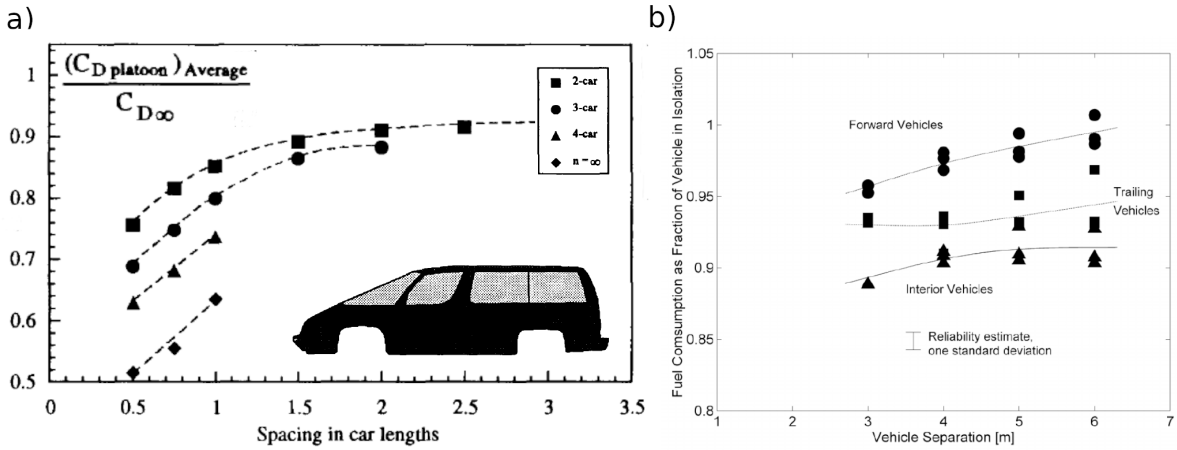

Figure 1.16: Platooning results:drag reduction for a van model platoon in wind tunnel(a) and fuel saving for a real case car platooning (b). Taken from [126], [82].

Pagliarella et al. [86] studied on the wind tunnel the platooning of two *Ahmed bodies* with a combination of different slant angles in the models. Considering the overall drag reduction, this study clearly evidences the increasing benefits of the platoon within the approaching of the models in all configurations. Although, some conditions are identified were the drag actually increases. This results does not concur with other researches for similar bodies, as Watkins and Vino [120]. In this last study the trends are more favorable regarding the drag reduction, but anyway showing an increasing of the drag for distances between 0.1 and 1 model lengths for the front vehicle. More evidence of the benefits of platooning over the aerodynamic drag can be found in the numerical studies of Vegendla et al. [115] and Hamiga [61] over truck and squared models respectively. Finally, Salari and Ortega [100] tested a series of truck-trailer models in wind tunnel, analyzing also the air supply for cooling. The drag results resembles all the studies cited before, but also evidences the problem of cooling: for the closest configurations the following vehicles may experiment a lack of incoming flow, reducing the efficiency of the radiators.

In conclusion, the platooning of vehicles seems to be a interesting approach to achieve high drag reduction. In fact, many public and private institutions are showing a growing interest on developing this concept. The mechanism behind the aerodynamic enhancement of two vehicles can be divided in function of the distance between them: close following (less that one vehicle of distance) and far following (more than one vehicle of distance). The best results are obtained for the close following, with an exponential increasing of the benefits when approaching. This could be associated to the interaction of the following model with the near wake of the leading one. The far following evidence a less intense drag reduction but less sensitive to the gap between vehicles, linked to the dynamic pressure deficit behind the leading model. For more than two vehicles, the platoon presents three characteristic positions: Leading, middle and tail vehicles. The middle are the most benefited, followed by the tail and lastly the leading vehicles.

1.4 Fuel consumption and emissions

There is no discussion about the importance on reducing the emission of pollutant gases to the atmosphere, in particular the ones that produce greenhouse effect as CO_2, methane, nitrous oxide and others. In the last years the European Union evidenced the urgent necessity of reducing the emissions, which involve several areas of influence as burning combustibles, deforestation, livestock faring and more. The transport emissions (https://ec.europa.eu/clima/policies/transport_en) represent approximately one quarter of the greenhouse gases production in Europe, but the most important issue is that has a growing tendency. In order to revert this situation the development of high efficiency or zero-emission vehicles is prompted, aiming to a 60% of emission reduction regarding the '90 by year 2050. But the adverse effect that this restrictive policy may produce is the reduction of the economic activity, so is imperative to find new ways of enhance the efficiency of vehicles to meet the requirements. Since the argument of thesis is the aerodynamics of vehicles, the emission-reduction methodologies regarding the propulsion and transmission systems will not be evaluated. Furthermore, the aerodynamic improvement of a vehicle represent an energetic benefit independent from the powertrain: it could be expressed in terms of fuel-consumption reduction for ICE or improved range for electric vehicles. Even though the electric vehicles evidence a high compatibility with the city driving, ICE vehicles present many advantages on highway driving. In fact, no practical options are available for this vehicles in terms of range. Due to this the improvement of fuel-consumption on ICE vehicles is yet an important matter, and even more if is considered that the most of the commercial vehicles are ICE driven. Because of this, reducing the aerodynamic drag of vehicles could be one of the most important aspects of emission reduction.
In order to link the emissions of ICE vehicles with the fuel consumption and the aerodynamics, some standard conditions need to be settled. In the following section will be defined the driving schedules, the relationship between fuel consumption and the drag variation and finally the emission produced.

Finding a relationship between the aerodynamic drag and the fuel consumption reduction is not an easy task, since the parameters involving this equation may change with the vehicle, road and overall conditions. Aiming to address this problem were developed the *EPA cycle* in the United States and the *Euromix cycle* for the European Union, both described in Canale et al. [30]. These standard cycles simulate a typical driving situation of a vehicle traveling on urban and highway conditions. The *EPA cycle* is based in two parts: a Highway driving schedule and a urban driving schedule, both shown in figure 1.17a. The final fuel consumption is given by the 55% of the fuel consumption on urban schedule and 45% of the highway schedule. The *Euromix cycle* is composed by three parts: an *Economic Commission for Europe* (ECE) urban driving schedule shown in figure1.17b , a constant-speed cycle at $90Km/h$ and a constant-speed cycle at $120Km/h$. The final fuel consumption is the average of these three cycles. These two schedules represent the standard benchmark for fuel efficiency comparison. Nowadays, the consumption of vehicles claimed by the factories are evaluated with these schedules (or eventually the legal cycle defined in the country where the vehicle is being sell)

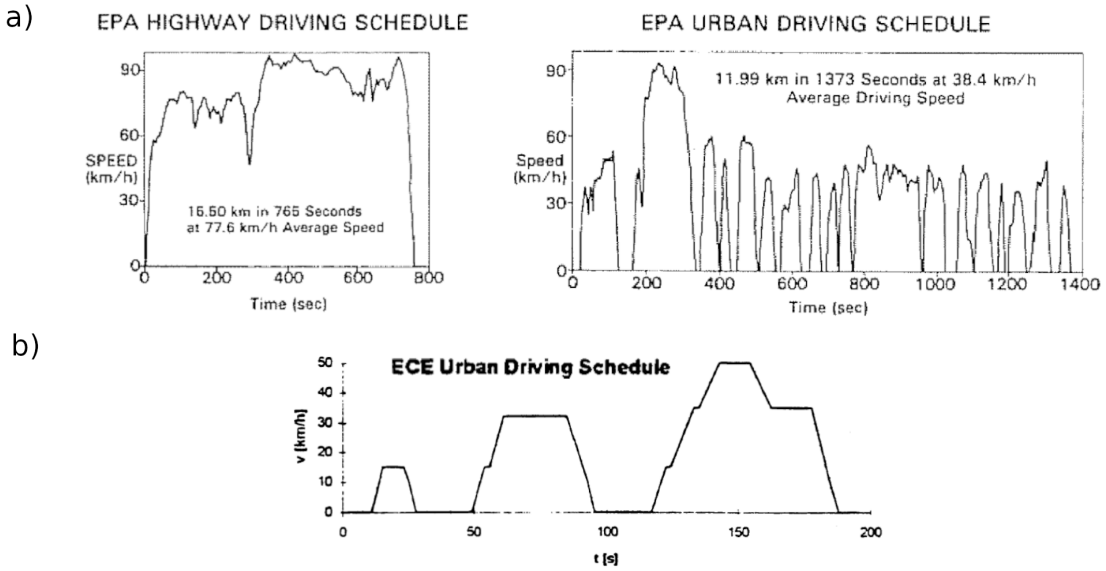

Figure 1.17: Euromix and EPA cycles. Taken from [107] and [30].

These cycles also established a criteria for the correlation between the aerodynamic drag and the fuel consumption. Hucho and Sovran [63] highlights that for the *Euromix cycle* the relationship between the Aerodynamic drag variation $\Delta C_D/C_{D_0}$ is correlated with the reduction of the fuel consumption $\Delta B/B_0$ as follows:

$$\frac{\Delta C_D/C_{D_0}}{\Delta B/B_0} = K \tag{1.7}$$

Where $K = 0.3$ for Otto engines and $K = 0.4$ for Diesel engines.

The fuel consumption may be also expressed in the quantity of emissions to the atmosphere. In particular, the most harmful product of the combustion is the CO_2, being this the parameter that is generally observed when analyzing the emissions. To calculate the products of the combustion the chemistry of the certain combustible needs to be analyzed. In table 1.2 are present the chemical characteristics of petrol and diesel combustibles. As seen, the petrol produces less CO_2 emissions that the

Combustible type	Density [grams/liters]	Carbon contain [grams/liters]	CO_2 emission [grams/liters]
Diesel	835	720	2640
Petrol	750	652	2392

Table 1.2: Characteristics of petrol and diesel combustibles.

diesel. But this is only a from a chemical point of view, because if considered the fact that the diesel engines are more efficient in the fuel consumption the overall emissions will be less than the petrol ones.
In concussion, once the fuel consumption variation is calculated in function of the aerodynamic drag variation, as presented in equation 1.7, the emissions' variations can be easily calculated with the data from table 1.2.

To have a glance of the impact of these emissions lets consider the typical emission of a diesel van in one year of work. Assuming that the mean fuel consumption is $8Lts/100Km$ and that the vehicle runs $50.000Km/year$, it will generate 10 Tons of CO_2 per year. If extrapolated regarding the 4 million commercial vans only in Italy, this number rises to 40 million Tons of CO_2 per year!. Now considering drag reductions between 0.5 and 1.5% and calculating the reduction of emission with equation 1.7, we can expect a reduction of the emissions (only for Italy) as shown in figure 1.18.

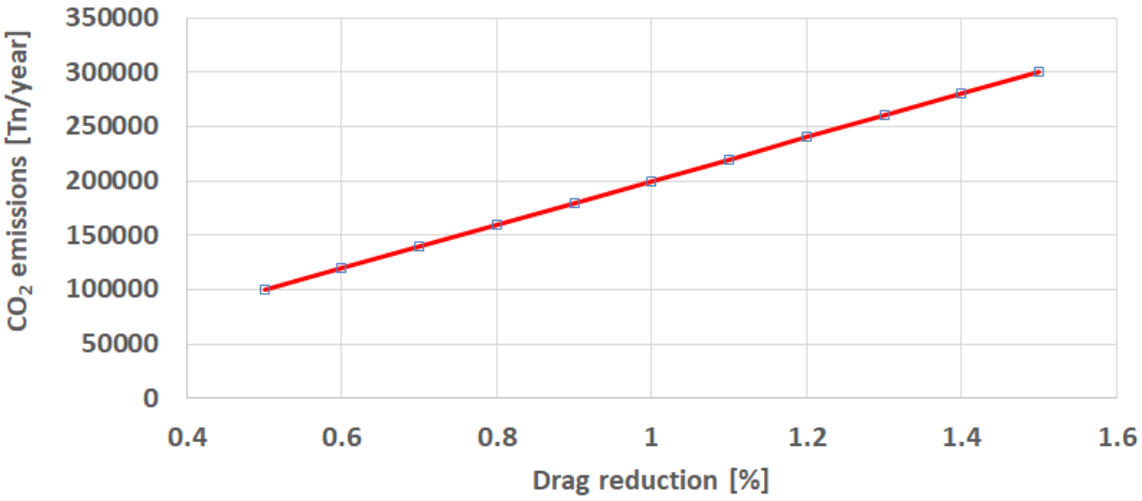

Figure 1.18: Emission reduction for small percentages of drag reduction.

It is clear that a small amount of drag reduction of an isolated vehicle is irrelevant regarding the emissions, but if this number is extrapolated to a community these values grow enormously. In fact, a 1% of drag reduction on commercial vans may reduce in 200000 Tn the year emissions of CO_2.

Chapter 2: Experimental Setup and Data Processing

In this chapter a complete description of the model will be given with a brief overview of the aerodynamic characteristics and the description of the instruments within, including the pressure sensors and the active flow control system. Moreover, the wind tunnel will be illustrated including the turbulence control, boundary layer control and drag balance. The pitot tube, hot wire and PIV anemometry devices will be described, with particular attention to the components of each measurement chain. Finally, the data acquisition hardware will be described as well as the connections between components and the mathematical tools used to process the data.

2.1 Model

The shape of the model respond to the typical shape of a commercial transport vehicles, particularly the small and medium size utility vans (figure 2.1a). The squared geometry with a blunted rear allows maximum internal capacity and easy access through the rear and side parts, which are the dominant design targets for this kind of vehicles. As seen from figure 2.1a the vehicle can adopt different configurations, and therefore different geometries, but somehow conserving the same ratios. This allows one model to fit almost all configurations of a utility van.

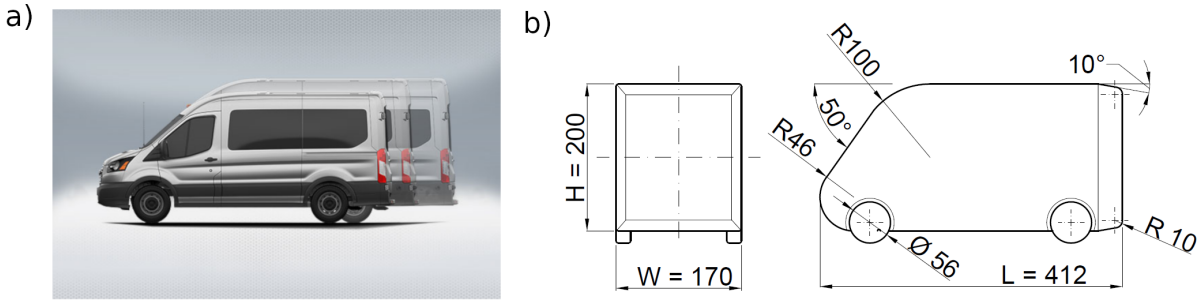

Figure 2.1: Model sketch with characteristic dimensions and reference axis (a). Different utility vans' sizes (b). Taken from *www.gatorford.com*.

The model used in this research is characterized by a box-shaped geometry with a slant front end, rounded edges of $R = 4mm$, a 10° boat-tail (tapered rear edges) and four wheels. The size of the model is a compromise between the dimension of the wind

tunnel's test chamber (blockage and border conditions) and the devices that the model must fit (sensors and active flow control devices). The slanted front end is a particular characteristic that is present in almost all utility vehicles; a good compromise for this angle was found averaging the mean front-end angles of the vehicles of the market. The resulting model's sketch is shown in figure 2.1 b, and the external dimensions are: length (L) $412mm$, height (H) $200mm$, width (W) $170mm$. Based on the existing utility vans, the average scale of the model is $1:10$. A complete description of the geometry can be found in *Appendix 1*. The 10° tapered edges on the rear part are a significant characteristic of the model that is not presented in the real case vehicles. This aft is made to fit the AFC actuators, further explained on section 2.1.2. The effects of boat-tailing were profusely studied by several authors as Choi et al. [36], Hasaan et al. [62], Bonnavion and Cadot [23] and many others. They all agree that the boat tail produces a decreasing of the drag due to the reduction of the recirculating structures of the near wake, meaning that this model will have a slightly lower drag coefficient regarding to a squared-back. In addition, boat tailing reduces the bistability phenomena of the wake after a taper angle of 6° and disappears for angles over 12°, as demonstrated by Pavia et al. [90]. Nevertheless this differences regarding the real vehicles, the model is still in agreement with the target geometry and the magnitude of the drag value will be approximately the same. The model was 3D printed on polyacrilic plastic (PLA) and the roughness of the surface was improved by grinding and painting. The mounted model and main structural components are shown in figure 2.2a and b.

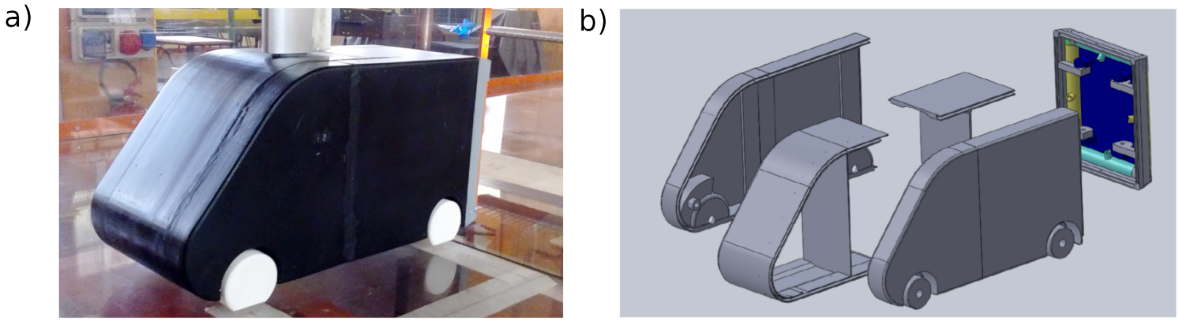

Figure 2.2: Model mounted on the wind tunnel (a) and main printed components (b).

2.1.1 Sensors within the model: Mean pressure and fluctuating pressure.

The model fits inside two pressure-measurement devices. The first is a *Scanivalve ZOC 33* pressure transducer, shown in the right of figure 2.3a, with 64 pressure inlets and a full scale of $2.5kPa$. It allows sampling rates until $500Hz$ with an accuracy of $\pm 0.15\%$ FS. This pressure transducer is used to measure the mean value of the pressure distribution of the model and the data is send to a computer via LAN connection through a TCP/IP protocol. The pressure inlets are connected to pressure taps mounted on the model's surface through plastic tubes of $1.5mm$ internal diameter and a mean length of $200mm$. In order to comprehend the resonant effects that this configuration may present, the natural frequency of fluctuation of the transducer-tube couple was analyzed based on the studies of Berg and Tijdeman [18]. This was calculated considering a one-end closed tube of $1.5mm$ of internal diameter and $200mm$ long, with a transducer volume of $3 \times 10^{-7} m^3$. The resulting value was $f(transducer - tube) = 218Hz$.

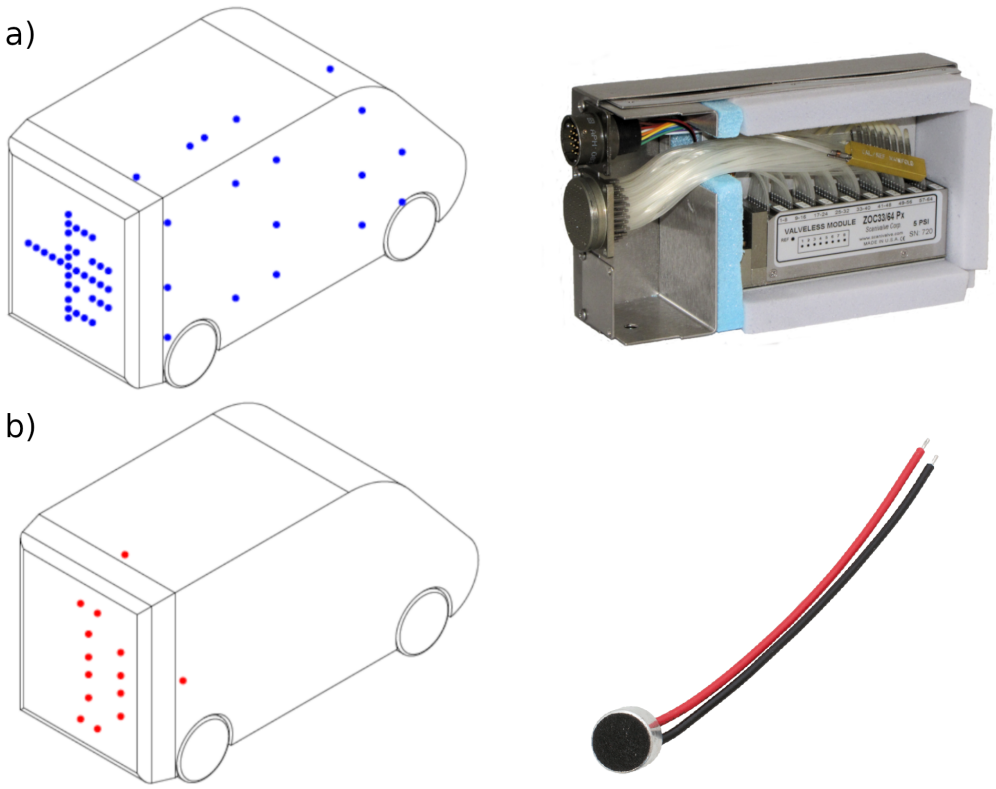

Figure 2.3: Positions of the pressure taps (blue) and Scanivalve ZOC 33 Pressure transducer (a). Position of the microphones (red) and the electret microphone capsule. Taken from *www.scanivalve.com*, *www.tandyonline.com*

Considering the typical shedding frequencies for this kind of bodies (around $10Hz$) the natural frequency of the transducer-tube is one order of magnitude greater, so any effect on the frequency response can be neglected. The pressure taps are distributed in three groups over the model's surface: right half of the rear base, right-side face and a cutting plane parallel to the right-side surface, near to the vertical symmetry plane. These positions allow to obtain the pressure distribution on the lateral side, rear face and the periphery, and they are represented on figure 2.3a. Due to the isometric projection of the figure the taps present on the bottom part and the front are not visible. A complete description of the positions is given in *Appendix 1*.

The second devices are a series of 16 *electret capacitive microphone capsules*, shown in figure 2.3b. They have a sensibility of $-64 \pm 3dB$, a bandwidth of $50Hz$ to $13kHz$, and return a current signal reaching a maximum of $0.4mA$. These microphones are only capable of measuring the pressure fluctuations, but at higher frequencies regarding the ZOC 33 transducer. The microphones are mounted in *pin-hole* configuration, with a hole of $1mm$ diameter and $1mm$ length, and their positions over the model are shown in figure 2.3b. Only two microphones are not at sight on the figure, being present in the bottom and left faces. Detailed reference of the positioning of the microphones can be found in *Appendix 1*. Different from the pressure transducer, this microphone's data need to be acquired, calibrated and mapped through a high quality microphone. The microphone used for the calibration is a Brüel & Kjær (B&K). it performs a flat response between $10Hz$ and $10KHz$ and a sensitivity of $100mV/Pa$.

2.1.2 Active flow control. Control parameters and devices.

The model mounts an active flow control system based on four cylindrical actuators that blown air through a tangent-to-surface rectangular slot on the edges of the rear part, as evidenced in figure 2.4a and in the detailed section of 2.4b. These actuators are mounted on a structure that allows rotation at discrete angles through a built-in gear and a blocking clip, being able to change the Θ_j angle between 25° and 85° degrees in steps of 10°. This structure and the actuators are shown in figure 2.4c, where the vertical actuators are orange and the horizontals are white. As mentioned before, the rear end of the model presents a 10° boat-tail. This taper is product of the actuator's range of rotation and the internal tubing that feeds the jets. A detail of the vertical cylindrical actuator is shown in figure 2.4d. The tangent-to-surface slot is observable and in the left end is present the built-in gear (white part). The rectangular blowing slots have $1mm$ of width and a length of $104mm$ for the top and bottom actuators and $132mm$ for the lateral ones. Therefore, the two control parameters of the AFC are the blowing speed V_j and the blowing angle θ_j. The velocity of top and bottom jets can be controlled individually, whilst the lateral jets work coupled.

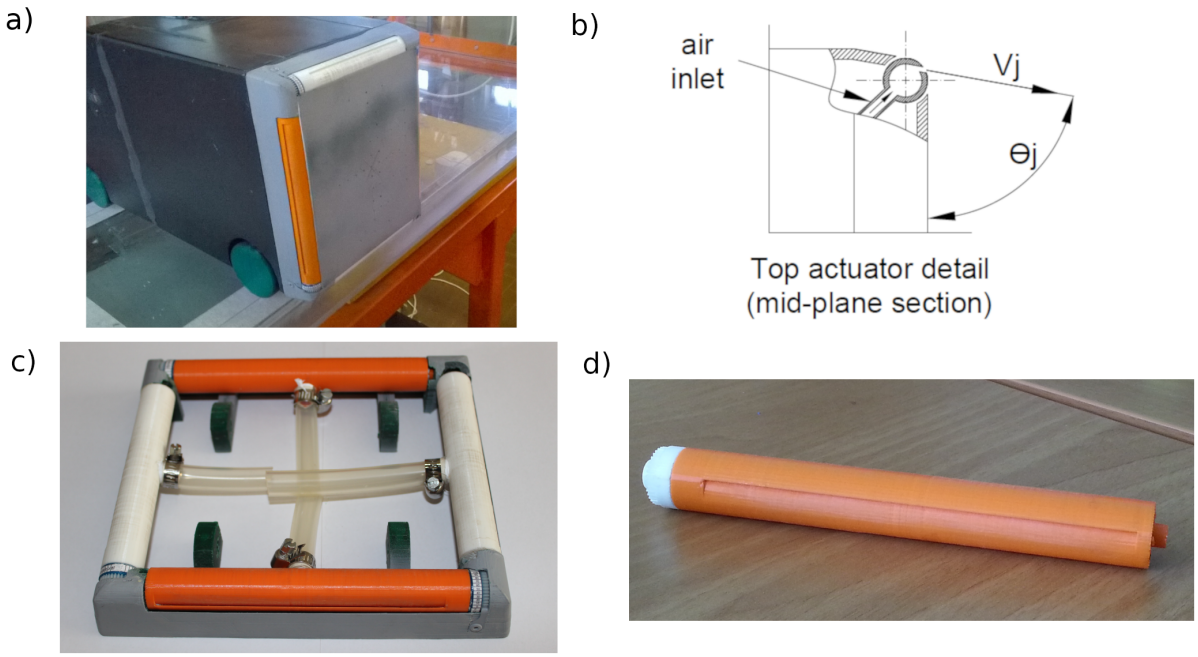

Figure 2.4: Slot positions on the rear (a) and section view of the model's rear with the control parameters (b). Actuator's support structure with tubing (c) and the vertical cylindrical actuator (d). Taken from [102].

The tangent blowing over the rounded surface on the trailing edges (see figure 2.4b) is intended to enhance the jet actuators' efficiency making profit of the Coandă effect. This mechanism tends to attach the flow to a highly-curved surface by introducing tangential momentum to the superficial flow layers. Was first evidenced by Coandă [38], and then deeply studied by Wille and Fernholtz [122]. Several years after, Geropp and Odenthal [56] applied this concept over the rear part of a car in order to reduce the drag by reattaching the trailing edge's separation. In this study, the tangent blowing over the rounded rear surface redirected the flow towards the inside, thus reducing the size of the recirculating bubble.

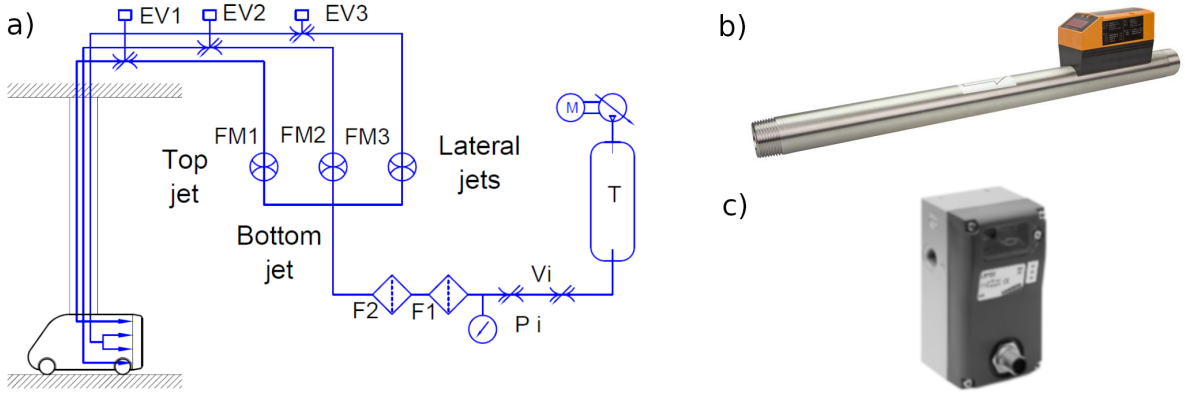

Figure 2.5: Sketch of the pneumatic lines of the AFC (a), Camozzi electrovalve (b) and IFM flow meter (c). Taken from *www.camozzi.com*, *www.ifm.com*.

Since performing and experimental analysis of optimal blowing angles is highly time-consuming, a computational alternative was exploited. From a preliminary research made by Sardu et al. [104], CFD results shown an optimal angle of blowing of jets of 65° for all actuators. Therefore all the experiments will be performed following this optimal configuration.

In order to perform, the AFC is feed with the compressed air system of the laboratory. In figure 2.5 is shown a sketch of the AFC's pneumatic lines connections. Here can be seen the compressor M and the main pressure vessel T, corresponding to the pneumatic facility of the lab. There is a pressure regulator V_i for the input, and after a manometer that gives the input pressure of the system. There are settled 2 filters ($F1$, $F2$) in order to avoid contamination and stop any debris that may damage the flow meters and valves. After these filters the pressure line divides in three lines corresponding to the top, bottom and lateral jets, with one *IFM SD8000* flow meter each. The *IFM SD8000* flow meter (figure 2.5b) has a measurement range of $3750 Nlts/min$ and a maximum line pressure of $16 bar$, and is mounted on a stainless 1" tube with $R1$ $DN25$ connections. Returns an analog signal of $4-20 mA$ together with a live digital lecture on a display in front of the instrument. The repeatability of the measure is 1.5% and the accuracy $\pm 3\% MW$, being MW the molecular weight of the gas being measured.

Until this point all pneumatic lines were 1" standard diameter; after the flow meters are settled reduction connectors, converting the two lines corresponding to the top and bottom jets to $8mm$ diameter plastic tubes, while the line for the lateral jets become $10mm$ diameter. On the test chamber's top and before the tubes enter the hollowed strut of the drag balance, each of this lines mount a *Camozzi LRWD2* electrovalve to control the velocity on each jet. The *Camozzi LRWD2* proportional electro-valve (figure 2.5c) has a one-input two-output pneumatic lines configuration, responding to an electric input signal ranging $0-10V$. The closed state is at $5V$, and the open positions are output 1 at 100% for $0V$ and output 2 at 100% for $10V$. The variation of the opening is almost linear for a linear variation of the input tension. The maximum flowrate for an input pressure of $6.6 bar$ is $700 Nlts/min$, and the maximum working frequency between 90% opening of the two exits is $60 Hz$.

2.1.3 Dummy models

Part of this thesis consist in the analysis of the interaction of vehicles in platoon configuration. For this purpose three replicas of the model were built, commonly called "dummy models", and are shown in figure 2.6. These reproductions were built with $10mm$ thick plywood, having a box shape with the same external dimensions of the model and reproducing the front angle. The wheels were printed and glued to each model and finally they were painted black in order to avoid reflections on the PIV visualizations. The slanted front of the dummy models was removable in order to set counterweights within, thus avoiding the model to move due to aerodynamic forces.

Figure 2.6: The three dummy models numbered. The third one has the slanted front open, where is observable the counterweight within.

2.2 Wind tunnel

The wind tunnel used is the orange wind tunnel of the “Modesto Panetti” aerodynamic lab of the Polytechnic of Turin. It is an open-circuit subsonic wind tunnel performing a maximum speed of approximately $10m/s$. Relevant photos of the wind tunnel are presented in figure 2.7a. Is powered by two 12-bladed propellers driven by two electric motors that force the air into a plenum of $32.5m^3$ ($H_p = 3.5m$, $W_p = 3m$, $L_p = 3.1m$). Inside this chamber are present a series of screens that reduce the fluctuations of the incoming flow. The motors can be driven independently from 0 to $1200RPM$, increasing linearly the freestream speed on the test chamber. After the settling chamber a convergent of $3m$ length and an aspect ratio of 10 reduces the transversal area to $1.17m^2$ ($H_{tc_i} = 0.9m$ x $W_{tc_i} = 1.3m$), which is the input area of the test chamber. Downstream is the $6.34m$ long test chamber. Is made from transparent acrylic panels of $e = 0.015m$ of thickness and a steel structure, allowing optical access to the complete internal volume. In order to compensate the boundary layer growth throughout its length, the width of the section increases from $1.3m$ on the exit of the suction module to $1.41m$ on the end of the chamber, keeping the height constant at $0.9m$. The maximum blockage ratio, giving by the ratio of the model's frontal area and the test chamber section is less than 3%. At $2m$ of the input of the test chamber is the fixing point of the model, composed by a hollowed strut coming from the top. This strut is connected to a load cell and covered by a hull, and houses the tubing to feed

the AFC and the connections of the internal sensors. A complete description of the drag balance will be given in section 2.2.3.

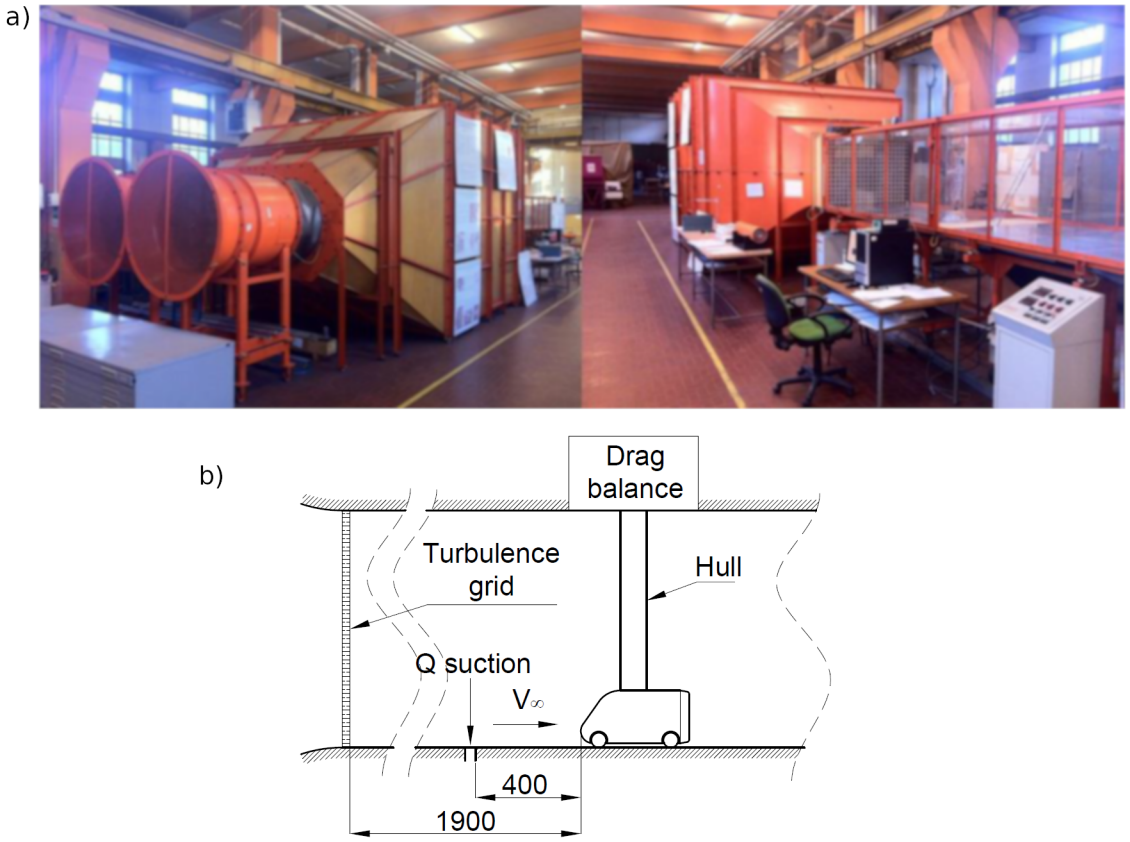

Figure 2.7: Wind tunnel lateral views (a) and sketch of the test chamber with model position and characteristic components (b).

This way of fixing the model is very popular in the automotive field, in particular on wheeled models, since does not interfere with the underflow. Moreover, it allows the passage of the air lines that feed the AFC with the minimum interference on the surrounding flow. Several examples of this mounting configuration and their variations are presented in *Race car Aerodynamics* [69].

2.2.1 Free stream turbulence control

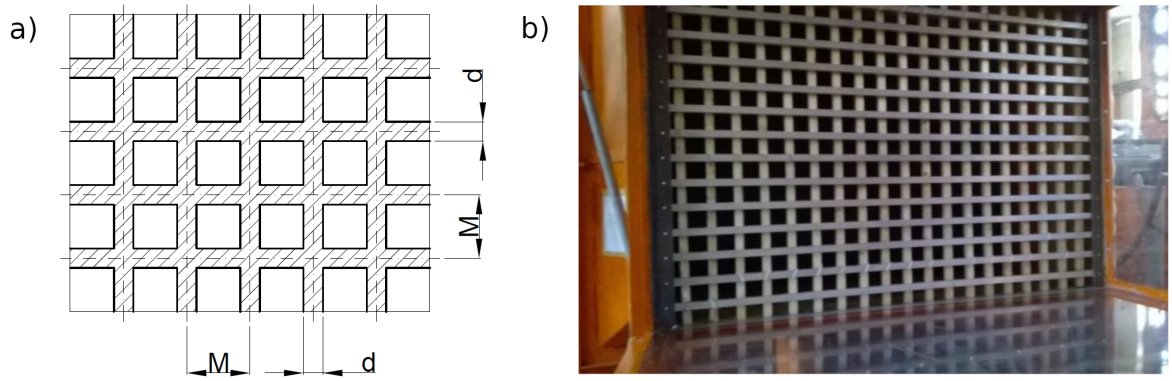

Figure 2.8: Turbulence grid. Sketch with characteristic dimensions (a) and actual grid (b).

Between the exit of the convergent and the input of the test chamber, a turbulence grid is settled as shown in figure 2.7b. Is composed by squared-rods with a dimension of $d = 0.02m$ and a distance between centers of $M = 0.06m$, as reported in figure 2.8a. The actual grid is shown in 2.8b, where are observable the squared rods that compose the grid. Following the studies of Laws and Livesey [72] the turbulence index can be estimated through the geometry of the grid. In this case, the turbulence level in the model's positions is 4%. For further details, the complete characterization of this turbulence grid was performed by Cerutti [33].

2.2.2 Boundary layer control

In order to control the boundary layer on the wind tunnel's floor, a rectangular suction slot is settled ahead the model at $400mm$, as shown in the sketch of figure 2.7b. The suction slot is shown in figure 2.9a, the dimensions of the slot are $6mm$ times $260mm$ and is connected to a *DVP LC105* vacuum pump (see figure 2.9b) with a maximum suction of $70.4Nm3/h$ corresponding to a suction speed of $12.5m/s$. The suction was directly measured by settling one of the *IFM SD800* flow meters on the aspiration line. The slot is connected to the vacuum pump with a 1 1/2" structured tube length approximately $2m$.

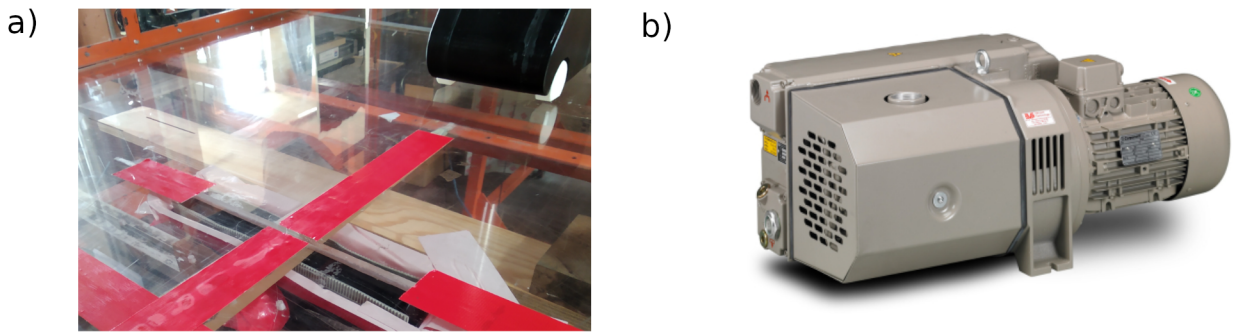

Figure 2.9: Suction slot in front of the model (a) and DVP vacuum pump (b).

Considering the results of Hucho et al. [64], with this configuration the boundary

layer could be reduced approximately 20% regarding the original values. Further demonstrations of theirs capabilities will be given in section 2.2.2.

2.2.3 Drag balance

The drag balance is a mechanism composed by a Load cell, a leverage system and a counterweight that measures the streamwise component of the resultant aerodynamic forces over the model. The sketch of the drag balance is shown in figure 2.10a. A vertical hollowed strut is suspended thanks to a transversal-to-flow axis from the top of the wind tunnel. It connects the model with the load cell, and the counterweight balance the model in horizontal position. The axis rotates over two ball bearings, at each side of the strut. The load cell's support and bearings support are made on transparent acrylic and fixed to the top wall of the wind tunnel, as shown in figure 2.10b. The leverage ratio of the drag balance represents the amplification factor that the drag undergo regarding to the value given by the load cell, and is obtained by the relationship between the distance from the center of pressure on the model and the rotation axis, and the fixing point of the load cell and the rotation axis. Since the load cell is in a fixed position the distance will be constant, but the center of pressure on the model may change, thus changing the distance to the axis of rotation. Nevertheless, the variations on the center of pressure will be bounded in the model's height, which is small regarding to the length of the strut. Considering this and the fact that the hollowed strut has approximately $1m$ long, the leverage ratio of the drag balance will be around 10 (The force measured by the load cell will be ≈ 10 times bigger than the force over the model).

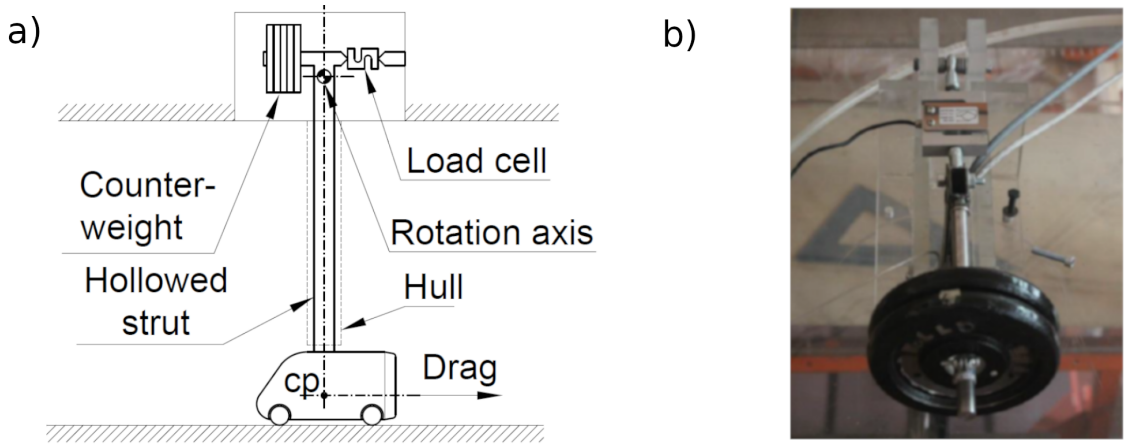

Figure 2.10: Drag balance sketch (a) and Load cell and counterweight (b).

Fixed to the roof of the test chamber there is a hull that covers the hollowed strut until the top of the model (seen in figure 2.10a in dashed line), in order to avoid measurement contamination due to aerodynamic forces over the strut.
The load cell used is a *Dacell UU-K002*, with a full scale of $2Kgf$, and accuracy of 0.03% FS and a constant of $1.0024mV/V$. Considering the leverage ratio the maximum force allowed over the model will be $\approx 200Gr$. An amplification and filtering system is applied to reduce the environmental noise and increase the output tension of the load cell.

2.3 Velocity measurement techniques

2.3.1 Pitot probe and pressure transducer

In order to measure the dynamic pressure and successively the air velocity, a pitot probe and a pressure transducer are used. The pressure transducer is a *Setra 239* differential pressure transducer with a range of $\pm 1 PSID$ and an accuracy of 0.073% FS. The output of the transducer is $\pm 2.5V$. The tension data given by the transducer is logged with the *National Instruments* acquisition hardware and post-processed with *MatLab* to calculate the air velocity, based on the calibration slope given by the manufacturer. The constant of this transducer is $550 Pa/V$. The pitot probe has a diameter of $3mm$, with a length of the streamwise probe of $39mm$, with 6 static pressure taps of $0.1mm$ diameter at $13mm$ from the probe tip. The connections are performed by a couple of plastic tubes of $3mm$ diameter with different lengths depending on the task.

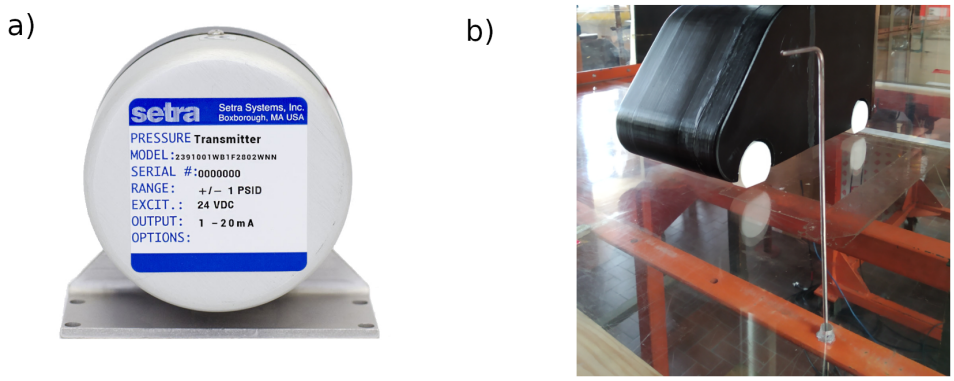

Figure 2.11: Setra pressure transducer (a) and pitot probe (b). Taken from *www.setra.com*.

2.3.2 Hot-wire anemometry

For high time-resolve velocity measurements a hot-wire technique is used. In this case single-filament hot wire were used through a DISA 56C13 CTA bridge. The hot wire probes, performing $1.2mm$ of sensor length, have a resistance of near 3.3 Ohm at 20° and a typical working temperature of approximately $300°C$. One is shown in figure 2.12a. Different supports were used to set the hot wire in position, being the most commonly used a straight one with $200mm$ length and a 90° also with $200mm$ length, this last shown in figure 2.12b. All these supports have $3mm$ of diameter, in order to avoid large modifications on the flowfield. Secondary accessories like guides, rubbers, supports and clamps were also used to set the required position of the anemometer. The bridge was balanced at $5V$ and the output produces a tension ranging from 1.5 to $3V$, and this output was connected to the A/D module of the acquisition hardware.

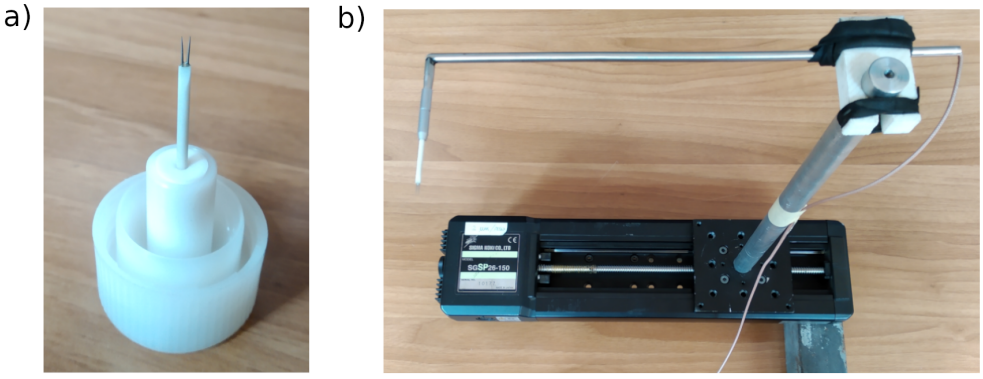

Figure 2.12: Hot wire probe (a) and hot wire mounted on the probe support and fixed to a linear actuator on the base (b).

In figure 2.12b is present a linear actuator, which is capable of remotely move the probe. Is a *Sigma-Koki* stepper actuator with near $170mm$ of moving range and 2000 $steps/mm$, and is controlled by a remote control or computer via a dedicated software.

2.3.3 Particle image velocimetry (PIV) and stereo PIV

For the PIV visualizations two *Andor Zyla sCMOS 5.5Mpx* cameras were available, with *Nikon* objectives of $60mm$ and $105mm$. These elements are shown in figure 2.13a and b . The camera performs $40fps$ at 16-bit and full resolution (2560 x 2160) with 33000 : 1 dynamic range. The connection to the PC is through USB 3.0 protocol. Two in-house built supports with one-axis *Scheimpflug* adjustments are used to link the cameras with the objectives, allowing optical improvement when using angled configurations. This setup is shown in figure 2.13c, where is also observed the black knob on the top that changes the angle between the camera and the objective. Moreover, the cameras are mounted on a *Manfrotto* head allowing the rotation in three perpendicular angles using in-house built adapter, also seen in figure 2.13c.

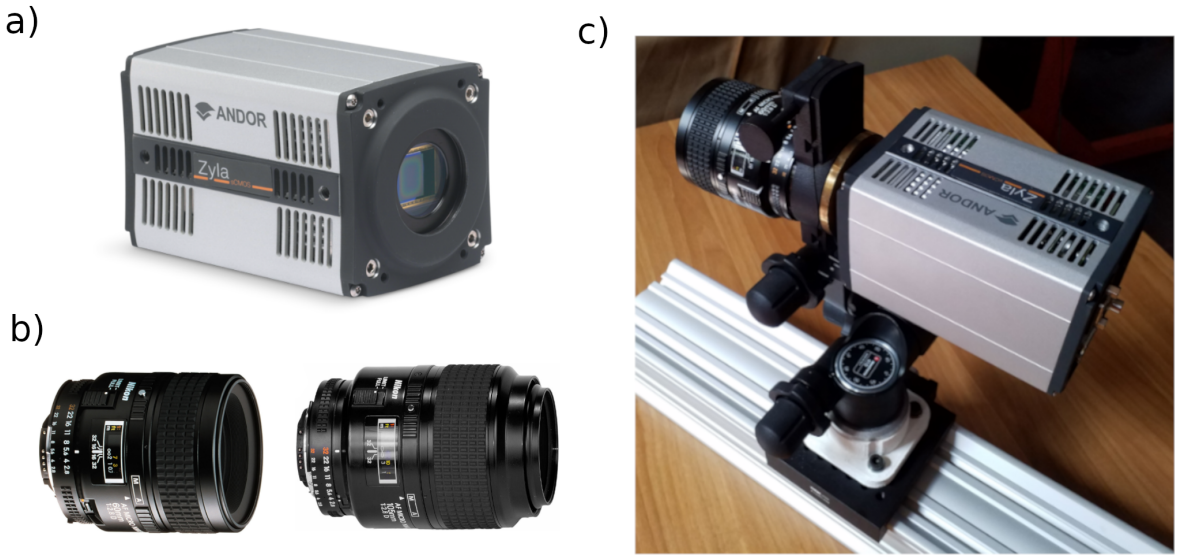

Figure 2.13: Andor Zyla camera (a), Nikon AF 60mm and 105 mm (b) and Camera mounting setup (c). Taken from *www.andor.com*, *www.nikon.com*.

The laser used is a *Litron Laser 240 Dual-Power* with $200mJ/pulse$. It generates a laser sheet of approximately $1mm$ thick on the interest zone through a spherical ($1000mm$ focal length) and a cylindrical ($-50mm$ focal length) lenses. The laser and the mounted lenses are shown in figure 2.14a.

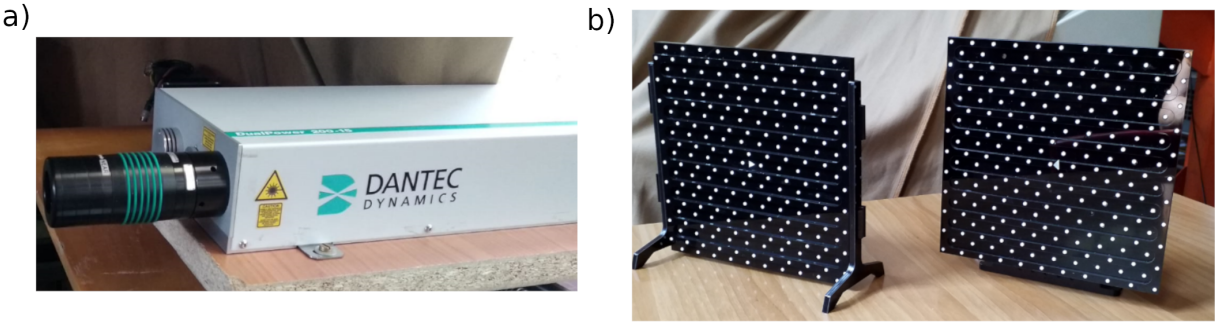

Figure 2.14: Litron laser with mounted lenses (a), two-sided and one-sided $200x200mm$ targets (b).

In order to set the focus of the cameras and align the laser, two targets were built and both and shown in figure 2.14b. The one in the right is a one-sided target of two planes with a $3mm$ offset. Has a dimension of $200x200mm$, the dots are $3mm$ diameter with a horizontal and vertical distance in between of $8.94mm$. It allows the alignment of the laser and focus of the cameras when they are placed at one side of the target's plane. This is particularly useful when performing two-dimensional two-components (2D2C) measurements. The second one is two-sided, allowing the settling of the cameras at both sides of the target's plane. It has four planes with an offset of $3mm$, with two of them pointing one side and the remaining couple to the other. This target is used when settling the PIV system for two-dimensional thee-components (2D3C) measurements, also called stereo PIV. In this case both cameras are used, one at each side of the target's plane. The dimensions of the dots and their positions are the same that the one-sided target.
A *Martin Magnum 1200* smoke generator using *Safex nebelfluide extra clean* smoke oil performs the seeding of the air inside the test chamber, both shown on figure 2.15. This device is settled on the inside of the wind tunnel's plenum pointing upstream to obtain homogeneous and disperse distribution of the smoke around the model, and is controlled by a remote control on the outside of the plenum.

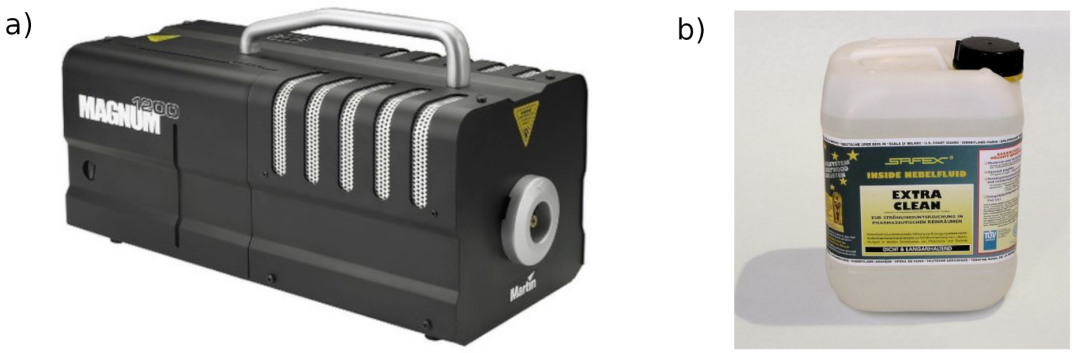

Figure 2.15: Martin Magnum 1200 smoke generator (a) and Safex nebelfluide extra clean (b). Taken from *www.martin.com*, *www.safex.de*.

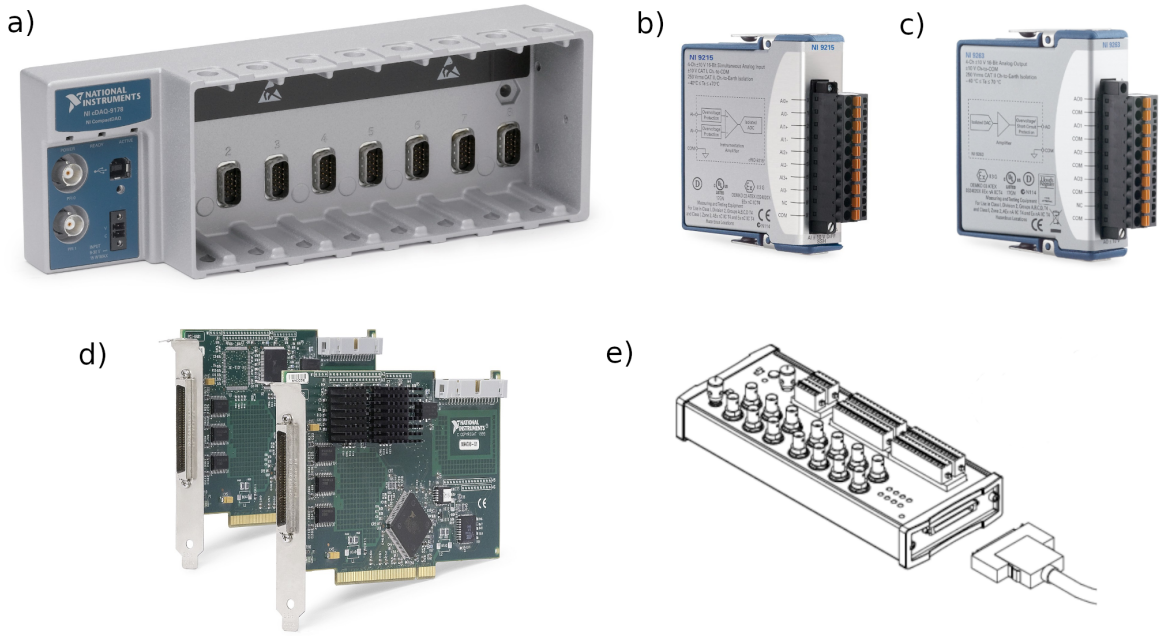

Figure 2.16: National instruments cDaq 9178 (a), 9215 analog input (b) and 9263 analog output (c) modules. National Instruments PCI 6602 counter/timer (d) and BNC 2121 connection board (e). Taken from *www.ni.com*

2.4 Data acquisition and signal generation

2.4.1 Hardware and I/O modules.

The entire I/O hardware is based in *National Instruments* components, except for the ZOC transducer. There are two main systems: the test itself and the PIV visualizations. In the following lines are explained the connections of both systems and the devices used in function of the necessity.
The test is based in a *Compact Daq 9178* chassis (reported in figure 2.16a) in which are mounted the modules required for each specific task and is settled on the top on the test chamber. The signals of the microphones were measured through four NI 9215 A/D modules with four analog inputs each, with a range of $\pm 10V$, 16 bit of resolution and a maximum sampling rate of $100kHz$. This A/D module is shown in figure 2.16b and the connections travel to the inside of the model through the hollowed strut. The sampling frequency for the microphones is $10kHz$, allowing spectral measurement until $5kHz$ considering Nyquist. The output from the three flow meters are $4-20mA$ current signals, and were converted in tension through a $390Ohm$ $\pm 5\%$ resistor. The load cell, instead, returns a tension value between 0 and 2 volts. These four tension signals were read by another NI 9215 module but in this case at $1kHz$, since theirs response does not require high sampling frequencies. The electrovalves control the proportional opening of a circular valve through a voltage signal, ranging from 0 to $10V$. To control them, a NI 9263 D/A module is used, performing four analog outputs from $\pm 10V$, $100kHz$ of maximum frequency and a resolution of 16bit. This D/A module is reported in figure 2.16c. Depending on the test, it could be necessary to perform velocity measurement using a pitot or a hot-wire probe. In this case an extra NI 9215 A/D module is available, gathering the signals of the pressure transducer in case of using a pitot, or from the Wheatstone Bridge of the hot-wire. Finally, the ZOC 33 pressure transducer inside the model sends the data through LAN connection directly

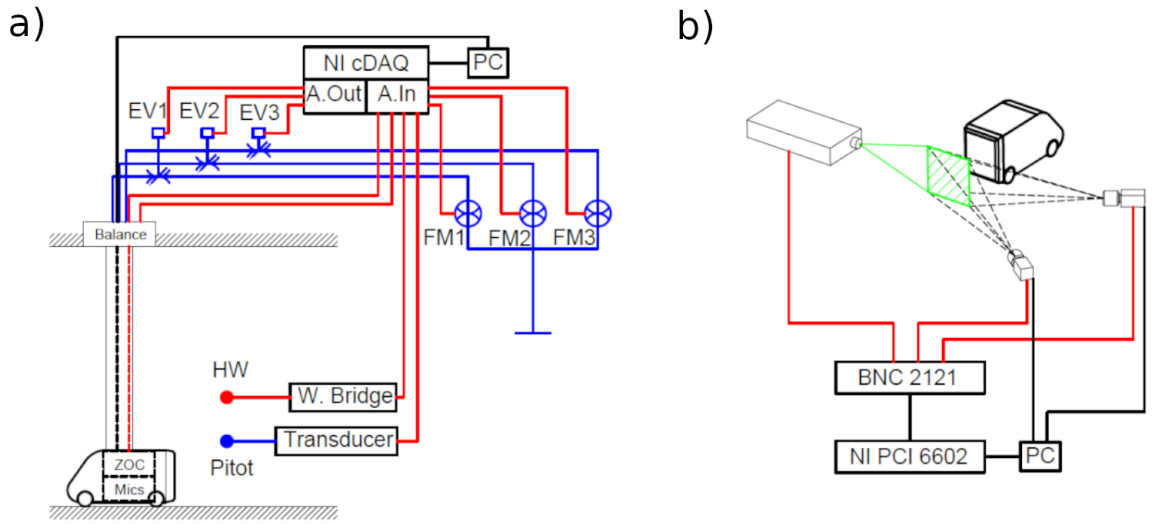

Figure 2.17: Conncection diagram for the test (a) and the PIV measurement system (b). Pneumatic lines in blue, electric lines in red and USB and LAN in black.

to the PC. The LAN cable passes inside the hollowed strut as the microphone's cables and the pneumatic tubes. The connection diagram of all these components is shown in figure 2.17a.
The PIV is commanded by a NI PCI 6602 counter/timer board mounted inside the computer and a BNC 2121 external connection board, respectively reported in figure 2.16d and e. The reason behind using an individual hardware to the PIV measurements was the low lag on the response, needed to accurately perform the optical measures. This system provides the trigger signal for both laser generators inside the laser module and the cameras. The imagine data from the cameras were transmitted to the PC via USB 3.0 in order to have a high bus of data, allowing sampling frequencies of $15Hz$. A sketch of the connection of this system is presented in 2.17b.

2.4.2 Software and file formats

The *LabView* suite provides a developing ground to create a program that respond to all the testing necessities. In this thesis, several programs were designed to cover different aspects of each test, and they could be divided in 3 main groups: logging of data, logging data and generating signals and feedback controls. The first ones only save the data given by the test, for example the drag values for different freestream speeds. The second ones log the data and controls the valves. For example, the program that characterizes the jets. This set the electrovalves in a certain configuration, then read the results from the sensors and finally save them. The feedback control, process the data received by the sensors and actuates the electrovalves according to a certain algorithm. It also saves data at determinate moments of the process. These programs are presented in *Appendix 2*. The file format mainly used are TDMS, since the high compression of the data and the possibility of opening with any Excel software. Are also used the HDF5 files, and the classic ASCII (txt) files.
The programs can also run in "live" or acquisition-only conditions. In the "live" condition the data from the test is displayed on the screen in real time, with a refresh rate of $100Hz$. The control of the valves is also performed in this condition, being possible to set the speed of each of the three jets by regulating the electrovalve tension. This

program is useful for the verification of the test conditions and for academic purposes. In the acquisition-only condition the data acquired is saved on files and not shown on the display. This allows higher sampling frequencies and times.
For the PIV control, an in-house software manage the acquisition parameters of the cameras and the laser triggers. It returns couples of $*.tiff$ images which dimensions are settled by software. A pre-process is applied to the images to remove the historical minimum, and the image deformation and velocity vectors interpolations are performed using the functions of Astarita [8] and Astarita [10]. Following the procedure of Astarita [9], a *Blackmann* weighting window is used during the correlation process to tune the spatial resolution of the PIV.

2.5 Data Processing

Many of the signals sampled by the acquisition hardware need to be processed previously to the analysis. For example, to adequate the electric signals from the microphonic capsules a calibration process was performed on a resonance tube. Moreover, a filtering process was applied to mitigate the spurious fluctuations within the flow that may exist. Sardu et al. [103] describes this calibration and filtering process. Here are summarized the algorithms used on the development of this thesis, from the spectra to the wavelet.

2.5.1 Signal filtering, cross correlation, spectral and cross spectral analysis

When analyzing the signals, especially in the frequency domain, is important to reduce the signal's spectra to a certain useful range, mitigating the effects of undesirable phenomena. This could be achieved by using physical filters on the measurement lines, but this means that part of the information contained on the signal will be lost. For this, the filtering of the signals will be always performed by software. The function used in the signal filtering cases is the *idfilt()* from *MatLab*. An ideal filter restricts the frequency range into certain defined limits.

To evaluate the level of fluctuation of a signal the Root Mean Squared (RMS) operation is used. The definition is given in equation 2.1:

$$x(i)_{RMS} = \sqrt{\frac{1}{N-1}\sum_{i=1}^{N}(x(i) - \overline{x(i)})^2} \tag{2.1}$$

In case of a couple of discrete signals, the cross-correlation returns the similarity af those by performing an inner product, and is defined as follows (equation 2.2):

$$\hat{R}_{x,y}(\tau) = \frac{1}{N}\sum_{i=1}^{N-k} x_{i+\tau} * y_i^* \tag{2.2}$$

Where x and y are discrete signals of equal length N and k is the time shift (or lag) where the cross-correlation is performed. The cross-correlations represents, in a range from 0 to 1, how similar are the two signals in the different time-lags given by τ. When

the two signals used are equal, the correlation is called autocorrelation and represented as $\hat{R}_{x,x}(\tau)$.

For the power spectral density (PSD) calculation the Welch approach is used, who returns a PSD estimate based on the Welch's overlapped segment averaging estimator. The algorithm of the Welch PSD is defined in equation 2.3, which is correlated to the autocorrelation as follows:

$$P_{xx}(f) = \frac{1}{f_s} \sum_{m=-\infty}^{\infty} \hat{R}_{x,x}(m) e^{-j2\pi m f/f_s} \tag{2.3}$$

The function used to perform this calculation is the *pwelch*() from *MatLab*. The Cross-PSD calculation is described in equation 2.4, and performed with the *cpsd*() function of Matlab® that returns the Cross-PSD estimate based on the previous described Welch method of two signals.

Emerging from the Cross-PSD calculations are the coherence and phase of the signals, both defined in equation 2.5 and 2.6:

$$P_{j,k}(\tau, \omega) = \int_{-\infty}^{\infty} R_{j,k}(t, \tau) e^{-j\omega t} dt \tag{2.4}$$

$$C_{j,k}(f) = \frac{|P_{j,k}(f)|^2}{P_{j,j}(f) P_{k,k}(f)} \tag{2.5}$$

$$\theta_{j,k}(f) = arctan\left(\frac{Im[P_{j,k}(f)]}{Re[P_{j,k}(f)]}\right) \tag{2.6}$$

Where $P_{1,2}(f)$ is the Cross-PSD of the signals 1 and 2. $P_{1,1}(f)$ and $P_{2,2}(f)$ are the auto spectra of signals 1 and 2.

2.5.2 Proper orthogonal decomposition (POD)

The POD decompose an ensemble of signals into modes and modal coefficients, as explained by Berkooz et al. [20] on the analysis of turbulence. This decomposition considers that a given fluctuating signal may be reproduced by the sum of a series of eigenfunctions, as demonstrated by equation 2.7, were the eigenfunctions $\varphi(x, y)$ need to agree the condition given on equation 2.8.

$$p'(x, y, t) = \sum_k a_k(t) \varphi(x, y) \tag{2.7}$$

$$\int \langle p'(x, y, t) p'(x, y, t)^T \rangle_t \varphi_j dy dx = \lambda_j \varphi_j(x, y) \tag{2.8}$$

Where p' is the fluctuating pressure, x, y are the positions of the degrees of freedom (DOF), t the time domain, $a_k(t)$ the modal coefficients, the subindex k represent the modes and λ_j the eigenvalues matrix.
For a series of discrete data, resolving the equation 2.8 is equivalent to resolve the eigenvalues problem of the autocovariance matrix given by the product of the signal's matrix by his transpose, as defined in equation 2.9.

$$K_{XX} = [S][S]^T \tag{2.9}$$

Where K_{XX} is the autocovariance of S, which is the matrix given by the number of DOF in the rows and the discrete time samples in the columns. This resolving practice was also used by Bastine et al. [15] on the wake of an actuator disk on large eddy simulations and Zheng et al. [128] on the wake of a triangular body. For the eigenvalues and eigenvectors calculations the function *eig*() of *MatLab* is used. The Eigenvectors are used to draw the modes of fluctuation of the rear and the Eigenvalues to calculate the relative energy associated to each mode. Since is a discrete decomposition, the number of eigenvalues and eigenvectors will be defined by the number of DOF.

2.5.2.1 Signal reconstruction: time history of the POD modes

An average reconstruction of each mode could be performed by the product of the mode itself times the relative energy (Eigenvalues) times the original signals. This allows us to use the POD decomposition like a filter, obtaining the decomposition of the signal's time history. This methodology is useful to analyze the isolated the effect of a certain mode that could be associated to a physical behavior. For example, the vortex shedding on the trailing edges of a squared-back bluff body could be associated with a horizontal and vertical symmetry-breaking mode of the pressure distribution on the model's rear base, as demonstrated by Grandemange et al. [58]. The signal reconstruction of the mode allows us to analyze the effect of that mode alone on the time domain.

2.5.2.2 Validation of the algorithm

In order to verify the correct performance, the algorithm is feed with known signals and the response is analyzed. To easily visualize the output, the distribution of microphones on the rear base are considered as the degrees of freedom (DOF) of the input, and for each DOF a sinusoidal signal is generated and properly phased in order to create three fluctuation shapes: a flat, a vertical-symmetry breaking (VSB) and a horizontal symmetry-breaking (HSB). Each of these shapes can also be regulated in intensity. Finally, all these signals are joined in a unique one and used as input, and these synthetic signals represent the benchmark in which the algorithm will be tested. For this particular case the characteristics of the input are summarized in table 2.1. The input and output of the POD algorithm are shown in figure 2.18. The three input synthetic modes are displayed in figure 2.18a and the eigenvectors of the output, in a colormap over the positions of the dof, are plotted in figure 2.18b. In figure 2.18c are shown the relative energy of the signals and the PSD of the reconstructed modes.

	Synthetic mode 1 *Flat*	**Synthetic mode 2** *VSB*	**Synthetic mode 3** *HSB*
Frequency $[Hz]$	1	5	10
Relative intensity	0.6	0.3	0.1

Table 2.1: POD Synthetic signal values.

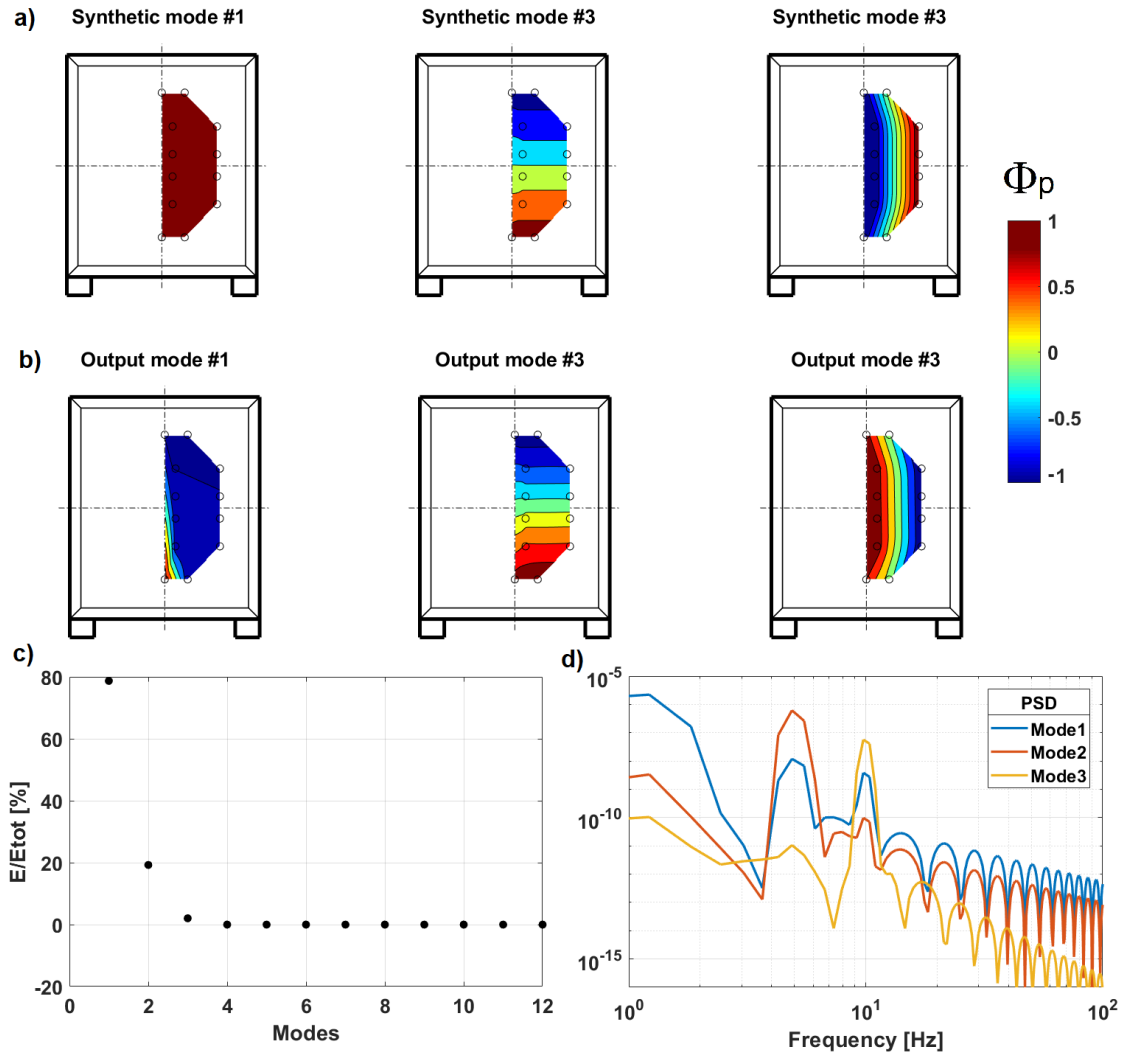

Figure 2.18: POD Validation. Synthetic modes (a), Output modes (b) and relative energy (c) and PSD of the output modes (d).

The eigenvalues obtained show almost the same shapes than the input modes. There is a small difference on the first mode, in which the last DOF evidences a peak. This could be explained by the nature of the POD: since this mode is a free-mode, cannot be represented mathematically. The algorithm forces a result by generating an opposite peak on the last DOF, slightly mismatching the input. Supporting this results, the second and third modes (not free-modes) shown perfect similitude with the input. Regardless this small deviation on the first mode, the result is accurate enough to clearly analyze the output. The energy distribution evidence some differences regarding to the input case, that may be linked to the same mathematical deviation reported before. Nevertheless, the values are not far from the input and can be considered acceptable. Finally, the PSD of the reconstructed signals shows excellent agreement with the frequency values given by the output, clearly evidencing the dominant frequencies of each mode reported on table 2.1.

2.5.3 Wavelet transform (WT)

The wavelet transform obtains, through a convolution between the signal and a scaled and translated function deriving from a so called "mother wavelet", the spectrum of the signal on the time domain. From Daubechies [43] and then first introduced in turbulence flows by Farge [52], the continuous wavelet transform coefficients are defined in equation 2.10:

$$\tilde{f}(l, x') = \langle \psi_{l,x'} | f \rangle = \int_{R^n} f(x) \psi^*_{l,x'}(x) d^n x \tag{2.10}$$

Where $\tilde{f}$ is the wavelet coefficient, l is the scale or pseudo-frequency, x' is the sample position, $\psi_{(l,x')}$ is the mother wavelet family, f is the signal, x is the main variable and * denotes the complex conjugate. The family of functions $\psi_{(l,x')}$ are defined in equation 2.11.

$$\psi_{l,x'} = l^{-n/2} \psi[\frac{x - x'}{l}] \tag{2.11}$$

The mother wavelet (ψ) is a function that must comply the admissibility condition, which for an integrable function is equivalent with an average equal to zero. The parameter $l^{-n/2}$ normalizes the wavelet function in order to obtain the same energy on each $\psi_{(l,x')}$, being n the number of spatial dimensions. The mother wavelet is deformed on his width to fit different frequencies and is moved through the time domain doing a convolution with the input signal at each instant of time, returning the wavelet coefficient for the given instant and scale (pseudo-frequency).
The function used for this calculation is the built-in *cwt*() of *Matlab*, which is a one-dimensional continuous wavelet transform and returns the wavelet coefficient magnitude. The results of the WT are presented on a "scalogram", a three dimensional chart in which the pseudo-frequency is represented on abscise and the time in ordinates. The color of each point of the chart represents the intensity of the wavelet coefficient, corresponding with the level of fluctuations at the certain frequency and instant.

2.5.3.1 Mother wavelets

Different mother wavelets are available to analyze signals, as described by Ahuja et al. [4] and Lee and Yamamoto [74]. In figure 2.19 are presented four of them.

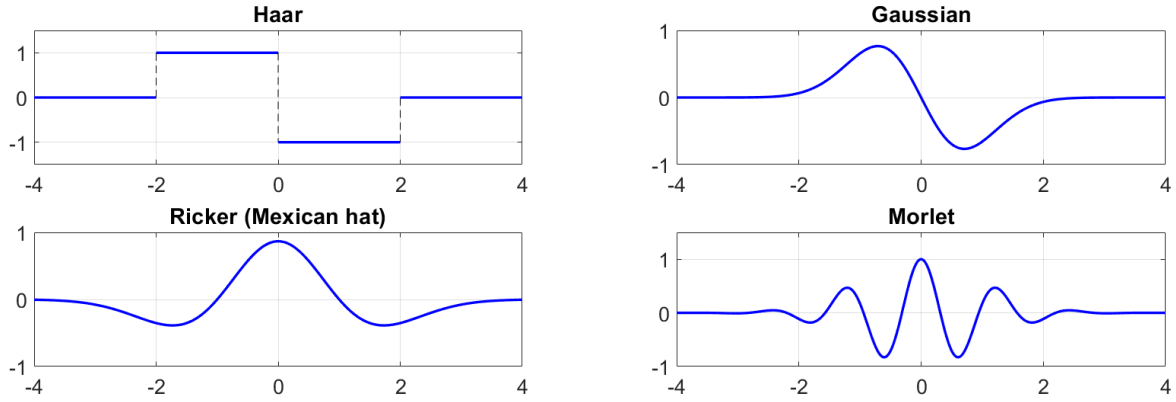

Figure 2.19: Haar, Gaussian, Ricker (Mexican Hat) and Morlet mother wavelets.

The mother wavelets resumed on the figure are representative of some typical characteristics:

the *Haar* is a non-continuous function with a finite support. These characteristics make this mother wavelet a bad choice for frequency domain localization, but very accurate when analyzing step-like time domain signals.
The *Gaussian* is a continuous function with infinite support, with improved frequency localization capabilities regarding the *Haar*. In fact, this function present optimal time-frequency localization, meaning that the resolution on the time and frequency domains is the best achievable.
The *Ricker (Mexican Hat)* is the second derivate of the Gaussian mother wavelet, therefore also with infinite support. As all the Gaussian derivates they present a good time-frequency localization, but not as good as this initial one.
In this study the *Morlet* mother wavelet will be used, and the function that defines his shape is in equation 2.12. As claimed by Torrence and Compo [112], the mother wavelet should reflect the type of features of the time series. Since the measurements are fluctuations of pressure, this mother wavelet is an accurate choice. Furthermore, it presents the minimum time-bandwidth product (as the Gaussian), meaning that it has an optimum ratio between the localization in the time and frequency domains of the wavelet coefficients.

$$\psi(x) = \frac{1}{\sqrt{2\pi}} e^{j\omega_0 x} e^{-\frac{x^2}{2}} \tag{2.12}$$

2.5.3.2 Events identification

To analyze the WT coefficients of a certain scale (pseudo-frequency), a Local Intermittency Measurement (LIM) was developed. As explained by Farge [52], this allows extracting the information of a certain scale of the WT and measuring his intermittence on each instant regarding to a windowed mean value. The LIM analysis is defined in equation 2.13.

$$LIM(Scale, x) = \frac{|\tilde{f}(Scale, x)|^2}{\langle |\tilde{f}(Scale, x)|^2 \rangle_x} \tag{2.13}$$

Where $\tilde{f}$ represents the WT, the $Scale$ refers to the pseudo frequency on the WT, x is the time position and the denominator is averaged on a window around x. If $LIM(Scale, x) = 1$ there is no intermittency, numbers above 1 represents a fluctuation predominance of the point x over the average $\langle\rangle_x$. This average is performed over a window that can be modified to change the sensibility of the algorithm. Furthermore, since the LIM is defined as the square of the wavelet coefficients (equation 2.13) it could be interpreted as the energy contained in the signal in that instant. As explained by Camussi and Guj [29] the LIM is a good parameter to observe the energy fluctuations, and these could be associated to energetic structures of the passing flow. In order to identify the energy bursts, the "events" are defined: the peaks of the LIM that exceed a predefined trigger are considered an event, thus a point in which the instantaneous energy rises beyond a certain limit. The trigger used on this study is equal to 2, meaning that the intermittency energy on an event will be at least twice the mean around this same point. Nevertheless, there may exist cases in which this value could be excessive. Is task of the user to identify the most adequate trigger for each case. The intensity of the LIM is also an important component of the event, evidencing different kind of phenomena based on theirs energy. To complete the analysis, a LIM "No-event" was also defined, being the mid-point on the WT between LIM events instants. These points are useful to compare the signals of the LIM and No-LIM events, and characterize both states.

2.5.3.3 Validation of the WT and LIM algorithms

As in the precedent POD case, synthetic signals are generated to validate the response of the algorithm. Since the method used is one-dimensional, a unique signal with different components of amplitude and frequency that may vary in time is used. In particular, three cases are analyzed: 1) a signal composed by two sinusoidal functions with different frequencies each, 2) a sinusoidal signal that becomes null for a certain instant, and 3) a sinusoidal signal that changes frequency in a certain moment.

In figure 2.20 is shown the first case analyzed. The signal characteristics in terms of time and frequency are shown in 2.20a, performing a composition of two stationary sinusoidal components at 4 and $9Hz$. The signal is artificially generated at $10kHz$ with a length of $60s$, or 600000 samples. These frequency were chosen because they are in the neighborhood of the typical frequencies for our model. For example, if considered the vortex shedding ($St = 0.12$), the frequency will be around $6Hz$. The scalogram of wavelet transform coefficient in 2.20b shows the energy of the fluctuations on the scales versus time, and on the right colorbar the magnitude of the wavelet coefficient. The two frequencies of the input signal are represented by two constant zones of high magnitude around 4 and $9Hz$, with no trace of other components or noise. Moreover, two white dashed lines are observed on both initial and final moments in an almost-vertical position, which represents the cone of influence (COI) of the wavelet analysis. This means that the algorithm will lost precision outside those limits due to border effects. On the scalogram is visible a red dashed line at $6Hz$ that represents the scale in which the LIM is performed. The target scale was settled in between the two frequencies in order to capture both components of the input signal. The LIM value on the time axis is shown in 2.20c. In the LIM plot there is also a red dashed line, but in this case it represents the threshold in which the intermittency energy doubles the adjacent, as previously defined. The LIM plot do not show any variation except for the border effects of the wavelet and his value is constant at one, meaning that there is no intermittency on the signal. This result was expected, since there is no variation on the signal in the frequency or time domains. In figure 2.21 is shown the second validation case, where the input signal consist in a sinusoidal component at 9 Hz that is interrupted in the instant between 2.5 and $7.5s$, as shown in figure 2.21a. Different from the first, this input signal presents a non-stationary behavior that should prompt changes on the LIM values. In figure 2.21b are evidenced the high levels of magnitude around the $9Hz$ frequency and the lack of it in the 2.5 to 7.5 instant. As expected, the LIM measurements of figure 2.21c performed at $6Hz$ show two peaks at the end and beginning of the interruption. Now is intended to understand how the window and the scale in which the LIM is performed affect the result. In figure 2.22 are shown the results of the LIM calculation for the same input signal of the precedent case but now using different windows of calculation and in different scales.

Starting with the window in figure 2.22a, the analysis was performed in the range of 0.2 to $1.4s$ and in the $9Hz$ scale (agreeing the input signal). The LIM shown increasing values when increasing the window until $0.8s$ where reach $LIM = 2$. For higher values of windows the LIM value do not grow, but it increases the amplitude in time. This last effect is unfavorable since reduce the accuracy of the measurement. In conclusion, the $0.8s$ window allows maximum levels of LIM with the maximum resolution available at this level of frequency of the signal.

In sake of simplicity, the results of the window are shown only for the $9Hz$ input case. As seen, even if the frequency is not perfectly matched, the LIM algorithm performs

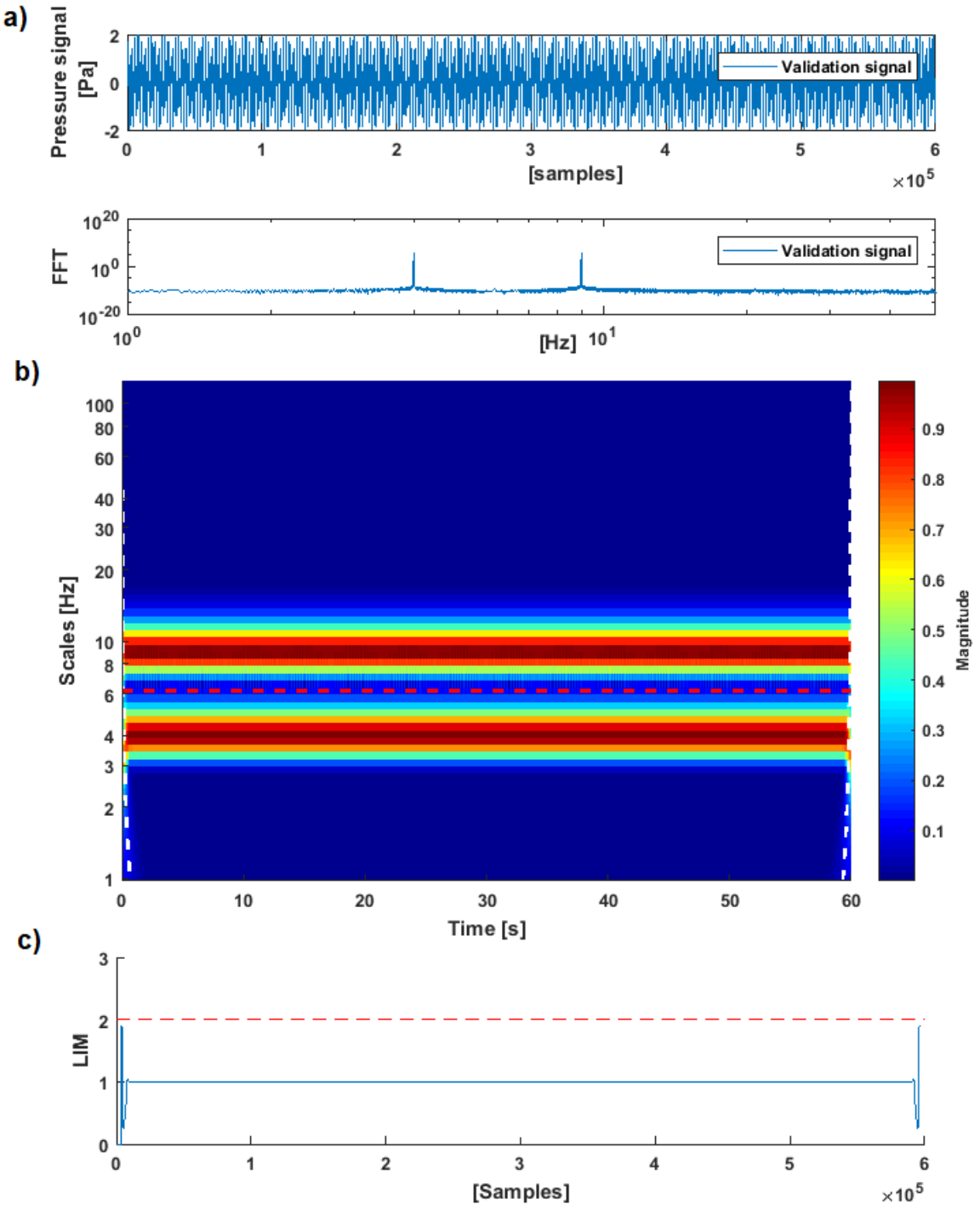

Figure 2.20: Wavelet Validation. Input signal containing two sinusoidal components at 4 and $9Hz$(a) and scalogram of the signal (b). The frequency in which the LIM analysis (c) is performed is evidenced with a red dashed line ($6.1Hz$).

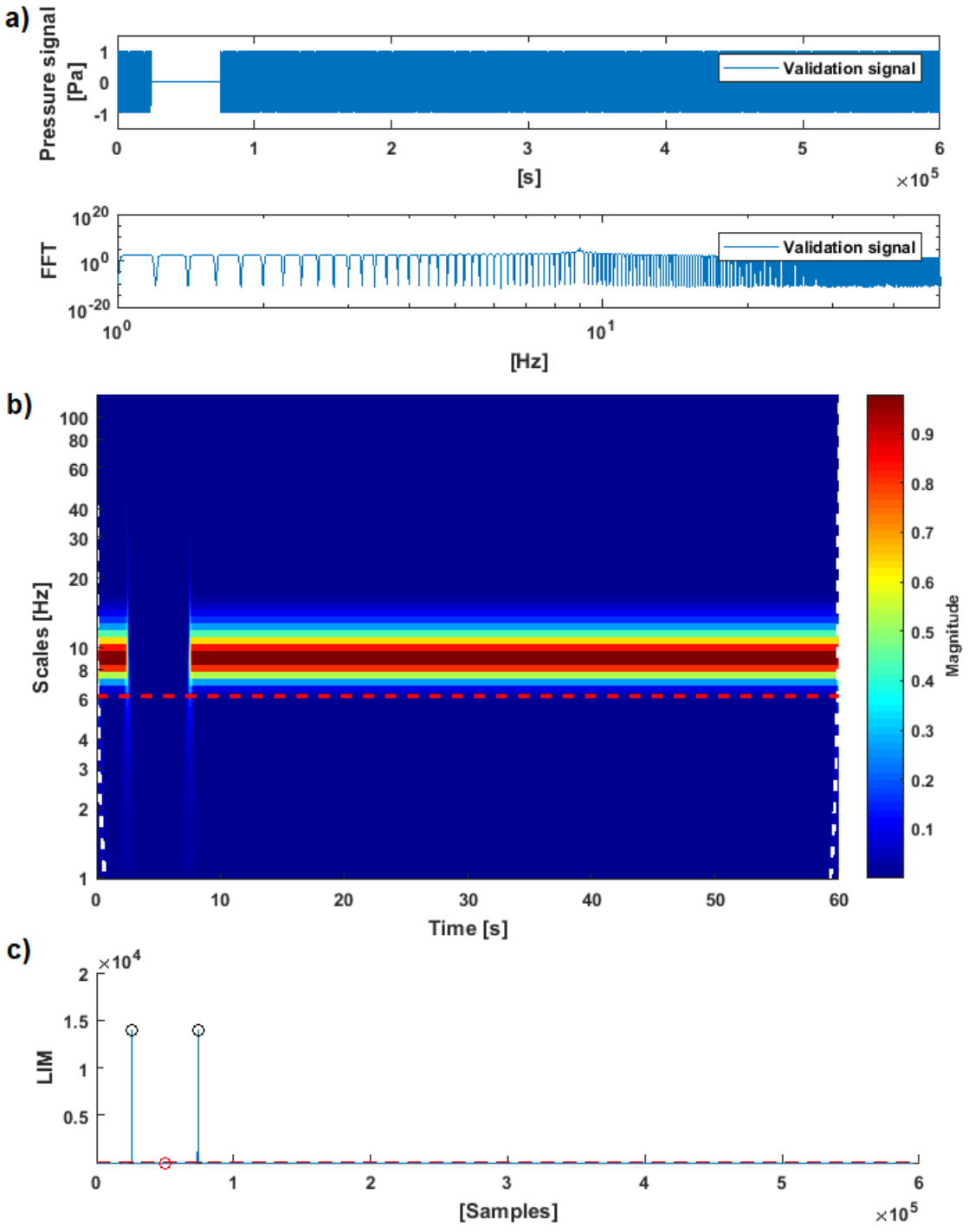

Figure 2.21: Wavelet Validation. Scalogram of an interrupted sinusoidal signal at $9Hz$. The frequency in which the LIM analysis is performed is evidenced with a red dashed line ($6.1Hz$).

very well and easily identifies the changes on the signal. Since the main frequencies of the test will be around this level of frequency, is concluded that the window of $0.8s$ is accurate enough for th calculation.
With the optimal window defined at $0.8s$, the response of the LIM is analyzed in the scales surroundings of the input signal's frequency ($9Hz$). The results are plotted in figure 2.22b and show a particular behavior: the LIM results for the closest frequency to the input one (Scale= $8.7Hz$) are less intense that the surrounding ones. This is because the denominator of the LIM algorithm has high values regarding the numerator for this particular validation signal, since in the analyzed scale the wavelet coefficient are high in the whole time domain. Nevertheless, the value of the LIM show a peak on the 2.5 and $7.5s$ that reach the trigger value, thus evidencing the event.

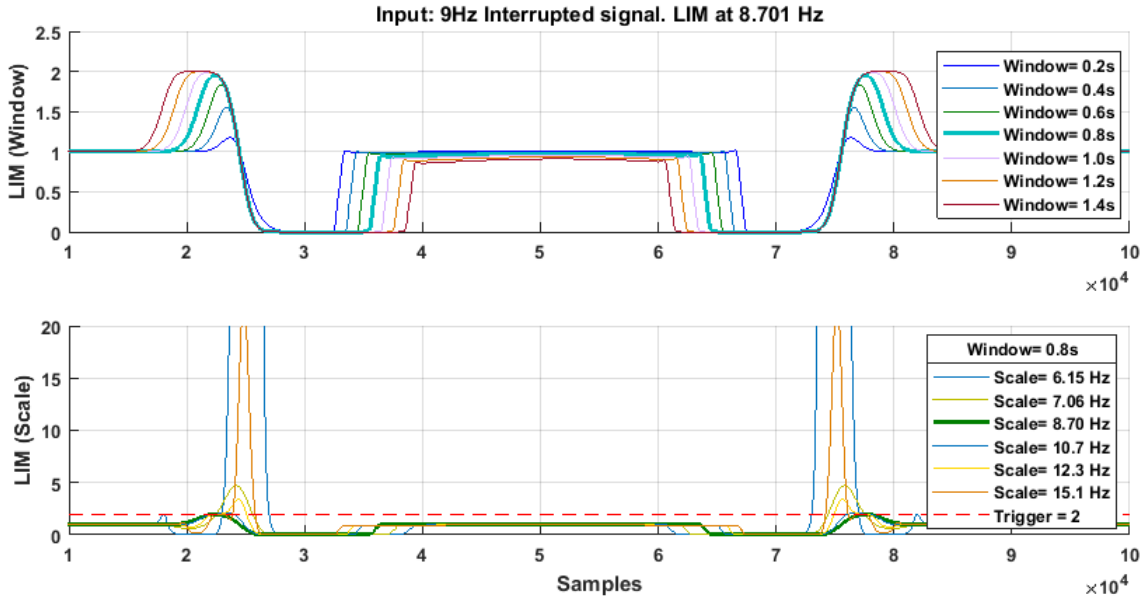

Figure 2.22: Wavelet Validation. LIM analysis for the interrupted signal case of figure 2.21. Instead of the time scale, here are used the samples.

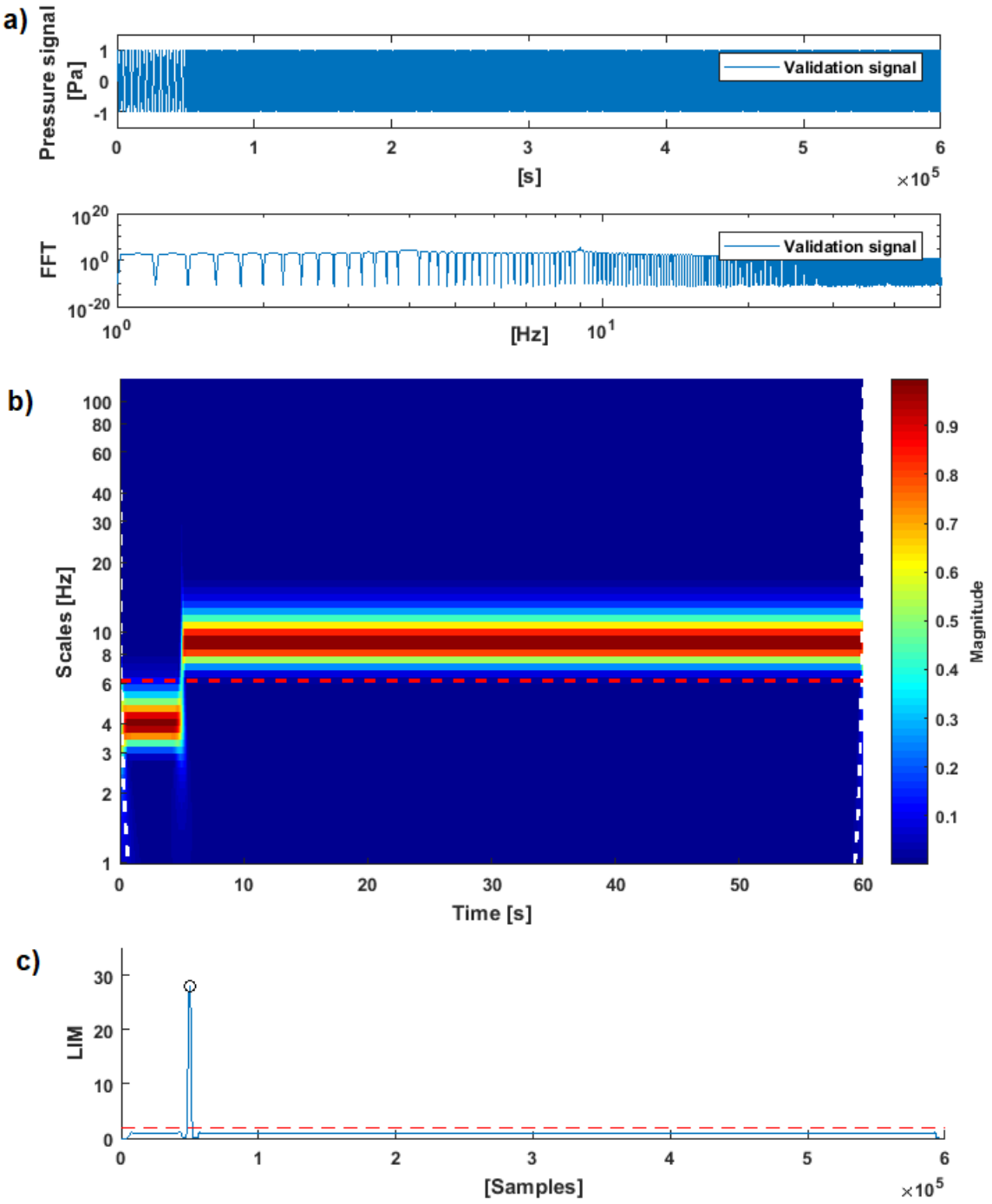

Figure 2.23: Wavelet Validation.

Finally, in figure 2.23 is shown the third validation case. The signal jumps from 4 to $9Hz$ at $5s$ as evidenced in figure 2.23a. In figure 2.23b the scalogram highlights the change on the frequency with the shift of the magnitudes from 4 to $9Hz$ and the LIM presents a peak in that exact moment (2.23c). This proves that the LIM is sensible to frequency changes on the signal even when the frequency being analyzed does not coincide with the two frequencies involved. In conclusion, the continuous wavelet transform is an adequate methodology to identify variations on time and frequency domains of a certain signal. The LIM analysis of the scales help identifying changes on the two domains, in the surroundings of a certain level of frequency. These two tools will be useful when analyzing the pressure fluctuations on the rear part of the model.

2.5.4 Combined POD and WT analysis

As evidenced in section 2.5.2 the POD decomposes the signal in modes, and these can reproduce a mean time history of each one of them. This evidences the filtering property of this methodology, in function of the "shape" of the fluctuations. In a similar way, the WT also can be considered as a filter since returns the energy levels at certain scales of the input signal. In this case, the filtering has a frequency nature. This kind of analysis was performed by Zheng et al. [128] on the wake of a triangular bluff body, applying continuous WT to POD modes and discrete WT coefficients. Inspired by these results and considering the possible association of certain modes to particular aerodynamic phenomena, the WT could be applied to the POD modes' time histories aiming to analyze the non-stationary mode's dynamics.
In order to do this, the WT will be simply applied to the reconstructed mean signals of the POD modes.

2.5.5 Image processing for PIV

The optical calibration of the whole system is performed at the beginning and end of each series of tests. Even if the alignment of cameras and laser is accurately performed, the effects of wind tunnel vibrations, movement of components and changes on the temperature may disturb these alignment. The corrections for the misalignment is obtained by a self-calibration procedure, described in Wieneke [121]. The error resulting of the calibration with the corrections is 0.05 pixels. A pre-process is applied to all images gathered in order to eliminate possible reflections of the laser on the wind tunnel walls and model by removing the historical minimum. The interpolation of the velocity vector field is carried out using spline functions (Astarita [8], Astarita [10]) and the correlation process uses a Blackmann weighting window to tune the spatial resolution of the PIV process (Astarita [9]). The final window size is 64×64 pixel (corresponding to $3.55 \times 3.55mm$), with 82% overlap. These conditions allows us to assess that the velocities' average error is smaller than 1%.

Chapter 3:
Wind Tunnel Methodology

In this chapter the methodology for the complete aerodynamic characterization of the model will be exposed and the test conditions will be described. The drag balance will be characterized in static and dynamic conditions, and the microphones will be compared with a high quality pressure sensor and successively mapped. The four blowing slots will be characterized on velocity profile and average blowing intensity as well as the valves and flow meters of the pneumatic lines. The PIV methodology will be described for the PIV and Stereo PIV measurements. Finally, the test conditions will be exposed including some main features of the baseline flow.

3.1 Drag balance calibration and measurement procedure

As explained in section 2.2.3, the leverage ratio of the drag balance changes with the position of the center of pressure, more specifically with the vertical component. Furthermore, the system's stiffness together with the counterweight produces small oscillations that need to be characterized. Finally, since the AFC uses blowing jets, the resultant thrust might introduce a component on the drag readings. All these issues will be assessed next.

3.1.1 Static characterization

To calibrate the output of the balance different known weights ranging from 50 to $125Gr$ were applied to the model using a circular clip with calibrated weight probes as shown in figure 3.1a. The weight was applied in increasing an then decreasing order to evaluate the hysteresis of the response. The application of the calibrating force must be in the center of pressure of the model in order to accurately measure the drag. Previous measurements of the pressure distribution around the model settle the model's vertical center of pressure (Y_{cp}) at $60 \pm 2.5mm$ from the bottom base. The measurements were made at 50, 60 and $70mm$ in order to cover all possible pressure center positions. Smaller steps between measures were not possible due to the complexity of the calibration system.
The relationship between the output tension of the balance regarding to the weights applied are plotted in figure 3.1b for the three positions. From this data the slope of the regressions were calculated for the three positions, thus representing the force/tension ratio (K) of the balance on each case. The results are presented in table 3.1. From

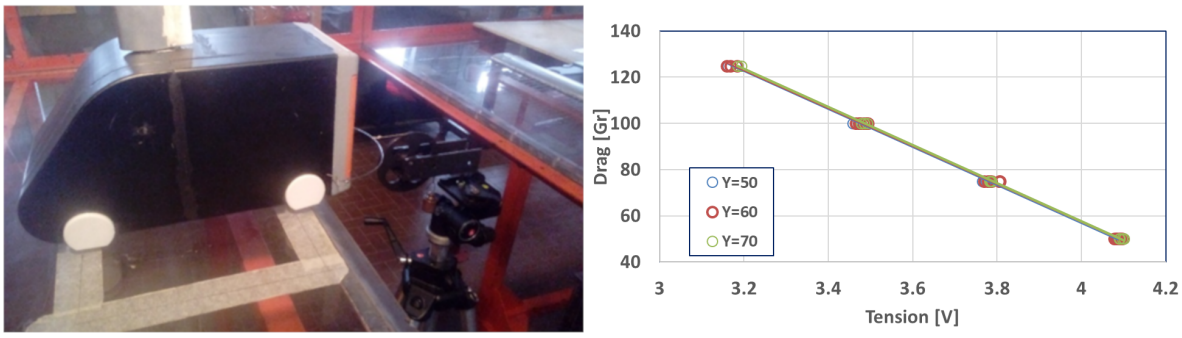

Figure 3.1: Calibration of the drag balance (a) and results of the calibration (b).

$Y_{cp}[mm]$	$K[Gr/V]$	R^2	$hyst[\%]$
50	82.2	0.999	0.56
60	81.8	0.998	0.52
70	82.69	0.997	0.50

Table 3.1: Linear regression parameters of the drag measurements at different heights

the values of the table and the regression graph is evidenced that the variation of the force's application has no relevance on the coefficient for the range measured. Since the position of the center of pressure is always around $60mm$ and the resulting regressions have no significant changes for the different positions applied, the chosen regression for the drag measurements will be the $Y_{cp} = 60mm$. Therefore the final values for the drag balance calibrations are $K = 81.8[Gr/V]$ with a coefficient of determination $R^2 = 0.998$ and a hysteresis of 0.52%.

3.1.2 Dynamic characterization

The elasticity and weight of the whole leverage and model system produces a natural oscillation of the model that, even if small, could induce deviations on the measurements. In order to obtain the natural frequency of oscillation of the balance in working condition, an impact test was performed. This consist on slightly hitting the front of the model when is on his equilibrium point and measuring the response of the drag. The results of the impact test are represented on figure 3.2 for the time (top) and frequency (bottom) domains. The results evidence a peak of energy of the response at $1.5Hz$ corresponding to the natural frequency of oscillation of the drag balance and model assembly. A positive aspect is that this value is near one order of magnitude below the typical shedding frequencies of the body, but on the other hand may cover low-frequency phenomena like bubble pumping. Considering the typical freestream speed ($9m/s$) and the width of the model ($W = 0.17m$), the Strouhal value is $St = 0.028$. Since this value is below the characteristic adimensional frequencies, the drag balance resonance should not affect neither the bubble pumping nor the vortex shedding readings.

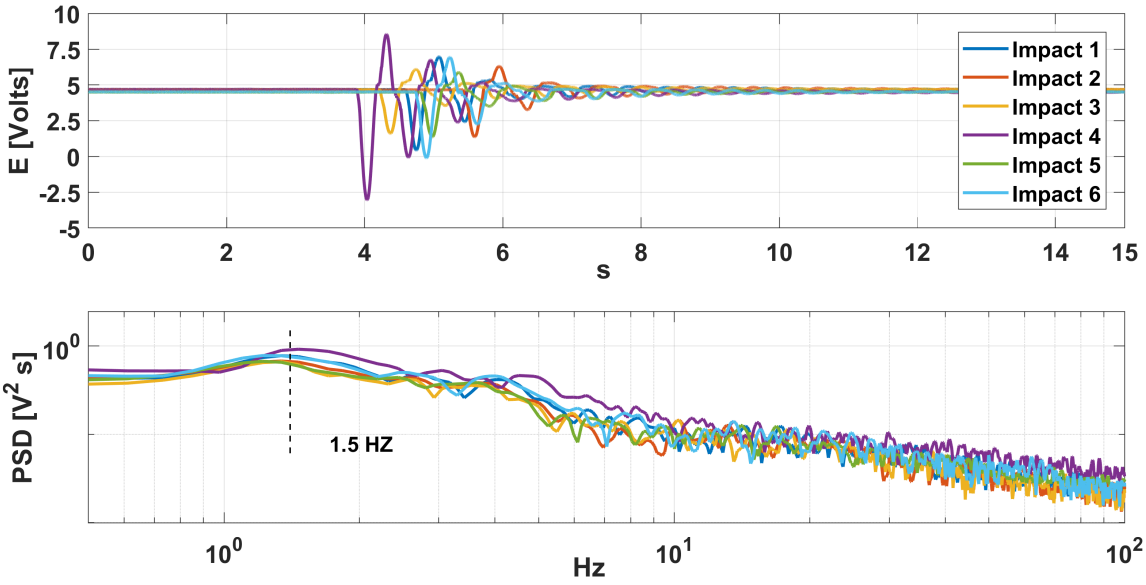

Figure 3.2: Drag measurement system response for impact tests in the time and frequency domains.

3.1.3 Effects of the jets on the drag measurements

Since a component of the AFC blows in the streamwise direction, there will be an effect of the drag purely associated to the thrust of the jets. To measure this, the AFC was activated with the wind tunnel at zero freestream speed. For this test only the bottom and lateral jets were used. The motivation of this will be later exposed on chapter 5. In figure 3.3 are represented the results of the test in an colormap, and the colorbar indicates the thrust in grams.

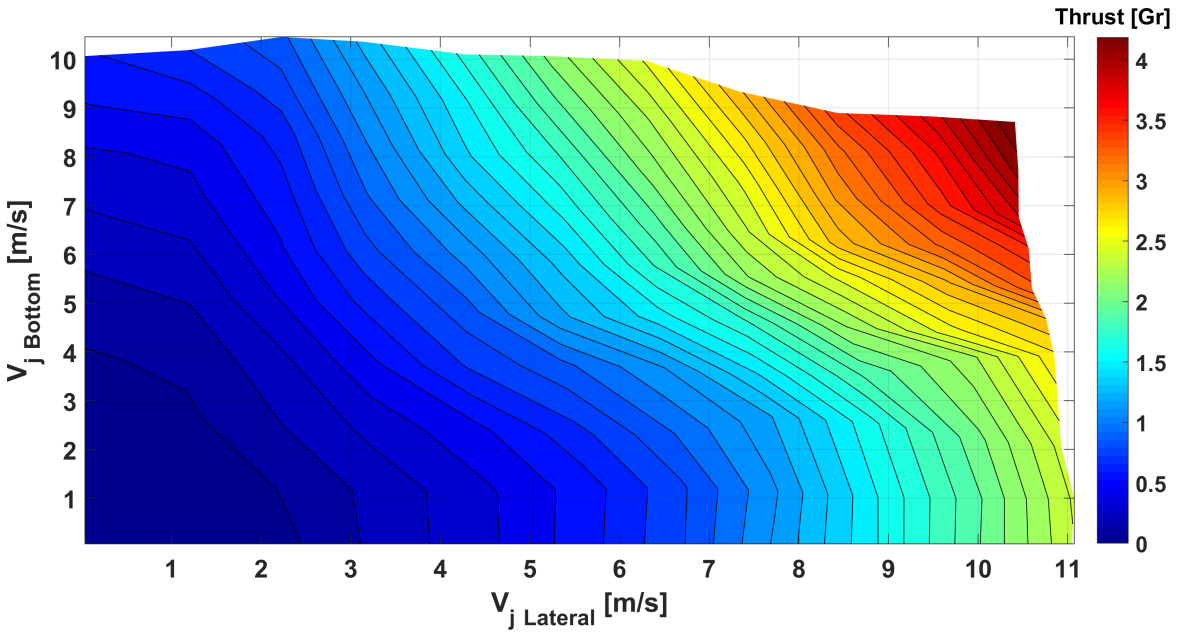

Figure 3.3: Thrust of the bottom and lateral jets at different speeds.

The thrust of the bottom jet shows negligible thrust when blowing by itself. The lateral jets instead, produce relevant thrust for values over $7m/s$. The effect of com-

bining both lateral and bottom jets further increases the thrust, showing significant increasing for values V_j Bottom and V_j Lateral over $5m/s$.

3.2 Fluctuating pressure sensors calibration

In order to calibrate the response of the microphones, their response was compared with the high-quality B&K microphone as described in Sardu et al. [103] and Sardu [102]. The calibration consist in the settling of the microphones on a circular plate asides the high-quality microphone. This plate was fixed to one end of a resonance tube and on the other end a loudspeaker was mounted, as reported in figure 3.4a. The loudspeaker generates white noise while the microphones measures the signals. Once the test is finished, the signals from the microphones are compared with the B&K and the calibration is applied in order to have the same frequency response intensity on each microphone. In figure 3.4 are shown the frequency response of the microphones before (3.4b) and after (3.4c) the calibration. Finally, the signal is converted to pressure, based on the mapping of the B&K output.

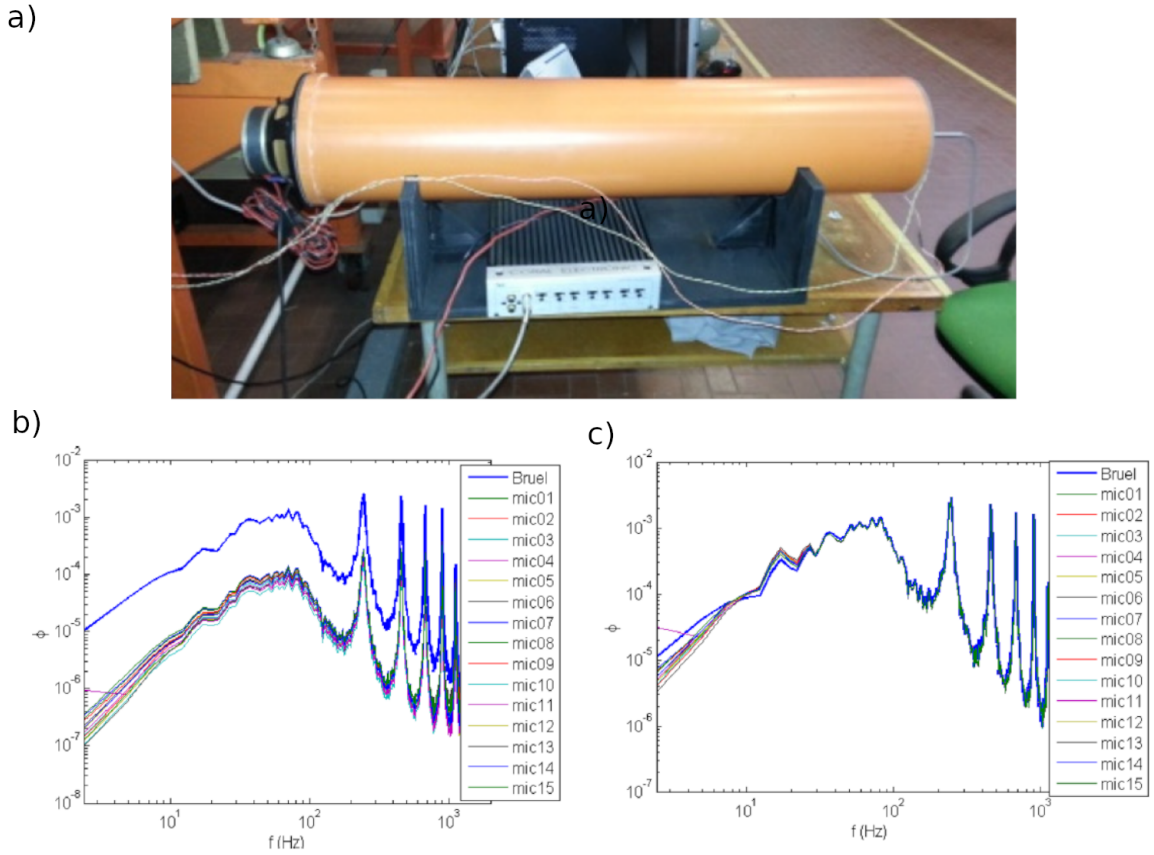

Figure 3.4: Resonance tube (a). Signal frequency response before (b) and after (c) calibration. Taken from [103]

3.3 Jets' characterization

The characterization of the jets was performed by correlating the flow meters output with the electrovalves input. The exit velocity of the jets was calculated by dividing the airflow of the lines, given by the display flow meters, by the output area of the jets. In addition, the output signal of the flow meters was characterized. Preliminary test evidence $2bar$ as the optimum input pressure of the system, allowing speeds until $15m/s$ on the lateral jets for the whole working range of the electrovalves. During the test the electrovalves were exited with an input tension between 5 and $10V$ and the airflow values were directly read from the flowmeter display and logged. Simultaneously, the output signal of the flow meters was logged. The results of the flow meters output and jets velocity are plotted in figure 3.5a and b respectively, and the calibration equations are 3.1, 3.2, 3.3 for the jets and 3.4, 3.5, 3.6 for the flowmeters. The measurement were performed in near normal conditions ($1Atm$, $25°C$) in order to match the calibration condition of the flow meters.

$$(V_j)_{Top}[m/s] = -0.6877V^3 + 15.056V^2 - 98.603V + V_{0_T} \tag{3.1}$$

$$(V_j)_{Bottom}[m/s] = -0.7212V^3 + 15.855V^2 - 105.37V + V_{0_B} \tag{3.2}$$

$$(V_j)_{Lateral}[m/s] = -0.2217V^3 + 5.1095V2 - 34.745V + V_{0_L} \tag{3.3}$$

For input tensions between 5 and $10V$. Typically, $V_{0_T} = 201.44$, $V_{0_B} = 220.43$ and $V_{0_L} = 73.533$.

$$(Q_j)_{Top}[Nlts/min] = 611,43V - Q_{0_T} \tag{3.4}$$

$$(Q_j)_{Bottom}[Nlts/min] = 613,23V - Q_{0_B} \tag{3.5}$$

$$(Q_j)_{Lateral}[Nlts/min] = 270,23V - Q_{0_L} \tag{3.6}$$

For output tensions between 1.5 and $2.5V$. Typically, $Q_{0_T} = 945,46$, $Q_{0_B} = 947,03$ and $Q_{0_L} = 415,55$.

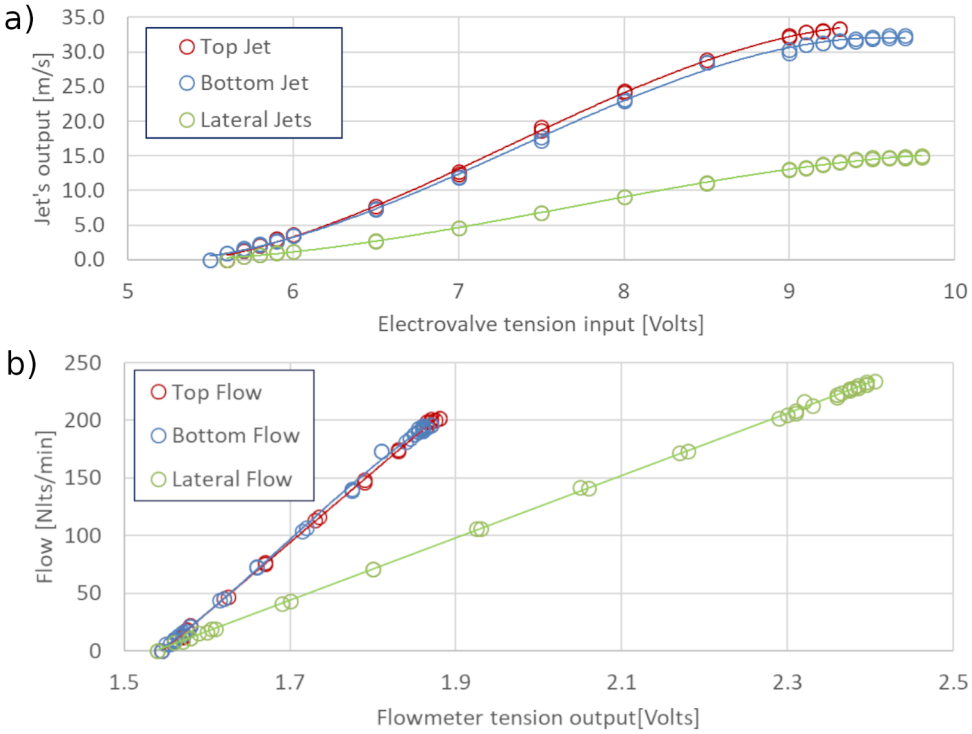

Figure 3.5: Calibration of the jets' velocity (a) and lines' flow (b).

3.3.1 Jet's velocity distribution

Due to the nature of the 3D printing construction, the actuators may present some irregularities on the geometry, thus changing locally the behavior of the flow inside the actuator. This means that the blowing air may suffer variations on the speed through the output length. In order to evaluate this deviation air speed measurements were performed positioning a hot-wire parallel to the slot width and moving it throughout the length. The results of this measurements are shown in figure 3.6. In blue is the trend of the output speed ratio (V_i/V_{output}) and in red its mean value, regarding to a blowing speed of $10m/s$. In the vertical scale is represented the velocity ratio given by the measured speed versus the output speed, and in the horizontal axis the number of measurements with the length steps in mm. The measurements were taken from left to right for the horizontal actuators and from bottom to top on the vertical. All four results show small level of irregularity on the output speed except for the right actuator. In this case the asymmetry is relevant, showing a growing tendency towards the top. Several methodologies were tested in order to compensate this non-uniformity but none of them succeed. From the mean values of all positions is observable that there is a lack of mean velocity at the output. Due to the reduced dimensions of the slot and hot wire the correct alignment of the anemometer was not possible, being this the cause of the lack of output speed. Finally, the same measurements were repeated at 5 and $7.5m/s$, obtaining the same distributions.

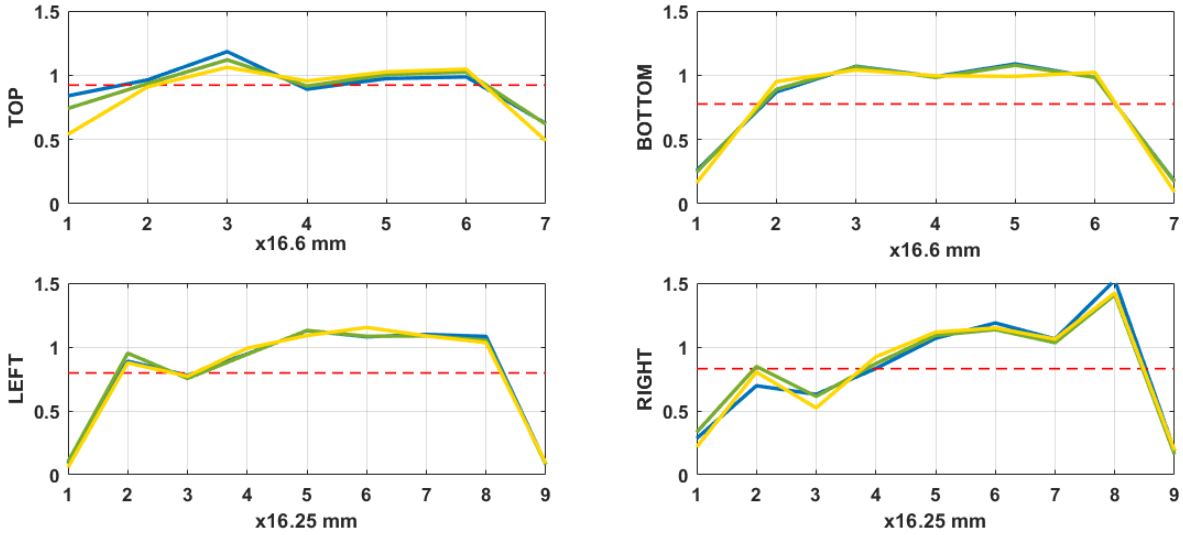

Figure 3.6: Jets' velocity ratio (V_i/V_{output}) profiles for $10m/s$ (blue), $7.5m/s$ (green) and $5m/s$ (yellow) of output velocity in function of the position over the length in steps of $16.6mm$ for the top and bottom and $16.25mm$ for the laterals.

It is evident that there is non-uniformity on the speed through the slots, nevertheless they can be considered good from a mean point of view. This also means that a non-uniformity on the flow field could be observed when the AFC is activated due to this irregularity.

3.3.2 Jet's dynamic response

The lag between the activation of the valve and the actual blowing was characterized for a sinusoidal input signal with 90% of opening of the valves. In figure 3.7 are presented the results from 0 to $35Hz$.
The first observation is the error of the measurements, around $+0.05s$. The lateral jets evidence no lag in the frequency domain, while the top and bottom jets present a peak of delay at $30Hz$. The fact that this peak is only present on the top and bottom jets points to a resonance of the pneumatic line, which have the same dimensions. Nevertheless, the phase of the signal is $0.03s$ which is very small and for higher frequencies the lag disappear.

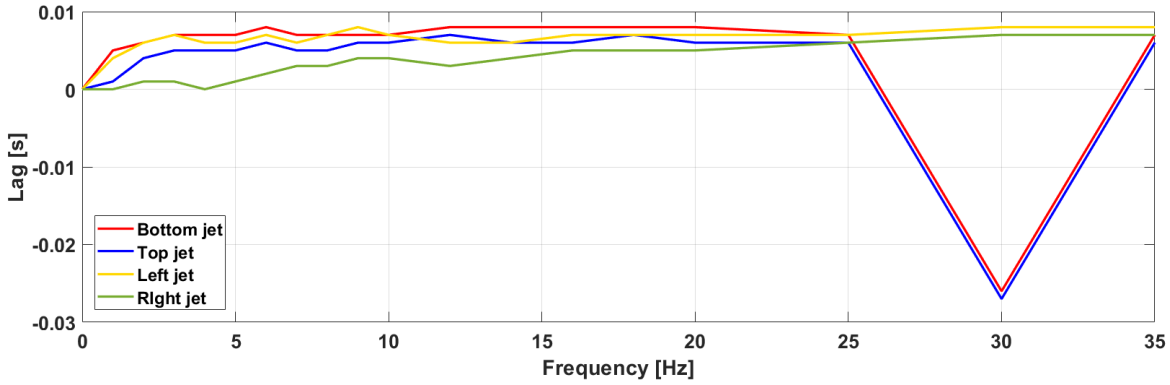

Figure 3.7: Phase between the velocity output and a sinusoidal input signal of the valves in function of the frequency.

3.4 Calibration of the Hot-wire sensor

The calibrations of the hot-wire (HW) anemometers were performed in-situ, using as a reference a pitot probe, as show in figure 3.8. The typical calibration is performed with a 5th order polynomial, shown in the right part of figure 3.8, with the correspondent coefficients. Orders smaller than 5 reduce significantly the accuracy of the interpolation and above 6 the difference between interpolations is negligible. Since the flow on the wake of the model may vary in a wide range between the freestream speed and almost zero, the calibration of the hot-wire anemometer is performed in the whole speed range.

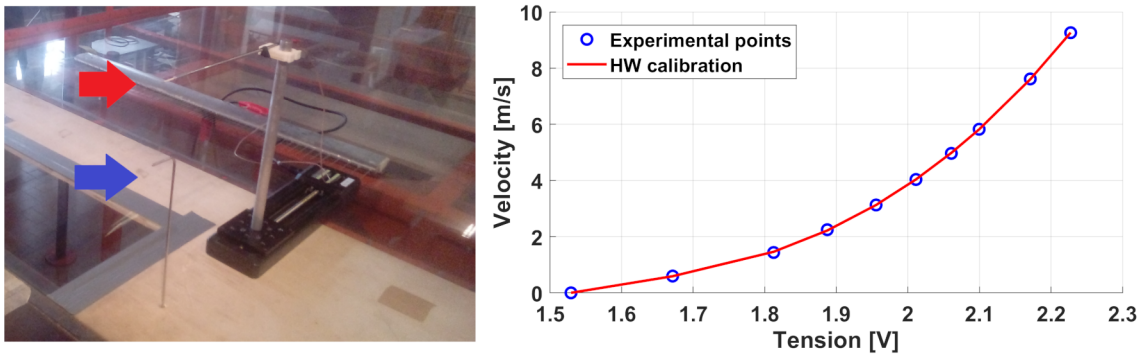

Figure 3.8: Hot wire calibration. In the left foto are evidenced the Hot-wire in red and the reference pitot in blue, and at the right a typical calibration interpolation.

The calibration of the hot-wire anemometer was performed in all cases on the beginning of each test campaigns. In the case of test of more than one day long, the calibration was performed before the first test of the day.

3.5 Power consumed by the AFC system

As already explained in equation 1.6 of section 2.1.2, the energy budget of a certain active configuration is given by the ratio of power gain and consumed. The power gain

is relatively straightforward to obtain, since it will be given by the drag reduction. This power is defined in equation 3.7

$$P_g = \Delta C_D V_\infty \tag{3.7}$$

Where ΔC_D is the drag variation and V_∞ the freestream speed. In regard to the power consumed by the jets is defined in equation 3.8.

$$P_c = \Sigma \frac{1}{2} \rho V_{j_i}^3 A_{j_i} + \Sigma \Delta P_{losses} \tag{3.8}$$

Where V_{j_i} is the blowing speed of the i^{th} jet, A_{j_i} the output area of the jet's slot and P_{losses} are the pressure losses accounting for the pneumatic lines. This approach was fist applied by Sardu [102], where was also defined the pressure losses of each pneumatic line. The calculation of the power consumed aims to a near-realistic condition, this means that the pressure losses taken into account should be only those inside the vehicle. This presents a problem since the pressure and flow measurements are performed on the exterior of the wind tunnel. In figure 3.9 are represented the parts of pneumatic lines involved on the power measurement (nodes) and evidence the portion of these lines where the pressure losses are relevant. The flow measurements are performed further upstream the pressure lines.

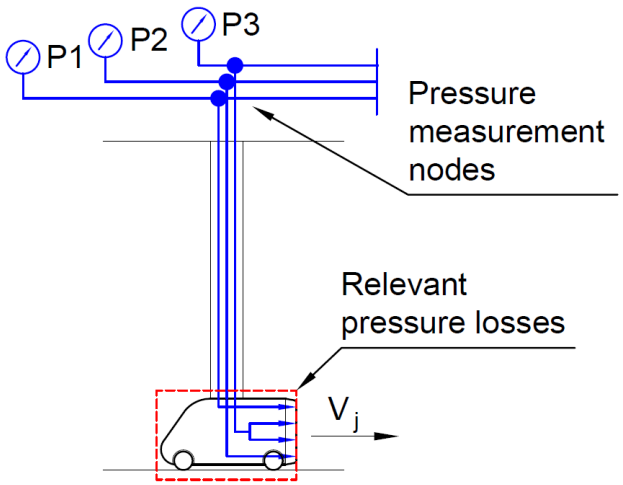

Figure 3.9: Measurement of the power of the jets.

This means that the measurements of the pressure losses will consider the whole pressure line from the jets until the measurement nodes. To obtain the fraction of the pressure losses that corresponds only to the internal part of the model, the individual pressure losses of each component of the pneumatic line from the jet's exit to the manometers (See figure 3.9). This procedure is based on the estimations of pressure losses given by *Handbook of hydraulic resistance* [68] and described in Sardu [102].
The pressure loss is calculated based on the pressure drop measured between the manometers $P1$, $P2$ and $P3$ shown in figure 3.9 and the output of the jets, considered as the ambient conditions.
In the studies of Sardu [102] the conclusions evidence that the pressure losses correspondent to the vehicle only were 15% of the whole line's losses. In this study the pneumatic line is different and the pressure measurements are performed on the exit of the strut, as seen in figure 3.9. For this case, the losses correspondent to the internal parts of the model are 25% of the measured losses.

3.6 Reference dynamic pressure

The dynamic pressure on the test chamber can be measured in two ways: direct measurement with Pitot probe or calculated by the pressure variation of the convergent. The first method involves the introduction of a pitot probe on the test chamber. The Pitot is connected to the pressure transducer (both described in section 2.3.1) which provides a tension output in function of the pressure difference, and since this difference is P_0 - P_∞ the tension output will be representative of the dynamic pressure q_∞. This procedure allows measurements on different parts of the test chamber depending on the geometry of the Pitot probe.
The second uses a the pressure difference of the convergent in order to calculate the dynamic pressure. This differential pressure measurement is performed using 2 inputs of the ZOC transducer shown in 3.10, and the dynamic pressure is obtained by the equation 3.9.

$$q_\infty = 1.0846\Delta P_{convergent} + 0.06789 \tag{3.9}$$

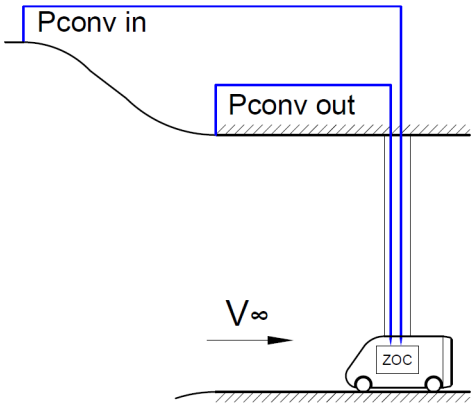

Figure 3.10: Connection of the ZOC into two static pressure taps at the begining and end of the wind tunnel convergent.

3.7 PIV technique

The PIV concept consist in measuring the displacement of a particle that moves within the flow in a predefined period of time, from which is extracted the velocity. To measure this, the flow field is inseminated with small particles (smoke) that travel within the fluid. A laser sheet is settled to illuminate the survey area and a camera is coordinated to get an image each time the laser sheet flashes. The images are acquired in couples by the camera with short delay between the expositions and these two images are then compared through a cross correlation analysis, following one particle at the time. Measuring the displacement of the particles and considering the time between shots, the velocity is calculated. By calculating the velocity of all particles on the image the velocity distributions on the studied plane is obtained.

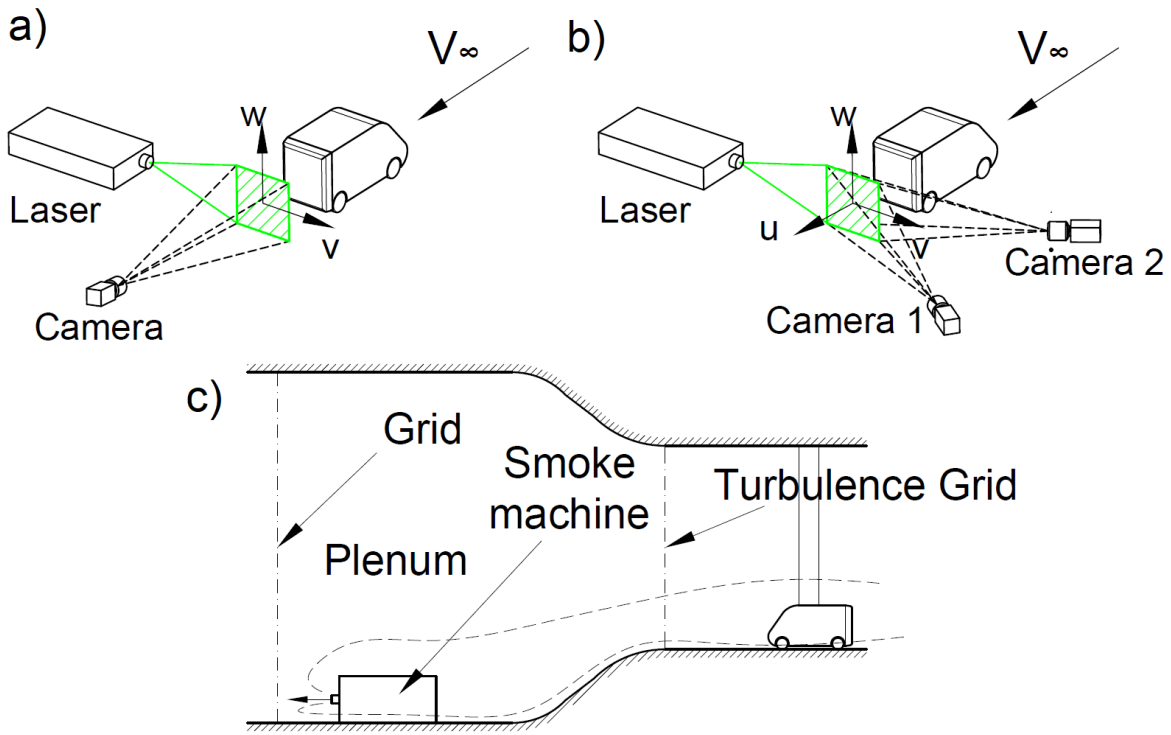

Figure 3.11: PIV setup for 2D2C or planar(a) and 2D3C or stereo(b). Sketch of the flow insemination (c).

Finally, the insemination of the flow is performed by settling the smoke machine on the floor of the plenum and pointing upstream, as described in figure 3.11c. This setup produces an uniform distribution of the smoke on the flow surrounding the model.

3.7.1 Planar PIV (2D2C)

The 2D2C PIV is the most simple way of measuring the flow velocity in a plane since only one camera is needed, and the typical configuration for this measurement is shown in figure 3.11a. For this setup the camera if is settled perpendicular to the measurement plane. The Objective of $105mm$ was used, allowing to obtain a smaller field of visualization with high resolution but also conceding a bigger field of visualization with the cameras far from the target. This last case represents and advantage when measuring the velocity on planes parallel to the model's rear base, since the cameras can be settled far from the model and even outside the test chamber in order to not interfere with the flowfield.
The time between shots of the laser was 140 μs, and the cameras obtained 3000 images at a frequency of $10Hz$ for each couple. The interrogation window was 24×24 pixels ($2.5 \times 2.5mm$) and the overlap 75%. The f number used in this case was $f_{\#} = 16$.

3.7.2 Stereo PIV (2D3C)

The 2D2C PIV is very simple, but is only limited to planar measurements. Yet, there is an arrangement that allows adding a third component to the planar ones. If the couple of images are captured by two cameras instead of one, the binocular perspective allows measuring also the perpendicular-to-plane component of the particle. Using

this methodology, the three components of the velocity can be calculated for the whole captured plane, which is called two-dimension three-component (2D3C) PIV, or stereo PIV, and the setup for this test is sketched in figure 3.11b.
The stereo PIV is more complex since involves two cameras and the Scheimpflug correction is needed. Furthermore, a more complex calibration process is required to combine the two cameras' images. In this setup, the two cameras and the laser were mounted on rails in order to change the visualization plane easily. For this setup the cameras mount the $60mm$ objective with $f_{\#} = 16$. Between the objective and the camera is mounted a one-axis Scheimpflug correction, to improve the focus of the image. The $60mm$ objectives allow a wider field than the $105mm$, therefore the cameras are positioned closer to the target area. The time between shots of the laser was 60 μs producing an average particle displacement of 6 to 8 pixels in the crosswise plane, and the cameras obtained 2000 images at a frequency of $15Hz$ for each couple, per each visualization average. The interrogation window was 64×64 pixels ($3.55 \times 3.55mm$) and the overlap 82%. The errors on the velocity measurements regarding the freestream speed are below 1%.

3.8 Test conditions

3.8.1 Control of the wind tunnel's velocity

In order to correctly perform the test the flow on the test chamber needs to be uniform. The first characteristic to set is the freestream speed uniformity on the horizontal plane, measured through hot-wire measurements at two symmetric positions regarding to the vertical symmetry plane of the test chamber.

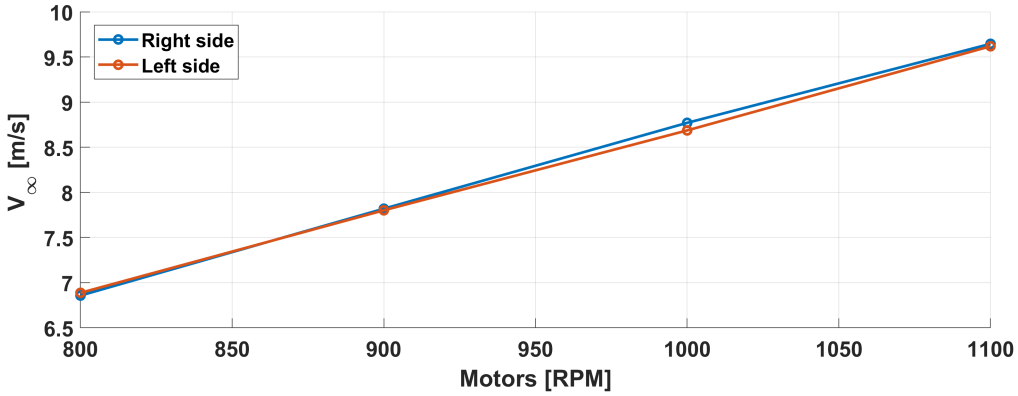

Figure 3.12: Freestream speed on two symmetric positions regarding the mid-vertical plane of the model.

The measurements were performed at $200mm$ from the wind tunnel's floor avoiding the boundary layer effects and at $300mm$ from the model's symmetry plane. As explained in section 2.2 the wind tunnel is activated through two propellers in side-by-side configuration on the horizontal plane, therefore the two speed measurements are able to identify if these two propellers are blowing equally. From a series of different measurements, is found that the blowing is uniform on the horizontal plane when the

spin rate of the motors are even.

$$V_\infty = 0.00875 \times Spinrate[RPM] \tag{3.10}$$

This relationship between the motors' speeds is valid for all the range of the motors (0 to 1100 RPM), and guarantees a minimum difference on the flow field. Furthermore, with the velocities obtained from these measurements a first approximation of the wind tunnel velocity regarding the spin rate of the motors can be obtained. In figure 3.12 are shown the trends of the velocities and in equation 3.10 the relation of the free stream speed with the spin rate.

3.8.2 Free stream turbulence

In order to evaluate the effect of the grid on the freestream turbulence we refer to the study of Laws and Livesey [72] where the flow downstream different kinds of screens was studied. The behavior of the variance of the fluctuations is estimated in function of the geometry and the distance from the grid, following the equation 3.11.

$$\overline{u^2} = \frac{M \cdot K}{b(x - x_0)} V_\infty^2 \tag{3.11}$$

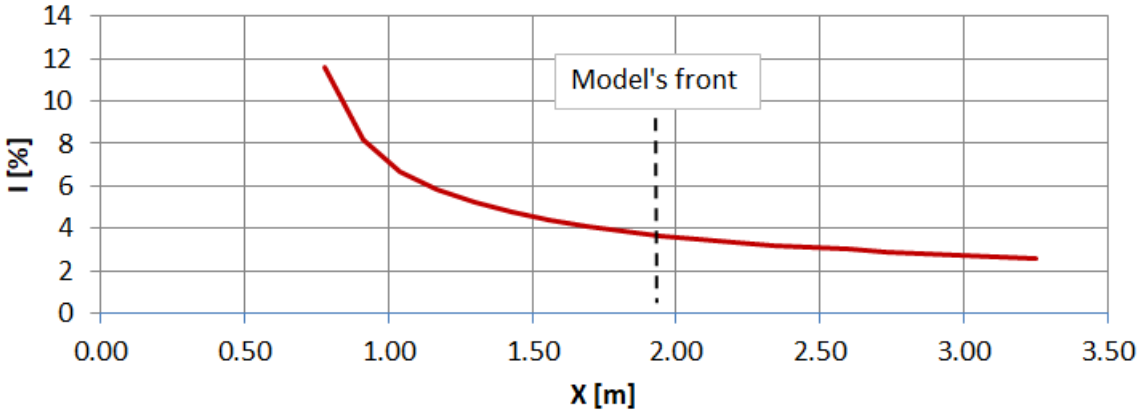

Figure 3.13: Turbulence index from the grid.

Where $\overline{u^2}$ is the average square fluctuation of the streamwise velocity, M is the mesh length, K is the resistant coefficient, b is an empiric constant, x_0 is $10M$, V_∞ is the freestream speed and x the position downstream the grid. The turbulence index is given by $I = u_{RMS}/V_\infty * 100$. and the trend of this value regarding the distance from the grid is shown in figure 3.13. Considering that the position of the model is $1900mm$ from the grid, the turbulence index at that position is 4%. This value was verified with hot-wire measurements performed previously.

3.8.3 Ground boundary layer

The top and lateral boundary layers present no significant effects on the flow field surrounding the model, but the floor boundary layer is a common issue in near-ground

vehicle testing. The presence of this non-uniformity of the velocity represents a lack of kinematic similarity, so actions need to be taken to mitigate this effect. Different solutions are feasible to solve this problem, being the most used the bottom plate, boundary later suction and moving belts. For our test the only suitable solution is the aspiration slot, since there is no possibility of modifying the wind tunnel floor to fit a moving belt and no vertical movement of the model is allowed to fit a plate below.

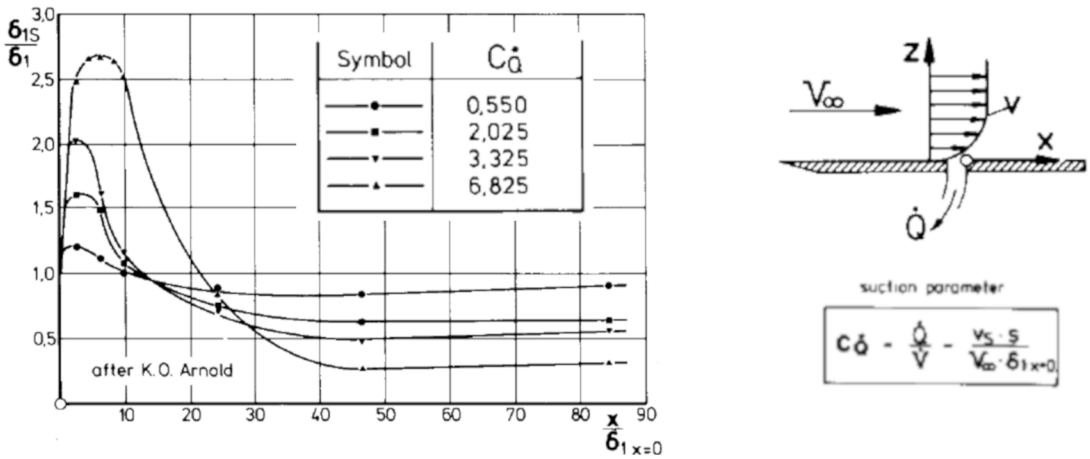

Figure 3.14: Boundary layer reduction by slot suction. Taken from [64].

The boundary layer suction is presented by Hucho et al. [64] as the most promising technique to reduce the boundary layer due to its technical simplicity, and their results are shown on figure 3.14. They develop an empiric solution, using the results of slot suction applied to high-lift airfoils, that returns the displacement boundary layer in function of a suction parameter $C_{\dot{Q}}$ and the position in the flow direction. Now considering the suction flow and the freestream speed on the test chamber, the suction parameter is $C_{\dot{Q}} = 0.64$. From figure 3.14 the optimal position of the slot regarding the model must be $x \approx 40\delta_1$.
Using a Pitot probe mounted on a vertical translation actuator the velocity profile on the ground of the test chamber is measured. The criteria for the boundary layer height (δ) is 99% of the freestream speed. In table 3.2 are shown the results of the boundary layer on the model's position for the baseline and suction cases, and in figure 3.15 the resultant ground boundary layer profile.

	δ_1	δ_1/C
without BL suction	3.1	0.15
BL suction	1.65	0.082

Table 3.2: Boundary layer characteristics on the wind tunnel floor

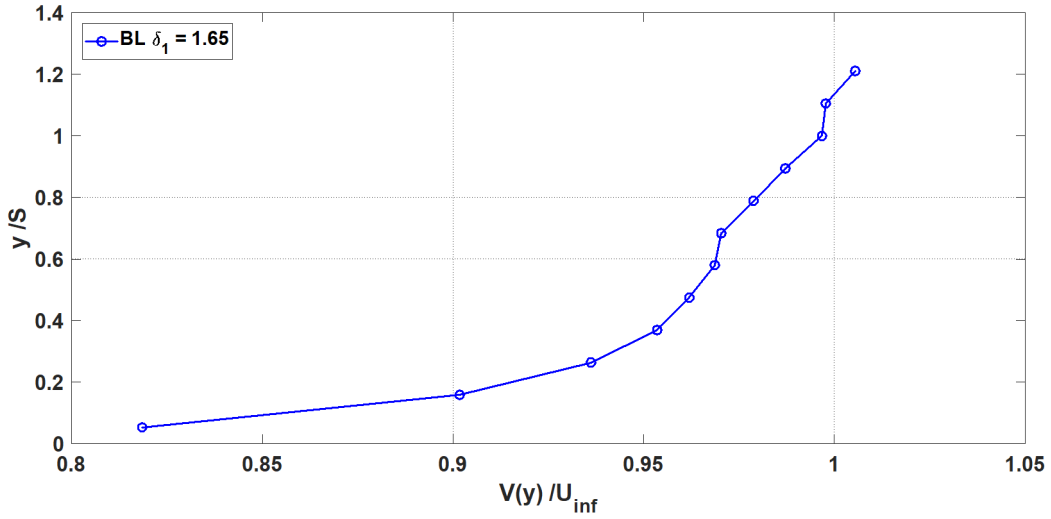

Figure 3.15: Adimensional boundary layer velocity distribution.

With the suction the displacement boundary layer was reduced in approximately 46% regarding the original value. The ratio with the ground clearance (C) agrees with the typical values given by Hucho et al. [64] for an acceptable boundary layer condition ($\delta_1/C \approx 0.085$). Even if the velocity profile presents a slight lost of continuity on the tendency above $y/S = 0.7$, these values are very close to the freestream speed ($0.97V_\infty < V_i < V_\infty$).

3.8.4 Reynolds number effect (Cd vs Reynolds)

If consider the typical length of a commercial van, around $4m$, a speed of $100Km/h$ and normal atmospheric conditions the Reynolds will be:

$$Re_L = \frac{\rho V_\infty L_{ref}}{\mu} = \frac{1.225 \times 27.8 \times 4}{1.8 \times 10^{-5}} = 7.5 \times 10^6 \tag{3.12}$$

Reproducing this Reynolds number on this test means a freestream speed of approximately $280m/s$ on the test chamber. This is obviously impossible not only because the maximum freestream speed is around $10m/s$ ($\approx Re_L = 2.5 \times 10^5$), but also because of the compressible effects of the air a that speed. In fact the Mach number in this condition is:

$$Ma = \frac{V_\infty}{a} = \frac{280m/s}{340m/s} = 0.82 \tag{3.13}$$

Where a is the speed of sound in air. Even if the Reynolds number of the test is one order of magnitude smaller that the real-case does not mean that the test is not valid. Actually, the wind tunnel tests are commonly performed at lower Reynolds due to the limitations of the facility. Some examples of this can be observed in table 1.1, where the Reynolds of each test are exposed. All these test present the same aerodynamic characteristics (Drag coefficient, vortex shedding, bistability) than the real case. In *Race car aerodynamics* [69] the Reynolds number effect is addressed, claiming that for lower values the flow will have more tendency to the separation regarding higher Reynolds. This behavior should not affect our study since the squareback geometry onset the separation. Nevertheless actions should be taken in order to increase the Reynolds similarity. In this research the turbulence of the flow was artificially increased

by the turbulence grid, as described in section 3.8.2. The increased turbulence increases the level of energy of the flow promoting the attachment, as explained in section 1.1 for simple bluff bodies. This effect attenuates the lack of Reynolds number.

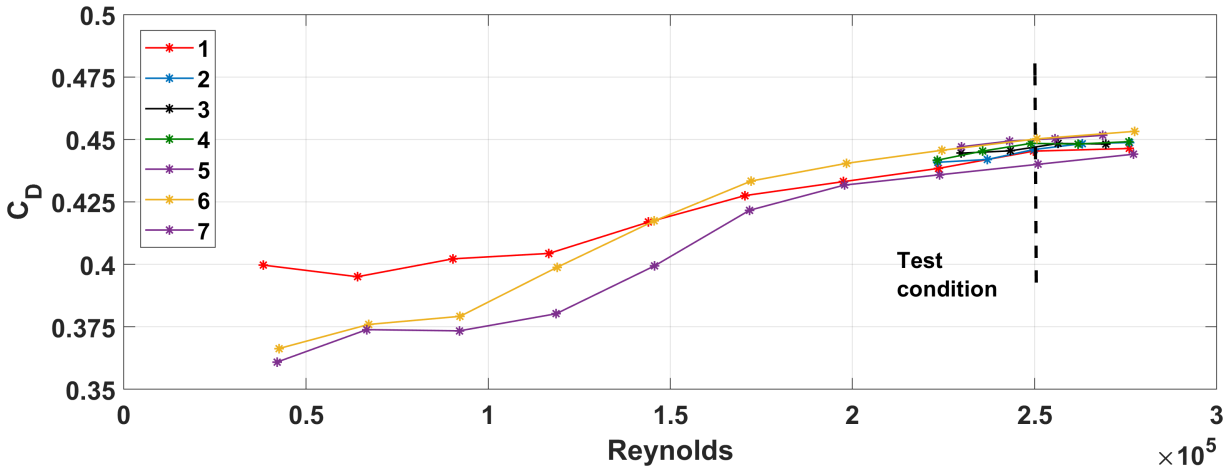

Figure 3.16: Drag coefficient (C_D) versus Reynolds for seven different tests.

A series of test were performed measuring the drag over the vehicle for different freestream speeds, and using the model's Length as a reference the Reynolds number was calculated. The results are sown in figure 3.16. While some test were performed from the lowest speed of the wind tunnel, others where performed only on the speed range enclosing the Reynolds of the test, at $Re_L = 2.5 \times 10^5$. The test condition is evidenced on the graph with a dashed line. As shown in the graph the C_D trend evidences the typical tendency of post-critical three-dimensional bluff bodies (see figure 1.1b of section 1.1), and also for two-dimensional cylinders, as evidenced by Rodríguez et al. [94]. The constant behavior of the C_D is reached below the test condition, which guarantees the dynamic similarity of the flowfield. Now considering the flat C_D results in the Reynold's test condition range it is possible to calculate the C_D of our the model, and the value and standard deviation are presented in table 3.3. This value agrees with the results of *Aerodynamics of road vehicles* [65], pointing that the C_D values of a van ranges from 0.4 to 0.58.

Re_L	C_D	$STD\ C_D$
2.5×10^5	0.4518	0.0033

Table 3.3: Baseline drag coefficient

3.8.5 Model's ground clearance

During the whole research period (three years) a variation of the ground clearance was observed, in particular with the change of seasons. The vertical position of the model moves in a range between two extremum positions, reached approximately on winter and summer (the maximum and minimum clearance respectively). In order to evaluate this variation, a series of measurements were performed in different months of the year by measuring the clearance of the model in four points. In figure 3.17a are shown the reference points of measurements of one side of the model. The clearance was

calculated as the average value of the four measurements taken. These were performed in order to cover the typical range of temperature of the aerodynamic laboratory, in the range of 17° to 27°C, and the results of the variation of the clearance in function of the temperature are shown in figure 3.17b.

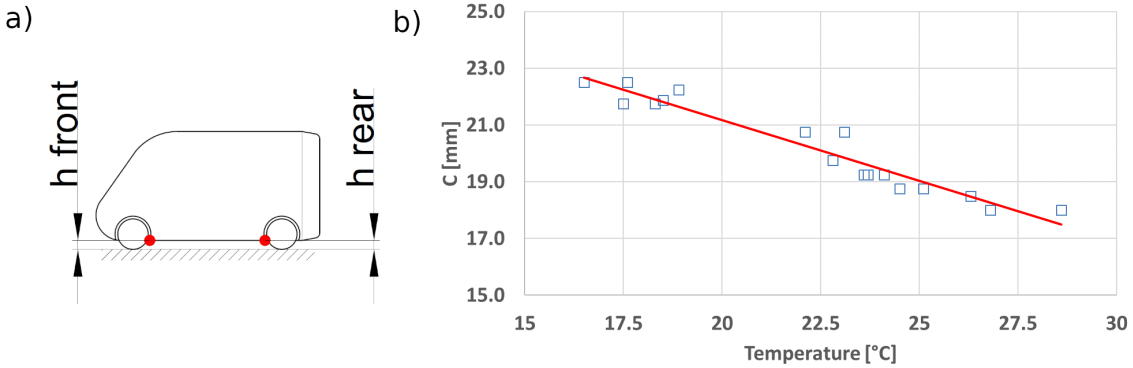

Figure 3.17: Change on the vertical position of the model. Measuring points (a) and measurement trends (b).

The scatter results show a linear tendency (evidenced with a red line) to increase the clearance with the lower temperature, ranging from 18 to 22mm on the operating range of temperature. In sake of simplicity, the individual values of each point's clearance are not shown. These values evidence that the deformation of the ground is not regular, thus why the results do not follow a perfect linear behavior. Furthermore, internal tensions of the complete wind tunnel due to temperature gradients over the different components may also affect this irregular deformation. Nevertheless, the mean clearance value reaches a enough stable value to clearly evidence a dominant linear tendency. Since this variations happens in long periods of time (three to four months approximately) and the test are performed in periods of weeks, the effect of the ground clearance variation can be neglected. Moreover, a set of "summer" wheels were printed performing a flat bottom part in order to avoid contact with the wind tunnel floor and therefore affecting the drag measurement. Despite the modifications on clearance and wheels, no significant changes on the drag coefficient were observed. Considering the facts exposed before, the reference clearance of the model is calculated as the mid value of the clearance range, C= *20mm*.

3.8.6 Wind tunnel spurious effects

Wind tunnel's natural pulsation. The flow inside a wind tunnel may be affected by the resonant effects of the flow itself inside a confined space, as happens in *Helmholtz* resonators. This may induce pressure fluctuations in the flow field that could affect the test dynamics and bring out erroneous readings on the sensors. Because of this is important to understand the natural frequency of the wind tunnel to be aware of the possible fluctuations induced by this phenomenon. To calculate the wind tunnel's natural frequency the procedure described by Greenblatt [60] is used. Considering the general dimensions of the test chamber and convergent, the boundary conditions and the volume of the plenum the natural frequency obtained is $f_{wt} = 4Hz$, corresponding with a Strouhal number of $St = 0.075$. This frequency is very close to the bubble pumping, and therefore may cover this fluctuating phenomenon. Unfortunately there is no way to reduce it without interfering with the test, therefore there is a possibility

of finding a spurious peak of energy around this frequency.

Mechanical vibrations. Since the wind tunnel is made with relatively large plates of acrylic, these may vibrate at their natural frequencies inducing pressure fluctuations on the test chamber. Furthermore, the smallest misbalance on the motors might also induce vibrations to the whole facility. These vibrations were analyzed by a free-end load cell test, consisting in fixing a load cell to the test chamber and leaving the other end free. The spectra resulting from these measurements are presented in figure 3.18.

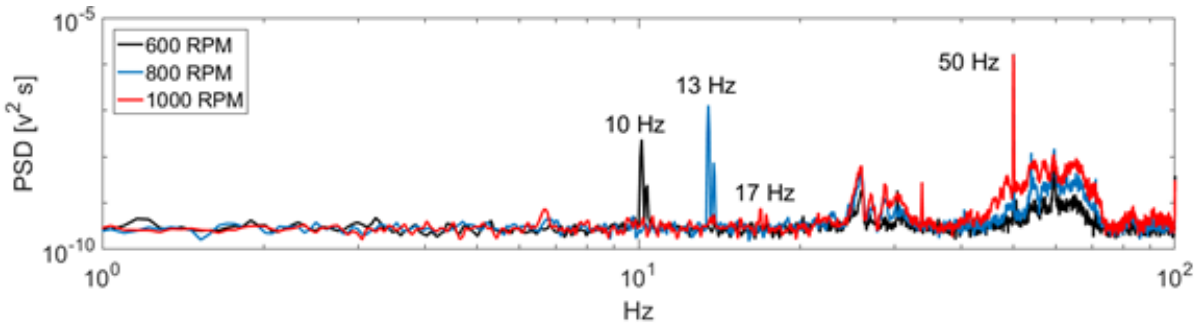

Figure 3.18: Spectra of the free-end load cell for different wind tunnel velocities.

Peaks at 10, 13 and 17Hz are observed for 600, 800 and 1000RPM respectively, evidencing the mechanic nature of these readings since they agree with the misbalance of the motors. This is easily checked by dividing the spin rate of the motors times 60, in order to express the result in frequency (for example, $600RPM/60s = 10Hz$). The $17Hzpeak$ at $1000RPM$ is less intense than expected, since the two previous peaks were growing in intensity. This could be associated to damping effects of the system. There is a very intense and narrow peak at $50Hz$ for all three measurements. This agrees with the electric lines frequency that may introduce noise to the signals. This is supported by the shape of this peak, being very precise regarding to the mechanic nature ones.

				m		
780x850 mm	*f[Hz]*	1	2	3	4	5
	1	5.2	13.7	27.9	47.7	73.2
	2	12.4	20.9	***35.1***	54.9	80.4
n	3	24.3	***32.8***	47.0	***66.8***	92.3
	4	41.0	49.5	63.7	83.5	109.0
	5	62.5	71.0	85.2	105.0	130.5
				m		
600x850 mm	*f[Hz]*	1	2	3	4	5
	1	7.2	21.5	45.5	79.0	122.1
	2	14.3	***28.7***	52.7	86.2	129.3
n	3	26.3	40.6	***64.6***	98.1	141.2
	4	43.0	57.3	81.3	114.8	157.9
	5	64.4	78.8	102.8	136.3	179.4

Table 3.4: Natural frequencies of the acrylic plates.

Around 30 and 60Hz are present two zones of energy concentration that remain

constant for all three different cases, slightly increasing the levels of energy with the spin rates of the motors. If compared with the motor's frequency peak these are way less defined, pointing to a less regular vibrating phenomenon. Knowing that the wind tunnel is composed by plates that might be slightly different, these energy concentration could be associated to the walls vibrations. In order to check this asseveration, the natural frequency of vibration of the wind tunnel walls were estimated taking into account their dimensions and considering the estimation for rectangular plates with homogeneous material given by *Vibration of plates* [75].
There are two different panels of acrylic that compose the wind tunnel, in table 3.4 are shown the results for both in functions of m and n, which are the deformation modes of each axis. The border conditions of the plates were considered as simple support (only translation restrain). From table 3.4 can be observed that certain frequencies of the walls' vibration coincide with the peaks observed on the vibration of the wind tunnel (evidenced in bold). This may explain the concentration of energy of figure 3.18 around 30 and $60Hz$. The fact that there is concentration of energy rather than a peak respond to the fact that the walls may slightly vary theirs dimensions. Moreover, some of the plates have slots or holes, that might also affect the natural frequencies.

Microphones spectra investigation at different speeds.
Following the same criteria of identifying spurious effect, the spectra of the whole set of microphones was analyzed for the same spin rates of the free-end load cell test and the results are shown in figure 3.19. In thick lines are highlighted the microphones settled on the lateral parts of the model (1 to 4), and the rest are the ones on the rear base (5 to 16). The idea behind this analysis is to follow the main fluctuations in order to comprehend if they are part of the aerodynamic characteristics or a spurious effect of the test. From the three spectra, two kinds of energy peaks can be discriminated. The spinrate-dependent (or Strouhal-independent) and spinrate-independent (evidenced with a dashed black line). Within the Strouhal-independent peaks are present the aerodynamic phenomena and the motor-induced vibrations. The identification on each case will be given by the typical Strouhal values of the aerodynamics. The spinrate-independent peaks might be produced by the natural frequencies of the structure or electric noise.
The first analysis will consider the spinrate-independent fluctuations:
Recalling the peaks found on the wind tunnel structure from the free-end load test, on figures 3.19a, b and c are observable the two same energy concentrations at 31.7 and $67Hz$. This founding confirm the spurious nature of this fluctuations, associated to the vibrations of the wind tunnel's walls. Furthermore, the intensity of the fluctuations grows with the spinrate of the motors, evidencing an increasing level of excitation. A new peak is found at $91Hz$ that was not observable on the precedent test. Nevertheless, this fluctuation's peak shape have the same distribution than the vibrations of the walls, therefore could be linked to the same phenomena. The fact that is not observable on the free-end load cell test is unknown, but could be associated to the higher frequency. A weak spinrate-independent peak that presents a small level of energy is present at $4.88Hz$. This frequency is very close to the calculations of the wind tunnel's pulsation ($4Hz$), hence is highly probable that this peak of energy corresponds to this phenomena. Moreover, seems like the side microphones (1 to 4) are more sensitive to this phenomenon. The reason behind this may be that the other microphones are on the rear base, where the flow is completely separated and the fluctuations are intense, veiling this lower-energy fluctuation.

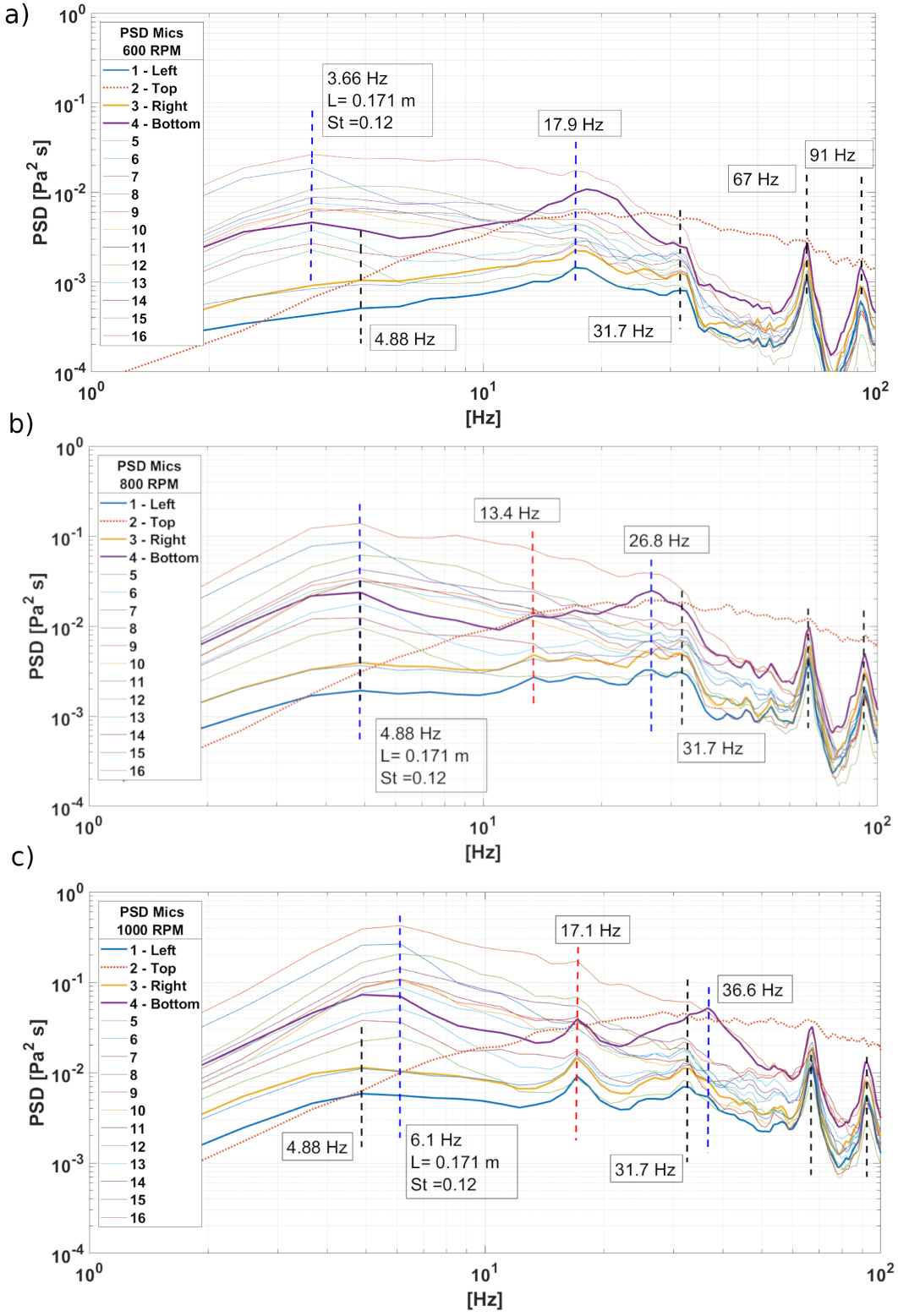

Figure 3.19: Spectra of the microphones at 600 (a), 800 (b) and 1000 (c) RPM.

The analysis now continues with the spinrate-dependent fluctuations:
The lowest spinrate-dependent fluctuation observed is the vortex shedding, at $St = 0.12$ for all three velocities and evidenced in a blue dashed line. As expected, the intensity of the peak grows with the increasing of the speed. An important observa-

tion is that the side microphones does not evidence this peak, demonstrating that this phenomenon is only present on the rear part of the model. This confirm the shedding nature of this fluctuation. From figure 3.19b and c are evidenced with a red dashed line the peaks at the same frequencies found on the free-end load cell test for the motor's misbalance. The fact that this peak is not observable in 3.19a could be associated the low energy of the fluctuations at the lowest spinrate. There is also a second peak that corresponds with twice of the misbalance frequencies of the motors, being $18.5Hz$ at $600RPM$, $26.8Hz$ at $800RPM$ and $36.6Hz$ at $1000RPM$ (see figure 3.19a, b and c). Since the motors does not work coupled, most probably this is product of the misbalance of the motors oscillating in counter-phase.

Chapter 4:
The non-controlled case: baseline

The mean and dynamic characteristics of the near wake will be presented through 2D2C, 2D3C PIV and spectral analysis, evidencing a regular pressure fluctuation between top and bottom parts of the rear coherent with a regular vortex shedding. The fluctuations distributions on the model's rear are characterized through POD, identifying the different phenomena. Lastly, a wavelet analysis evidence the presence of regular events affecting the vertical vortex shedding.

The aerodynamic characteristics of the model were obtained by a series of test with the isolated model and without the utilization of the AFC. This condition is also called the "Natural" case. The results will be presented in pressure distributions and on the frequency domains for a test freestream speed of $9m/s$, corresponding to $Re_L = 2.5 \times 10^5$. The baseline drag coefficient is $C_D = 0.452$ as defined in section 3.8.4 and the center of pressure regarding the model's underbody is settled at $Y_{CP} = 62.5mm$ with a standard deviation of $Y_{CP_{STD}} = 0.45mm$.

4.1 Mean pressure distribution over the model

Using the data from the pressure taps sampled at $40Hz$ for $240s$, the pressure coefficient is calculated and plotted over a sketch of the model, as shown in figure 4.1. In figure 4.1a are shown over the model's side a color map and the color scale regarding the C_p is in the right of the figure. The vectors perpendicular to the periphery of the model represent the C_p on each particular point. The blue and red arrows indicate

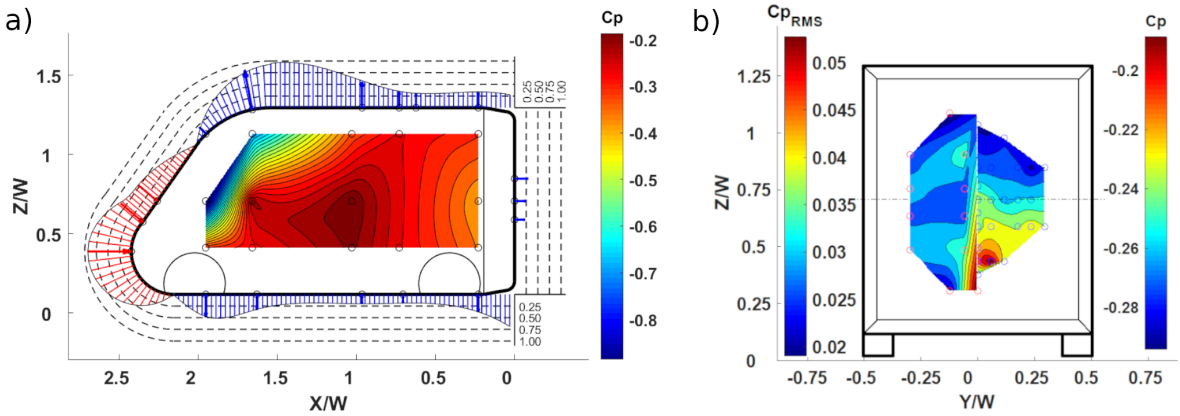

Figure 4.1: C_p distribution on the side view (a). C_p and C_pRMS distributions on the rear view (b).

negative and positive C_p respectively, and the length the intensity. The length scale is represented in dashed lines offset from the model's profile, growing in C_p while increasing the offset distance.
As expected the peak of high C_p is present at the "nose" of the model, in the front part, corresponding with the stagnation point. Towards the upper part of the model there is a decreasing of the C_p changing to negative values near three quarters of the model height. Reaching the rounded edge of the model's top the C_p values reach theirs minimum at $C_p = -1$. This distribution is originated by the acceleration of the flow in the top part, but also might contain a small component product of the presence of the hull. After this lower value and towards the rear part of the model, the C_p stabilizes at $C_p = -0.25$. From the "nose" and towards the bottom part, a similar trend is observed. The C_p decreases and stabilizes on the bottom part at $C_p = -0.2$. there are two zones where the C_p further decreases that coincides with the wheels. This may be due to the acceleration of the underflow in function of the passage area reduction. On the rear part are shown three C_p values corresponding with the measurement plane. these measurements evidence a pressure coefficient of approximately $C_p = -0.2$ on the rear part. Further details of the rear part distribution will be explained in the next paragraphs. On the color map of lateral part of the model the C_p distribution is almost constant at $C_p = -0.25$ except for the near-front zone. In this particular area the values of the C_p further diminish to values around $C_p = -0.9$. This pressure drop is caused by the presence of the "A-pillar" vortex produced by the slanted front. Details of this phenomenon are given in the studies of Levy and Brancher [76] for a slanted-front model, based on an inverted *Ahmed body*.
In figure 4.1b the pressure coefficient (equation 1.3) and pressure coefficient RMS (equation 2.1) are plotted on the rear model's sketch. The C_pRMS was calculated with the data of the microphones, sampled at $1000Hz$ for $15s$. The C_p distribution evidences a mean of $C_p = -0.24$, with a growing tendency from top to bottom. The values range from -0.19 to -0.29.The maximum is reached near the bottom part of the model, at approximately one quarter of the width from the model's underbody. The C_pRMS presents an uniform distribution at $C_pRMS = 0.02$ with two peaks of $C_pRMS = 0.03$ near the top and bottom in a symmetric position regarding the mid-height of the model.
These results concur with the measurements performed by Sardu [102] and Cerutti [33], supporting these new results and verifying the repeatability of the pressure measurement through long periods of time. Furthermore, Barros et al. [14] found for a squareback *Ahmed body* a highly similar C_p distribution on the rear, as well as Grandemange et al. [58].

4.2 Boundary layer around the model

In order to characterize the flow over the model, two velocity profiles were measured: one the roof of the model near the rear base, and the second on the wind tunnel's ground of the rear base's plane center ($X = 0$). In figure 4.2 are show the position of the measurements and velocity profiles obtained through hot wire anemometry. In figure 4.2a is shown the adimensional velocity profile at the ground level behind the model and in the mid plane, as sketched in the top reference image. The height is adimensionalized by the ground clearance. This velocity profile is also found in Fago

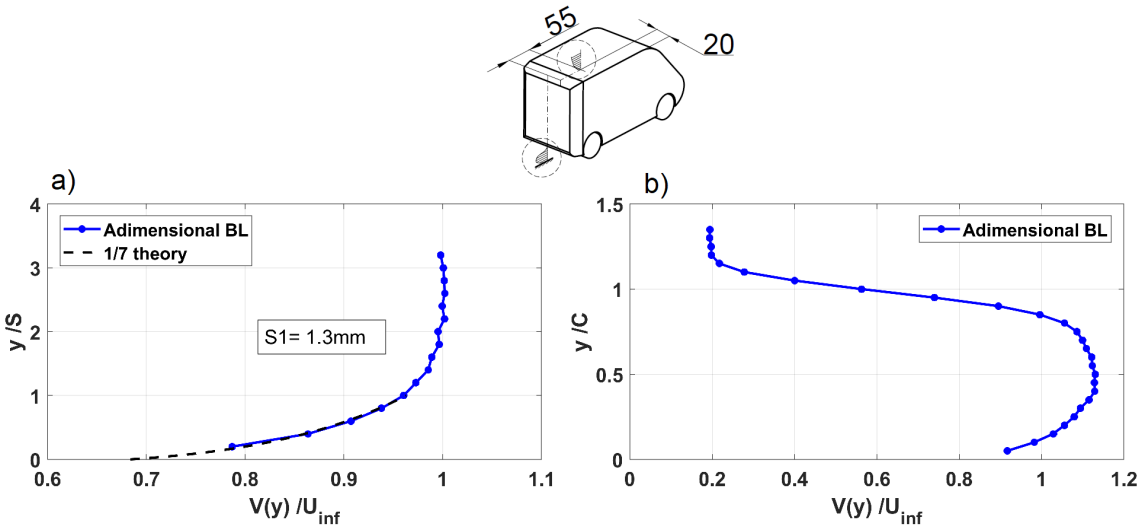

Figure 4.2: Velocity profiles on the model's roof (a) and on the wind tunnel's floor behind the model (b).

et al. [51] for a perforated-ground suction and Hucho and Sovran [63] for a steady ground, and they all present an increased speed regarding th freestream regardless of the model's shape.
The adimensional velocity profile of figure 4.2b evidences a good agreement with regard to the 1/7 law defined as $v(y)/V_\infty = (y/\delta)^{1/7}$ ([64]), corresponding to a turbulent boundary layer. In this case the adimensionalization of the vertical axis is performed with the boundary layer thickness at $99\%V_\infty$ ($\delta_{99\%}$). This evidences that the flow reaching the rear base is completely turbulent as in the real case condition. The displacement boundary layer at this point is $\delta_1 = 1.3mm$.

4.3 Wake analysis: PIV measurements

In order to understand the mean near wake the model a series of PIV measurements were performed behind the model. In figure 4.3 are shown the planes analyzed with PIV.

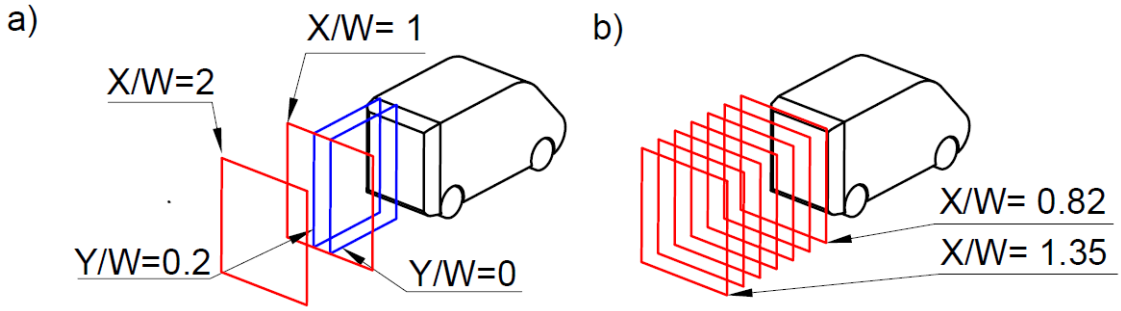

Figure 4.3: Reference planes for the PIV measurements 2D2C (a) and 2D3C (b).

Figure 4.3a displays the configurations for 2D2C PIV. The red planes are parallel to the rear base at $X/W = 1$ and $X/W = 2$, and blue planes parallel to the symmetry plane of the model at $Y/W = 0$ and $Y/W = 0.2$. The field of view is approximately $1.2W \times 1.2W$. In figure 4.3b are represented the seven planes for the 2D3C PIV,

being all parallel to the rear base and ranging from $0.82X/W$ to $1.35X/W$ in steps of $0.07X/W$.

4.3.1 Baseline near and far wake: 2D2C PIV

In figure 4.4 are shown the results on the $Y/W = 0$ (4.4a) and $Y/W = 0.2$ (4.4b) planes, previously defined in figure figure 4.3a. The recirculating structure is observed in both maps, composed by two counter rotating vortices. Also, in both bottom parts is observed the high speed flow coming from the underbody, as evidenced in 4.2a. The velocity field of the midplane (figure 4.4a) shows the nominal near-wake structure of squareback bluff bodies with the top vortex centered at $Z/W = 1.25$; $X/W = 0.15$ and the lower at $Z/W = 0.25$; $X/W = 0.75$. This structure is also observed in [77], [58], [36], [91] and many others; but in this case the main difference is the top vortex dominance regarding to the bottom one. This important difference may be explained by the differences on the models used, since all previous cited do not have wheels and the geometries differ from ours. Confirmation of this is given in [24] on a full-scale test over a *Peugeot 5008*, showing a very similar near-wake structure. The impingement point on the rear part in $Z/W = 0.2$ coincides with the maximum C_p observed on the rear part distribution of figure 4.1.
Towards the side of the model, on figure 4.4b, the counter rotating vortexes noticeably change their shapes and positions. The top vortex is centered at $Z/W = 1.2$; $X/W = 0.3$ and the lower at $Z/W = 0.25$; $X/W = 0.45$. Because of the toroidal shape of the recirculating wake structure this change on the vortexes was expected, since the visualization plane cuts vertically this structure. Moreover, is highlighted the intensity of the downwash on the symmetric plane of the model and how looses intensity towards the outside, as well as the reduced length of the whole near wake.

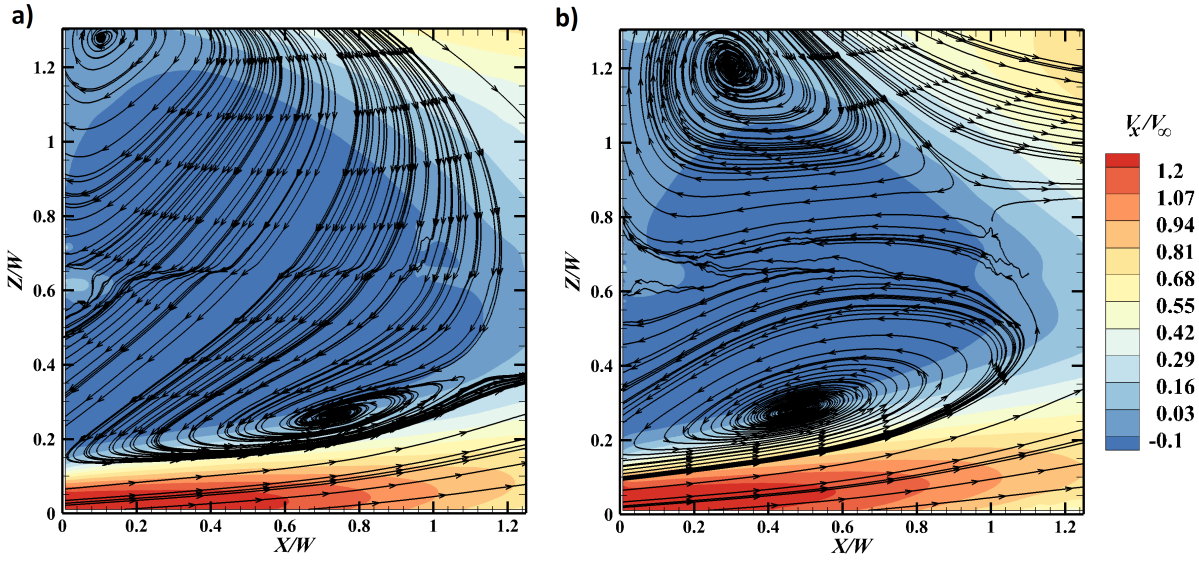

Figure 4.4: 2D2C PIV at the symmetry plane Y/W=0 (a) and Y/W=0.2 (b).

The PIV planes parallel to the rear model's base are presented in figure 4.5. for the $X/W = 1$ plane of figure 4.5a are clearly observed the two main counter-rotating streamwise vortexes, corresponding with the typical structure of squareback bluff bodies ([77], [58], [36], [91]). Theirs positions are approximately $Y/W = 0.2$ from the midplane and $Z/W = 0.4$. It is clearly seen the intense downwash on the symmetry

plane, actually the maximum velocities are reached at that point. In addition, if considered the plane parallel to the midplane at $Y/W = 0.2$ the wake structure explain the deformations observed on figure 4.4. Further downstream in the plane $X/W = 2$, the counter-rotating vortexes are strongly reduced in intensity and position, as demonstrated in figure 4.5b. Both vortical structures are bigger and positioned at $Y/W = 0.4$ from the midplane and corresponding with the model's base. This demonstrates the dissipation of these vortexes while traveling downstream.

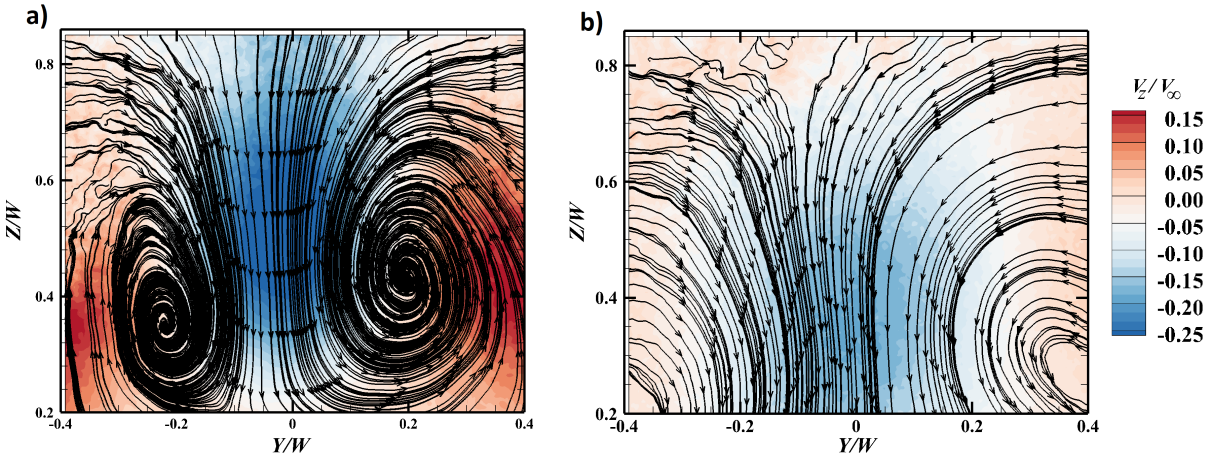

Figure 4.5: 2D2C PIV at the parallel-to-base planes X/W=1 (a) and X/W=2 (b).

4.3.2 Baseline near wake: 2D3C PIV

Using the information from the whole set of 2D3C results of the planes described in figure 4.3b, the near wake flowfield was reconstructed and presented in figure 4.6. The reconstruction clearly highlight the main recirculating structure in blue, defined by a iso-surface of $V/V_\infty = -0.1$ and extending until $X/W = 1.2$ approximately. On the $X/W = 0.83$ plane are evidenced the streamwise velocity values and the streamlines, showing again the counter-rotating vortex structure previously observed and the velocity deficit produced by the near wake. Finally, the high momentum flow for lateral and bottom parts roll-up into the low momentum region producing steady vortical structures, evidenced in green (left), purple (right) and yellow (bottom). The lateral iso-surfaces are defined as $\omega_z W/V_\infty = \pm 2.2$, while the bottom one $\omega_y W/V_\infty = -2$, where ω_z and ω_y are the angular velocities around Z and Y axis respectively.

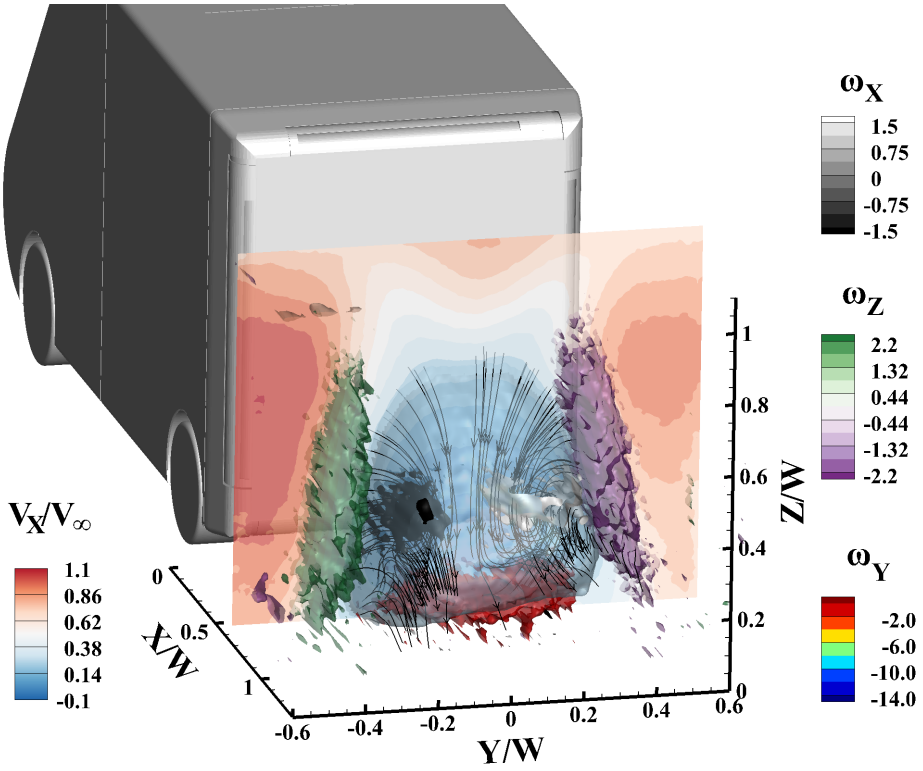

Figure 4.6: Reconstructed wake from 2D3C PIV.

4.3.3 Average wake structure

Taking into account both precedent results of the PIV, an average model of the wake can be sketched, evidencing the main characteristics.

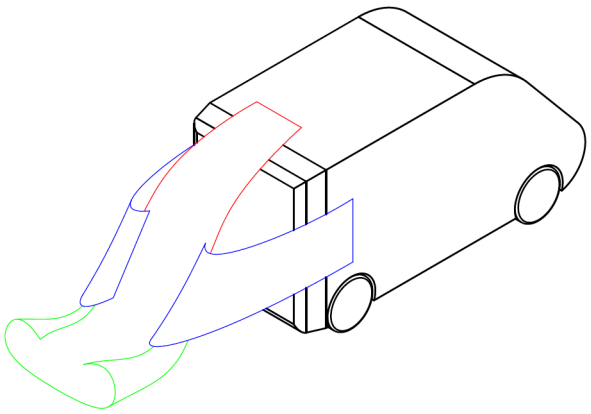

Figure 4.7: Sketch of the average wake of the model.

The red stripe on the top represent the top flow and the blue the lateral. The flow-field asymmetry on the XZ axis produces the downwash, which is the major effect on the near wake. The lateral flow "wraps" from both sides the downwash generating two counter rotating vortexes that evolve to a streamwise direction guided by the presence of the floor, as evidenced in green. Further downstream these two vortexes dissipate, reducing the intensity and increasing theirs dimensions.

4.4 Wake dynamics

The first analysis performed after the average values found in the previous investigation is the analysis of the signals on the frequency domain. The microphones are more adequate respect to the low-frequency pressure transducer for this kind of analysis, since they have a higher sensibility to the fluctuations. In addition, the sampling frequency is much higher ($10kHz$) allowing higher time resolution.
From the set of the pressure fluctuation sensors we identify the most significant positions to investigate. In this particular case (squareback model) four main microphones' positions are selected, corresponding with the top, bottom, center and lateral positions of the model's rear base. The physical positions chosen are evidenced on figure 4.8 with colors, while the other microphones are evidenced with circles. The cylindrical actuators are also represented with dashed lines.

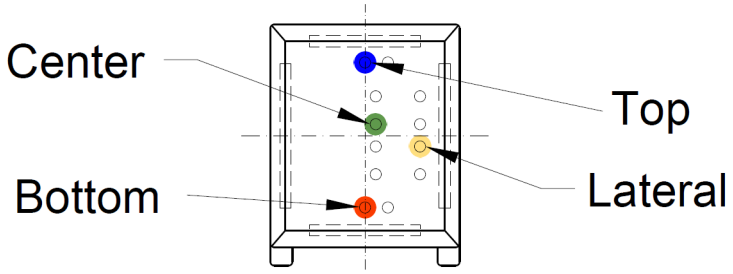

Figure 4.8: Microphones' characteristics positions on the rear base of the model.

4.4.1 Spectral analysis of the fluctuating pressure

In figure 4.9 are shown the PSD of the microphones referenced in figure 4.8, using the *Welch* algorithm with an integration window of 10000 samples and an overlap of 7500. Each signal has 600000 samples, corresponding to 60s of sampling time.

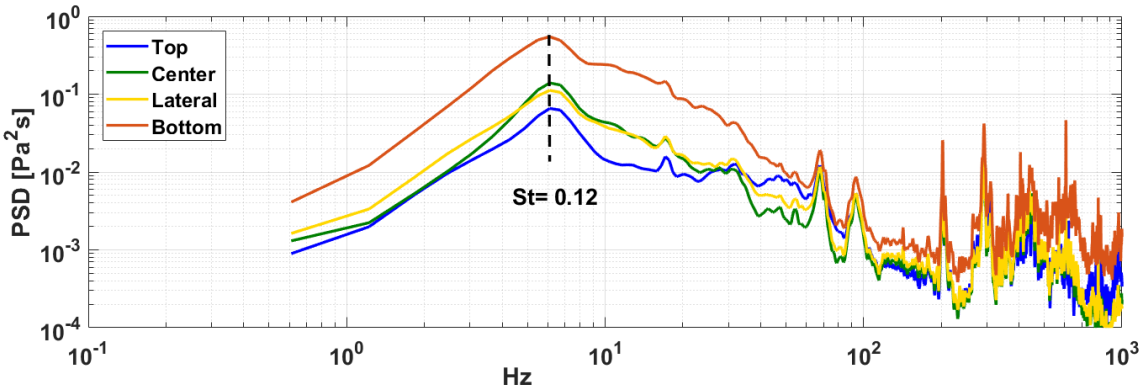

Figure 4.9: PSD of the microphones

For all signals the first peak of energy is centered on the frequency corresponding to a Strouhal number of $St = 0.12$, typically associated to the vortex shedding. The reference length used for the Strouhal calculation is the width W. The maximum energy levels are present for the bottom microphone, showing a decreasing while moving

towards the top. Both center and lateral spectra present merely the same levels of energy, except for a small reduction of the Strouhal peak for the lateral one. Above the shedding frequency the energy values decrease with different intensity in function of the position on the rear. For the top microphone the drop is severe, pointing to a dominant fluctuation given by the vortex shedding. The center and lateral microphones present almost the same trend, with higher levels of energy regarding the top. Finally, the bottom presents no slope around $10Hz$. This increasing level of fluctuation energy above the vortex shedding towards the bottom part of the model's rear base may be explained by the pressure fluctuations due to the presence of the ground and the impingement point of the near wake, as observed in figure 4.4a. For frequencies above $60Hz$ the energy levels for all microphones are almost equal and present secondary peaks associated to the test chamber, as described in section 3.8.6. Regarding to the frequency range of the PSD, from the spectra is also observable that frequencies below $1Hz$ do not have relevant information and above $100Hz$, when all collapse on the same energy levels, the signals are mostly due to test noise. From these reasons and from now on, the spectral analysis will be performed only on the range of interest, from 1 to $100Hz$. The results in function of coherence and phase of the signals are presented in figure 4.10 for the couple of microphones top-bottom, bottom-lateral and lateral-top.

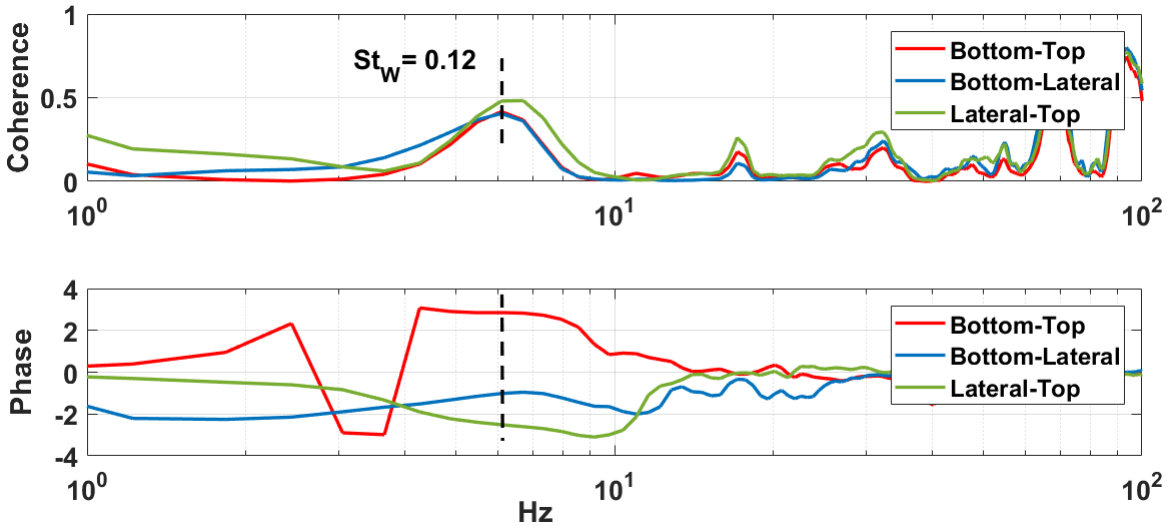

Figure 4.10: Cross PSD top-bottom, bottom-lateral and lateral-top.

Beginning from the coherence of the signals, it is evident that all three shown the same behavior with a peak on the vortex shedding frequency at $St = 0.12$. This means that all crossed signals are sensing the same shedding phenomena. Furthermore, the phase shows different behaviors on each case: The most noticeable is the bottom-top case showing a phase of $\sim \pi$ ranging from 3 to $7Hz$, meaning that the signals have a regular phase of $\sim 180°$. If considered that the vortex shedding produce pressure variations on the rear base, this may correspond with a regular 180°-phased vortex shedding between the top and bottom trailing edges of the model. Supporting this hypothesis is the Strouhal value, which agrees with the typical vortex shedding values for squareback vehicles.
Both Bottom-Lateral and Lateral-Top correlations show a similar distribution with a phase around $2/3\pi$ (120°) from 0 to $10Hz$. This phase might be product of the same Bottom-Top vortex shedding, since the sum of both phases at the shedding frequency

is approximately 180°.
Above $10Hz$ the phase begins to drop until reaching zero at $30Hz$ for all cases.
For the completeness of this analysis, the same cross PSD is performed for the Bottom-Top microphones but at different Reynolds. The results are shown in figure 4.11.

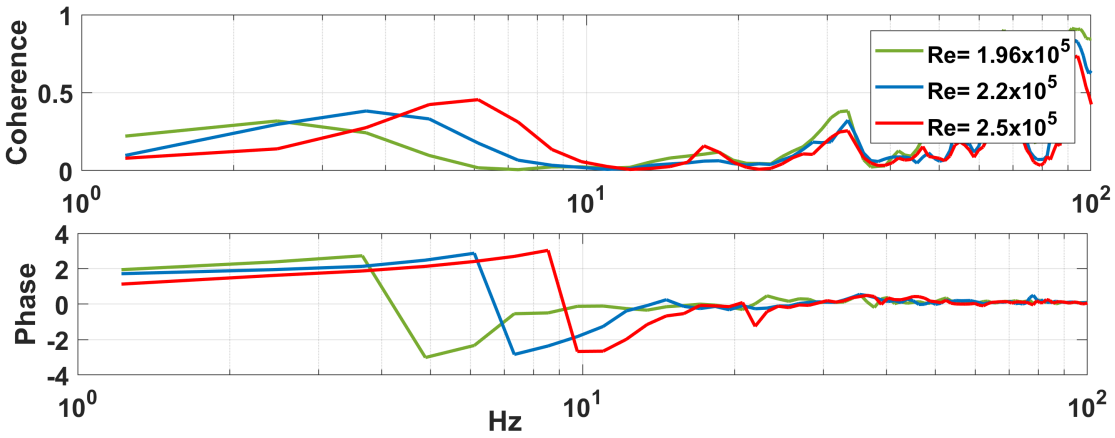

Figure 4.11: Cross PSD top-bottom for different Reynolds.

From the figure is clearly observed how the peak of coherence grows in frequency with the freestream speed, as well as the phase. The Strouhal of each peak is constant at $St = 0.12$, indicating the same phenomenon for each case.
A final analysis involving auto correlation and cross-correlation of the microphones' signals was performed, again taking into account the characteristic microphones defined in figure 4.8. In figure 4.12 is presented the autocorrelation of the top, bottom and lateral signals. The three evidence a a distance between peaks of $0.16s$, corresponding to a frequency of $1/0.16 = 6.25Hz$ which agrees with the vortex shedding.

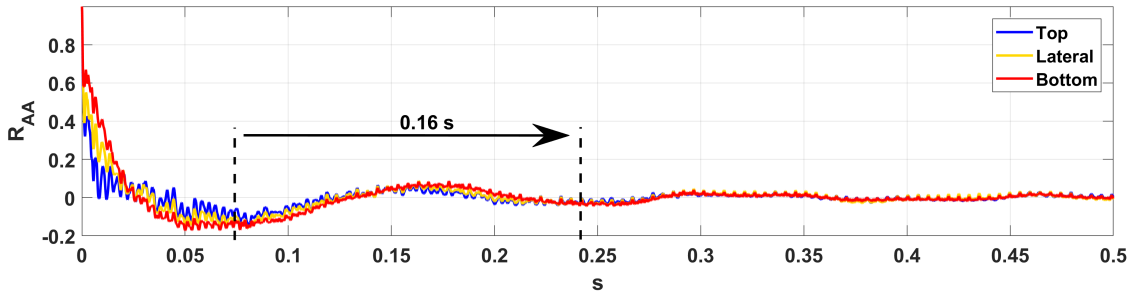

Figure 4.12: Autocorrelation of mics Top, Bottom and Lateral.

Using the same couples of the cross PSD analysis, a cross correlation of the signals is performed and presented in figure 4.13. The first peak of the cross correlation indicates the offset between signals and the distance between peaks the characteristic time of the major fluctuation between the signals. As in the autocorrelation case, the characteristic time between peaks of the three signals is $0.16s$, corresponding with the vortex shedding Strouhal value, $St = 0.12$. The initial offset of the top-bottom correlation is $0.8s$, which is exactly half of the characteristic time and therefore representing half cycle or 180° phase, verifying the results of the Cross PSD.

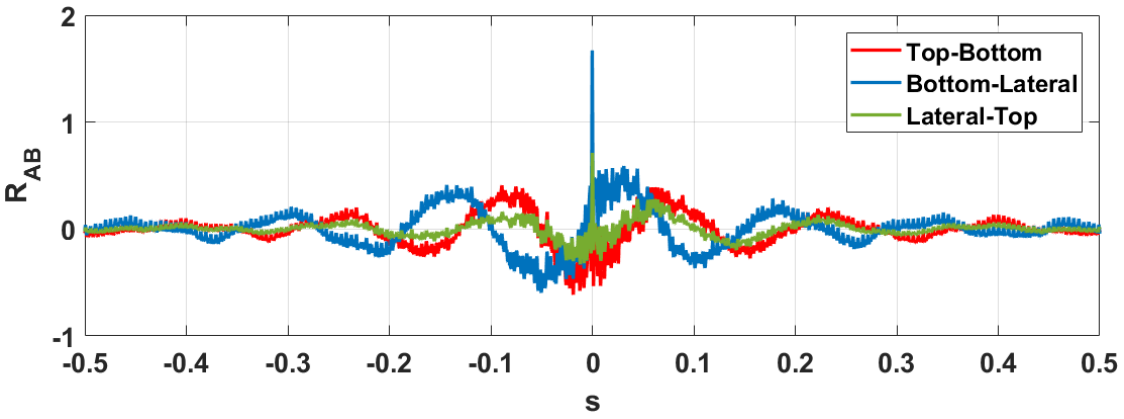

Figure 4.13: Cross correlation of the couples top-bottom, bottom-lateral and lateral-top.

4.4.2 Spectral analysis of the hot-wire measurements

Discrete velocity fluctuation measurements using hot wire were performed on the model's rear in order to further analyze the wake's dynamics, and the positions used are shown in figure 4.14. The hot wire was mounted as showed in figure 2.12 but using the linear actuator in vertical position and the acquisition parameters were $60s$ of sampling time at $20kHz$ (120000 samples per test). The disposition of the points in the space responds to the necessity of measuring the effects of the shear layers generated by the trailing edges at near and far distances from the model.

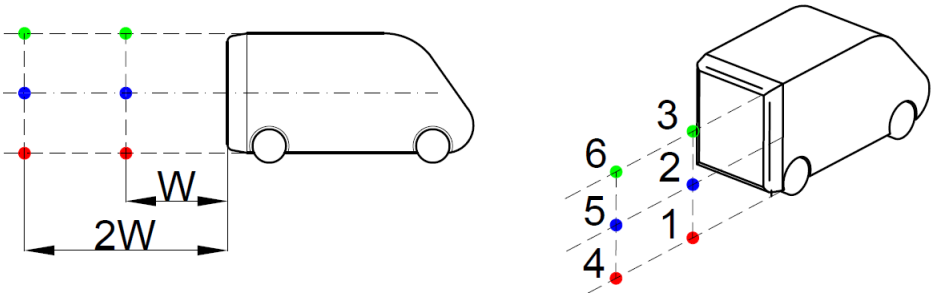

Figure 4.14: Positions of the velocity measurements regarding the model.

Figure 4.15a presents the results of the power spectra for the positions corresponding to the $X/W = 1$ plane. For the lowest measurement (1 in figure 4.14) there is a peak at $St = 0.12$ as in the power spectra of the microphones. While moving upwards (measurements 2 and 3 in figure 4.14) the intensity of the peak reduces. In fact, in the top measurement the peak disappears. This change on the velocity fluctuations agrees with the previous founding on the rear base of the model, where the pressure fluctuation intensity evidence an increment towards the bottom part. The fact that the peaks of pressure and velocity fluctuations coincide confirm the presence of the vortex shedding and highlights his dominant effect on the wake, since no other relevant peaks are observed on both measurements.

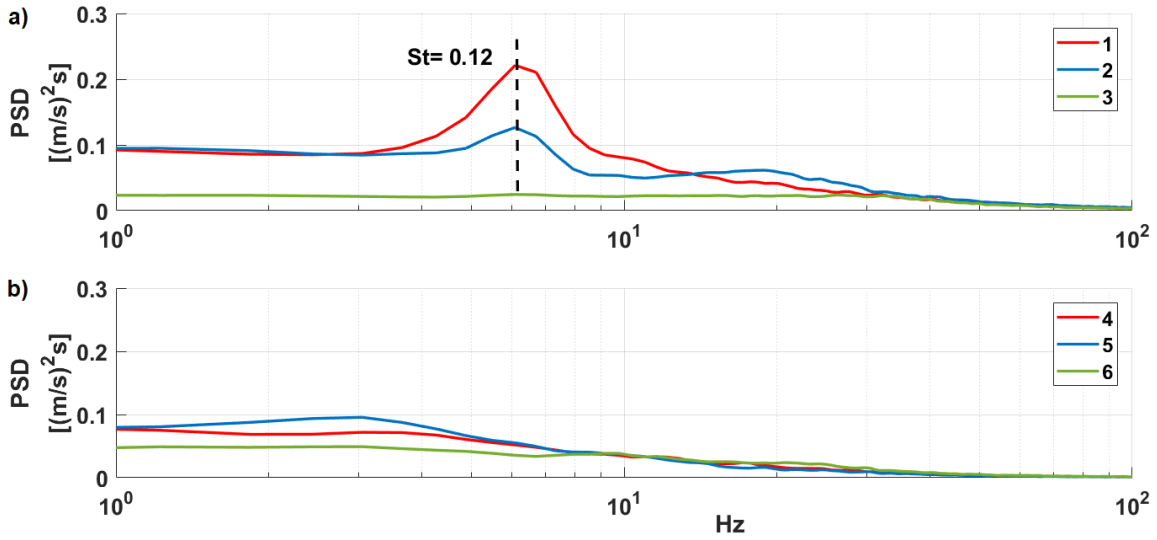

Figure 4.15: Spectra of the velocity measurements (positions in figure 4.14) at $X/W = 1$ (a) and $X/W = 2$ (b).

On figure 4.15b are shown the power spectra corresponding to the $X/W = 2$ position. In this case, the levels of velocity fluctuations are much lower than those from figure 4.15a and there is no trace of the $St = 0.12$ peak.

4.5 POD analysis of the pressure fluctuations

The POD analysis allows us to further interpret the results by observing how the pressure fluctuations of each DOF are related to each other.
Using the pressure signals from the microphones and the procedure described in 2.5.2, the eigenvalues and eigenvectors of the rear base's microphones are obtained. Using the eigenvalues, the relative energy of each mode was calculated. The energy fractions in percentage are reported in figure 4.16a. The reconstructed mean signal of the first four modes was analyzed through the *Welch* power spectra and plotted in 4.16b. Using the eigenvectors, the four first modes are constructed through a color map and plotted in figure 4.16c. It is clearly seen that the four first modes are the most relevant ones, gathering near 80% of the whole signals energy. For this reason and from now on, the eigenvector analysis will be performed on these four modes only. Now if observed the associated modes on figure 4.16c, the ♯1 is an almost planar mode with a quasi-uniform distribution of the fluctuation phase. This shape may corresponds with the bubble pumping of the wake but also with the spurious effect of the test chamber, since these vibrations reach the model in phase (as they were coming from a source at infinite distance).

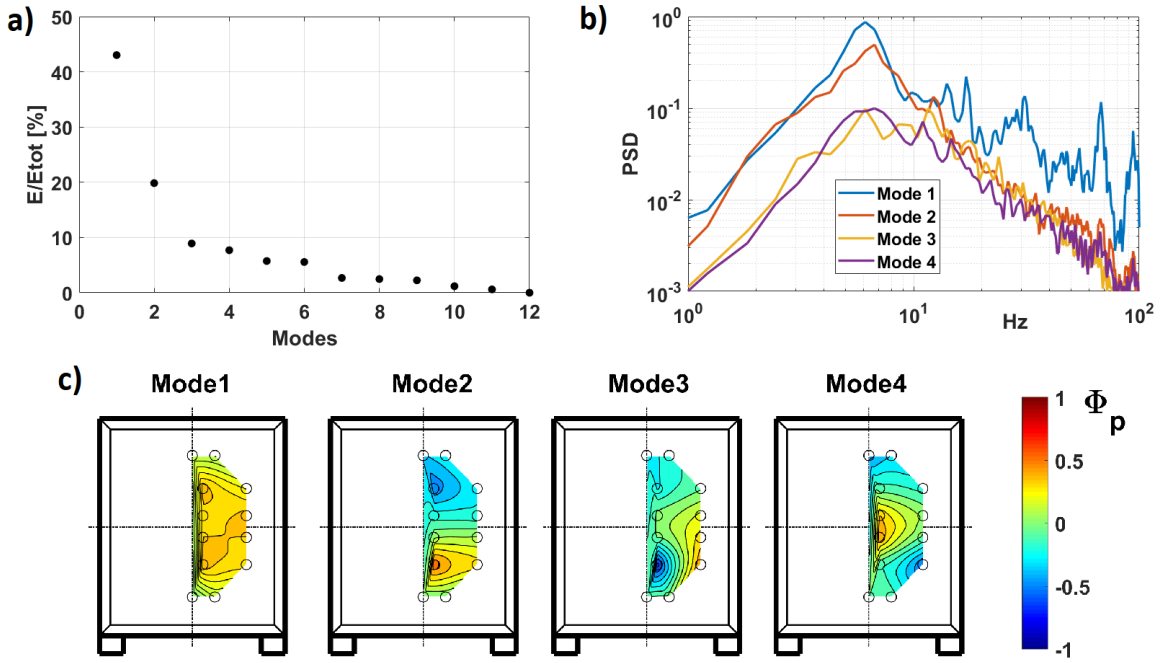

Figure 4.16: Energy of the relative to the 12 modes (a) and reconstructed mean signal of each mode for the first four modes (b). Shape of the first four modes (c).

The ♯2 mode resembles a vertically symmetry-braking mode, which agrees with a regular vortex shedding between the top and bottom trailing edges. This mode explain accurately the precedent results of 180°-phased fluctuation between the top and bottom zones. The ♯3 mode resembles an horizontal symmetry-breaking mode, with a slight increasing intensity on the bottom part, that might be associated to the horizontal vortex shedding of the vertical trailing edges. Finally, the ♯4 seems a bi-symmetric distribution of concentric isolines, representing a pressure fluctuation concentrated on the center of the model's rear base. No characteristic phenomena could be directly associated to this particular shape as in the precedent cases, but might be considered as a component of bubble pumping.
On the PSD of the reconstructed signal's modes are observed the four results of each mode. The ♯1 and ♯2 modes evidences the same trend from the lower frequencies until approximately $10Hz$ where the trends diverge: the first mode evidence a series of peaks at 17, 30, 60 and $90Hz$, and the second mode drops to the levels of the ♯3 and ♯4 modes. As demonstrated in section 3.8.6, these peaks correspond to the spurious effects of the test and the fact that they are present on the POD modes only as a flat fluctuation verifies this asseveration. It is interesting to notice that the ♯1 and ♯2 modes present theirs maximum levels of energy at $St = 0.12$, showing that there is a strong correlation between the vortex shedding observed on the precedent section and these two modes. The ♯3 and ♯4 modes have lower levels of energy regarding ♯1 and ♯2, but also presenting the maximum levels of energy around the same frequency range. In fact mode ♯3 present a maximum a $8Hz$ corresponding to a Strouhal of $St = 0.15$, supporting the hypothesis that this mode responds to the lateral vortex shedding. Mode ♯4 present the maximum energy peak at $6Hz$ as mode ♯1 and ♯2.

4.6 Wavelet analysis of the pressure fluctuations

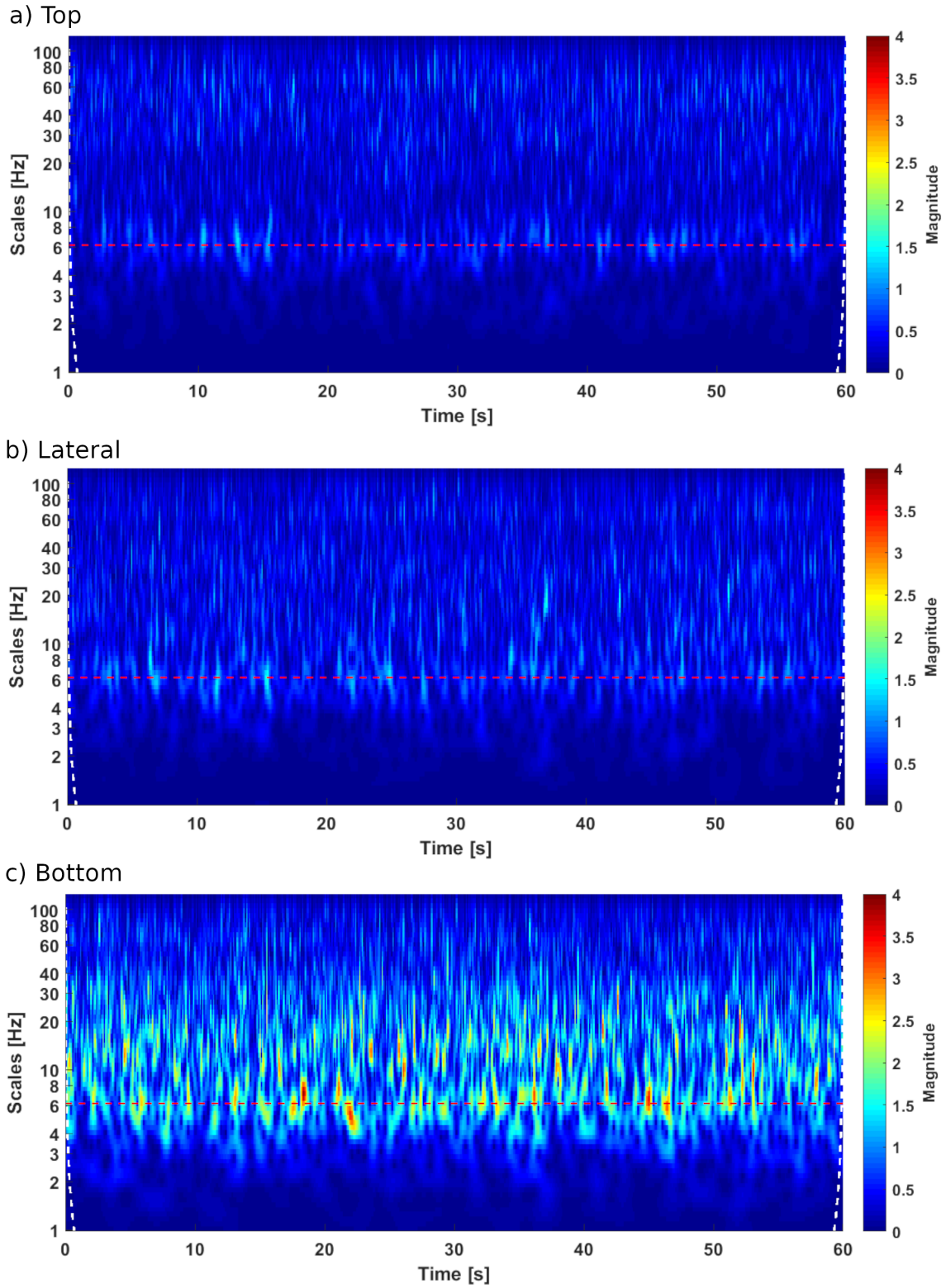

Figure 4.17: Wavelet coefficients for the top (a), lateral (b) and bottom (c) microphone's signals.

For the wavelet analysis the *Morlet* mother wavelet was used over 60s of microphone's signal, and the same characteristic positions of the precedent analysis were analyzed.

In figure 4.17 are shown the results of the wavelet analysis for the top, bottom and lateral reference microphones. With a red line is represented the $St = 0.12$ scale ($6.1Hz$), while the cone of influence is observed on white dashed lines on the left and right parts. The three color maps present different levels of magnitude and time distribution. Nevertheless, the maximum magnitudes are always around the vortex shedding frequency. Both top and lateral signals present almost the same low levels of wavelet coefficient, reaching a maximum of 2, while the bottom evidence twice this value. This was already observed on the spectra of figure 4.9, where the bottom signal highlight higher levels of energy regarding all others. In particular, the maximum burst of energy occur alternatively around the $St = 0.12$ line, showing a sort of alternative intensity vortex shedding.
From the dynamic analysis performed thus far it is clear that the bottom part of the rear is the most energetic one in terms of pressure fluctuation, due to different contributions such as the shedding, bottom boundary layer and the bottom of the model interacting with the underflow.

4.6.1 Events analysis

The LIM analysis was performed on the wavelet transform of the bottom signal in order to identify and evaluate possibles events. In figure 4.18 the trend of the LIM values evaluated on the $St = 0.12$ scale of the wavelet transform of the bottom microphone. The peaks that overcome the trigger (red dashed line, $LIM = 2$) are highlighted with a black dot and considered as an *Event*. The *no-Event* are evidenced with a red dot.

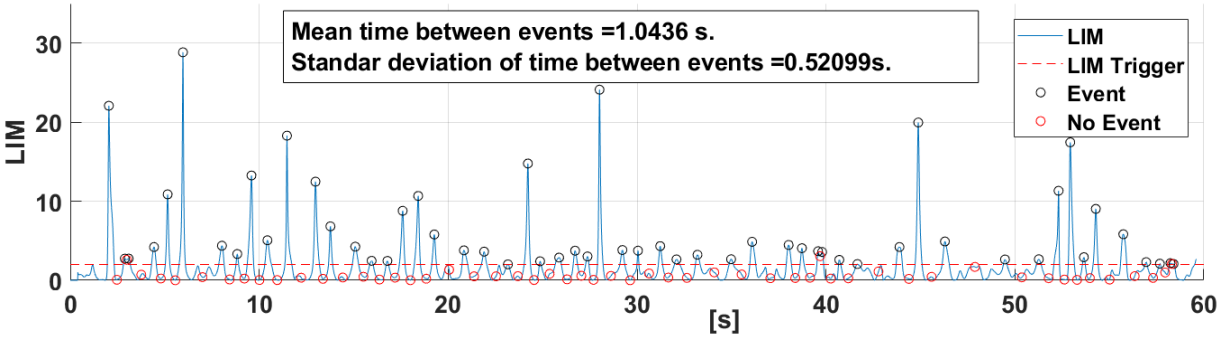

Figure 4.18: LIM analysis for the bottom microphone at the vortex shedding frequency ($St = 0.12$).

The events on the whole time domain show certain regularity in time and intensity. In fact most of the events are contained in the $2 < LIM < 10$ range and with a mean time between of $1.04s$.Further information about this can be obtained by analyzing the conditioned spectra around the events and no-events. For this analysis an event-centered window of one second was used and successively analyzed. For each event and no-event, the PSD is calculated and then averaged and the resultant average PSD for the event and no-event are shown in figure 4.19a.

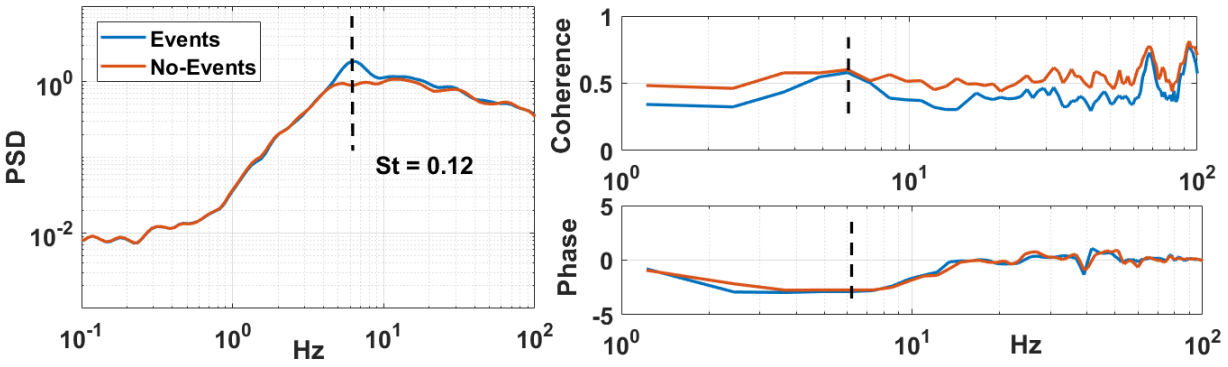

Figure 4.19: LIM analysis for the bottom microphone at the vortex shedding frequency.

The events seems to affect only the Strouhal peak, since non changes are observed for the rest of the power spectra. This means that each event and no-event are only linked to the vortex shedding and evidence a change on the intensity. To Further analyze this particular behavior a cross PSD analysis was performed on the event and no-event windows for the top and bottom microphones and shown in figure 4.19b. For the event, the coherence shows a peak on the Strouhal peak while the no-event has a flat coherence in a large frequency range. The phase evidence the same trend for both event and no-event, with a π value (180°) on the Strouhal peak. These last results evidence that the event only presents an increased intensity of the fluctuations on the Strouhal frequency regarding the no-event. Furthermore, in the no-event case the 180° phase is maintained, meaning that the regular vortex shedding does not disappears but reduces his intensity. The conclusion from this wavelet and events analysis is that the pressure fluctuations on the rear part, in particular the bottom, presents a spectra dominated by the vortex shedding at $St = 0.12$. Moreover the vortex shedding evidences a change on theirs intensity in the time domain, in almost regular periods of 1.04 seconds. This means that the near wake of the model will most probably switch between two "states": one dominated by the regular vortex shedding and another with a wider range of fluctuations. A sketch of these states is presented in figure 4.20.

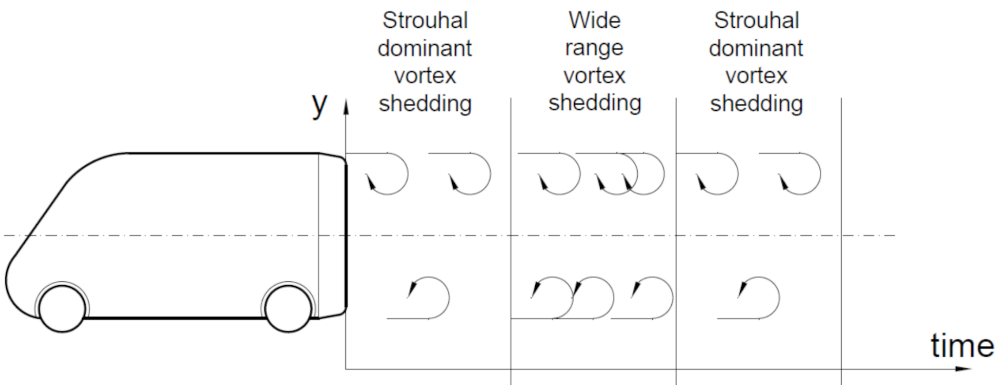

Figure 4.20: States of the wake in the vertical plane on the time domain.

Unfortunately, it is not clear the reason that promotes this phenomena, because do not correspond either to the bubble pumping (far away the typical Strouhal values) or the bistability (random nature). Considering also the spurious effects of the test, the closest one is the drag balance natural frequency at $1.5Hz$. But the frequency does not agree, and neither their harmonics.

4.7 Combined POD & wavelet analysis

It was observed from the LIM analysis that the events found on the wavelet coefficients evidences a variation only on the Strouhal peak, therefore associated to the vortex shedding only. Since the modes of the POD were associated with fluctuating phenomena, as the vortex shedding, the wavelet transform was applied to the reconstructed signals of the modes in order to analyze the time-frequency domain, and the results are displayed on figure 4.21 for the first three modes. As in the precedent cases, the vortex shedding is highlighted with a dashed red line. The wavelet transform of the reconstructed first mode on figure 4.21a evidences a high intensity of fluctuations in almost whole field of measurement, with a slightly higher concentration around $St = 0.12$. It is evident that this "flat" first mode (see figure 4.16) is influenced largely by the higher frequencies, way above the Strouhal, mostly associated with the test spurious effects. The analysis on the reconstructed second mode of figure 4.21b evidences an important fact: the major portion of energy associated with this mode is on the vortex shedding reference line, and performing almost the same intensity that the precedent mode. This further evidence the association of the second mode to the vortex shedding on the model's trailing edge. The third's mode wavelet shows an important reduction of the intensity, reaching half of the values regarding the precedent cases of mode 1 and 2. As explained before, the shape of this mode could be associated to the lateral vortex shedding of the vertical trailing edges of the model, and since the Strouhal numbers are associated to a reference length, the lateral vortex shedding should have a higher frequency regarding the top-bottom. In the wavelet transform is observed that the concentration energy zone is above the Strouhal frequency, this agreeing with the last premise.
As in the precedent wavelet analysis the LIM is performed at the $St = 0.12$ scale and the results are shown in figure 4.22 for the three modes. Both LIM analysis of mode's one and two shown regularity on time and intensity of the events, but the peaks of the second mode LIM are higher than one's. This agrees with the outcomes of the POD, where the energy around $St = 0.12$ was of the same order, and supports the hypothesis that associate this mode with the vertical regular vortex shedding. The third mode's LIM presents a more irregular distribution of the peaks with no apparent regularity of the events, therefore is irrelevant for the analysis. In conclusion, this last analysis confirms the hypothesis exposed on figure 4.20 of two "states" of the wake dominated by a regular vortex shedding and a wider rage of fluctuations, since the wavelet of the second mode evidence the same timing of events observed before and concentrated on the vortex shedding frequency, $St = 0.12$.

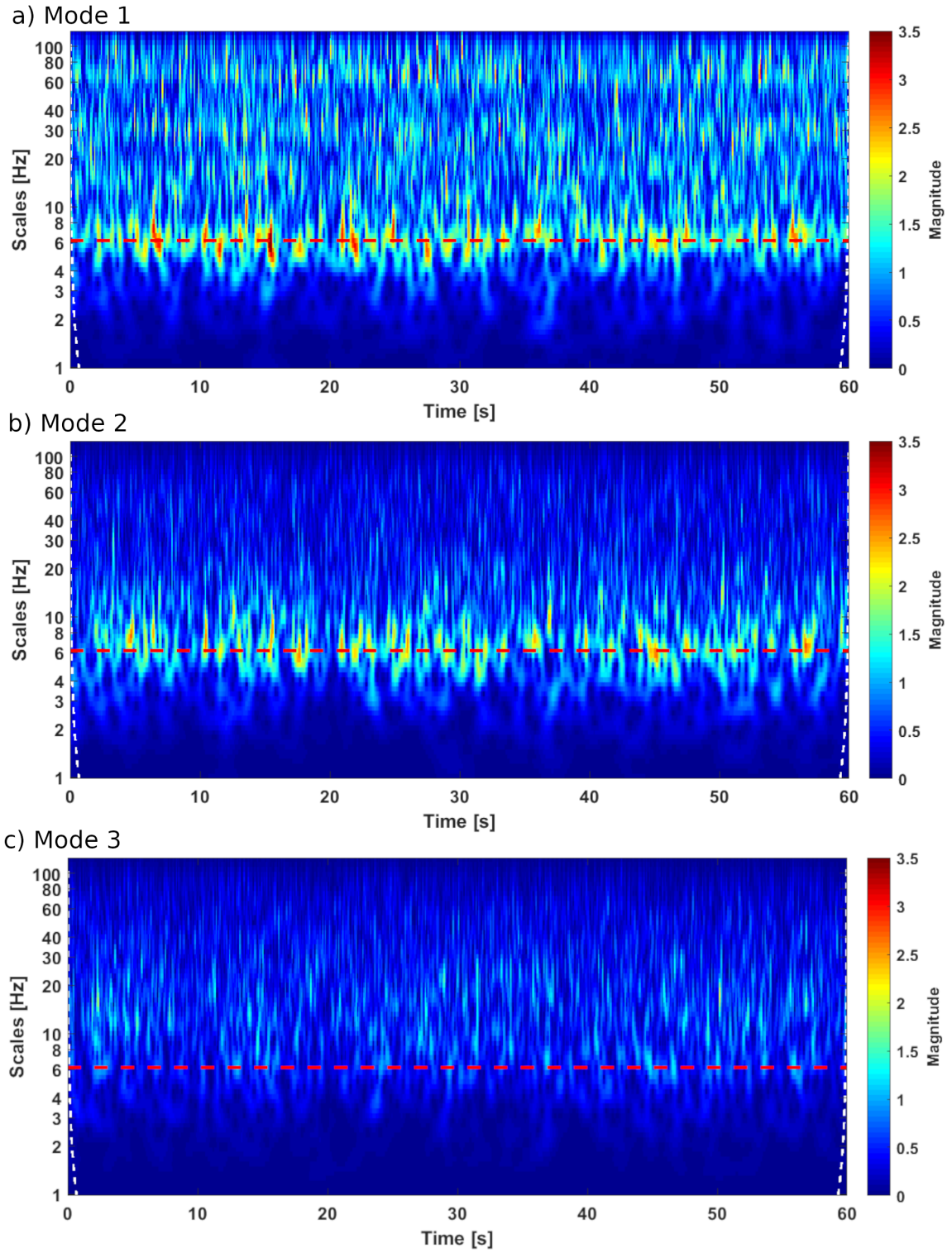

Figure 4.21: Wavelet transform applied to the reconstructed signals from the first(a), second (b) and third (c) POD modes.

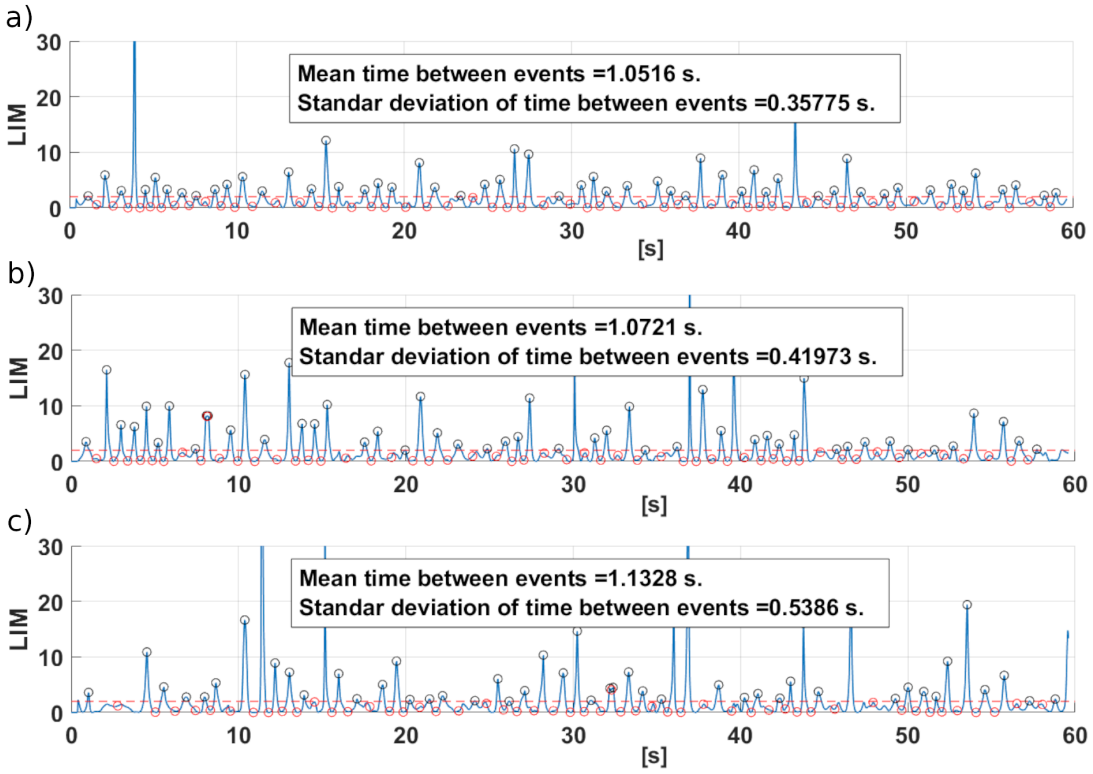

Figure 4.22: LIM calculation at $6.1Hz$ ($St = 0.12$) from the wavelet of the first (a), second (b) and third (c) reconstructed POD modes.

Chapter 5:
Continuous blowing flow control

In this chapter the characterization of the active flow control is performed, evaluating the individual and combined effect of the blowing jets. As in the baseline case, the mean pressure distribution, pressure fluctuations and PIV are analyzed as well as the wake's characteristics in each case.

The conditions of the tests in all cases were the same defined in precedence, with a freestream speed of $9m/s$ ($Re = 2.5 \times 10^5$). As explained in chapter 2 the lateral jets blown at the same speed and the blowing angle of all jets is $\varphi = 65°$.

5.1 Effects of the single jets

The first test with the active blowing was performed to characterize the response over the drag of the individual jets. The results are presented in figure 5.1.

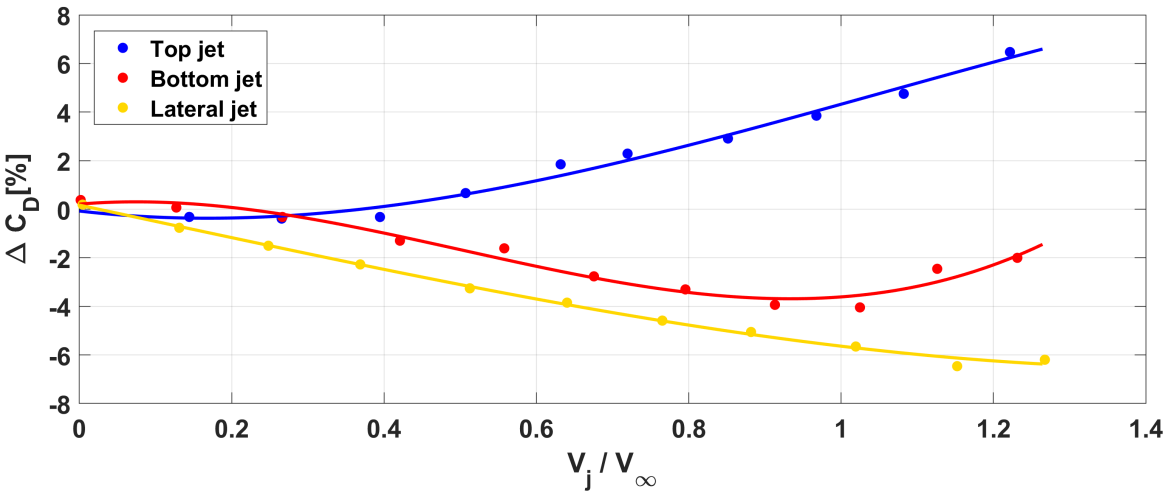

Figure 5.1: Single jet effect on the model's drag in function of V_j/V_∞.

The plot displays the drag variation of the model (ΔC_D) in function of the blowing ratio V_j/V_∞. The top and bottom blowing evidence no relevant response on the drag variation for values of V_j/V_∞ below 0.4, while the lateral below 0.1. Both bottom and lateral blowing show an almost linear drag reduction, reaching -4% for the bottom and -6% for the lateral at $V_j/V_\infty = 1$ and $V_j/V_\infty = 1.15$ respectively. The top jet shows the opposite behavior, increasing the drag linearly with blowing. This opposite behavior could be associated to the effect of the top jet on the near wake: in figure 4.4a is observed the near wake on the midplane of the model with the recirculation

structure, being the top vortex bigger than the bottom one. As exposed by Evrard et al. [49] and Lucas et al. [78] a symmetric recirculating structure can be associated to smaller drag values regarding the non-symmetric ones. Therefore, the drag increasing could be a result of the increased asymmetry of the near wake due to the top jet's blowing. The drag increasing of the top jet is not necessary a disadvantage. For example, might be used to improve the breaking of the vehicle. But since this research is focused in the drag reduction this effect will not be considered.

The response of the jets could be also analyzed in terms of the momentum applied to the wake. In order to do that is introduced the blowing coefficient, defined in equation 5.1.

$$C_\mu = \frac{\sum \frac{1}{2}\rho_i A_i V_{j,i}^2}{\frac{1}{2}\rho_\infty HWV_\infty^2} \tag{5.1}$$

Where H and W are the height and width of the model, V_∞ the freestream speed and ρ_∞ the ambient density; A_i are the exit areas, $V_{j,i}$ the blowing speed and ρ_i the output density of the $i-th$ jet. This coefficient represents the adimensional blowing momentum of the jets, and was used by several authors as Zhang et al. [127], McNally et al. [81] and Manosalvas-Kjono et al. [79] for different kinds of blowing.
In figure 5.2 are plotted the drag variation regarding the C_μ for the three jets.

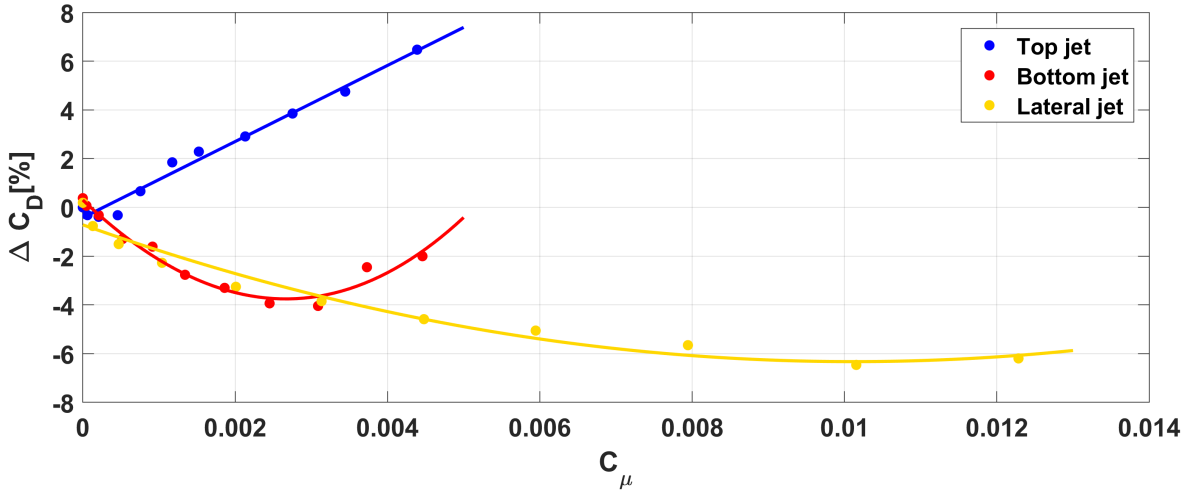

Figure 5.2: Single jet effect on the model's drag in function of C_μ.

Since the output area of the lateral jets is 160% larger than the bottom and top, the C_μ values are more than twice for this slots. By using the blowing coefficient instead of the velocity ratio the drag response is now independent from the dimension of the jet output area. This allows us to observe that the lower jet presents the higher slope regarding lateral and top jets, meaning that the bottom jet is the most efficient in terms of momentum applied to the wake. Similar values of blowing coefficient and drag reductions were also found by Barros et al. [14] using pulsed blowing and Evrard et al. [49] for continuous blowing, supporting our results.

Even if the individual blowing of the lateral and bottom jets produce drag reduction, the major potentialities of the control will surely related to the combination of the jet's capabilities. In the next section the combination of bottom and lateral jets will be studied.

5.2 Combined jets blowing

As demonstrated by Sardu [102], with all four jets blowing the drag reduction obtained is lower than using only the lateral and bottom jets. For this reason the combined effects will be only analyzed using the bottom and lateral jets.

5.2.1 Effects of the combined blowing over the drag and efficiency

A series of test were performed including all possible combinations of blowing. The results in terms of drag reduction are observed in figure 5.3.

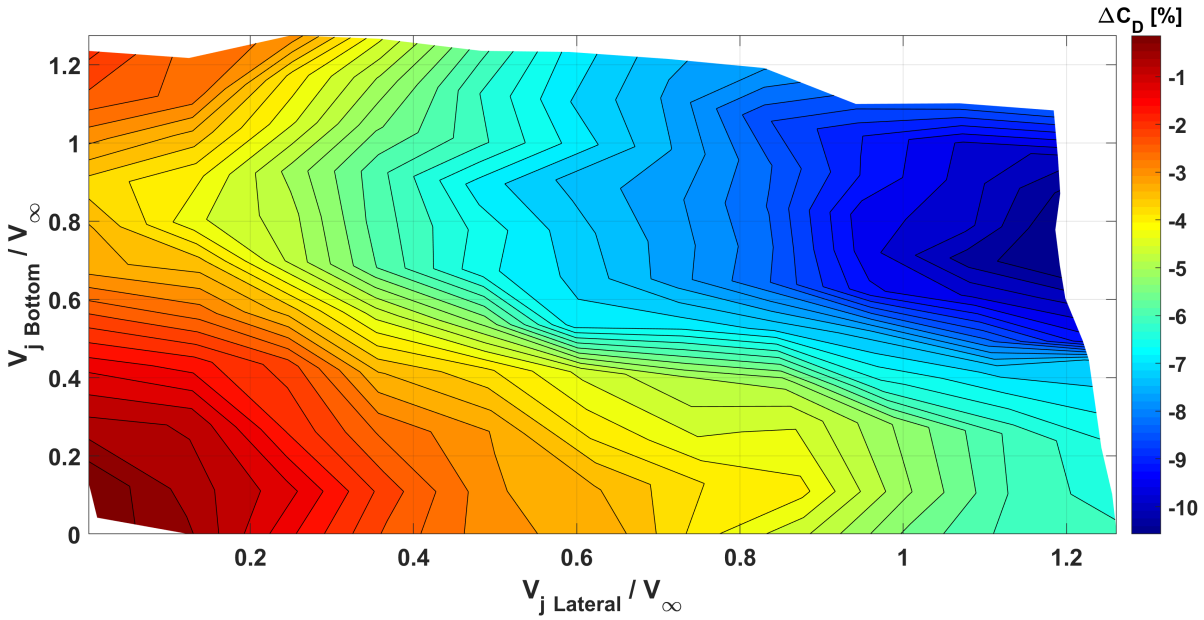

Figure 5.3: Drag variation map in function of bottom and lateral blowing.

The axes of the color map represent the blowing speed ratio of bottom and lateral jet, and the colors the drag variation. The drag variation considered in the latter colormap includes the effect of the jets' thrust, shown in figure 3.3. Other authors as [14] subtract the thrust effect in order to consider only the control over the wake. In this study the effects of the jets' thrust are considered since the power of the blowing jets are taken into account on the energy budget of the control.
In general, the drag presents a decreasing tendency while increasing the blowing. For the blowing of jets with small components of combination ($V_B/V_\infty < 0.2$; $V_L/V_\infty < 0.2$) the results replicate the previous findings of figure 5.1 without significant changes. Above $V_B/V_\infty = V_L/V_\infty = 0.4$ the effects of the combined jets become evident and the drag reduction is always below the minimum reachable with the single jets ($\Delta C_D \approx -6\%$ for the lateral jets alone). Finally a minimum of $\Delta C_D = -10.6\%$ is reached at $V_B/V_\infty \approx 0.8$ and $V_L/V_\infty \approx 1.15$. This configuration of the AFC from now on will be refereed as "Maximum drag reduction" (Max DR). It is also noticeable the Max DR blowing velocities coincide with the blowing needed to reach the maximum drag reduction for each individual jet, evidencing a possible additive property of the drag reduction. In fact, the resulting drag reduction is near the sum of the components of the maximums for the lateral and bottom jets.

While the value of the drag variation evidences the aerodynamic efficiency of the vehicle, an analog analysis can be performed for the control through the wake receptivity, first introduced on the automotive field by Englar [46]. This coefficient is the ratio between the drag variation ΔC_D and the blowing coefficient C_μ, defined in equation 5.2, and represents the response of the wake to the control.

$$-\Delta C_D/C_\mu = \frac{-\Delta D}{\sum \frac{1}{2}\rho A_i V_{j,i}^2} \tag{5.2}$$

Where ΔD is the drag variation produced by the control, A_i are the exit areas and $V_{j,i}$ the blowing speed of the $i-th$ jet. The C_μ is the blowing coefficient. Values of wake receptivity equal to 1 means that the system is receiving, in terms of drag reduction, the same momentum given by the blowing.

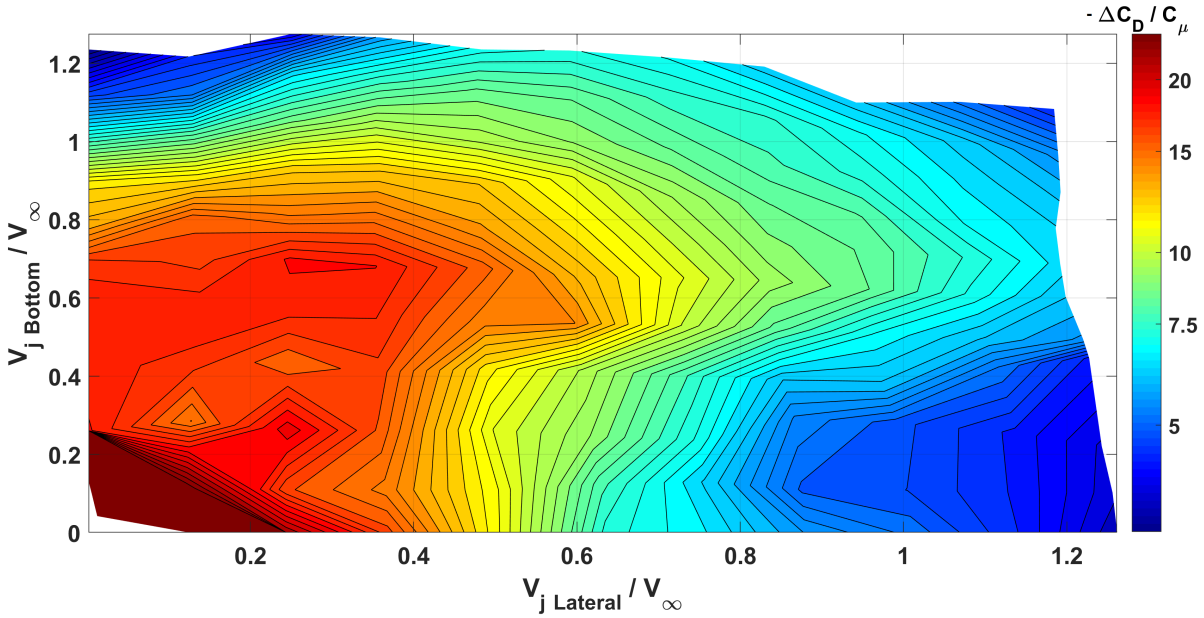

Figure 5.4: Wake receptivity of the combined top and lateral blowing.

In figure 5.4 is shown the color map of the wake receptivity for the same forcing configurations showed in figure 5.3. As the drag variation, the values of wake receptivity tend to reduce while the blowing increase but showing several peaks for configurations below $V_B/V_\infty = 0.8$ and $V_L/V_\infty = 0.4$. High values of wake receptivity are observed for bottom blowing, dropping only for values above $V_B/V_\infty = 0.8$. For the lateral jets, the drop begins at and $V_L/V_\infty = 0.4$. Below these two values the wake receptivity shows a plateau with some local peaks. The peak present at $V_B/V_\infty = 0.7$ and $V_L/V_\infty = 0.35$ presents the minimum drag regarding the others, evidencing the maximum capabilities of the actuation over the wake and therefore the best configuration in terms of overall energetic efficiency. This is another characteristic point of the control and will be called from now on "Best compromise" (BC). There is a second peak at $V_B/V_\infty = 0.15$ and $V_L/V_\infty = 0.15$ with higher values of wake receptivity, but this is product of the low values of C_μ. Furthermore the drag variation at those levels of blowing is negligible, dismissing the importance of this peak.
The main characteristic of an active flow control is how it manages the efficiency ξ. As explained in equation 1.6 of the Introduction, this is given by the ratio between the power gain and the power consumed, and values above one means an overall energy

gain. As described in section 3.5 the power consumed by the control only considers the power losses inside the model, eliminating the external pneumatic lines' losses and emulating a real case scenario. Equation 3.8 details how the power losses are calculated and 3.7 the power gain. In figure 5.5 is presented the efficiency color map for the combined bottom-lateral blowing analyzed before.

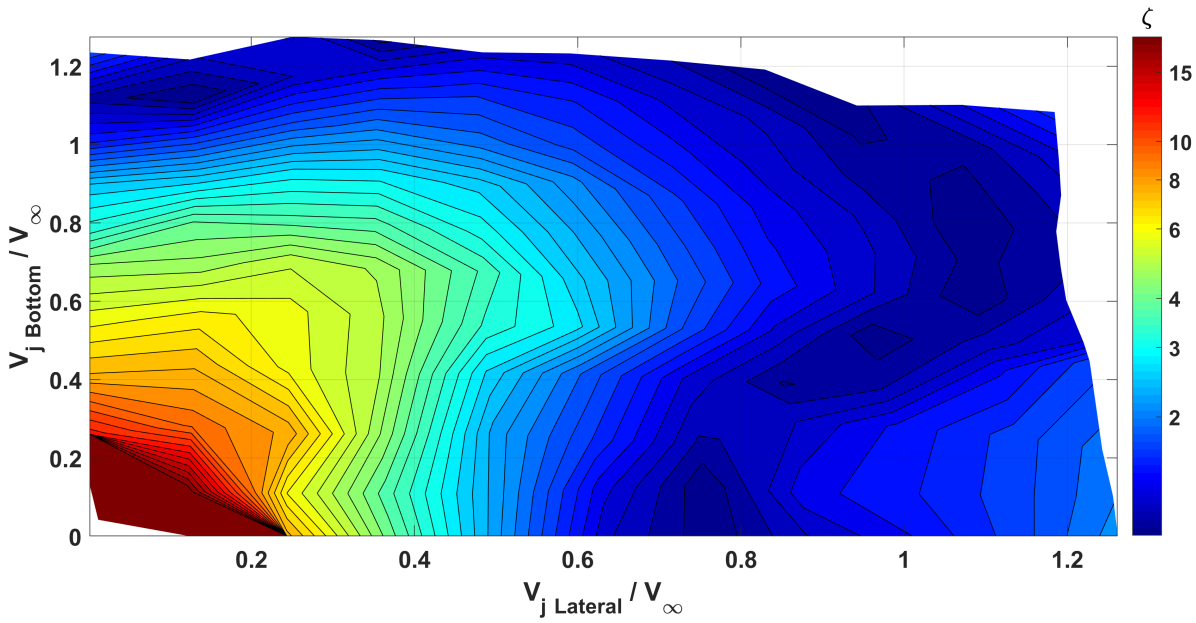

Figure 5.5: Efficiency of the combined top and lateral blowing.

The efficiency presents a decreasing distribution towards higher blowing velocities, but reaching values below one only for the outer edges of the map. This means that almost all configurations tested recover more power ($\xi > 1$), or at least the same ($\xi = 1$), than the used on the control. The combination of both jets seems to reach its optimal efficiency for the $0.6 < V_B/V_\infty < 0.8$ and $0.4 < V_L/V_\infty < 0.6$ zone, showing higher values regarding the surroundings. It seems that the blowing of the bottom jet helps improving the lateral ones, for example at $V_L/V_\infty < 0.6$ the efficiency rise when the bottom blowing reaches $V_B/V_\infty < 0.5$. Inside side this zone is present the BC configuration, that performs an efficiency of $\xi = 4.97$, meaning that the power recovery on the BC condition is almost five times more that the power applied to the control. Is also observed how the isolines reach higher efficiency levels towards the Max DR case regarding the surroundings. Nevertheless, the Max DR evidence values of efficiency lower than one ($\xi = 0.8$) meaning that the control uses more power that what is gained in terms of drag reduction. Even though, this maxima condition is important for the research and will be further studied successively.

In conclusion, from this section emerges that for the combined jets flow control coexist two characteristic conditions representing the Max DR and BC, which are the most interesting conditions since represent the maximum capabilities of the control. From now on, the analysis of the data will be concentrated in these two conditions only, which characteristics are resumed in table 5.1.

Configuration	Acronym	V_B/V_∞	V_L/V_∞	$\Delta C_D[\%]$	ξ
Maximum drag reduction	Max DR	0.8	1.15	-10.6	0.8
Best compromise	BC	0.7	0.35	-5.6	5

Table 5.1: Characteristic configurations of the controlled case.

5.2.2 Pressure distribution and fluctuation of the controlled cases

In order to understand the motives behind the drag reduction and analysis of the pressure distribution is performed, considering the same visualizations of figure 4.1.

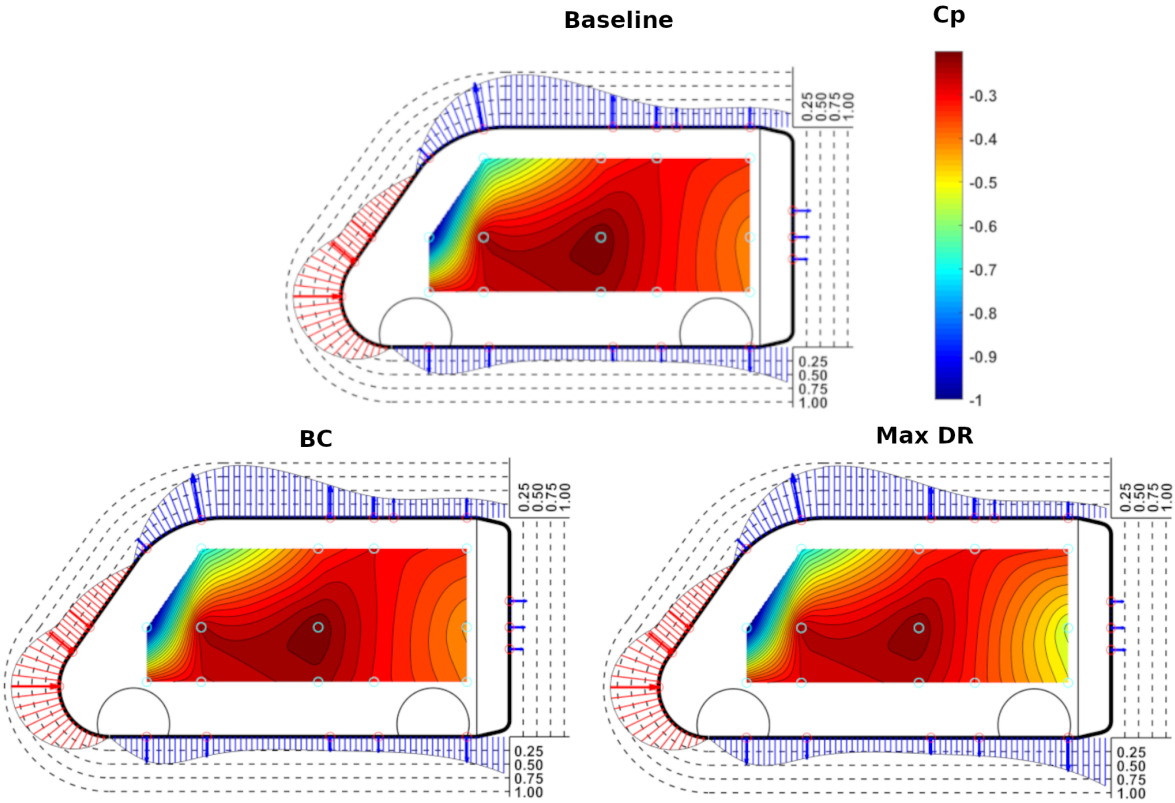

Figure 5.6: Pressure coefficient on the lateral part and periphery of the model for the baseline and controlled cases.

Figure 5.6 shows the pressure coefficient distribution on the lateral part of the model for the baseline and controlled cases in the same way of figure 4.1a. It is clear that the two controlled cases do not present a different distribution of the C_p in the periphery nor side distribution. There is only a slight decreasing of the pressure near the rear part, specially on the side colormap, but since is in the lateral face does not affect the drag. Figure 5.7 presents the pressure coefficient (C_p) distribution and pressure coefficient RMS (C_{pRMS}) on the rear part of the model. As in the baseline case, on the left part is presented the C_{pRMS} colormap and in the right the C_p's.

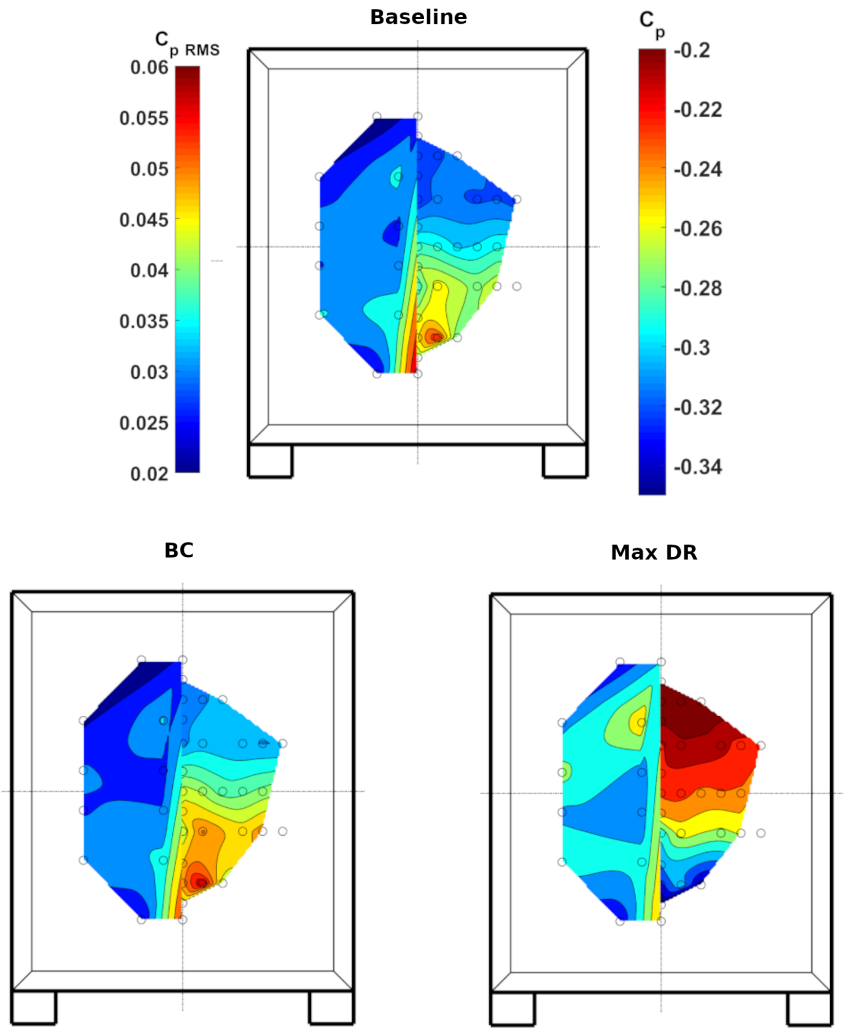

Figure 5.7: Pressure coefficient and pressure coefficient RMS on the rear part of the model for the baseline and controlled cases.

The figure shows a general behavior evidencing rise of the base pressure levels with the increasing intensity of the blowing, thus explaining the drag reductions on the controlled cases.
The BC configuration resembles the baseline, but with some modifications on the distribution and a higher C_p range. The most relevant changes are present in the lower part, showing larger pressure increase regarding the neighborhood. The C_{pRMS} distribution presents a general reduction regarding the baseline, retaining some of the original fluctuation levels on the bottom part.
The Max DR case present a completely different distribution, with the C_p growing upwards and significantly higher values of C_p. This distribution evidence major changes on the near wake distribution regarding the two precedent cases, but at this point there is no enough information to hypothesize the new wake structure. Further information regarding the near wake will be given on the PIV visualizations of the next section. The fluctuations of this case are increased regarding the baseline. Furthermore, there is a peak of fluctuations near the top part of the model. As in the C_p, the C_{pRMS} present significant modification of the distributions.

From these two last sets of figures is quite clear that the reasons of the drag reductions observed on the maps of figure 5.3 are a product of the increasing of the

base pressure only, without any influence of the fore part of the model. Furthermore, the pressure distribution on the rear resembles the baseline when the blowing velocity is relatively low regarding the freestream speed (as in the BC configuration) but for blowing near the freestream speed (Max DR configuration) the distribution severally changes, evidencing major differences on the near wake. This may explain also why the drag reduction does not descend below -10.6%: the wake reaches its optimal configuration thanks to the blowing, rising the base pressure. Increasing the blowing above this level will only cut down this condition due to the high speed of the jets and the consequent low pressure generated. Traces of this effect can be observed in figure 5.7 for the Max DR condition, where in the bottom part the pressure diminish presumably because the blowing effect. The next section will share some light regarding this hypothesis through the visualization of the near and far wakes of the model for the controlled cases.

5.3 PIV measurements for the controlled case

5.3.1 2D2C PIV, controlled near and far wake

Considering the same planes of visualization given in figure 4.3a the BC and Max DR conditions are analyzed. Figure 5.8 represent both $Y/W = 0$ and $Y/W = 0.2$ planes (left to right) for the two blowing configurations of the far wake.
As in the pressure distribution on the rear, the BC configuration resembles the baseline with small differences on the intensity and positions of the counter-rotating vortexes. For the midplane visualization of figure 5.8a ($Y/W = 0$) the bottom vortex seems slightly bigger than the baseline and at merely the same height, but in a closer position regarding the rear base, between $0.4 < X/W < 0.6$. The top vortex retain the same position and dimension regarding the baseline. The wake closes on a saddle point at the end of the visualization field at $Z/W = 0.6$, below the mid-height of the model. The stagnation point on the rear base of the model does not change the position. On the $Y/W = 0.2$ plane of figure 5.8b the changes regarding the baseline are negligible, evidencing a dominant effect of the entrainment of the lateral flow on the near wake. For the Max DR case, instead, the differences with the baseline are significant. The midplane ($Y/W = 0$) of figure 5.8c shows the bottom vortex very close to the model's base and in an upper position. The flowfield presents an upstream dominant flow product of the blowing of the lower jet, which is also evidenced by the high-speed upstream flow on the bottom part of the model. The top vortex is outside the visualization field, but it can be intuited that is present immediately above due to the shape of the streamlines. On the $Y/W = 0.2$ plane of figure 5.8d a dominant streamwise component of speed is present with a small recirculation zone attached to the rear of the model. Particularly, no saddle point is observed as in the precedent cases.
Finally, the most important change is the whole shape of the near wake. It is significantly smaller that the baseline, ending approximately at $X/W = 0.9$ with the saddle point in an upper position.

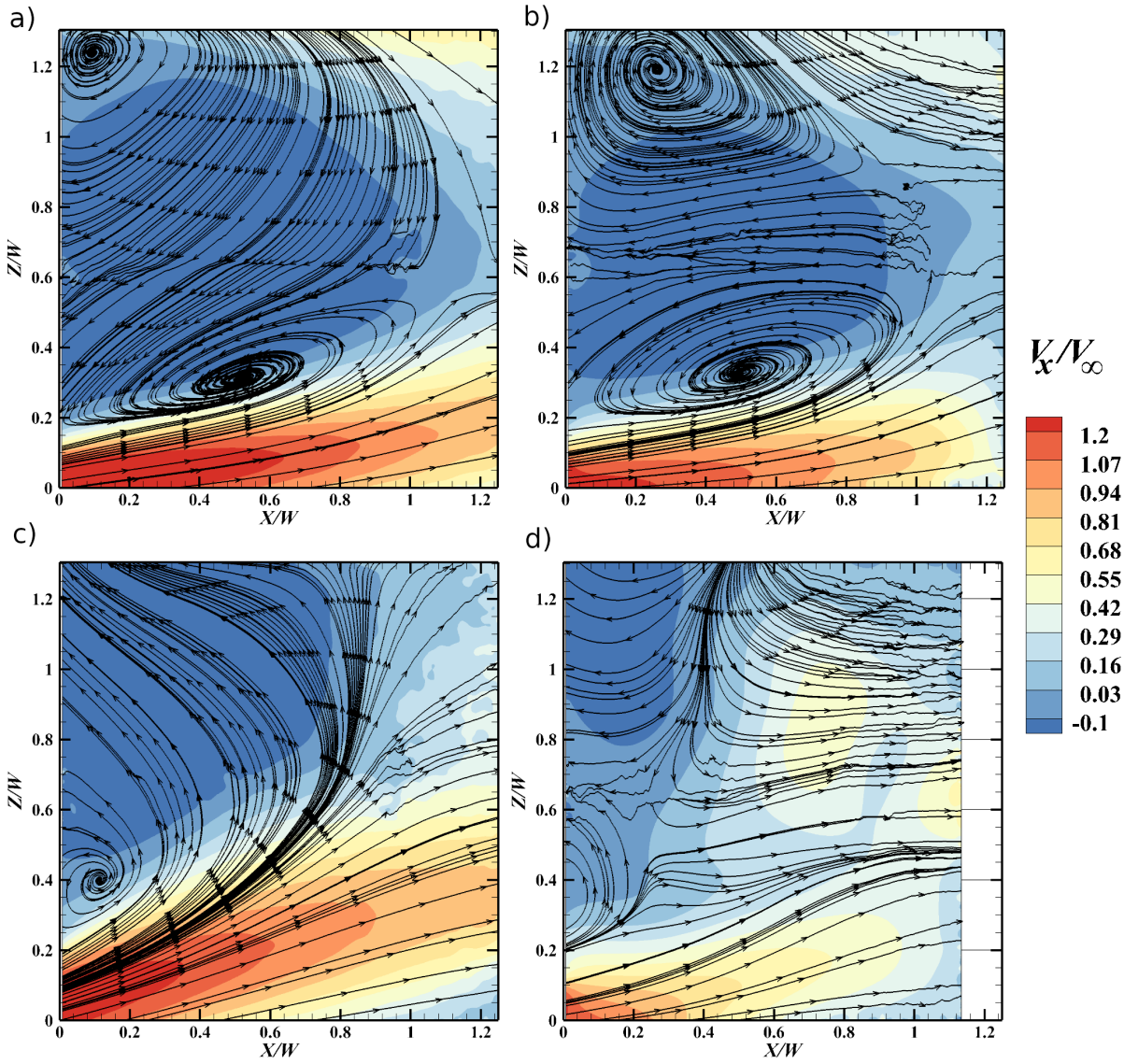

Figure 5.8: 2D2C PIV for best compromise $Y/W = 0$ (a), $Y/W = 0.2$ (b) and Max DR $Y/W = 0$ (c), $Y/W = 0.2$ (d).

In figure 5.9 are presented the PIV of the planes parallel to the rear base positioned at $X/W = 1$ and $X/W = 2$, representing the far wake for the controlled cases. Figures 5.9a and b correspond to the BC configuration. The streamlines show that the counter rotating streamwise vortexes are shifted to an upper position and slightly reduced in size regarding the baseline, but the horizontal distance between the vortexes center is retained. The dissipation of the vortexes with the distance presents the same behavior than the baseline. From the colormap of velocities is still present a strong component of downwash behind the model, for both distances. The Max DR, shown in figure 5.9c and d, demonstrates a completely different wake structure, composed by a double-symmetry distribution of the streamlines and no presence of downwash. Moreover this structure maintains the distribution in the distance, with only small dispacements of the center point.

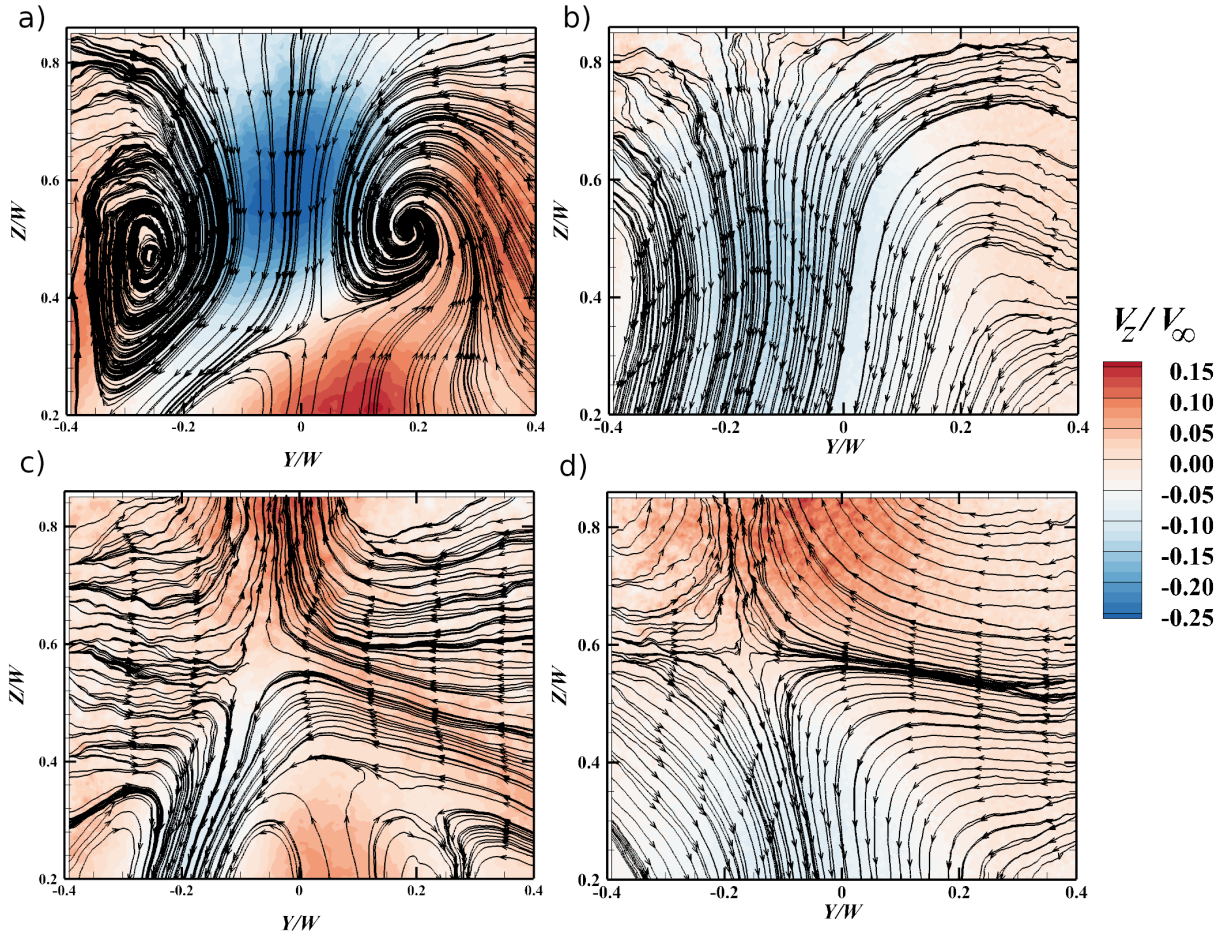

Figure 5.9: 2D2C PIV for best compromise $X/W = 1$ (a), $X/W = 2$ (b) and Max DR $X/W = 1$ (c), $X/W = 2$ (d).

From these far wake analysis is demonstrated the effect of the control, highlighting for the best compromise case a reduction the counter rotating vortexes' size together with an upper position regarding the baseline. Furthermore, comes to light a new wake configuration for the maximum drag reduction case, presenting a double-symmetry of the streamlines and a complete eradication of the counter rotating vortexes.
In addition, a lack of symmetry regarding the mid-vertical axis is observed for all four cases. This is a product of the uneven blowing of the lateral jets evidenced in figure 3.6. Unfortunately, this misbalance of the blowing could not be further compensated and the spurious effects of this defect are observed in the streamwise PIV's. Nevertheless, the average structure of the wake corresponds with the observations of other authors as Grandemange et al. [58], McNally et al. [80], Perry et al. [91] and Dalla Longa et al. [42], supporting our results.

5.3.2 2D3C PIV, controlled near wake

As for the baseline visualizations, the same planes defined in figure 4.3b are used, and the results of the reconstructed near wake are shown in figure 5.10 for both BC and Max DR.

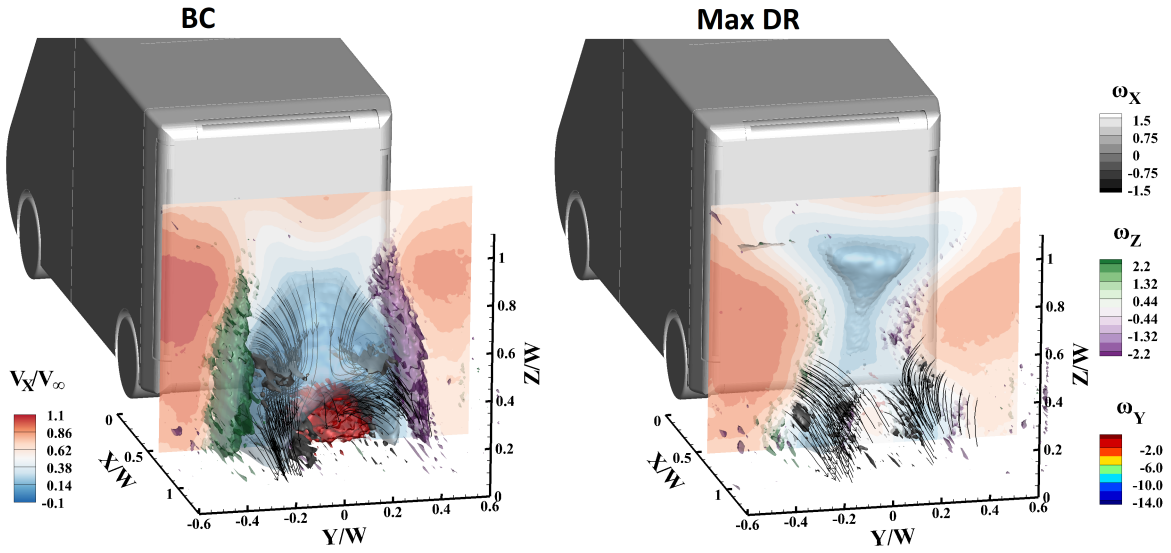

Figure 5.10: Reconstructed wake for the maximum drag reduction and best compromise cases.

The BC configuration on figure 5.10 presents the same main characteristics of the baseline wake, but with a $\approx 20\%$ smaller recirculation bubble settled in a lower position. The three shear layers of the laterals and bottom are still present but also with reduced dimension. The velocity plane highlighted at $X/W = 0.68$ shows barely the same distribution o the baseline Major changes are observed for the Max DR near wake instead, as shown in figure 5.10: The recirculating bubble is way smaller and positioned closer to the model's rear base, with a appendix on the top. The shear layers are almost canceled by the control effect and there is no trace of the generation of the streamwise vortexes. Actually, in the colored plane representing the streamwise speed is observable the large area reaching the freestream speed.
This last configuration shows that the blowing from the bottom jet compensates the downwash and the lateral jets severally reduces the left and right shear layers, pushing the wake to a symmetric distribution. In addition, the combined effect of lateral and bottom jets eliminate the generation of the streamwise vortices.

5.3.3 Conclusions of the controlled near and far wake

As seen from the PIV results of the near and far wakes, the control produces two main effects in function of the blowing intensity.
For blowing speeds below the freestream the modifications affect mainly the near wake. The control reduces the recirculation bubble and pushes it upwards and closer to the rear of the model. The counter-rotating streamwise vortexes are pushed upwards and reduced in size, but without affecting theirs dissipation on the far wake.
For blowing speeds on the order of the freestream and above, the near and far wakes changes majorly, reducing the recirculation bubble and pushing it near the rear of the vehicle, and eliminating the streamwise vortexes. The far wake becomes completely symmetric, showing a complete compensation of the downwash. This new wake structure represents the optimal ratio between blowing and deformation of the wake, since for higher blowing no improvements on the drag are observed. Furthermore, it presents the higher base pressure, linked to the strong reduction of the recirculating bubble.

5.4 Spectral analysis of the fluctuating pressure

The signals from the microphones were analyzed in the frequency domain for the two Max DR and BC cases, and the results are presented in figure 5.11.

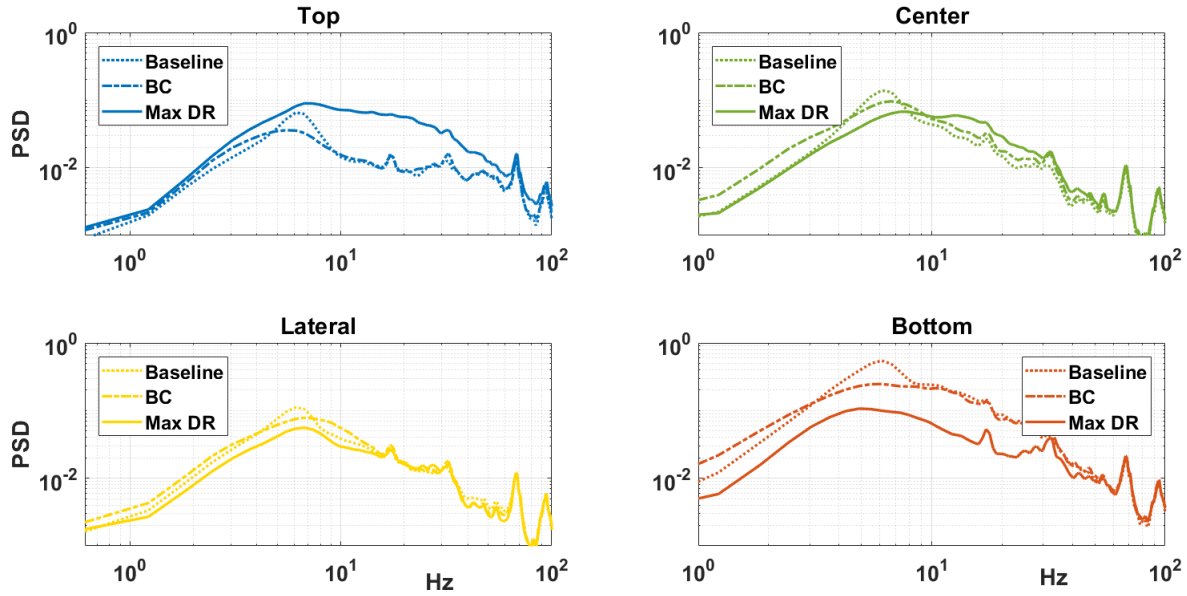

Figure 5.11: Spectra of the characteristic microphones of figure 4.8.

In figure 5.11 are presented the PSD of the Max DR and BC cases. The baseline case of chapter 4 is also represented in dashed line as a reference. The top microphone evidence a marked reduction of the Strouhal peak for the BC case, retaining the same distribution for the rest of the spectra. For the max DR case the overall energy rises on the range between 3 and $50Hz$, with a slight peak near the $St = 0.12$ frequency. This increasing on the power of fluctuations is explained by the presence of the appendix of the recirculation bubble near the top of the model, seen in figure 5.10b.
The lateral and center microphones have similar distributions of the PSD for all cases. The BC case reduce the Strouhal peak without significant changes on the rest of the distribution. For the maximum drag reduction is observed a reduction of the levels of fluctuations for both of them, conserving the maximum levels around $St = 0.12$.
The bottom microphone shows a similar behavior to the Lateral and center microphones but with stronger variations, evidencing the strong effect of the control on this particular area. Actually, for the Max DR case the overall fluctuation levels reduce significantly more than the precedent microphones.
Finally, the effects of the control are observed until approximately $60Hz$. From that frequency and on, there is no significant changes on the spectra.

From the baseline, the cross PSD between the top and bottom microphones of the rear evidenced the presence of the regular vortex shedding. In order to evaluate the effect of the control over this phenomena, the top-bottom cross PSD analysis is repeated for the BC and Max DR cases, and plotted on figure 5.12 in function of coherence and phase. The baseline case is also plotted as a reference.

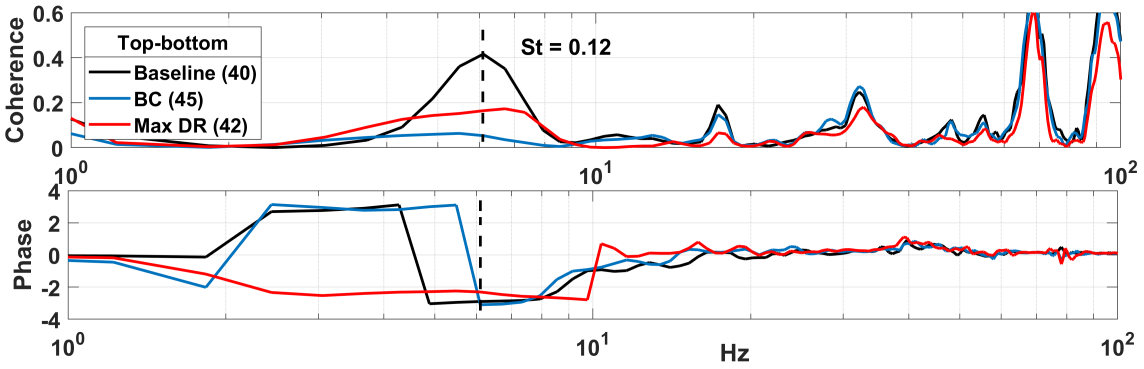

Figure 5.12: Cross PSD of the top and bottom microphones.

It is clearly seen that the control reduced the coherence of the signals around the Strouhal peak, representing a weakening of the top-bottom regular vortex shedding but without losing the phase. This means that the control strongly reduces this phenomenon but do not eliminate it completely. It is particular that the BC configuration shows lower values of coherence than the Max DR, but this could be associated to the increased fluctuations on the top microphone when blowing at the Max DR condition. Regarding to the rest of the frequency domain, no changes are observed on the Cross PSD.

As a closing remark on the effects of the control over the pressure fluctuations on the model's base, some salient points could be concluded: In all cases the effect of the control reduces the intensity and correlation of the top-bottom vortex shedding but conserving the 180° phase, this meaning that the vortex shedding phenomenon is always present. Lastly, the fluctuations on the bottom part seems to be the most sensitive to the control that the other positions. This same observation was highlighted for the mean values of the pressure on the precedent sections, and all this points to the bottom part as the most responsive to the control in terms of mean pressure and pressure fluctuations.

5.5 POD analysis of the pressure fluctuations

The POD modes and relative energy were calculated for the BC and Max DR cases and the relative energy and the modes are represented in figures 5.13 and 5.15 respectively.

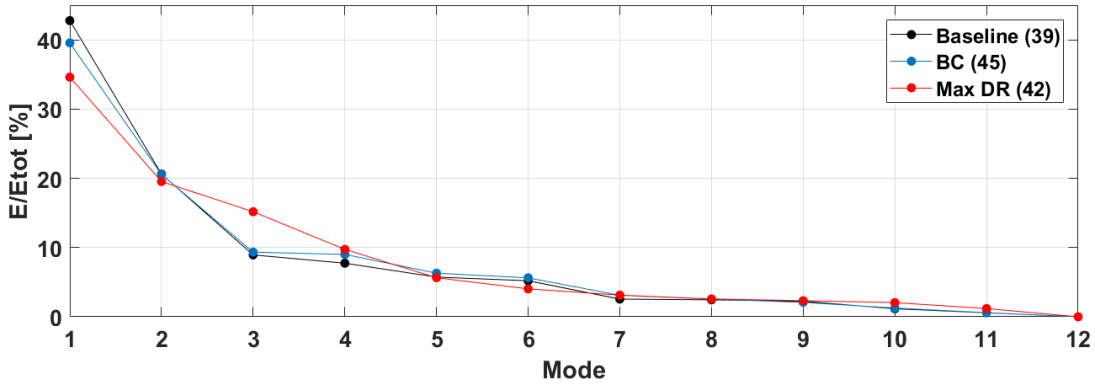

Figure 5.13: POD modes' relative energy of the controlled and baseline cases.

In figure 5.13 are presented the relative energy of the modes for the Baseline (no control), BC and Max DR. The first observation is that the effects of the control are only relevant until the fourth mode, showing almost no variation in the latter, and that the modes above the second mode increases while those below decreases with the increasing intensity of blowing. The first mode exhibit a clear decreasing tendency with the control intensity, reaching 40% at the BC and 35% at the Max DR. This could evidence a reduction of the bubble pumping, since this mode is associated with the streamwise fluctuations of the wake. The second mode does not evidence a significant change on the energy for the controlled cases. Notably, is constant for all cases evidencing a stable component of vortex shedding. The third mode do not evidence changes for the BC case, but a remarkable increasing for the Max DR case, and the fourth mode presents an almost linear growing energy with the blowing intensity but a much more lower energy levels.

In general, the effect of the control is to reduce the fluctuation of large structures represented by the first mode and increase the smaller ones, evidenced by the increasing energy of the higher modes. The modification of the near wake structures can be observed on the PIV results where the control produces a reduction of the wake structures and a decreasing of the fluctuations evidenced by the spectra, both seen in figures 5.10 and 5.11. The increasing on relative energy of the third and fourth mode might be speculated by the breaking of the structures in smaller ones with the control, as sketched in figure 5.14. These structures were also hypothesized by Duell and George [45] on the rear part of a squareback model where the shear layer generated growing eddies. Additionally to the breaking of larger structures, the control may further stimulate the generation of smaller eddies. Moreover, the blowing itself carry within small structures that can influence the resulting energy.

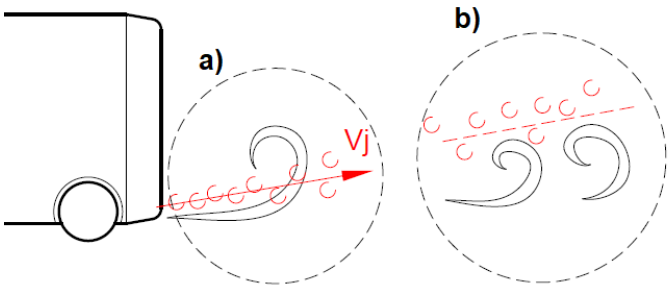

Figure 5.14: hypothesis of breaking of structures into smaller ones due to the control. Superposition of the incipient vortex and the jet (a) and the resulting effect with the smaller structures (b).

In figure 5.15 are presented the first POD modes for the BC and Max DR cases. The modes of the BC case resembles the baseline, showing the same modes' shape. Instead, the Max DR case exhibits a clear deformation of the modes. In the Max DR case the first mode is completely disappear and replaced by a fluctuation concentrated on the top part. This agrees with the results of the power spectra of figure 5.11, where the top microphone evidence an increasing on the fluctuation levels for the Max DR blowing. The fact that this effect corresponds with the first mode agrees also with the energetic levels shown. The second and third mode exhibit some similarities, both representing a sort of top-bottom symmetry-breaking like the second mode of the baseline and BC cases. The fourth mode evidences a fluctuation of pressure in

the top-right side of the model's rear, which is hardly associable to some previously noticed aerodynamic phenomena. Yet, the energy levels are pretty small and can be neglected.

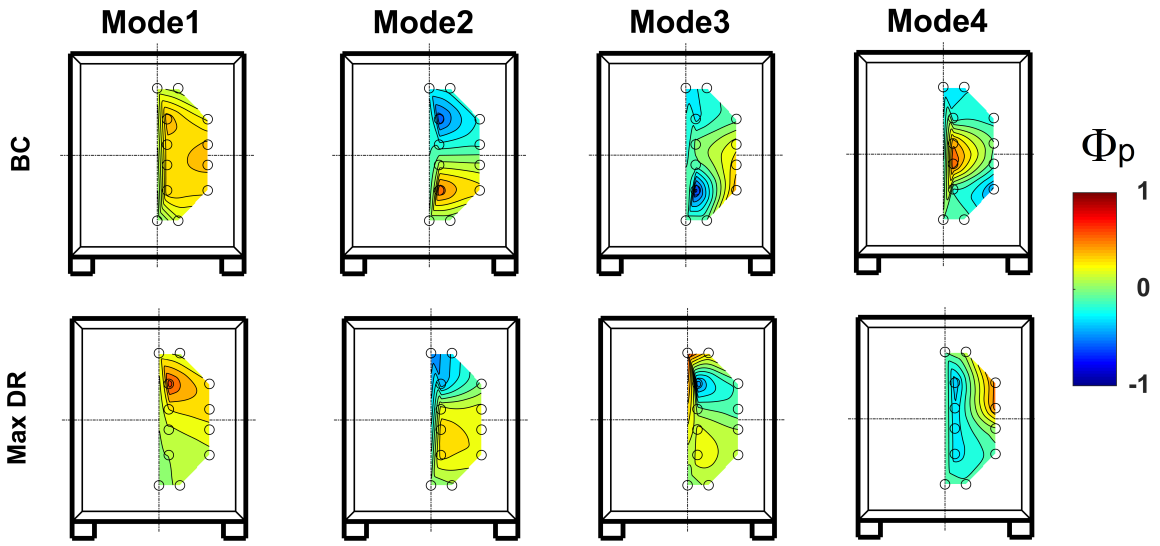

Figure 5.15: POD modes of the controlled cases.

It is clear that the highly intense blowing as in the Max DR case produce a complete reconfiguration of the near wake, as demonstrated in figure 5.10, and therefore a major change of the modes representing the rear base's pressure. In fact, the BC case (with a smaller blowing intensity regarding the Max DR) shows the same mode's shape present on the baseline, evidencing no significant changes on the near wake and supporting the PIV data.

5.6 Wavelet analysis

The wavelet transform was applied to the BC and Max DR cases over the same characteristic microphones positions described in figure 4.8 and as in the precedent cases the $St = 0.12$ is represented with a red dashed line. Both results are presented in figures 5.16 and 5.17.

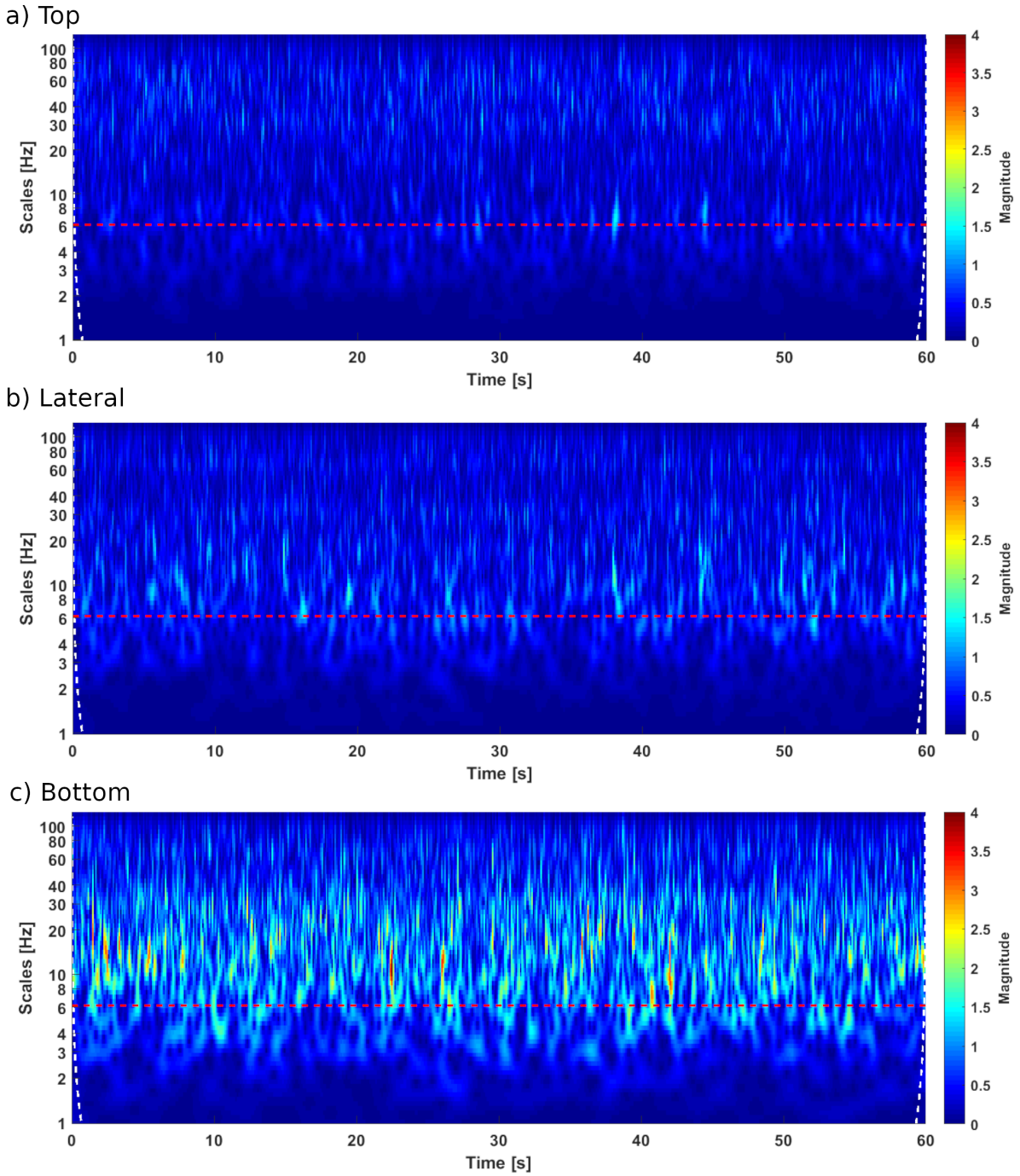

Figure 5.16: Wavelet transform of the top (a) bottom (b) and lateral (c) microphones on the best compromise controlled condition.

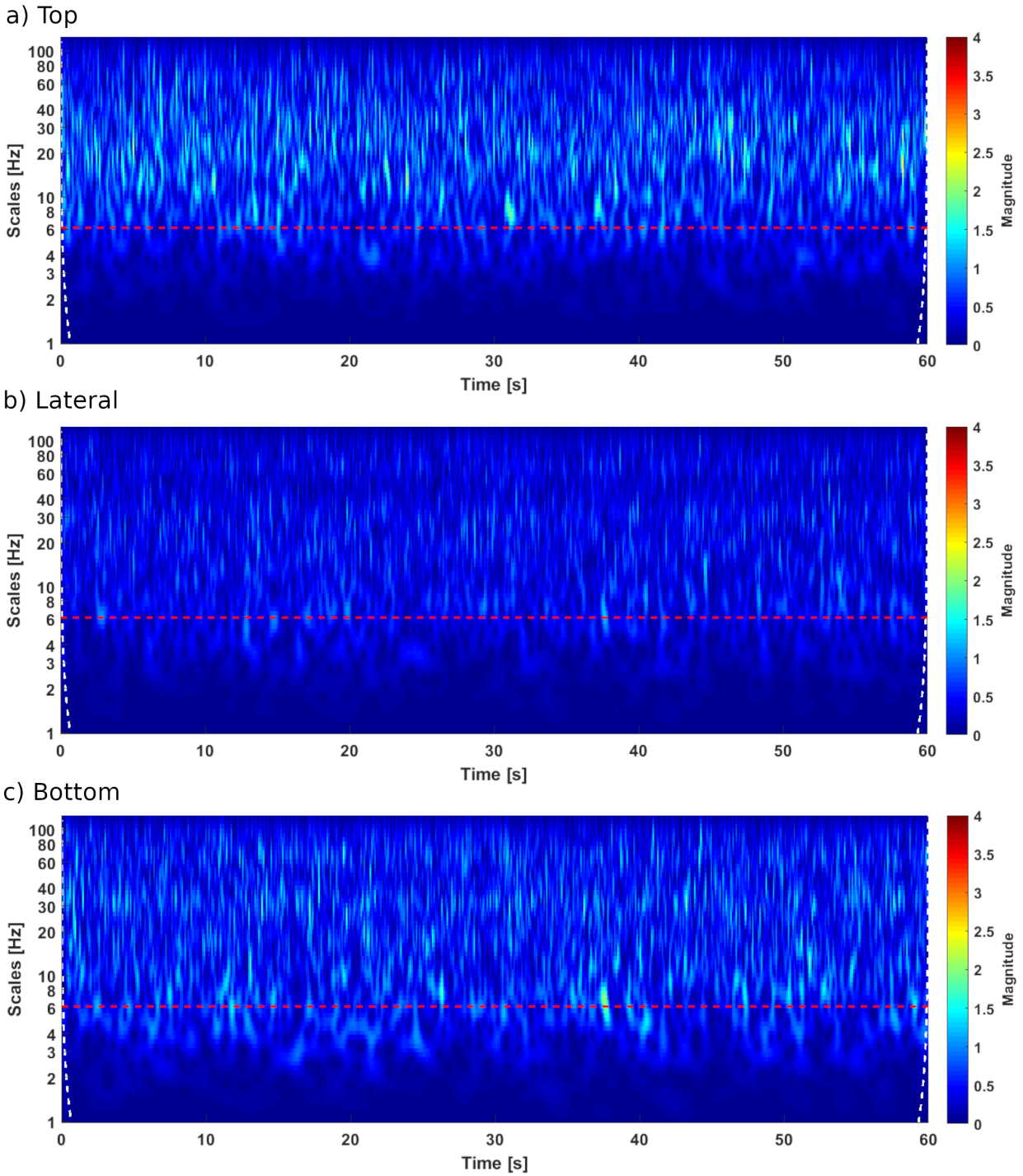

Figure 5.17: Wavelet transform of the top (a) bottom (b) and lateral (c) microphones on the maximum drag reduction controlled condition.

The first observation of the top and lateral positions (figure 5.16a and b) do not evidence relevant changes on the wavelet coefficient distributions. The bottom result (5.16c) evidence similar levels regarding the baseline but with the difference that the values are highly reduced surrounding the $St = 0.12$ frequency, as noticed on the power spectra. Furthermore, no periodic events are observable over the Strouhal frequency as in the baseline. Regarding to the Max DR case on figure 5.17 even lower levels of energy are present for the lateral and bottom cases, but the top present an increasing of the levels of fluctuation above the vortex shedding. The significant reduction on

the bottom part is evidence of the cancellation of the shedding phenomena, product of the strength of the forcing. The higher levels of wavelet coefficient evidenced by the top signal might be associated to the fluctuations produced by the interactions of the bottom jet and the upper shear layer coming from the top trailing edge. Actually, on the top part of figure 5.10b is present the largest part of the recirculating bubble, that may explain these fluctuations.

In accordance with the observations of the spectral and POD analysis, the control effect effectively reduces the energy of the vortex shedding and also the levels of fluctuations. The lower blowing speeds have a resonant effect over the vortex shedding only, while the higher extensively deform the baseline near wake pushing the remaining small recirculating bubble to the top part, thus increasing the levels of fluctuations at that particular position.

5.6.1 Events analysis

The LIM analysis is performed for the bottom microphone for the BC and Max DR cases, and presented in figure 5.18. The mean time between events and the standard deviation are calculated using the time between each successive event.

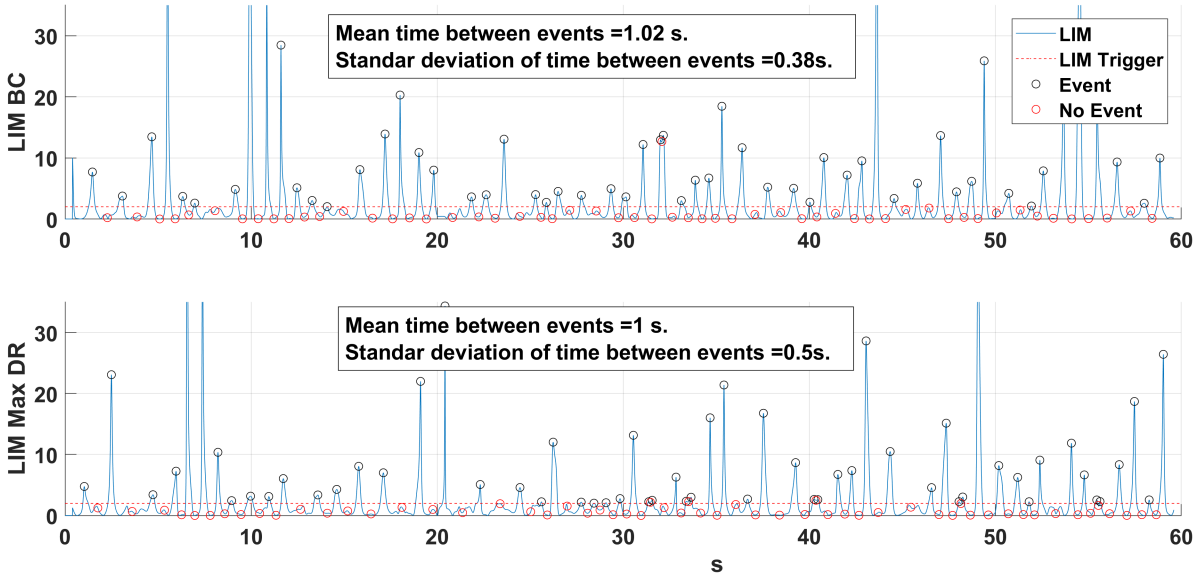

Figure 5.18: LIM of the controlled cases at the vortex shedding frequency.

The event's intensity is highly disperse with peaks that largely exceed the ranges of the baseline on both cases, pointing to an irregularity of the events. For the BC case the results are closer to the baseline, but yet more disperse. The differences are larger in the Max DR, where the peaks shows a relevant reduction of number and intensity, and jumps between very distant levels.

Due to the variability of these last results the POD and wavelet analysis will not be performed, since the lack of regularity aims to random phenomena hardly associable to regular modes. In fact, the POD analysis of the Max DR shows a set of modes that rarely can be associated to a physical phenomena as in the baseline. These two results (LIM and POD) support the asseveration that the Max DR control completely modifies the near wake and their dynamic behavior, breaking the regular structures evidenced on the baseline.

5.7 Different output geometries of the jets

The results of the control of figure 5.2 shows that the bottom part is the most sensitive to the momentum applied, presenting a higher $-\Delta C_D/C_\mu$ slope regarding the lateral and top jets. Furthermore, for the combined jets, the higher efficiencies are present when the bottom blowing is dominant. From this observations was intended to analyze the effect of different shapes of the blowing outputs, by partially cover the bottom and lateral jets in specific places of the bottom part. In figure 5.19 are shown the configurations tested with the modifications of the blowing slots and in figure 5.20 the results of ΔC_D in function of the blowing coefficient C_μ.

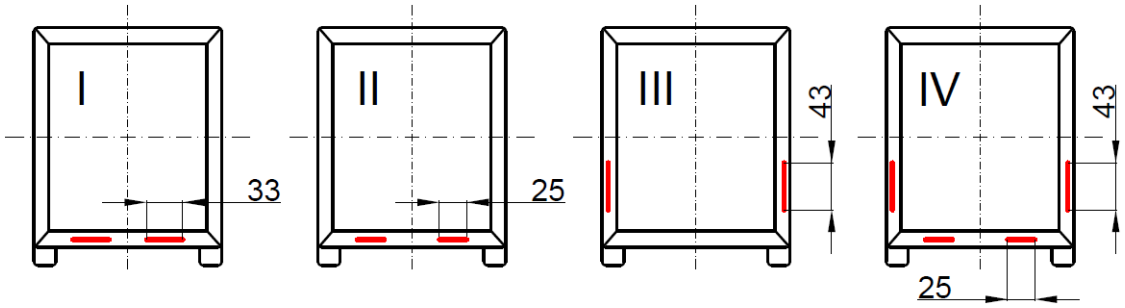

Figure 5.19: Explored configurations of the partially cover jets.

In figure 5.19 the output slots are evidenced in read for each case. The bottom jets were partially covered on the central part, leaving only the external part of the jets open with two different measurements representing 2/3 (I) and 1/2 (II) of the slot initial size. The lateral jets where covered in the top part, leaving only the bottom part open at 1/3 (III) of the original size. Finally, a combined configuration (IV) was tested using the jets of II and III.

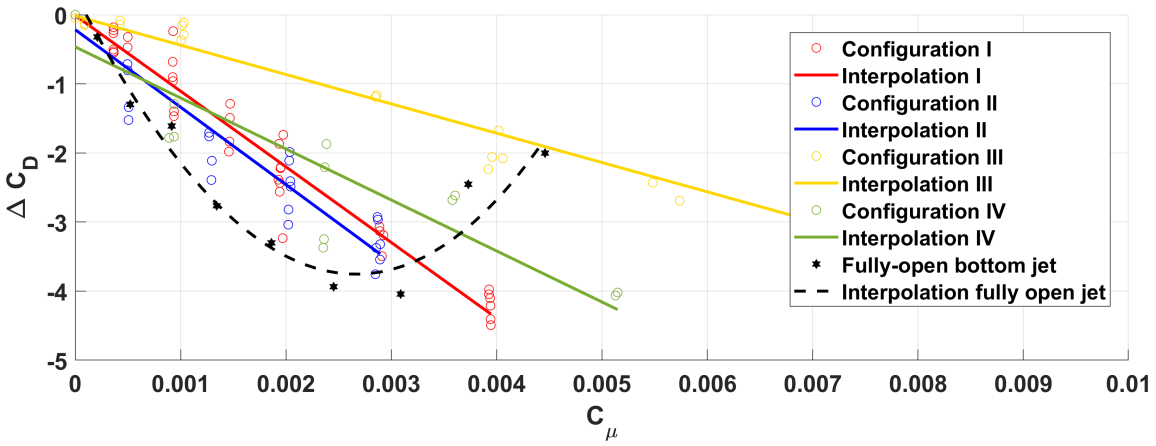

Figure 5.20: Drag reduction of the partially cover configurations in function of C_μ.

In figure 5.20 are shown the drag variations produced by the partially covered configurations in colored dots. An interpolation was plotted for each series of points in order to better understand the trends. As a reference, the response of the fully-open bottom slot was also plotted. Different from the results of the fully-open slots of figure 5.2, these results shown a much more linear trends and the configurations involving

the bottom blowing are always the most effective. In fact, the combined effect shows less drag reduction regarding the bottom blowing for equal C_μ in all cases. The less effective is, again, the lateral jet. If compared with the results of the fully-open bottom slot, all configurations evidence less drag reduction. This evidence a correlation of the drag reduction with the blowing geometry, reducing the efficiency of the jets while the slot is reduced.

5.8 Automatic drag control

Nowadays control systems tend to the feedback in order to target a certain condition. In the introduction different types of control were presented with theirs own characteristics. Our experimental setup does not allow a feedback control, but allows us to develop an automatic control by using te drag measurements as input for controlling the jets. A popular variable (or variables) for the feedback control are the pressure measurements on the rear base, which is also available in our measurements. Unfortunately, the way the data is transmitted to the PC do not allow a direct reading of the values making impossible to use as a "real-time" variable. The only one remaining is the drag balance, which will be used as a control input. But using the balance measurements as an input for the control is not straightforward, since the drag measurements carry many spurious effects, mainly due to the natural frequencies of the drag balance and the vibrations of the wind tunnel, as shown in section 3.1. This rules out the possibility of working with a real-time P, I, D or PID controls, since the high level of oscillations make the control unstable. To solve this problem an averaging window was used acting like a low-pass filter, obtaining stable values of drag for a sampling time of $30s$. This allows to use a maximum-seeking control based on the output given by the averaging, which is the control strategy that will be used.

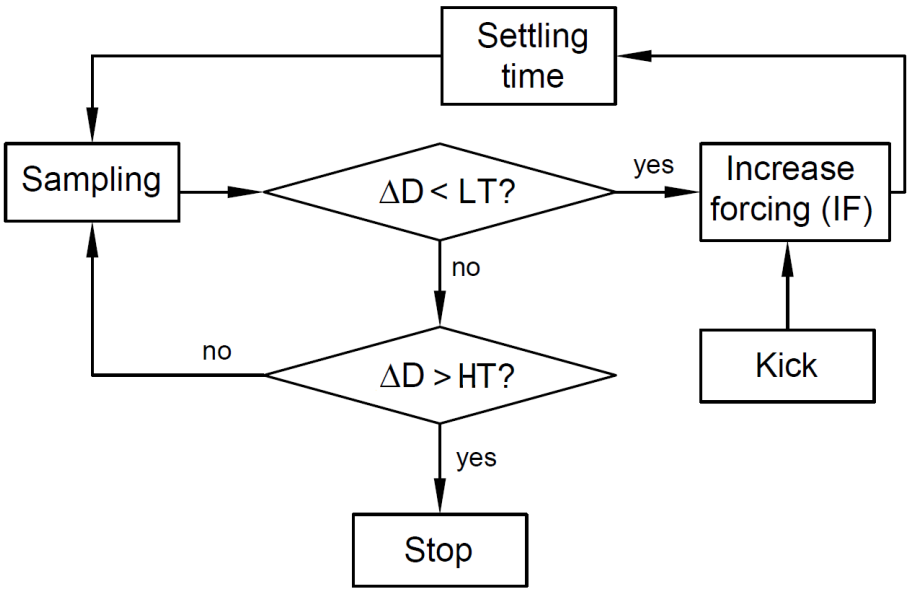

Figure 5.21: Sketch of the algorithm of the automatic drag control.

In figure 5.21 is a sketch of the algorithm of control used. Parameters as the settling time (time between a change in blowing and the start of the acquisition) and sampling time and frequency are obtained in function of the experience of the precedent tests

campaigns, and were settled to $5s$ of settling time, $30s$ of sampling time and $1000Hz$ of sampling frequency. The parameters that will affect the control are the higher trigger (HT), lower trigger (LT) and increase of the forcing (IF), being the triggers expressed in tension ($volts$) and the increasing forcing in velocity ratio Vj/V_∞. As explained before the variable used is the drag but instead of expressing it in grams, it was used the signal of the load cell in volts. The test begin with the blowing turned off and the wind tunnel in test condition. The program starts with a "kick" that increases the blowing a certain quantity. The drag is measured and if the drag variation is below a lower trigger (LT), the algorithm increases again the forcing. This loop continues until the new drag variation is above a higher trigger (HT). Once this happens, the program stops. The algorithm performs correctly when the program reaches the minimum drag value with only an initial kick. A series of preliminary test were performed in order to obtain the optimal triggers. The sensitivity of the trigger was evaluated from $0.003V$ ($\approx 3Gr$) down to $0.001V$ ($\approx 1Gr$), and the results are shown in figure 5.22 in function of the control loops. The increase of forcing used was $Vj/V_\infty = 0.1$, and the results show that from $T = 0.002V$ the algorithm performs well reaching drag reductions near the continuous results.

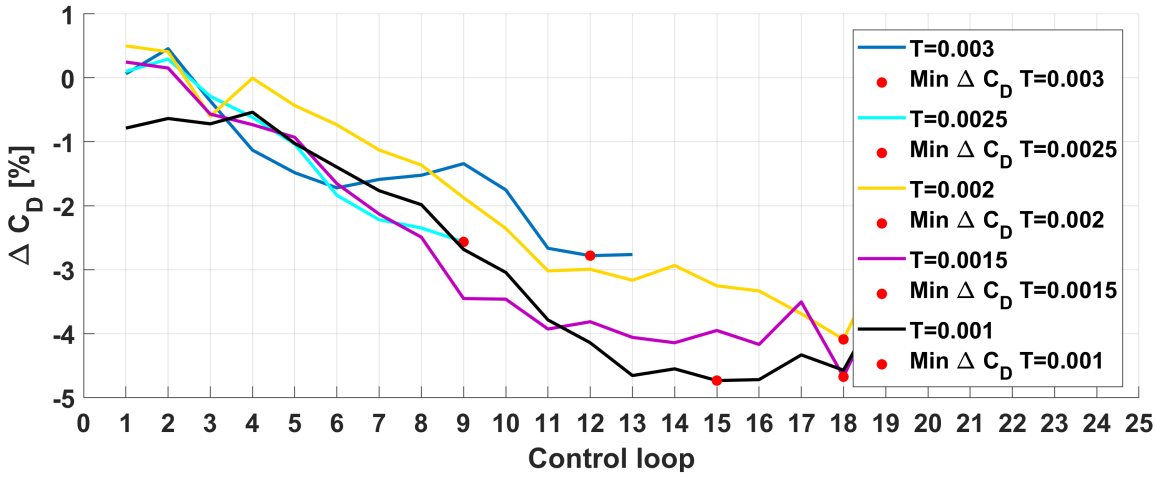

Figure 5.22: Sensibility test for the bottom jet. Blowing increase $Vj/V_\infty = 0.1$.

Successively, a series of test were performed in order to evaluate the potentiality of the automatic control for the bottom and lateral jets.

5.8.1 Bottom and Lateral jets automatic drag control

In figure 5.23 and 5.24 are presented the results of the automatic drag control for the bottom and lateral jets respectively. Each figure shows three charts: the first shows the drag variation, the second the blowing ratio and the third the kick tension. This last value represents the beginning of the automatic control, starting when the kick is $> 0V$. On both cases the kick is performed on the third loop cycle.
The bottom jet control of figure 5.23 reaches the minimum drag after 14 loop cycles with a quasi linear decrease of the drag and blowing increasing. A momentary stabilization is observed at the $10-th$ cycle, evidencing a lack of sensibility in that moment, but immediately the control evolution is recover. This evidence the robustness of the algorithm, being able to easily recover from a lapse of uncertainty and therefore avoiding possible errors due to the measurement.

The lateral jet control of figure 5.24 evidences the same behavior of the bottom jet, with a quasi-linear decreasing of the drag and blowing ratio increasing. In this case two momentary stabilization are observed at the $5-th$ and $10-th$ loop cycles, without affecting the final performance. In this case 10 cycles were needed to reach the minimum drag.

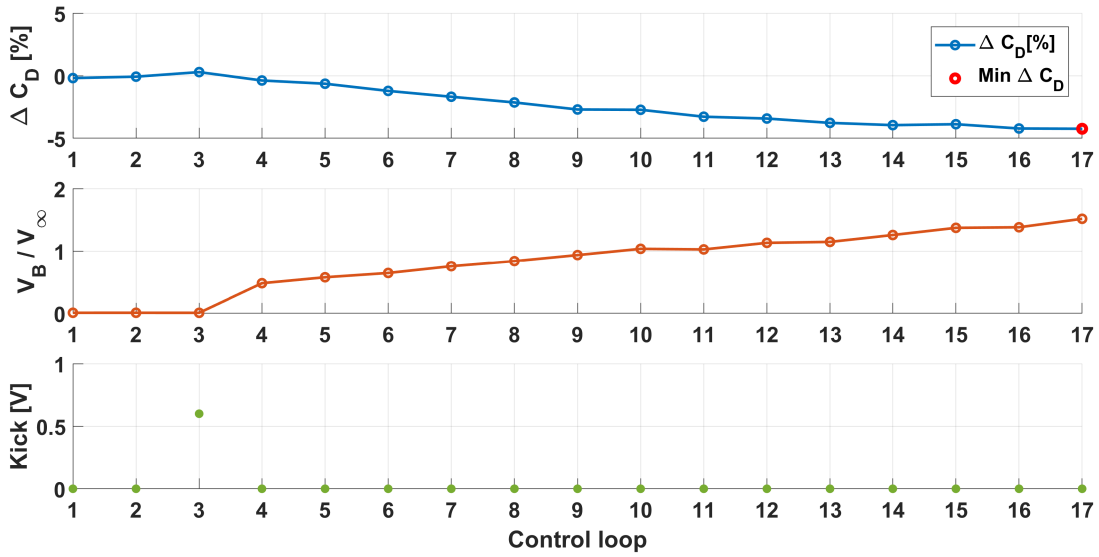

Figure 5.23: Automatic drag control for the bottom jet. $IF = 0.1\ V_B/V_\infty$, $T = 0.015V$, $LT = 0.03$, $Kick = 0.6V$.

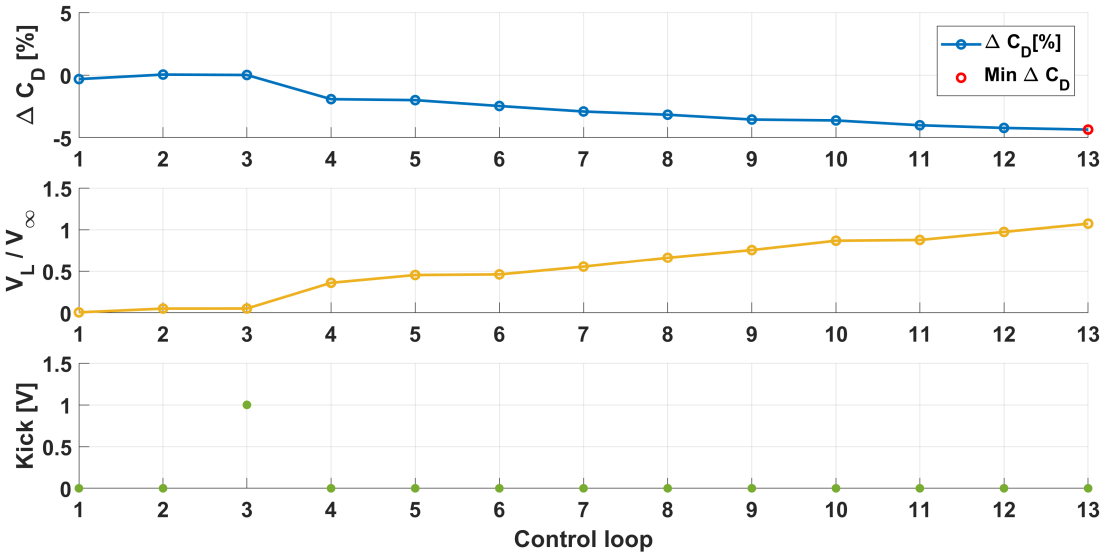

Figure 5.24: Automatic drag control for the bottom jet. $IF = 0.1\ V_L/V_\infty$, $T = 0.015V$, $LT = 0.03V$, $Kick = 1V$.

5.8.2 Reynolds effect on the automatic drag control

On a real case scenario the vehicle subject of the automatic control may range the driving speed, changing the initial condition. This situation can be simulated in the wind tunnel by changing the Reynolds number of the test. In figure 5.25 the effects of the automatic control using the bottom jet are analyzed for three different Reynolds:

1.96×10^5, 2.2×10^5 and 2.5×10^5, being the last the typical test condition. The top chart show the drag variation and the bottom the blowing ratio of the bottom jet in function of the control loop, for each Reynolds number. The trigger used in this case was $T = 0.001V$ in order to have more sensibility to the changes.

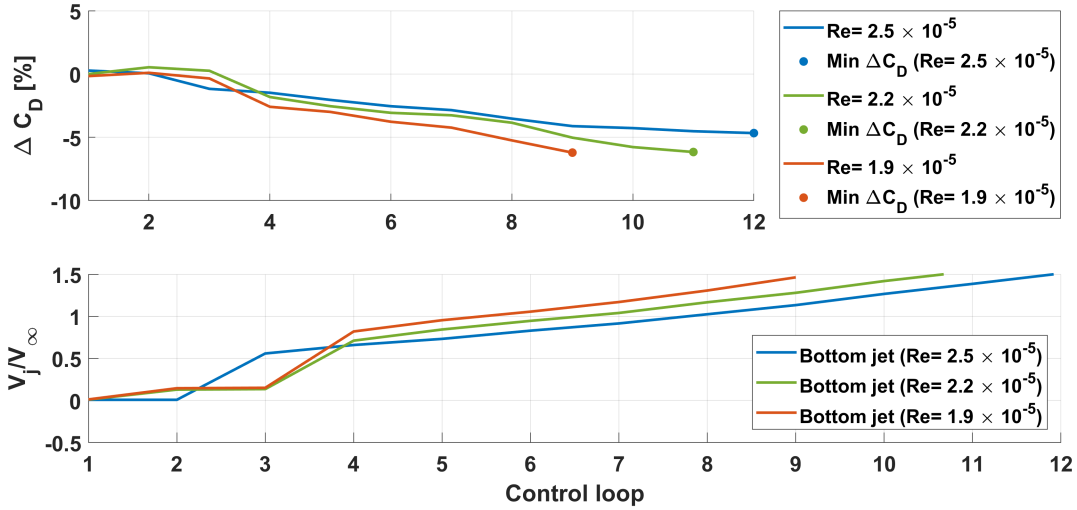

Figure 5.25: Reynolds effect over the automatic drag control for the bottom jet.

in the three different Reynolds the automatic control performed correctly, reaching a minimum drag condition. The drag variations show a slight increase of the drag reduction with the decreasing Reynolds, reaching values of $\approx 6\%$ for $Re = 1.9 \times 10^5$. As expected, reaching to the minimum drag requires less control loops while reducing the Reynolds since the increasing of forcing is the same in the three cases. In al three cases the blowing ratio is the same for the minimum drag condition. In sake of simplicity only the bottom jet will be analyzed, since similar effects are expected for the lateral.

Chapter 6:
Unsteady blowing flow control

On the baseline analysis was evidenced the unsteadiness of the wake, as also demonstrated by several authors. Since this unsteady behavior shows a dominant frequency it was intended to analyze the effects of blowing in a fluctuating fashion on the frequencies surrounding. In this analysis two ways of blowing were tested: pulsed blowing between zero and the freestream speed and fluctuating blowing between two nonzero velocities.

6.1 Main features of the unsteady blowing

When considering fluctuating actuation parameters, the intensity of blowing and frequency are the most relevant. But the waveform in which the forcing is applied might also play a relevant role. In sake of simplicity, for this test we will only use a square waveform witch allows us to control the frequency, intensity and duty cycle of the actuation. In figure 6.1 is present the square waveform with its characteristic parameters.

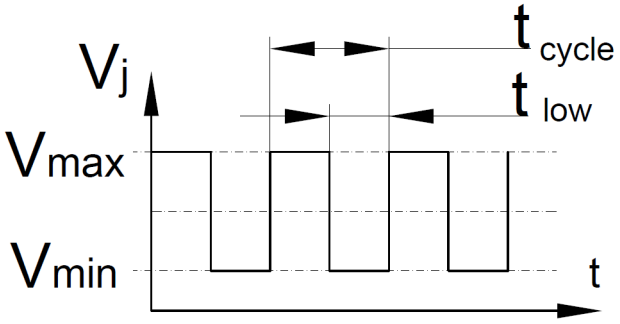

Figure 6.1: Wake receptivity of the combined top and lateral blowing.

The duty cycle (DC) represents the ratio between the the time the signal is in its lower value regarding one-cycle time in percent, as defined in equation 6.1. A duty cycle of 100% means a steady state of the lower intensity value, while 0% a steady state at the higher intensity level.

$$DC[\%] = \frac{t_{low}}{t_{cycle}} \times 100 \tag{6.1}$$

The proportional electrovalves allows us to set the velocity and the duty cycle until approximately $60Hz$. Above this frequency the electrovalves overheat and automatically

stop. From the first measurements an unexpected problem arise from the unsteady blowing: the frequency-domain measurements of pressure fluctuation were completely dominated by the effects of the control, screening the power spectra and making useless its analysis. This drawback is critical since it is impossible to trace how the unsteadiness of the wake changes with the fluctuating control. Despite of this, the drag measurements allow us to reach several conclusions about this type of control.

6.2 Pulsed blowing

The first analysis consist in pulsed blowing, i.e. from zero to a certain speed. In this case the maximum blowing speed will be equal to the freestream speed, and the test settled at the typical conditions ($Re = 2.5 \times 10^5$). The results are plotted in a colormap representing the drag variation ΔC_D in function of the duty cycle and the frequency, and for the bottom, top and combined jets.

In figure 6.2 are presented the results for the bottom jet. As expected, the colormap shows towards the 0% duty cycle the values tend to the steady controlled blowing. In general, with the increasing of the duty cycle the drag values drop, specially above 40%, presenting different levels of correlation with the frequency. Over the 30% duty cycle line are present three peaks of low drag, reaching almost the values of the continuous blowing. These peaks are present at 7, 14 and $21Hz$, corresponding almost exactly with the $St = 0.12$ frequency and their second and third harmonics. This results reveals that the vortex shedding on the wake is somehow responding to the pulse actuation, but not significantly enough to improve the drag above the continuous blowing. The fact that the higher peaks coincides with the harmonics of the Strouhal frequency confirms that the response on the drag is due to the interaction with the vortex shedding.

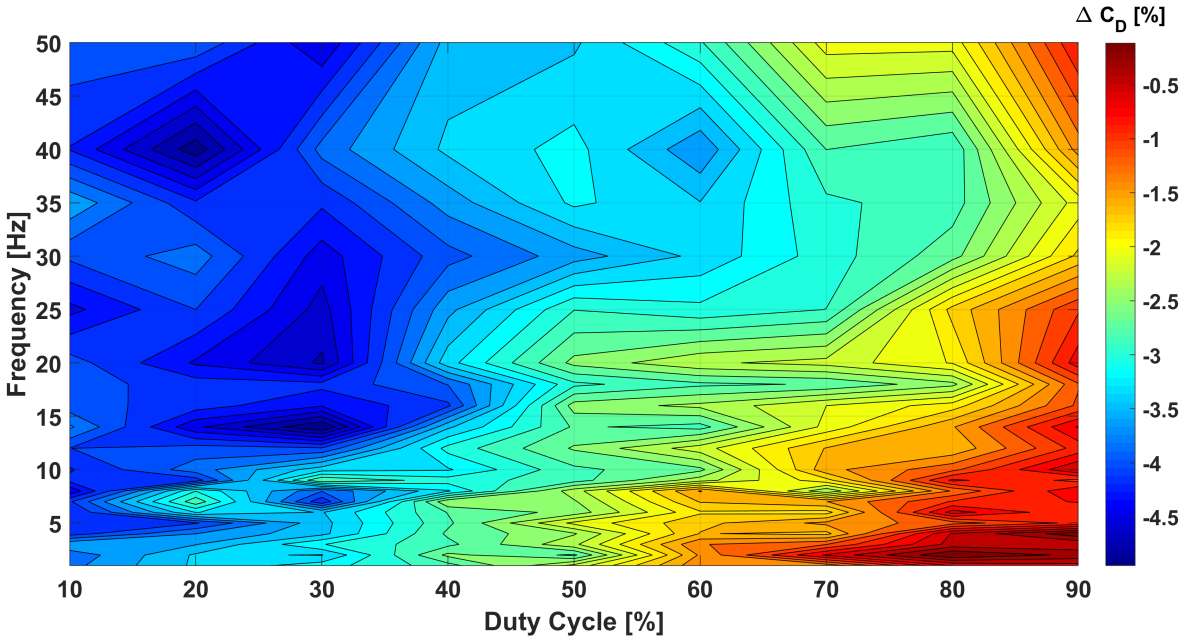

Figure 6.2: Drag variation in function of duty cycle and frequency for the bottom jet.

These results seems to be promising from the energetic point of view, since at duty cycle of 30% the flow introduced is equally lower. Nevertheless, the power loses due

to the unsteadiness of the pneumatic line and the energy needed to feed the valves are not being taking into account and will penalize the energy budget. Barros et al. [14] found also that the wake of a squareback *Ahmed body* respond to the Strouhal frequencies, in this case blowing streamwise on the four trailing edges with a 50% DC square waveform. But the results shows a drag increasing for vortex shedding-related frequencies, actually the drag reduction was reached only in the steady condition and for Strouhal above $St = 4$.
The effects of the unsteady lateral jets are presented in figure 6.3, presenting values of drag reduction way lower than the continuous. Actually, presents a large zone of drag increasing reaching almost 3% for the second and third harmonics of $St = 0.12$. In this case there is no response of the drag to the Strouhal frequencies as in the bottom blowing. It is known from the baseline measures that the dominant vortex shedding happens between the top and bottom trailing edges, being this the reason why the lateral jets do not excite the Strouhal frequencies and the bottom does.

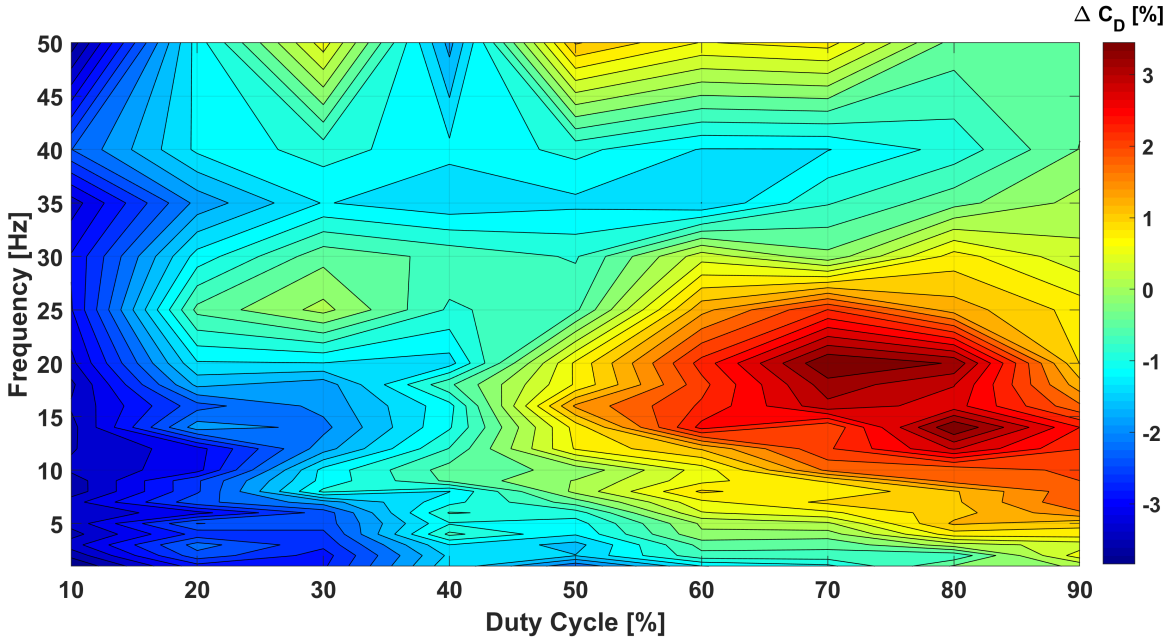

Figure 6.3: Drag variation in function of duty cycle and frequency for the lateral jet.

The effects due to the combination of bottom and lateral jets is presented on figure 6.4. As in the precedent cases, the drag reduction decreases while the duty cycle is increased. This configuration presents a peak of -7.2% of drag variation for 30% DC and $9Hz$ ($St = 0.17$).Regardless the low values, the combined blowing also responds with drag reduction near the Strouhal frequency as for the bottom blowing. This evidence an interaction of the forcing and the vortex shedding, but in a much more subtle way than the bottom jet.

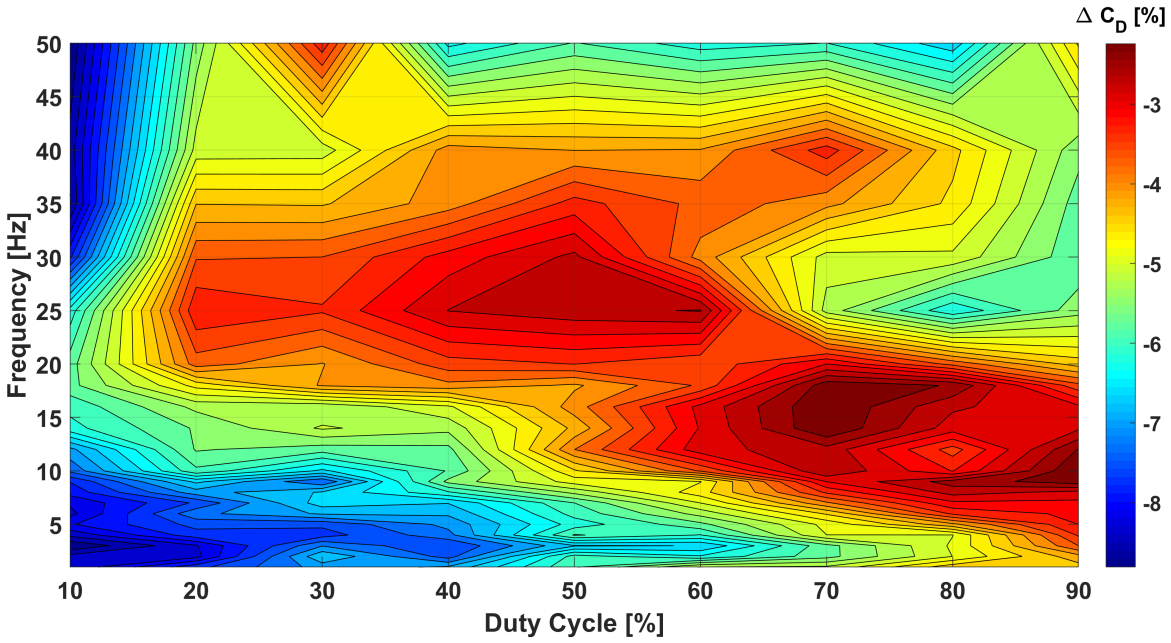

Figure 6.4: Drag variation in function of duty cycle and frequency the lateral and bottom jets.

As seen from the last three figures, the pulsed blowing do not produce drag variations above the values of the continuous flow.

6.3 Fluctuating blowing

In the precedent investigation the lower blowing velocity was zero, but in this new analysis the the maximum and minimum velocities have nonzero values. A new adimensional parameter will be introduced that represents the range between these two velocities, called *Range of forcing* and described in equation 6.2.

$$\Delta = \frac{V_{max} - V_{min}}{V_\infty} \tag{6.2}$$

Together with the Duty Cycle (DC) and the Strouhal value (St), an adimensional value is constructed called the *Control unsteadiness* and presented in equation 6.3.

$$ControlUnsteadiness = \frac{DC \times St}{\Delta} \tag{6.3}$$

This parameter represents the intensity of fluctuation of the control as a function of the range of blowing: values tending to zero represent a steady blowing, and rising values evidence the increment of the forcing unsteadiness. This value will be used to represent the control evolution on the drag variation. Finally, the mean value of the blowing velocity for the test will be always the freestream speed.

In figure 6.5 are presented the results of the drag variation produced by the bottom jet in function of the control unsteadiness. It is clearly observed that the increase unsteadiness reduces the efficiency of the control in terms of drag reduction. Following the trends of the different Δ is seen that there is a common trend for all of them: the values rise rapidly to a minimum for the first values of control unsteadiness and then

recovers until an asymptotic stabilization at around -2.5% ΔC_D. This initial "jump" to the minimum drag reduction values seem to be damped for smaller Δ. This might be explained by the reduced range of the jets, reducing the influence over the vortex shedding of the wake.

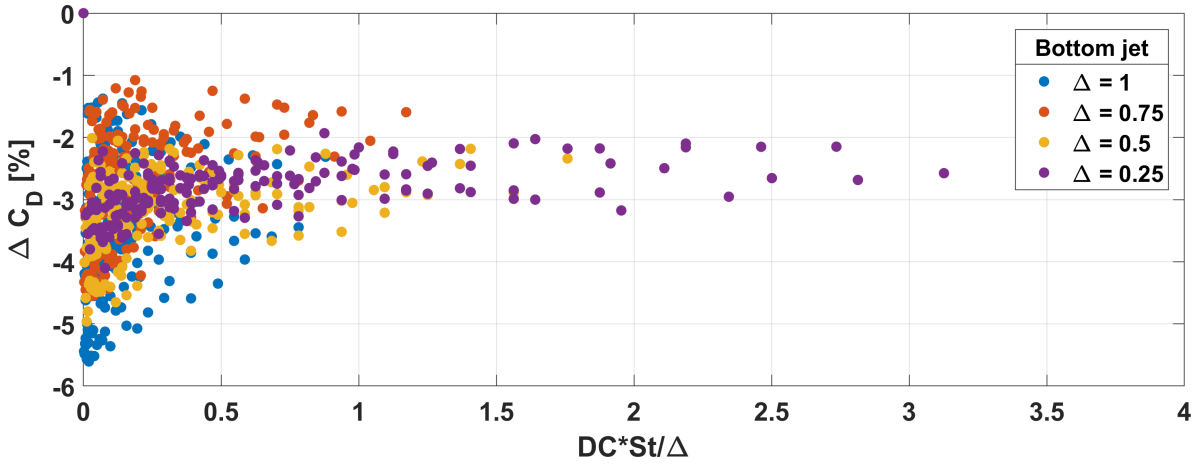

Figure 6.5: Drag variation regarding the control unsteadiness for the bottom jet.

The results of the lateral jets are observed in figure 6.6, and the trends previously evidenced are much more clearly defined but in this case reaching an asymptotic value of drag reduction around 4%. This evidence a smaller sensibility to the unsteady control regarding the bottom jet. Nevertheless, the peaks of drag variation in this case reaches drag increasing of 2%, showing a high loss in the blowing efficiency specially for $\Delta = 1$. For the lower value of Δ, the drag variation is almost independent of the control unsteadiness.

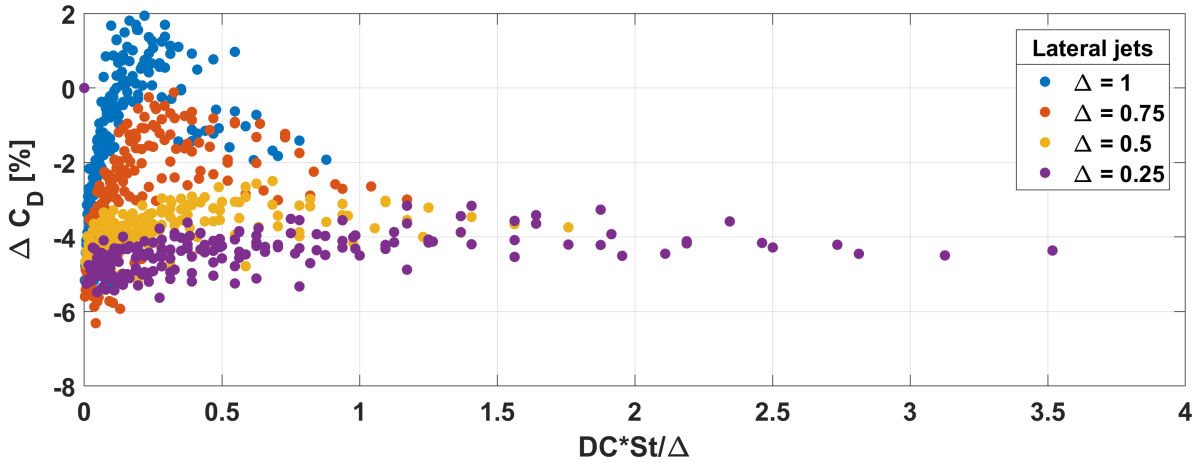

Figure 6.6: Drag variation regarding the control unsteadiness for the lateral jet.

Finally, the combined bottom and lateral blowing are presented in figure 6.7 for only two values of Δ: 1 and 0.5. As in the lateral jets, the characteristic trends are clearly visible resembling the results of the lateral jets. The asymptotic value in this case is about 6% of drag reduction with the minimum drag reduction peak reaching 2%. In this combined case the drag values never reach a drag increasing, but the minimum value suffers a drop of 8% as in the lateral case.

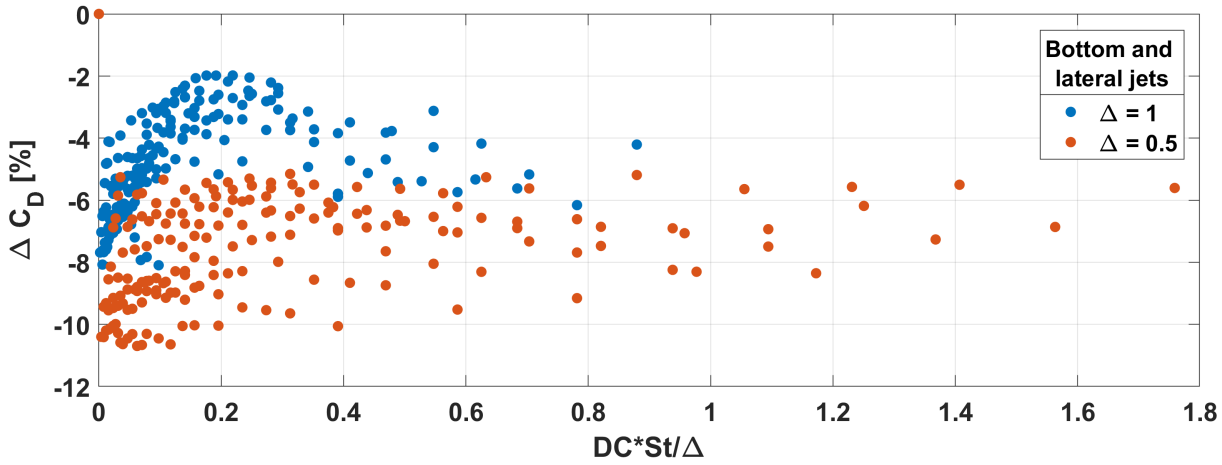

Figure 6.7: Drag variation regarding the control unsteadiness for the bottom and lateral jets.

As in the precedent pulsed case all configurations of the fluctuating blowing evidence a descent in the drag reduction capabilities regarding the steady blowing case while increasing the unsteadiness.

Chapter 7: Platooning

The increasing necessity of improving fuel consumption of vehicles, in particular those traveling for long distances and relatively high velocity, re-emerged the old concept of platooning. In this chapter our model will be tested in two, three and four vehicles convoy configurations. For the two-vehicle platoon the survey covers drag variation, pressure distribution and flowfield; while for the three and four-vehicle only the drag variation will be analyzed. Using these last results, an extrapolation is obtained that allows calculating the efficiency of a n-vehicle platoon.

7.1 Test conditions

The test conditions used were the same than the precedent cases ($Re = 2.5 \times 10^5$), but due to the nature of the configurations being tested the boundary layer suction had to be turned off. The main reason behind this is the different effect of suction over the possible positions, since the boundary layer control is fixed ahead the instrumented model. It is known that the lack of boundary layer control may variate the drag coefficient over the vehicles. Consequently, measurements were performed with and without boundary layer control evidencing a difference on the C_{D_0} below 2% in all cases. Furthermore, the variations of drag will be always expressed in drag variation (ΔC_D), reducing even further the influence of this effect.
Since there is only one instrumented model which concentrates all sensors and actuators, each position on the platooning configuration need to be specially settled up surrounding the instrumented model. This limits the extent of the platoon due to the dimensions of the test chamber. Nevertheless these limitations, the range of measurements available allow obtaining a sufficiently detailed picture of the platooning effects.

7.2 Two vehicle platoon

Using one of the "dummy" wooden models with a $1Kg$ counterweight inside, the different configurations of a two-vehicle platoon were reproduced and measured. The distances taken were refereed to the length of the model L, using 0.125 fractions for the range $0.125 < d/L < 0.75$ and 0.5 for $1 < d/L < 1$, ending with a final measure at $d/L = 3$. The maximum distance was given by the dimensions of the test chamber while the minimum was chosen large enough to allow some level of PIV visualizations. The results in terms of drag variation for the two vehicles are presented in figure 7.1 along with a sketch of the relative models' positions. In dashed line is represented

the *Overall Drag Variation* (*Overall* ΔC_D), representing the average ΔC_D of the n components of the platoon, expressed as (equation 7.1):

$$Overall \Delta C_D = \frac{\sum_{i=1}^{n} \Delta C_{D_i}(d/L)}{n} \tag{7.1}$$

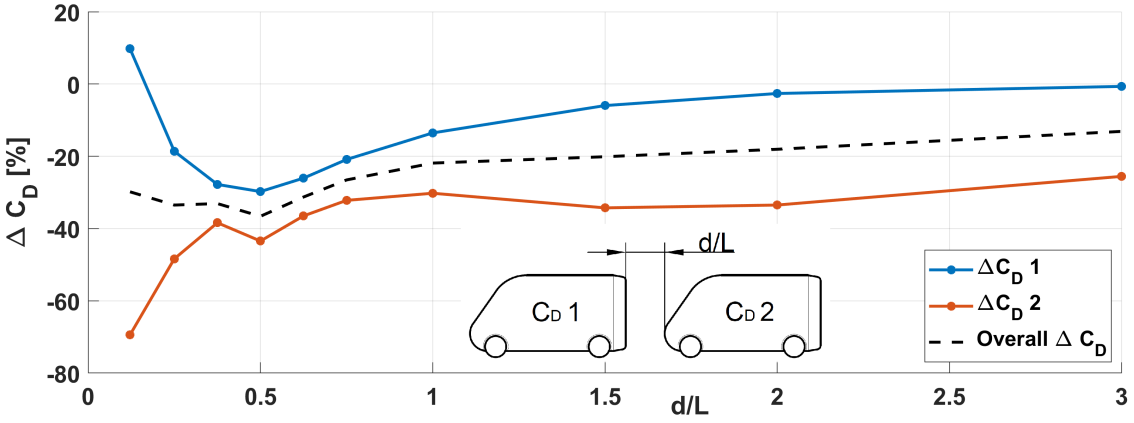

Figure 7.1: Drag variation on the platooning of two vehicles in function of d/L.

Beginning with the front vehicle (blue line in figure 7.1) it is clear that the influence of the rear vehicle on the drag begins at $d/L \approx 2$. For closing distances the drag begins to drop progressively until a minimum of 30% at $d/L = 0.5$, and then rises to 10% for $d/L = 0.125$. The reduction of the drag while the vehicle is approaching can be explained by the increasing back pressure product of the presence of the rear vehicle until $d/L = 0.5$. Below this distance the drag recovery and successive increasing is associated to the flowfield developed in between the models, as will be shown in the pressure distributions and flow visualizations.
The rear vehicle (red line in figure 7.1) displays a drag reduction of 23% for $d/L = 3$, further decreasing until 35% at $d/L = 2$. Below this distance and until $d/L = 0.75$ there is a stabilization of the drag reduction values with a slight drag recovery at $d/L = 1$. Beneath $d/L = 0.75$ the drag drops again to a local minimum of 42% at $d/L = 0.5$, then presents a slight drag recover and successively falls to 70% at $d/L = 0.125$. Most probably the drag reductions in the $1 < d/L < 3$ range are product of the dynamic pressure deficit produced by the front vehicle's wake, that begins to fade above $d/L = 2$. For distances closer to $d/L = 1$ the interaction with the front vehicle's near wake became dominant, increasing the drag reduction. In particular, the tendency of the drag variation for distances closer than $d/L = 0.5$ is the opposite that the front vehicle, evidencing that the rear drag savings are being "paid" by the front vehicle.
Now is considered the overall ΔC_D (dashed line), presenting an almost linear drop from $d/L = 3$ to $d/L = 1$ reaching $\approx 20\%$ of overall ΔC_D, and increasing the descending tendency from $0.5 < d/L < 1$. This last evidences again the near wake's effect over the drag. After $d/L = 0.5$ the overall ΔC_D stabilizes around 35%, highlighting the trade-off between the growing drag of the front vehicle and the reducing of the rear exposed before.

The beneficial effects of the platooning configuration have been demonstrated in many papers considering also different shapes of vehicles. It is interesting to compare some representative results of the literature to extract some common features

whichever is the shape used. In figure 7.2 are presented some of the most salient studies for bluff bodies similar to ours in two-vehicle platoon configuration, expressing the distance in vehicle lengths (d/L) and the C_D/C_{D_0} ratio for the front and rear vehicles regarding the isolated case. The data was extracted from the studies of Romberg et al. [95] using a Nascar model, Zabat et al. [126] using a van model and Pagliarella et al. [86] and Watkins and Vino [120] both using *Ahmed bodies*. The main characteristics of each test are resumed in table 7.1.

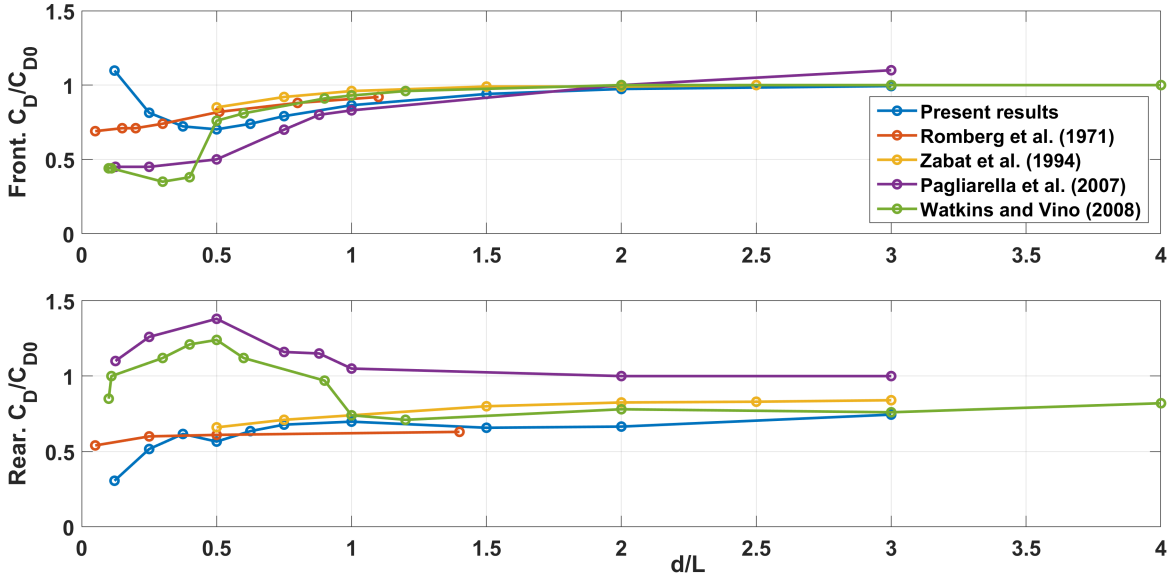

Figure 7.2: Drag variation comparison for a two vehicle's platoon of different authors.

Authors	Model	Reynolds	BL Control
Romberg et al. [95]	3:8 Nascar	–	Individual ground panels
Zabat et al. [126]	1:8 Squareback van	$3-4\times10^5$	Hollowed floor w./suction
Pagliarella et al. [86]	3:4 Ahmed body	1.85×10^6	No
Watkins and Vino [120]	1:1 Ahmed body	2.3×10^6	No
Present results	1:10 Van model	2.5×10^5	No

Table 7.1: Characteristic of the different two-model platoon tests considered.

For the front vehicle and distances above $d/L = 0.5$ the results collapse in an almost unique curve, evidencing independence from the model's shape. Below this distance the shape of the body becomes relevant showing different trends for all cases analyzed. The results of Pagliarella et al. [86] and Watkins and Vino [120] evidence similar values, way below the present results and those from Romberg et al. [95], demonstrating that the a slanted rear produces higher benefits regarding the other configurations. Unfortunately, the test of Zabat et al. [126] reached only $d/L = 0.5$ an therefore cannot be compared.
For the rear vehicle and $d/L > 1$ the drag variation seems roughly independent from the shape of the vehicle, similarly to the front. The only results that differs regarding the rest is the one of [86] showing an increase of the drag instead a reduction. We decide to discard this results because differs even for the studies of [120], that use the same model. Below $d/L = 1$ the shape of the model begins to affect the result,

most probably because of the interaction with the front model's near wake. While Zabat et al. [126], Romberg et al. [95] and the present results reduce the drag with the approaching, [120] evidence an increasing. Again, seems like the slanted rear *Ahmed body* produces a largely different interaction in between the bodies.
It is clear that the platooning report benefits regarding the isolated driving independently from the vehicle's shape if the distances are above one vehicle length. Below this following distance the slanted-rear *Ahmed bodies* present marked differences regarding the other models, further dropping the drag values for the front and increasing the drag for the rear. The squareback instead, shows a more stable drag variation trend in both front and rear C_D variations highlighting some deviations for the closest distances of Our results, that could be justified by the slanted front. Finally, the results demonstrate that boundary layer effect plays a secondary role on the drag variations. Both cases presenting some kind of boundary layer control seem to have a slightly smaller drag variations, but these differences are not consistent enough to evidence a boundary layer effect.

7.2.1 Pressure distribution

The analysis of the pressure distribution around the model can help interpreting the results of the drag variation. In sake of simplicity only three characteristic points will be analyzed: $d/L = 3$, 0.5 , 0.125, corresponding with an overall drag variation of $17\%; 22\%; 30\%$, and fo the front and rear positions. This three points represent the far-following condition, the minimum Overall ΔC_D and the closer case.

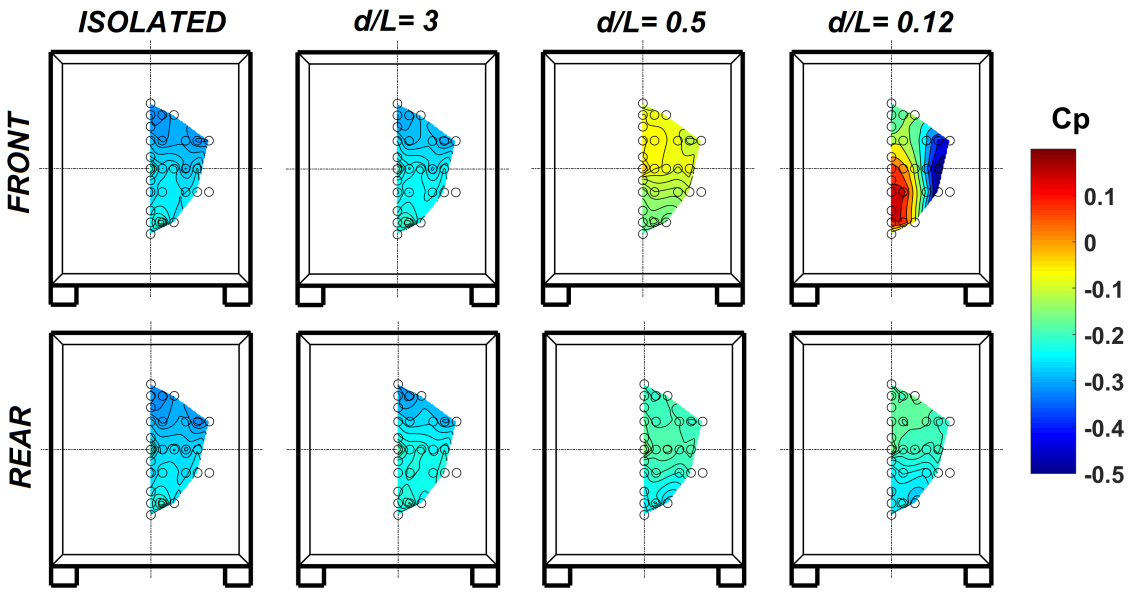

Figure 7.3: Pressure coefficient distribution on the rear parts of the front and rear vehicles.

In figure 7.3 are represented the C_p distribution of the rear base for the front and rear vehicles in the previously defined positions. The baseline distribution is also presented as a reference. Considering the front vehicle the corresponding pressure distributions are shown in the first row of 7.3. For distance $d/L = 3$ the pressure coefficient distribution closely resembles the natural case one. At $d/L = 0.5$ the pressure coefficient distribution shows a switch in the pressure gradient direction, which

is directed upwards. Furthermore, a more significant pressure recovery is experienced in this case, with the C_p attaining values in the range $-0.15 < C_p < -0.05$. For $d/L = 0.125$ the pressure coefficient distribution shows a complex distribution characterized by regions with peaks of positive and negative values. In particular a high-pressure recovery zone on the center of the base and a low-pressure on the lateral edge are present, originating intense lateral pressure gradients. This result is in agreement with Fletcher and Stewart [53]. They showed that, in the case of squared-front and rear vehicles, small distances between the vehicles prompt a recirculating-flow region within the two models, increasing the pressure coefficient on both rear and front vehicles. The rear vehicle, in the second row of figure 7.3, evidence no significant change on the rear C_p distribution. Only a slight pressure coefficient recovery is observed for $d/L = 0.5; 0.125$ of $C_p \approx -0.15$. The pressure coefficient distributions for the rest of the model are shown in figure 7.4 for the same precedent positions. The first column represents the front vehicle and the second the following. Considering the rear vehicle, the pressure coefficient distribution at $d/L = 3$ reveals a reduction of the C_p values on the front, reaching almost 50% of the natural case value. There is an increase of the C_p on the roof of the model, and also an increase of the low pressure C_p zone on the side of the model of almost 50% respect to the natural case. The rest of the distribution remains almost equal to the natural case. When approaching the front vehicle, the distribution changes severely. At $d/L = 0.5$ the C_p distributions on the front part reach almost the zero value and significant increasing on the top part is also achieved. The lateral part seems to be less affected than the rest, only evidencing a reduction near the rear part and also a reduction of the A-pillar effect. Lastly, the position $d/L = 0.125$ exhibits a particular C_p distribution. On the front part, the C_p changes the sign becoming negative, and the rest of the distribution resembles the former one. The lateral pressure distribution shows no evidence of the presence of the A-Pillar vortex. This drastic modification is due to the very nearness the wake that wraps completely the vehicle behind. The C_p distribution of the front model shown in figure 7.4 does not evidence significant changes, only a small trace of increasing pressure on the top rear-end for the closest case. The rear part evidence relevant changes, as already observed in figure 7.3.

As seen, the pressure distribution proves that the drag reductions observed for the front model is only a product of the increasing base pressure, while for the rear vehicle the major effect is the reduction of the incoming dynamic pressure product of the front vehicle's wake. The closest position ($d/L = 0.125$) shows an interesting interaction between the front model rear base and the rear model's front, thus producing a strong reduction of the rear vehicle's drag and an increase on the front. The next section will share some light over this particular phenomenon.

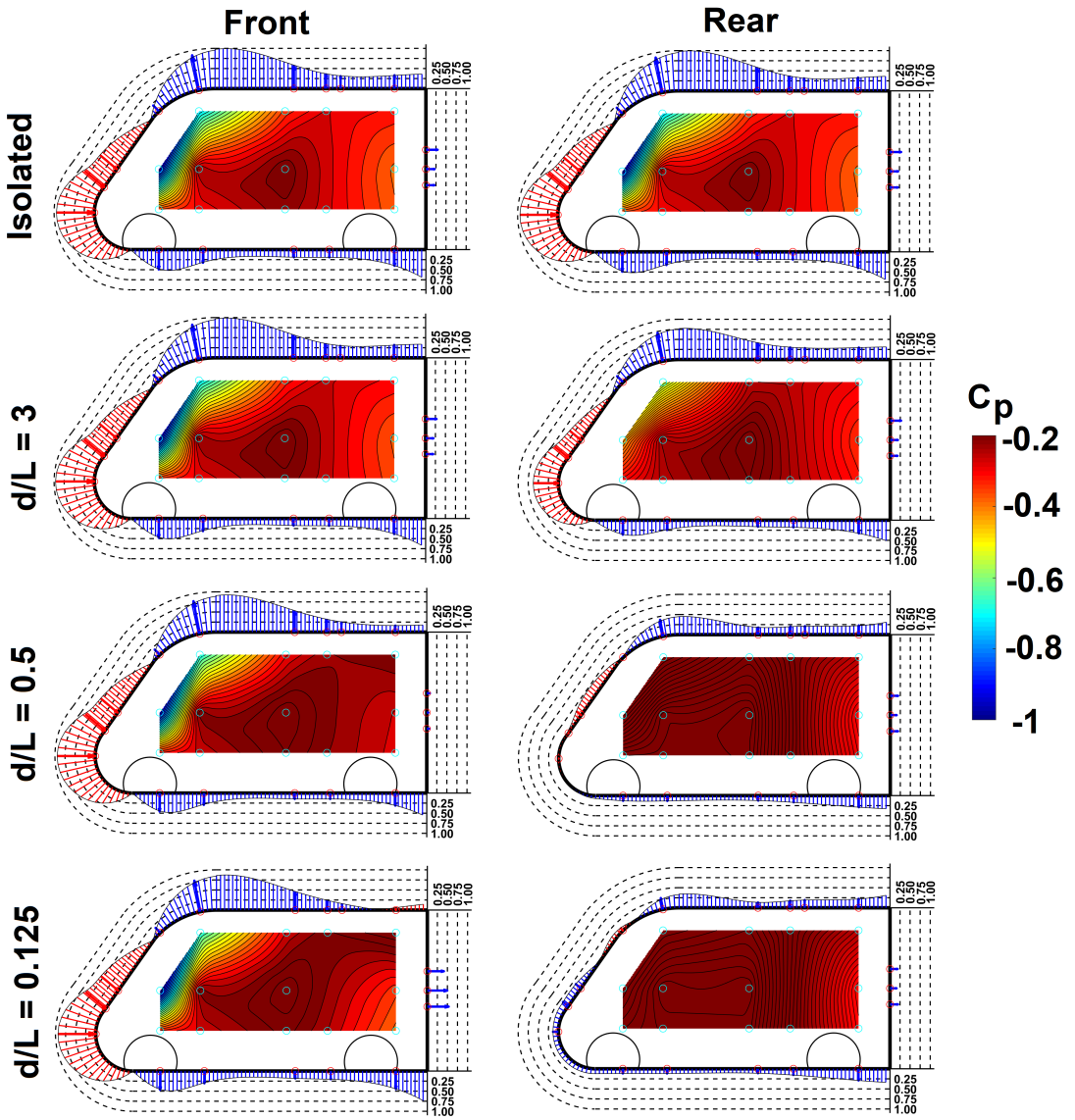

Figure 7.4: Pressure coefficient distribution on the side part of the front and rear vehicles.

7.2.2 PIV

The flowfield analysis of the platoon configuration was analyzed only in the XY plane (symmetry plane) by 2D2C PIV. This choice was motivated by the optical limitations presented by the two bodies configuration. Despite this drawback, the symmetry plane presents interesting characteristics as the asymmetry of the near wake, the counter rotating vortexes and underflow, that may bring light to the interaction between bodies and flow. In addition, the slanted front part of the model is a characteristic of the symmetry plane, thus allowing the analysis of geometry. The results for the front model's wake is presented in figure 7.5 while for the rear in figure 7.6, and in both cases the baseline (Isolated) case is showed as a reference.
Beginning with the front vehicle in figure 7.5 the $d/L = 3$ position, as expected, is quite similar to the isolated case. When the rear model approaches at $d/L = 0.5$ the lower vortex becomes dominant pushing the impingement and saddle points towards upper positions. In addition, the underflow of the body shows and upstream tendency,

following the trend of the near wake.

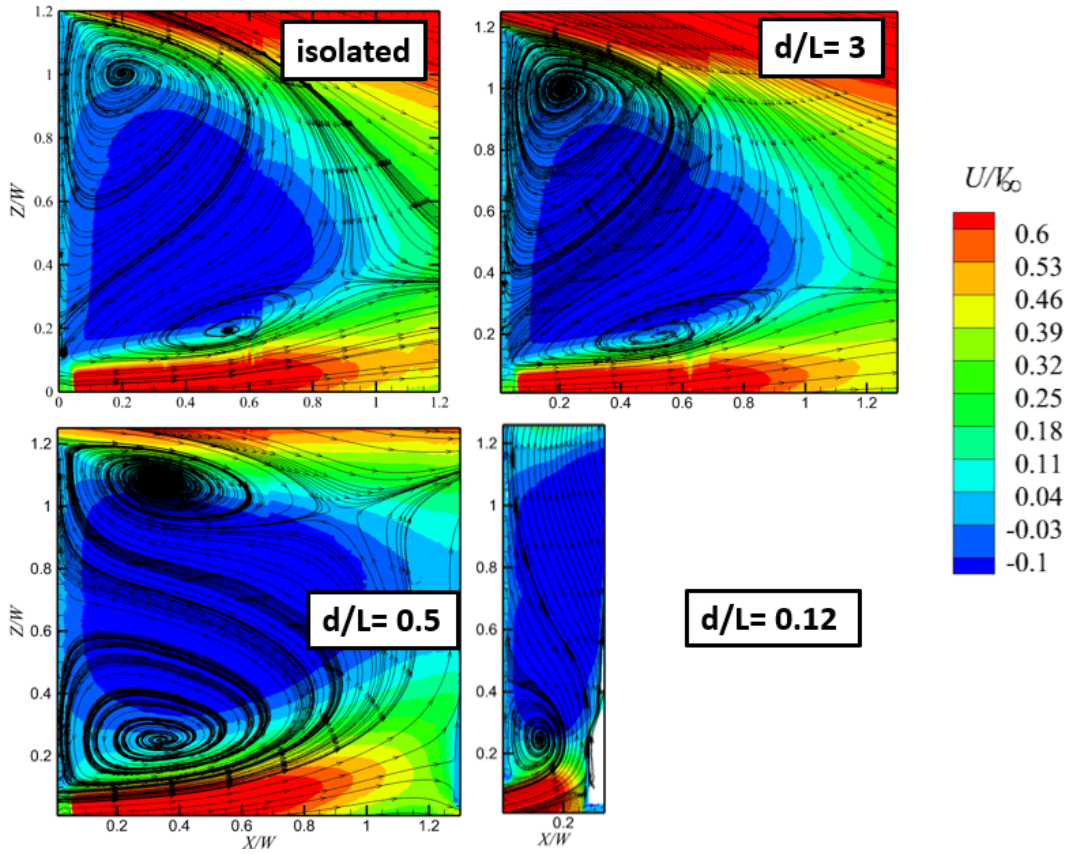

Figure 7.5: 2D2C PIV on the front model's wake.

The closer distance ($d/L = 0.125$) has a reduced field of view due to the presence of the following model that screens the laser. Still, the remaining field allows us to obtain some conclusions. The lower vortex is clearly seen, evidencing a significant reduction and being "trapped" in between the nose from the rear vehicle and the base of the front. Is also observed that the underflow points upwards, energizing this vortex. On the top part are seen the traces of a dominant vortex, settled in the remaining space between the rear model's slanted front and the front model's base.
Figure 7.6 presents for $d/L = 3$ a more symmetric wake and slightly higher impingement and saddle points, with a lower vortex closer to the rear base and reduced underflow velocity. For $d/L = 0.5$ the wake is completely different, with a even smaller lower vortex attached to the model's base and noticeably reduced underflow. The top vortex is now dominant, pushing the saddle point near the floor and further rising the stagnation point on the rear base. Finally, at $d/L = 0.125$ the wakes switches to the opposite position, with the saddle and stagnation points on the upper part, dominant bottom vortex and a secondary vortex near the ground downstream the model. A slight recovery of the underflow is also observed. The PIV visualizations presented evidenced a high correlation with the precedent C_p measurements. The trend of the front vehicle's wake explains the reduction on the dynamic pressure on the rear one. Moreover, the inversion of the C_p in the front of the rear model observed in figure 7.4 for the closer distance, is probably generated by the trapped vortex on the lower part. In the rear model's wake, the movement towards upper positions of the stagnation point resembles the pressure distribution changes.

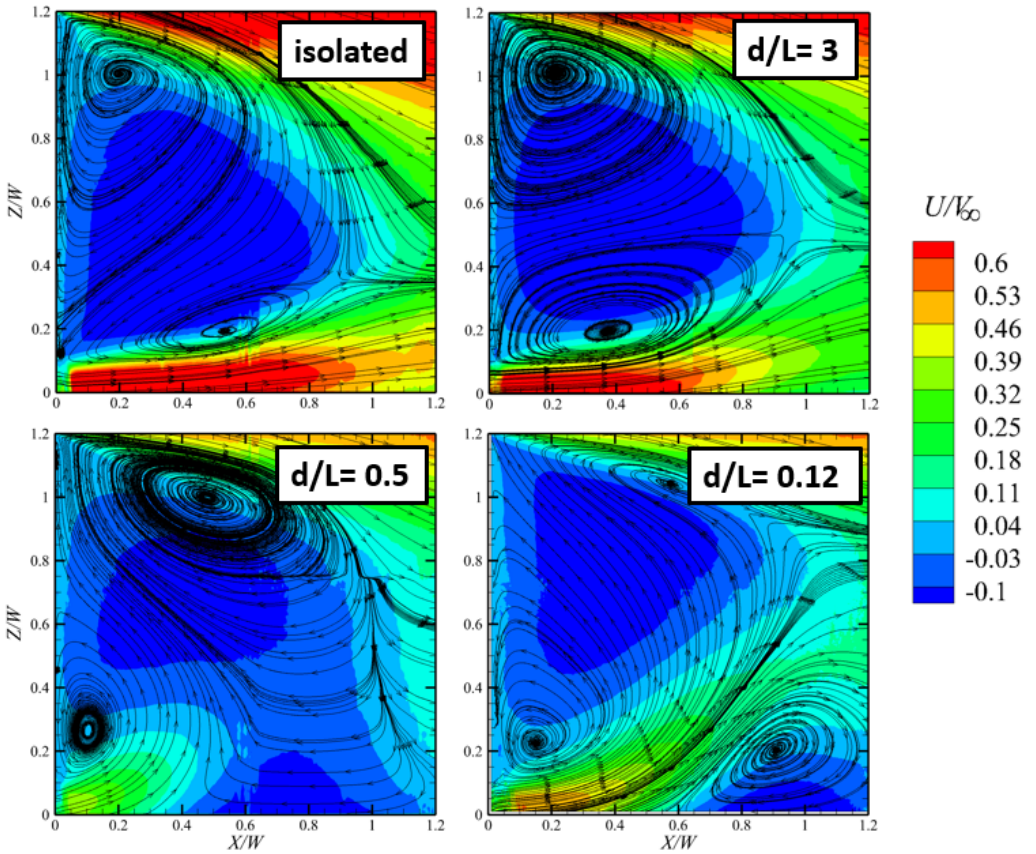

Figure 7.6: 2D2C PIV on the rear model's wake.

7.2.3 Spectral analysis

In figures 7.7 and 7.8 are presented the PSD of the characteristic microphones presented in figure 4.8, for the front and rear models.

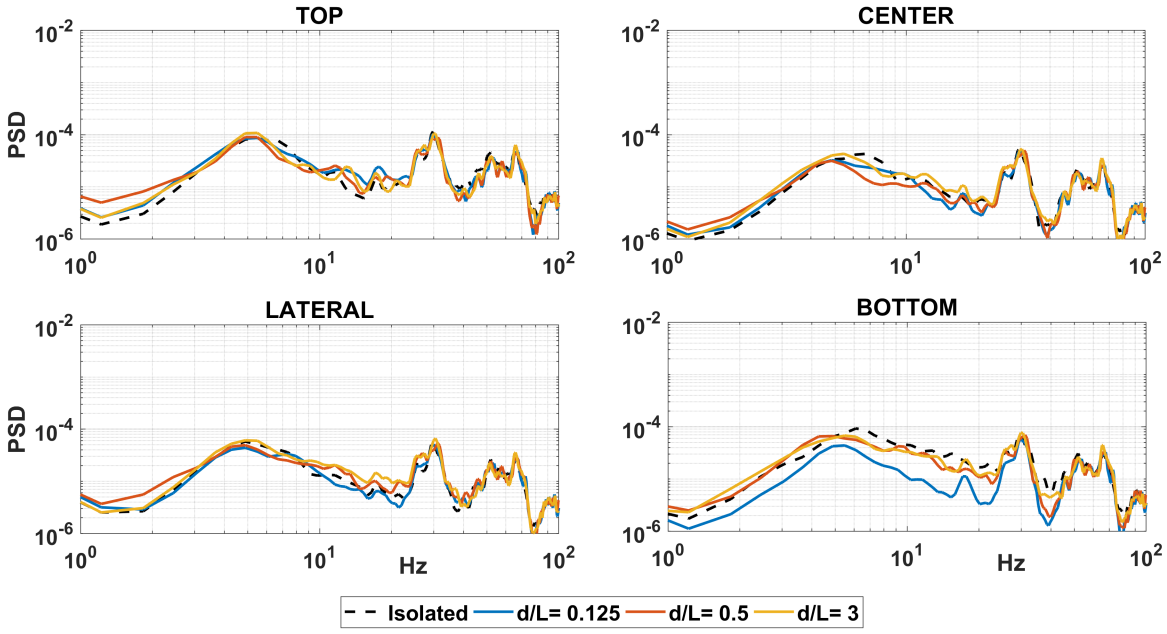

Figure 7.7: PSD of the characteristic microphones' signals of the rear vehicle.

In figure 7.7 the PSD on the rear model do not evidence significant variations of the distributions, just a reduction of the general fluctuations on the bottom for the bottom microphone at $d/L = 0.12$. The front vehicle instead evidence an increasing of the fluctuations when the vehicles approach, as shown in figure 7.8. This increment is noticeable only for distances closer than $d/L = 0.5$, being noticeable higher for $d/L = 0.12$. This general increasing do not show any particular variation on the vortex shedding, but it does show further increasing for the higher frequencies (above the Strouhal). This is associated to the fluctuations triggered in between the models, that grows when approaching. The increasing at lower frequencies near to zero is associated to the increasing of the rear base pressure.

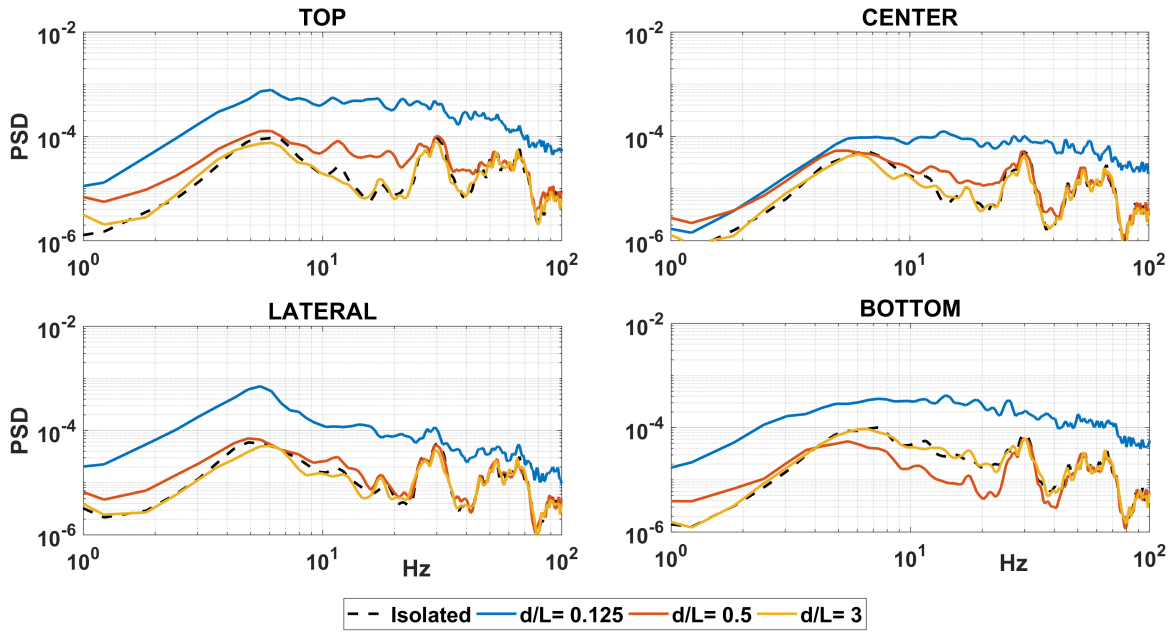

Figure 7.8: PSD of the characteristic microphones' signals of the front vehicle.

7.2.4 POD

The relative energy from the POD of the microphones' signals is presented in figure 7.9 for the front ad rear vehicles in the positions previously analyzed.

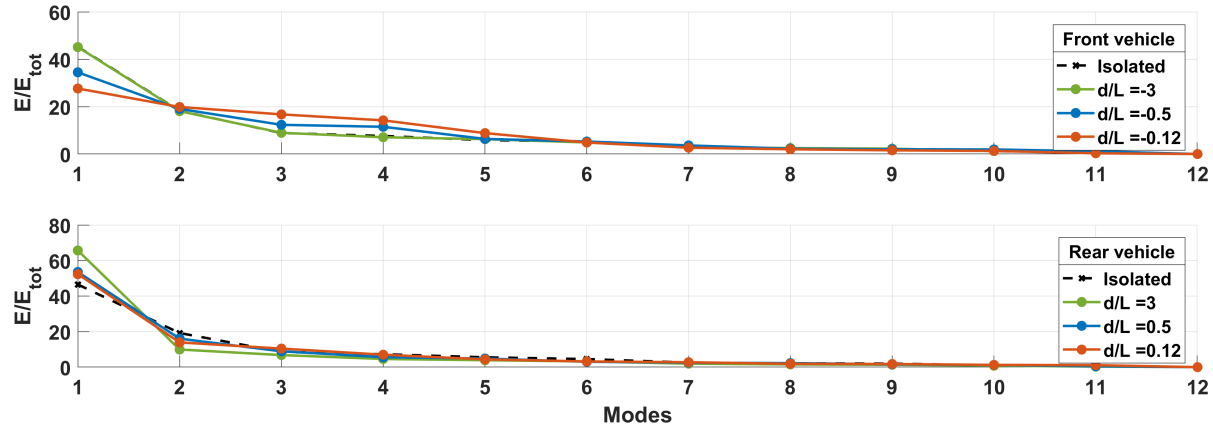

Figure 7.9: Relative energy of the POD for the front and rear models.

For the front vehicle is observed that the relevant modes are the first four, reducing

the first mode and increasing the third and fourth when approaching the vehicles. This rise on the higher modes energy may be product of the increasing fluctuations trapped in between the models.

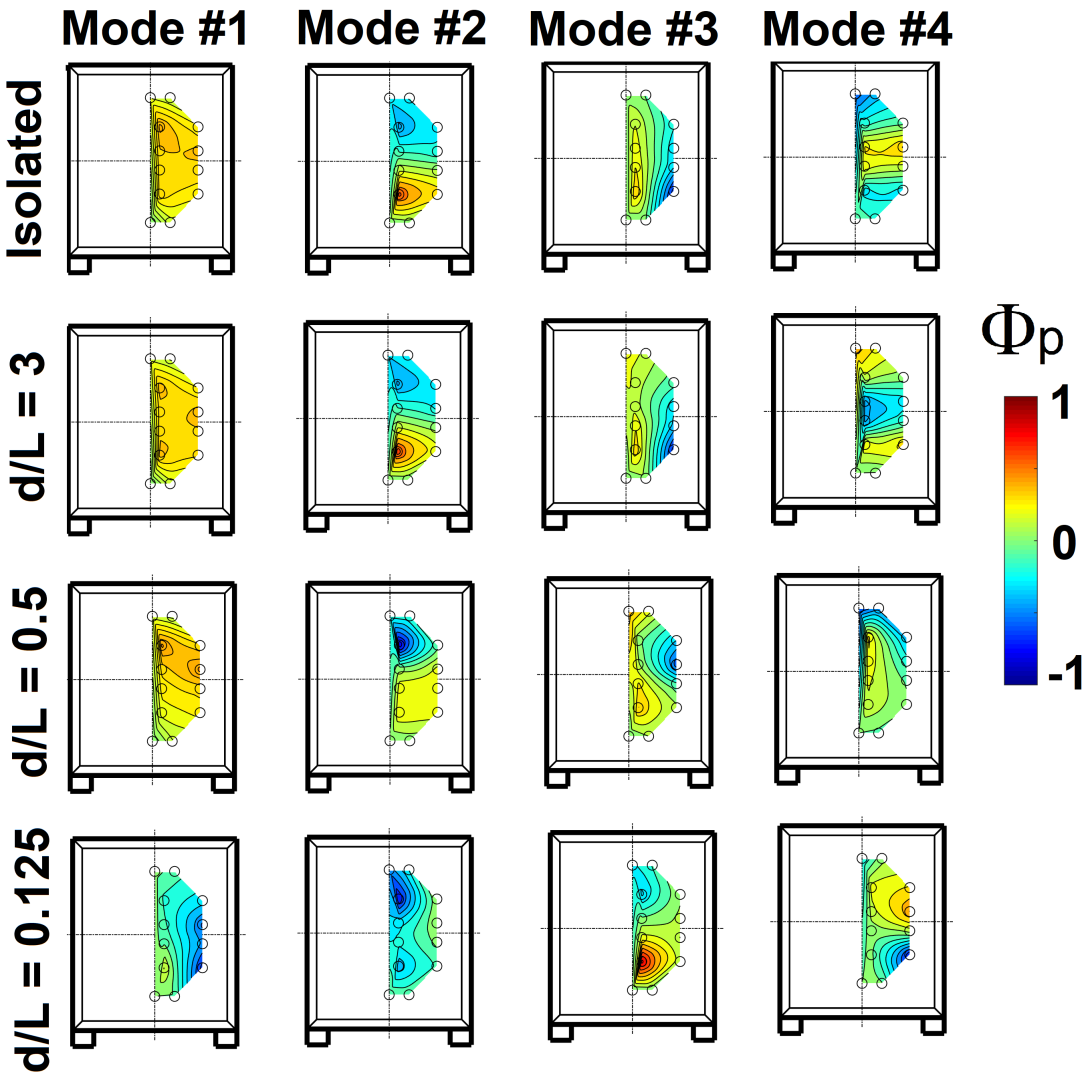

Figure 7.10: POD of the front's model base microphones' signals for the platooning cases.

For the rear vehicle, the trends are irregular, showing an increasing of the first mode's energy when approaching. Opposite to the precedent case, the higher modes seems to loss energy. As in the baseline and controlled cases, the POD modes on the rear base are extracted from the signals of the microphones and shown in figure 7.10 for the front vehicle and figure 7.11 for the rear. The isolated POD modes are also shown as a reference.

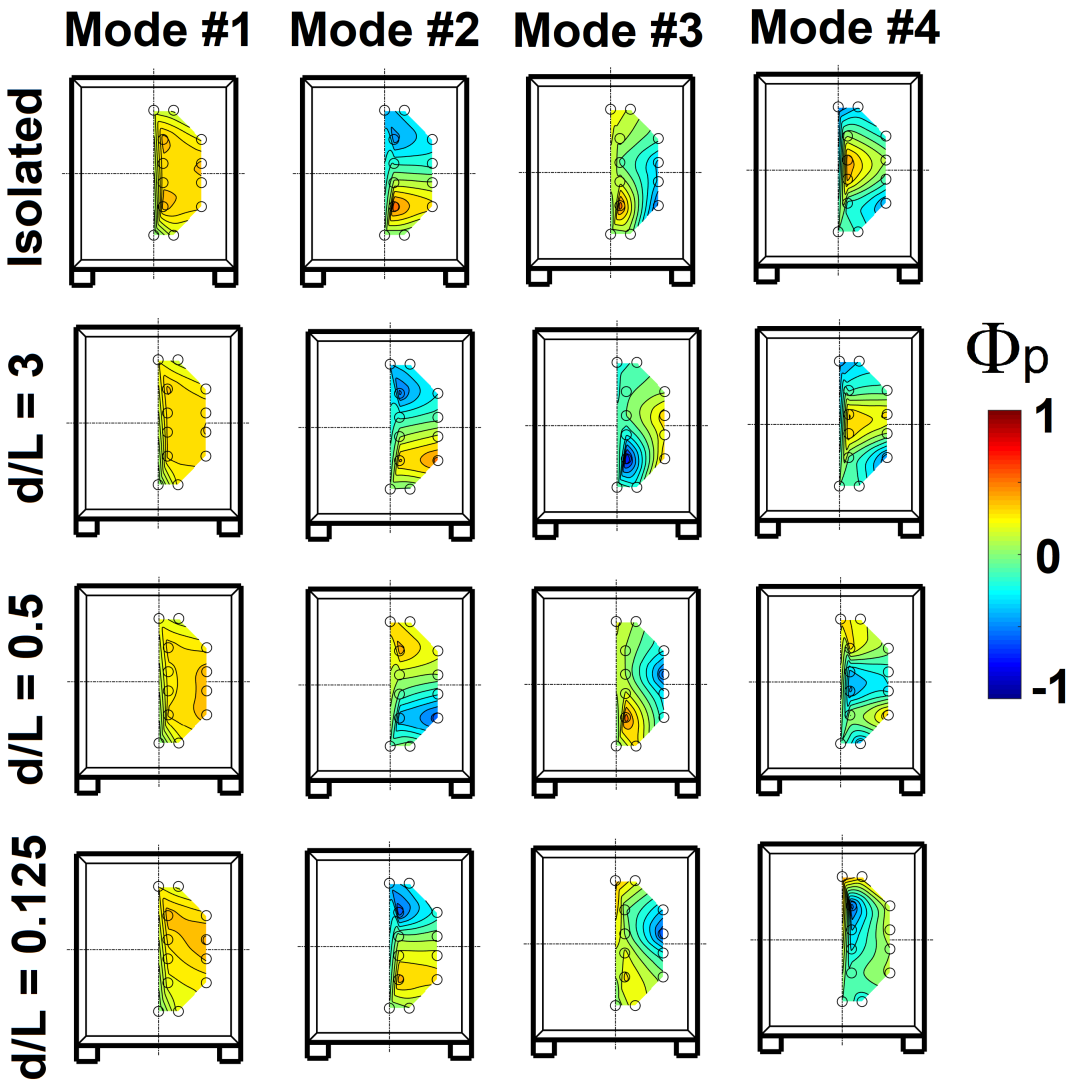

Figure 7.11: POD of the rear's model base microphones' signals for the platooning cases.

For $d/L = 3$ there is no change in the modes regarding the isolated vehicle. At $d/L = 0.5$ some changes are observed. The first mode looses his uniformity, showing higher values towards the upper part. The second and third modes are somehow faded, yet retaining theirs general shape. The most important changes are on the fourth mode, that now resembles a lateral symmetry-breaking mode as the third. for the $d/L = 0.125$ position the changes are severe. Now the first mode is lateral symmetry-breaking, followed by an fluctuation concentrated on the top part as a second mode. The vortex shedding now is represented by the third mode and the fourth evidences an regular oscillation over the side on the vertical direction. The front vehicle's modes evidence a modification when the models approach highlighting a dominant lateral mode for the closest case, in agreement with the observations of the C_p distributions (see figure 7.3). Furthermore, the mode representing the vortex shedding is always present but with modifications on his relative energy. Different from the precedent case, the rear vehicle shows much more stable modes. In fact, only the closer distance shows significant variations on the fourth mode. This indicates that the fluctuating structures remain merely the same.

7.3 Three and four vehicles platoon

Using the remaining two dummy models available the configurations of three and four vehicles in convoy were characterized. Due to the complexity of the vehicles' array no PIV were performed. By settling the dummy models ahead and behind the instrumented model, each position of the platoon was characterized and the results for the three and four vehicles platoon are shown in figure 7.12.

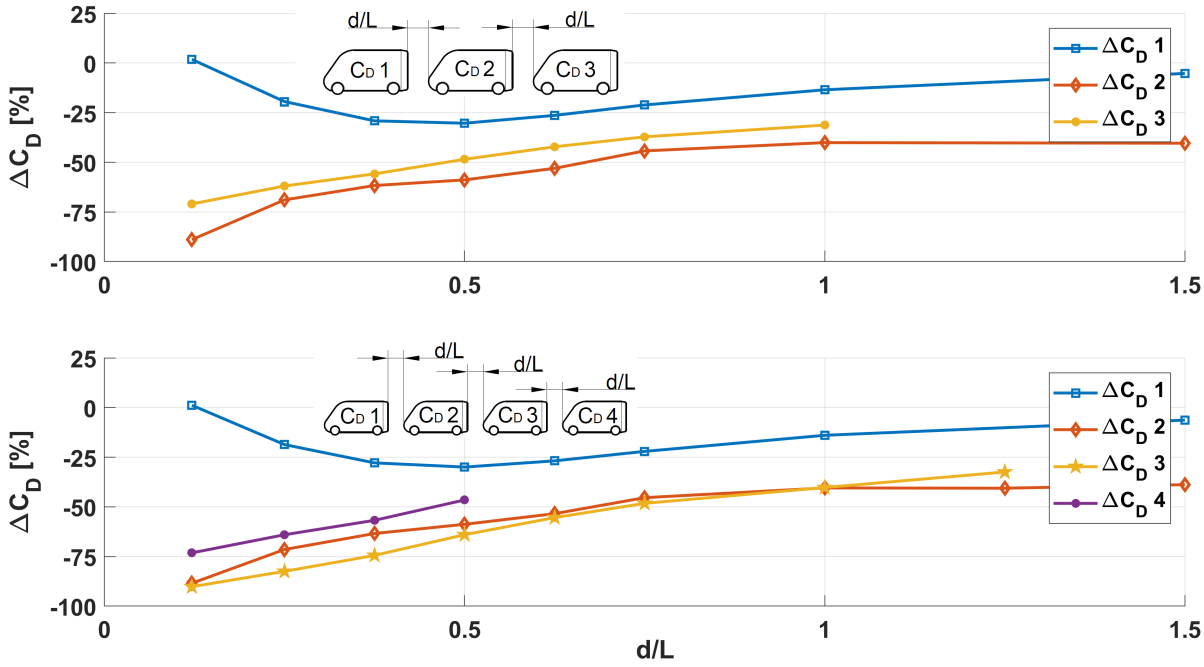

Figure 7.12: Drag variation on platooning of three and four vehicles.

The first observation for both plots is that the last vehicles of the platoon have less measures than the front. This is due to the fact that the available space ahead the instrumented model is limited. Observing the three-vehicle platoon results, the front vehicle (blue line) evidence a very similar trend regarding the two vehicle platoon. The differences begin with the middle and tail vehicles: The tail vehicle presents an almost linear decrease with the approaching, reaching drag reductions of $\approx 70\%$ at $d/L = 0.125$. This tendency demonstrates an enhancing of the drag reduction capabilities regarding the two-vehicle platoon, most probably due to the large low-pressure zone behind the two vehicles ahead. The middle vehicle exhibit the best drag reduction of the whole convoy. This was expected, since the middle position profits the low-pressure behind the leading vehicle and the increased pressure on the rear due to the presence of the following vehicle. The tendency of the drag with the approaching is similar to the rear vehicle, but in this case shifted to a lower drag position and reaching 90% of drag reduction for $d/L = 0.125$.
Considering now the four vehicle platoon, the front vehicle presents the same values of the precedent case, demonstrating that the front position's drag trend is independent of the number of vehicles behind. Furthermore, the two middle vehicles have almost the same distribution of drag reduction values, with only slight differences on $0.25 < d/L < 0.375$. Finally the tail vehicle only presents 4 measurements of the drag between $0.125 < d/L < 0.5$, but the trend is the same observed on the previous case.

As seen from the two precedent cases, there are some aspects of the more-than-two vehicle platooning that can be extracted. The first are the three characteristic positions, being those front, middle and tail. The front vehicle exhibit the same behavior and the tail as well for the two convoys. There are some differences on the middle vehicle, but the order of magnitude of the drag reduction is the same. This points to a repeatability of the results which allows us to make an estimation of the behavior of larger convoys, that will be explained in the next section.

7.3.1 N-vehicle extrapolation

Zabat et al. [126] developed an overall drag variation law for n-vehicle platoon, considering the addition of a certain amount of drag for each vehicle joining the convoy for $d/L < 1$ space. This estimation is very straightforward, but we consider that there is room for some improvements.

Considering the data from the front, middle and tail vehicles of all platooning configurations reported in figure 7.12, is possible to interpolate the results with three curves that represent these three characteristic positions of the platoon. This three curves, are obtained through a "spline" interpolation performed on *MatLab*, using the function *fit()*, with "smoothing spline" algorithm, and plotted in figure 7.13a. For the following vehicles (middle and tail) there is no enough data to reach the isolated values as in the front one. A good compromise is to consider that the front vehicles has no effects from $d/L = 5$ and on, agreeing with the largest distance analyzed in [120]. Moreover, the tendency to the isolated case should be asymptotic. Thus was reached by imposing the null derivate al $d/L = 5$. By using this three interpolations the overall drag variation can be extrapolated for a growing number of elements of the platoon for the different distances as described by equation 7.2.

$$Overall\Delta C_D(d/L, n_m) = \frac{\Delta C_{D_{Front}}(d/L) + \Delta C_{D_{Tail}}(d/L) + n_m \times \Delta C_{D_{Middle}}(d/L)}{n_m + 2} \tag{7.2}$$

Where $Overall\ \Delta C_D(d/L, n_m)$ is the overall drag variation of a convoy with n_m middle models, all equally separated d/L. $\Delta C_{D_{Front}}$,$\Delta C_{D_{Tail}}$ and $\Delta C_{D_{Middle}}$ are the front, tail and middle vehicle's drag variation at d/L, obtained from the interpolation of 7.13a. The *Overall* ΔC_D extrapolation for until 20 vehicles is shown in 7.13b for the characteristic distances previously analyzed. Is clear that the efficiency of the platooning grows with the number of vehicles in asymptotic way. In order to calculate this asymptotic value is applied the limit for $n_m \longrightarrow \infty$ and considering the l'Hopital rule as follows (equation 7.3):

$$\mid Overall\Delta C_D(d/L) \mid_{n_m \longrightarrow \infty} = \Delta C_{D_{Middle}}(d/L) \tag{7.3}$$

The ratio of drag variations and asymptotic value of each case are plotted in figure 7.13c.

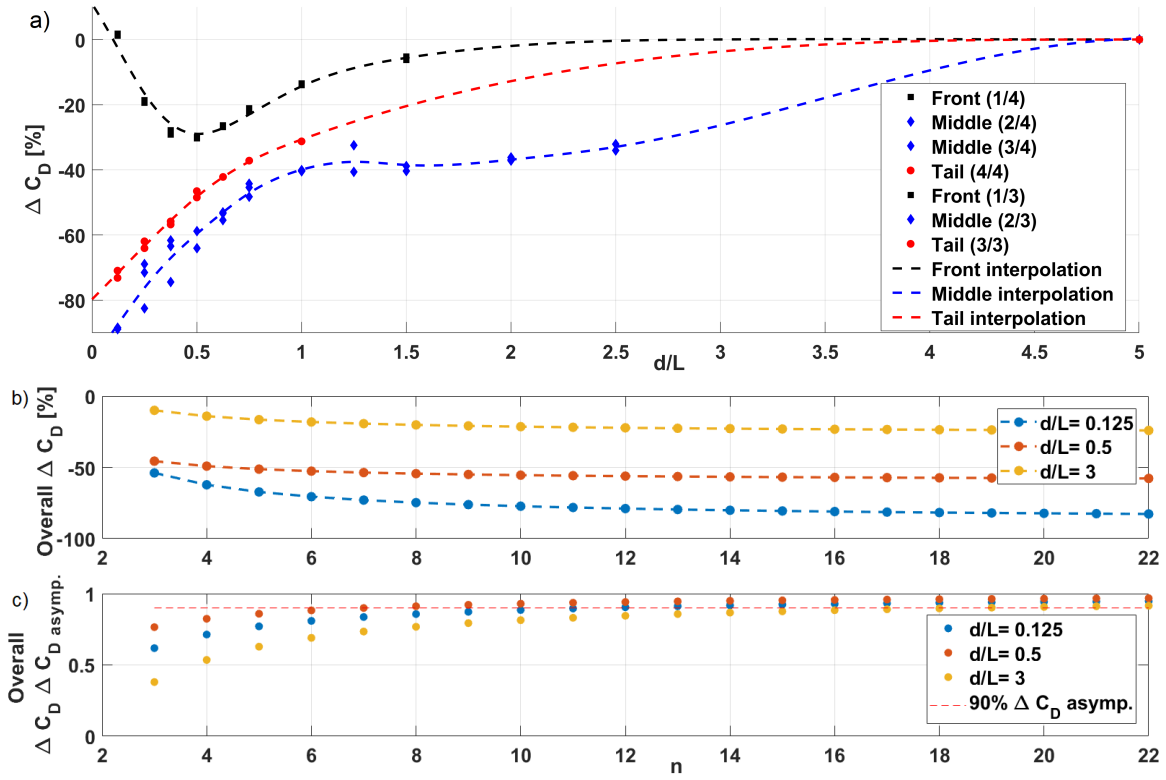

Figure 7.13: Interpolation of data and extrapolation for n vehicles, where $n = n_m + 2$.

7.4 Safe distances between vehicles

Now is intended to evaluate how much the aerodynamic drag could be improved with human-drive vehicles while keeping a safe distance in between. For this calculation, some constrains are defined: all vehicles involved are equal and have the same breaking deceleration $a_{deceleration}$, the same initial speed $V_{initial}$ and the same distance d/L in between. The typical length for this kind of commercial vehicles is four meters. Different studies gathered by Summala [108] reveal that the reaction time ($t_{reaction}$) of a person ranges from about 0.7 to 2.5s, so the condition for avoiding a collision is that the distance between vehicles must be at least (equation 7.4):

$$Safedistance[m] = t_{reaction} \times V_{initial} \tag{7.4}$$

This distance should guarantee, for a given speed, enough time for a person to react to a front vehicle suddenly breaking. This distance is used to calculate the overall drag reduction of the platoon in function of the number of vehicles involved, following equation 7.2. In this particular case the calculations are made for the $n = \infty$ vehicles, which corresponds to the maximum drag reduction reachable. The minimum distances between vehicles for different traveling speeds and the associated overall drag variation are presented in Table 1 for three characteristic times of reaction, given by the faster ($t = 0.7s$), the slower ($t = 2.5s$) and an average ($t = 1.6s$) reaction times. As seen in table 7.2, the only profitable configurations are the ones with the lowest reaction times, with a high risk of accident in case of emergency breaking. This evidences the unviability of the platooning configurations for human-driven vehicles, being the automatic controls the most fitted to assess this problem.

$t_reaction = 0.7s$	Safe distance [m]	d/L	$\Delta C_D[\%]$
$60kM/h$	11.6	2.9	-36.7
$80kM/h$	15.5	3.8	-23.9
$100kM/h$	19.6	4.8	-4.2
$t_reaction = 1.6s$			
$60kM/h$	26.6	6.65	0
$80kM/h$	35.8	8.96	0
$100kM/h$	44.5	11.1	0
$t_reaction = 2.5s$			
$60kM/h$	41.5	10.4	0
$80kM/h$	55.5	13.9	0
$100kM/h$	69.5	17.4	0

Table 7.2: Characteristic configurations of the controlled case.

Conclusions

This survey has explored the aerodynamic baseline of a commercial van model and three drag reduction methodologies consistent in steady active flow control, unsteady active flow control and platooning of two three and four vehicles. The most salient achievements of this thesis will be resumed in this chapter.

A wind tunnel investigation over a 1:10 scaled van model was performed, aimed to characterize the drag variations produced by an active flow control (AFC) system mounted on the model and based on four blowing slots on the trailing edges, and a platooning of models by using three wooden reproductions of the original.

The first results obtained were the **characterization of the isolated model** with no flow control (baseline). Through Drag, mean pressure and PIV measurements was found that the van model presents the characteristic near and far wake of squareback models, performing a $C_D = 0.4518$ at a testing Reynolds number of $Re = 2.5 \times 10^5$, in agreement with the definitions of *Aerodynamics of road vehicles* ([65]).
The PIV measurements shows us that the near wake on the symmetry plane of the model presents the typical recirculating structure also observed by Grandemange et al. [58], McNally et al. [80] and Capone and Romano [31] for similar bluff bodies, characterized by two counter-rotating vortexes being the top the dominant in size and intensity. Furthermore, two streamwise counter-rotating vortexes are generated on the near wake due to the interaction of the top and lateral flows, that trail away downstream and dissipate with the distance. The pressure distribution evidences over the model some salient characteristics: the stagnation point on the nose of the model and the effect of the A-pillar vortex on the side of the model, as evidenced by Levy and Brancher [76], creating a low pressure zone on the side face near the front edge. The base of the model evidence a low-pressure distribution with a growing tendency towards the bottom, most probably due to the asymmetry of the near wake observed on the PIV. The dynamic analysis of the pressure fluctuations on the near wake evidence a dominant phenomenon involving the vortex shedding between the top and bottom trailing edges, at an adimensional frequency of $St = 0.12$. This values correspond with the nominal values for vortex shedding also found by Volpe et al. [117], Evrard et al. [49], Brackston et al. [26] and many others. It is also present an uniform pressure fluctuation on the whole rear part in agreement with the bubble pumping observed by Duell and George [45] and Khalighi et al. [70] but with its peak of energy a the same Strouhal frequency.

The search for the drag reduction begins with the use of **steady blowing** on the rear trailing edges of the vehicle. The first series of tests involve the characterization of the top, lateral and bottom jets individually. While the bottom and lateral jets performed maximum drag reductions of 4% and 6% respectively, the top jet produces

a drag increasing. This negative effect could be associated to the increased asymmetry on the near wake, further increasing the wake size and consequently the drag. Due to his negative effect on the drag reduction, the top jet was dismissed for a successive combined-jets analysis. The drag reduction results of bottom and lateral jets were compared with the blowing momentum of the jets, evidencing the bottom one as the one with the higher drag reduction/blowing momentum ratio (Wake receptivity). This points to the bottom part of the model as the most sensible to the control.
After the individual jets characterization a combined bottom-lateral analysis was performed, by testing combinations of different blowing speeds for the jets. This analysis evidences two characteristic points of the control: The maximum drag reduction performing 10.6% of drag reduction and the best compromise reaching 5.6%. The first point was obtained from the minimum drag variation reached while the second was given by the peak of wake receptivity. An efficiency analysis of the loses on the pneumatic lines inside of the model regarding the power gained by the drag reduction shows that the best compromise case recovers five time the power consumed by the flow control, while for the maximum drag reduction the power spent by the jets is higher that what is being obtained by the drag reduction. This might rule out the possibility of using the maximum drag reduction condition, but there are conditions where a lower drag is requested and the energy budget is not a problem. For example, in a passing maneuver could be very positive to have less drag even if this means a cost in terms of energy. From the wake receptivity of the combined jets also comes to light the higher efficiency of the bottom jet regarding the lateral, as previously evidenced for the individual jets. All configurations involving bottom blowing between $0.6 < V_j/V_\infty < 0.8$ highlights maximum wake receptivity. This is also visible on the efficiency of the system, that shows higher values when the bottom blowing is dominant. The analysis of the pressure distribution surrounding the model shows that the only part affected by the control is the rear base, performing an average increase for growing blowing speeds and being this the reason behind the drag reduction. For the best compromise the pressure distribution resembles the baseline but with higher pressure values. The maximum drag reduction shows a completely different distribution with higher pressure values than the precedent case and a growing tendency towards the upper part, thus evidencing significant changes on the near wake.
The visualizations on the near and far wakes for the controlled cases share light on the changes produced by the actuation. For the best compromise case (blowing speed below the freestream) the control reduce the size of the recirculation bubble by introducing momentum on the bottom and lateral parts. The streamwise vortexes are also reduced and pushed upwards, thanks to the reduction of the downwash of the top flow behind the model. The control produces significant changes on the wake architecture when the blowing reaches the maximum drag reduction (bowing speeds around the freestream), eliminating the shear layers, counter rotating streamwise vortexes and significantly reducing the recirculating bubble. This wake configuration explains the larger changes in the rear base pressure distribution previously exposed.
The unsteadiness of the wake, dominated by the vortex shedding on the baseline, are reduced with the control. Actually, the $St = 0.12$ energy peak is progressively reduced with the increasing of the control intensity. For the maximum drag reduction configuration this peak is severally reduced, but not completely eliminated.
The possibility of automatically control the drag reduction was studied using an automatic drag control algorithm. It was demonstrated, through a very simple program, that the control system can reach the minimum drag without external intervention for

steady condition.

The study of the **unsteady blowing** of the flow shown negative results, with no improvements regarding the steady blowing. Moreover, for the lateral jets are presented some cases that evidence a drag increasing. This rules out any possibility of applying this system in a real case since it means an added complication to an already complicated system without getting any advantage. Despite of this there is a significant result regarding the bottom pulsed jets. The drag variation map shows peaks at the vortex shedding frequency and the two successive harmonics, evidencing a response of the wake when excited on their natural frequencies. This response is not observed on the lateral jets, highlighting the top-bottom dominant dynamic characteristics the wake. In this thesis only the square-waveform forcing was studied. Therefore remains open the possibility of analyzing different waveforms as sinusoidal, saw-teeth and others, and theirs effects over the drag as a future study.

The last tests performed were the **Platooning** driving configurations involving two, three and four models. For the two-model case the drag reduction of both vehicles decrease when approaching until half-model of distance in between, reaching 30% and 42% of drag reduction for the front and rear vehicles respectively. Above this distance the front model begins to recover drag while the rear drop even further. The pressure distributions demonstrates that the drag reduction on the front vehicle is only product of the base pressure increasing while the rear vehicle's due to the reduced pressure in front of the model, due to the front's model wake. For three and four vehicles convoy was demonstrated that exist three characteristic positions independent from the number of vehicles: front, middle and rear. Each one of this positions performs the same drag reductions in function of the distance, being the middle the best in terms of drag reduction by making profit of the benefits of the front vehicle's wake and the rear base increasing product of the following vehicles. The identification of the three characteristic positions allows us to make an extrapolation to an infinite number of vehicles, demonstrating that a platoon needs at least 18 models to reach an almost optimal drag configuration. All the configurations analyzed present significant drag reductions for relatively close distance between vehicles, representing a high risk situation when human-driven is involved. This demonstrated that the platooning of vehicles could be only safely obtained by an autonomous driving control performing faster response than humans.

Recalling the emission reduction map of the Introduction, the methodologies of aerodynamic drag reduction analyzed represent significant decrements on the emissions of pollutants to the atmosphere.

Methodology	Condition	Reference ΔC_D	individual CO_2 reduction	$4x10^6$ vehicles CO_2 reduction
Steady blowing	BC	-5.6%	$280\ Kg/Yr$	$1.12 \times 10^6\ Tn/Yr$
Platooning	Average	-30%	$1500\ Kg/Yr$	$6 \times 10^6\ Tn/Yr$

Table 9.1: CO_2 mission reductions per vehicle, for the methodologies studied.

In table 9.1 are presented the potential emission reduction for individual and 4

million vehicles, agreeing with the van population in Italy. The individual values do not represent a significant change, but when they are extrapolated to a population these values increase dramatically. This considerable reduction of emissions thanks to the aerodynamics and the development of new technologies for the engines and transmissions could be the solution of the CO_2 emission problem for the transport industry in the near future.

Appendix I:
Model geometry and manufacturing

As described in Chapter 2, the model reproduces the geometry of a commercial van scaled $\approx 1:10$. The technology used to build it was PLA 3D printing, and successively painted black with mate paint.

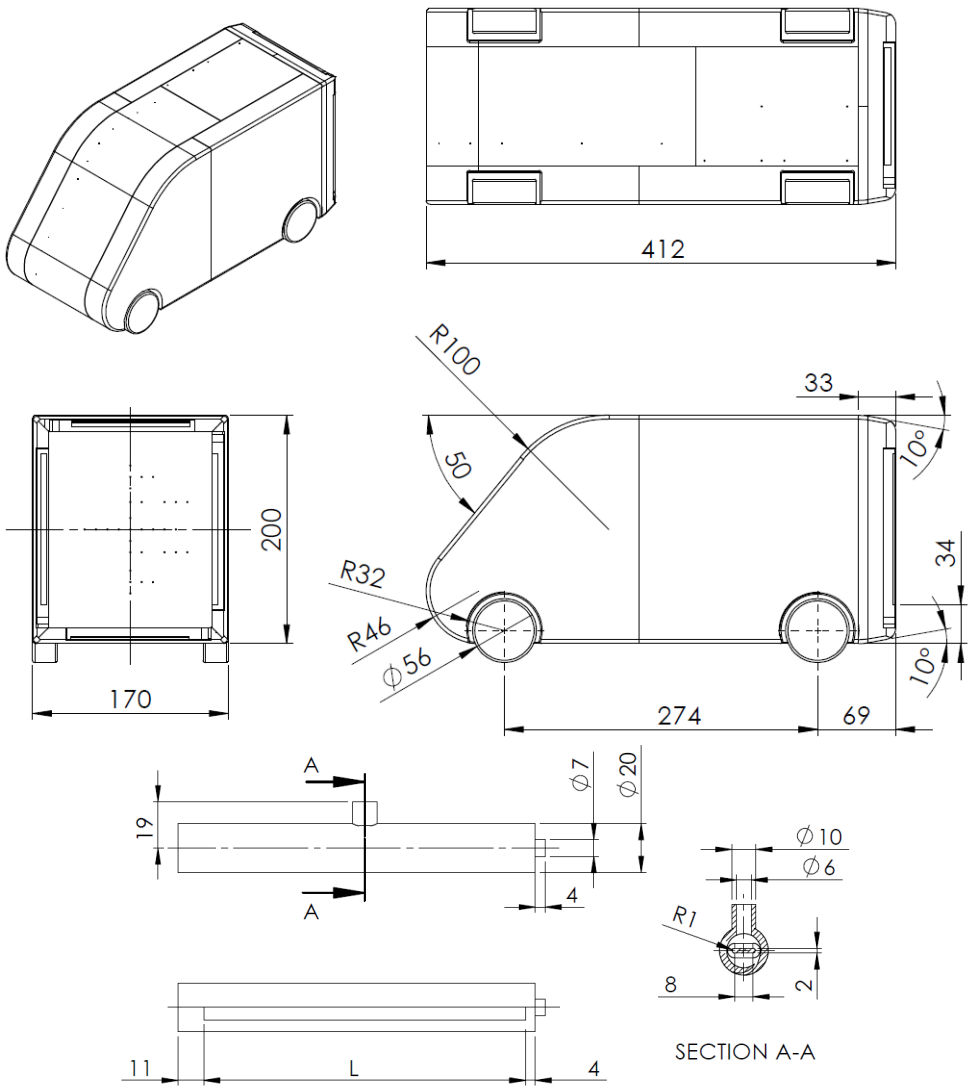

Figure 9.1: Main views and dimensions of the model.

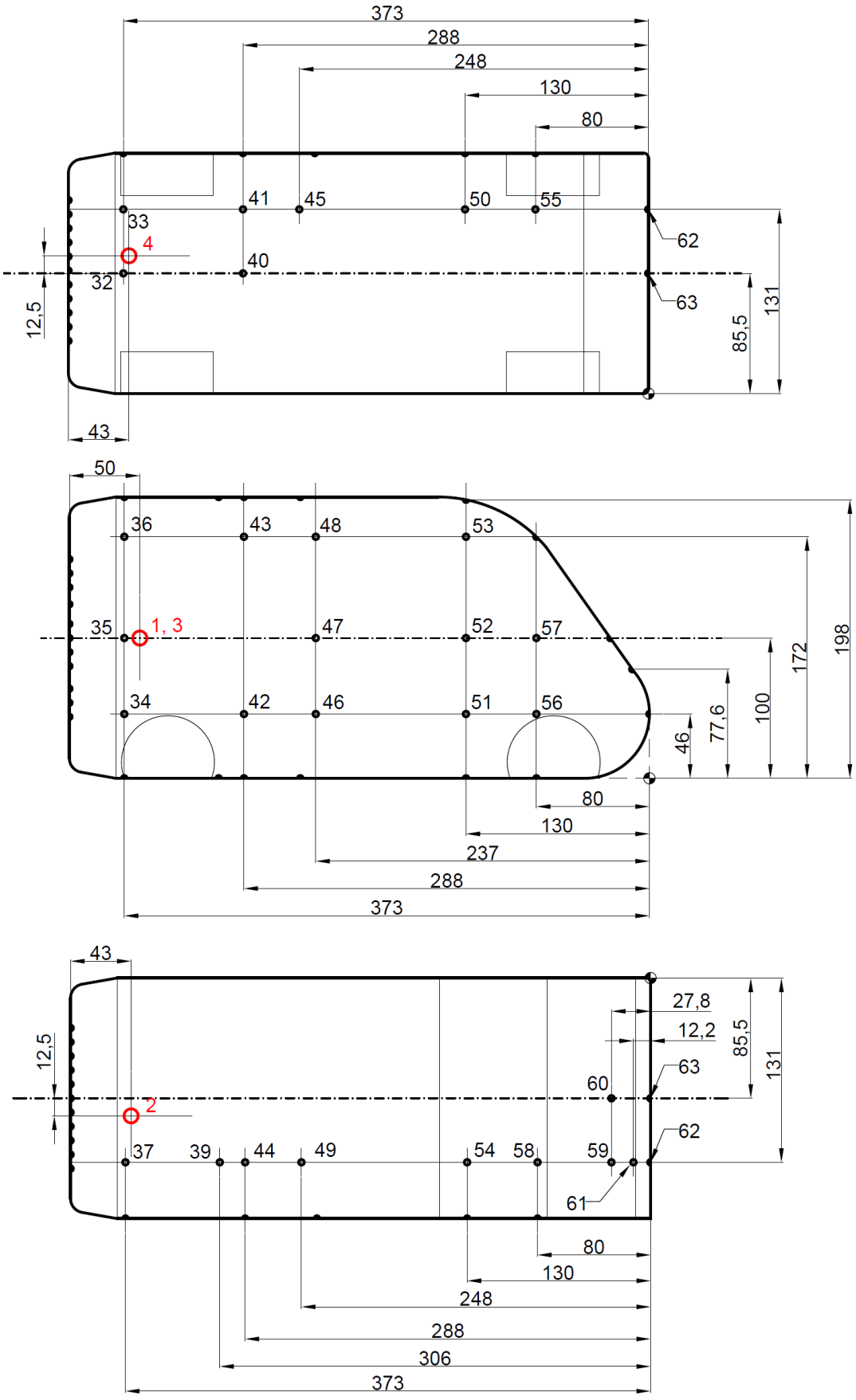

Figure 9.2: Positions of the taps and mics on the model.

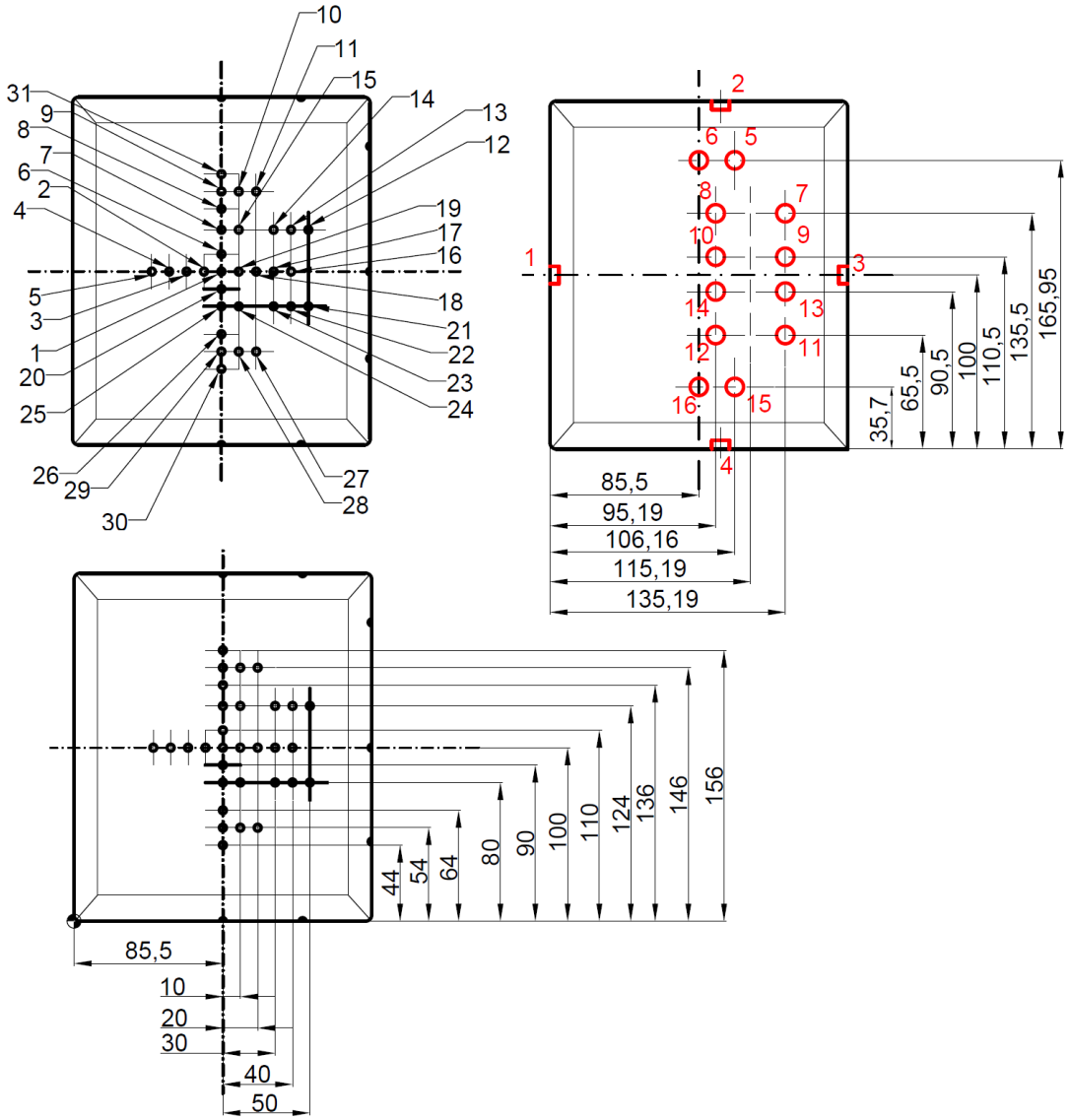

Figure 9.3: Positions of the taps and mics on the rear part of the model.

In figure 9.1 are the three main views of the model and an isometric, as well the dimensions. Moreover, there is also a detail of the actuator with the internal disposition and the generic quote L, that represents the length of the blowing slot and is $L = 100mm$ for the top and bottom jets and $L = 130mm$ for the lateral jets.
In figures 9.2 and 9.3 are defined the positions of the pressure taps in black circles and microphones in red circles. The dimensions of these circles are representative of the size of the sensors. Asides the position is the number identifying each tap or microphone.
In figure 9.4 are the components of the model in an exploded view. In the bottom image there is a detailed view of the AFC components, including the actuator's support, the four cylindrical actuators and the base plate.

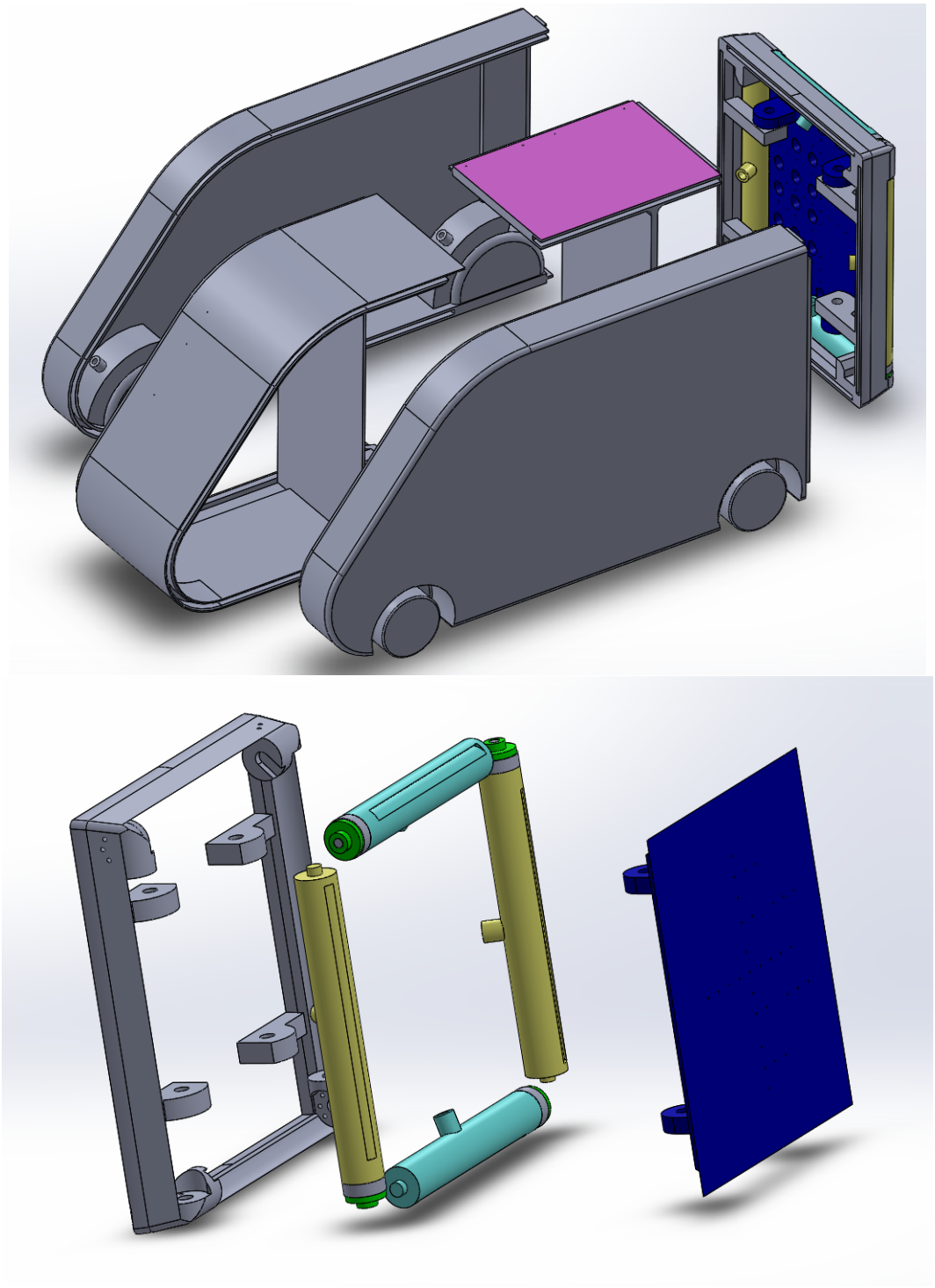

Figure 9.4: Exploded components of the 3D model of the front and rear components.

Appendix II: Acquisition/actuation programs

All programs developed in this section have been programmed in LabView platform.

Continuous blowing and pulsed blowing acquisition

The program performs acquisitions of load cell, microphones and flow meters for each configuration of the jets predefined. The input of the blowing conditions is performed by a **.txt* file with three columns, indicating the blowing speed of each jet in m/s. Each row on the file corresponds to a blowing configuration. The rest of the parameters like sampling time and frequency, settling time before measurements (seconds to wait), output folder and test number are loaded manually for each test campaign, as seen in the top-left part of figure 9.5. Below this input part is the output preview. By pressing the refresh button the program reads the input files and data and displays the number of configurations to test, the sampling time of each test and the estimated time for the whole test campaign. On the right part a matrix shows the blowing velocity of each jet for the loaded configurations. Once all inputs are ready, the wind tunnel can be turned on until test regime and then the program may start. This is performed by clicking the start button. On the right side is the status part, that becomes active once the program is started. On the status part there are three

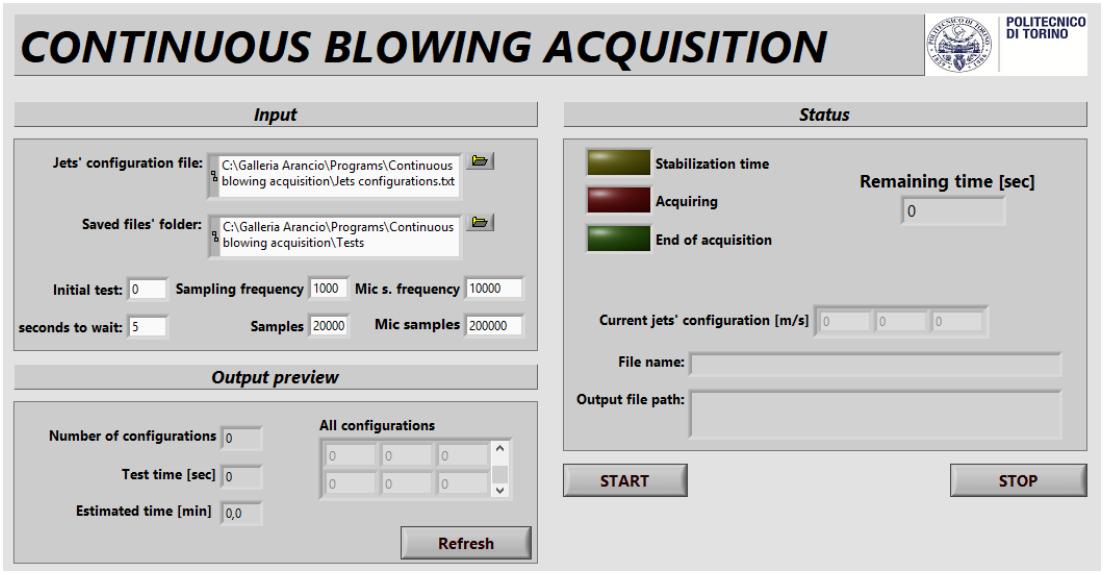

Figure 9.5: Continuous blowing acquisition program.

rectangular light indicators that show at each moment the program state. They alternate between Acquiring and Stabilization time until the test campaign is finished and

the End of acquisition is turned on. On the right part there is a counter that displays the remaining time of the test in seconds, and below there is a three component vector showing the current blowing configuration in m/s. Finally, on the bottom part are displayed the File name and Output file path. The output files are *.TDMS, being able to save large amounts of organized data in an easy-readable format.

In figure 9.6 is the UI of the Pulsed Blowing Acquisition program, which is the equivalent of the previous one but using unsteady blowing. The input file in this case is more complex, describing the maximum and minimum velocities for each jet, the frequency and the duty cycle. The only waveform available is the square, but the column was introduced for possible future tests of different waveforms. The status of the program shows a window where are plotted the signals of each electrovalve in volts, for a one second period. The program works in the same way that the precedent, logging the same data also in *.TDMS format.

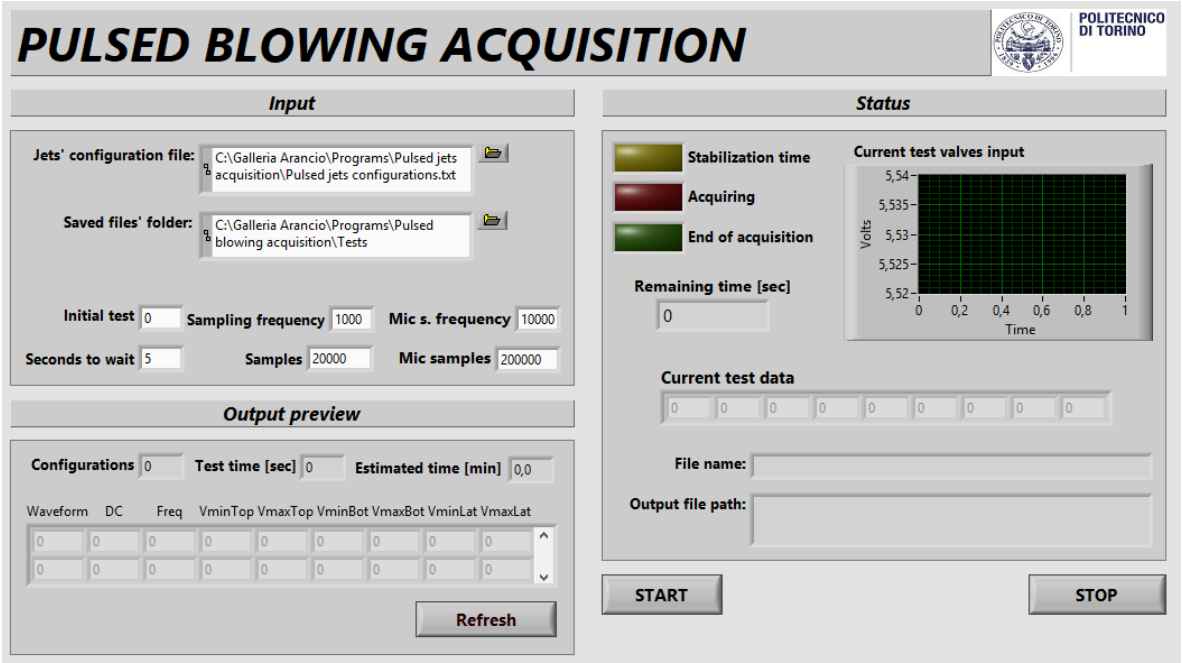

Figure 9.6: Pulsed blowing acquisition program.

Automatic drag control program

As described in section 5.8, this program searches through a very simple algorithm described in 5.21 the minimum value of the drag. The main variables are expressed in volts instead the real dimension in sake on simplicity of the programming. For example the trigger and valve increase are in Volts instead of Grams and meters per second.
In figure 9.7 is shown the UI of the automatic drag control program. In the left part is the input part, where the initial parameters of the program are defined. It is possible to select the active jets and analyze the individual or combined results. The kick is the parameter that start the program, as explained in section 5.8. When the *Save data?* button is activated, the program saves the data of each control loop. The reset button in the bottom turn all jets off.
On the right part is the status panel showing three main charts: the first is the raw load

cell lecture, the second is the filtered load cell signal and the third is the windowed and filtered load cell signal. The filter applied is a low-pass, cutting off the undesirable high frequencies associated to noise of the system. The window eliminates the transient of the filter, remaining only the steady value of the filtered load cell signal. With this last values the mean of the load cell is calculated on each algorithm loop. ON the bottom part are displayed the current and previous average values as well as the difference between them.

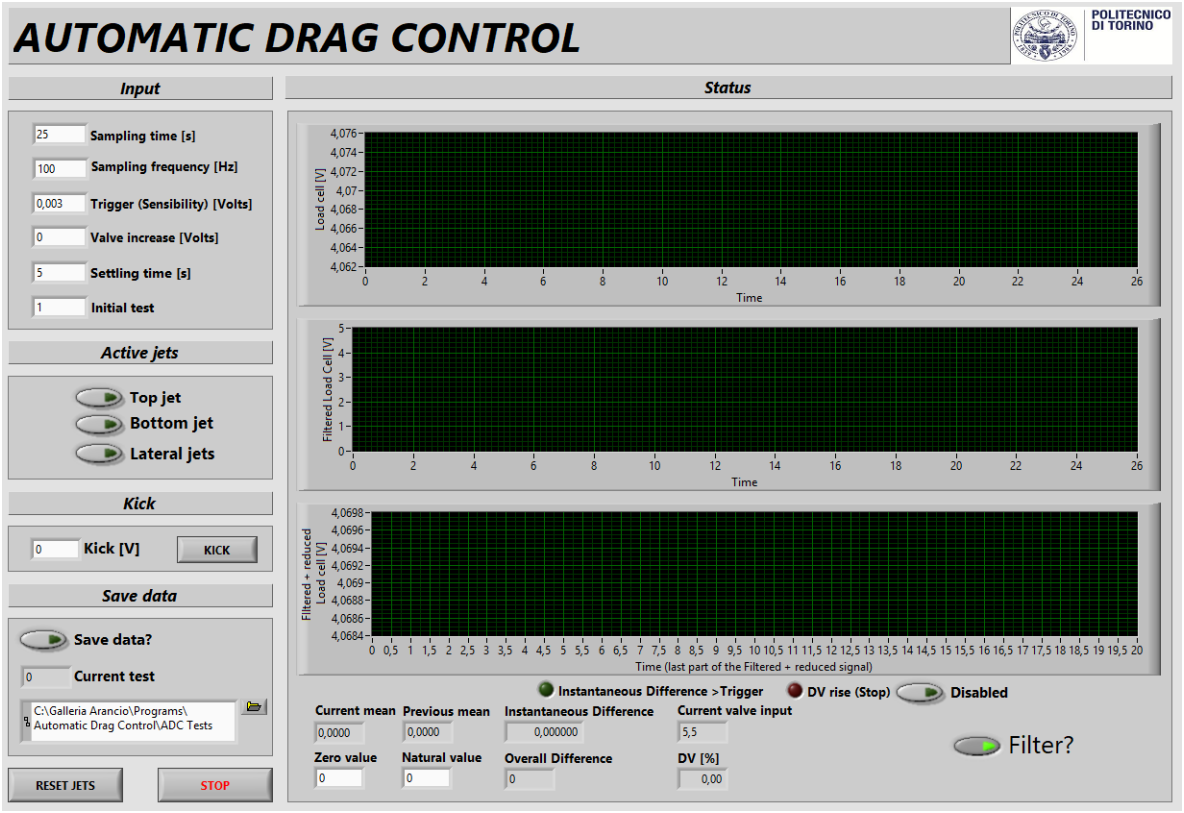

Figure 9.7: Automatic drag control.

Live control panel

The live control panel is simply a program that plots on real time the output of the load cell and flow meters, and have the possibility of settling the speed of each of the jets independently. This program is useful for checking the overall working of the system or when investigating the transients of the drag in function of changes in the control. Different from the precedent programs the live control panel do not have input parameters, since they could be changed at any moment. The UI of the program is shown in figure 9.8. In the left part there are three bars, that control the blowing speed of the jets. Below, there are the parameters of the test as freestream speed, zero drag value and drag reference used to calculate the drag variation. On the right part there are the drag measurements, including drag, C_D and drag variation in %. On the bottom part is shown a simple acquisition label, where data can be logged but limited to a $100Hz$ of sampling frequency, which is the refresh rate of the program.

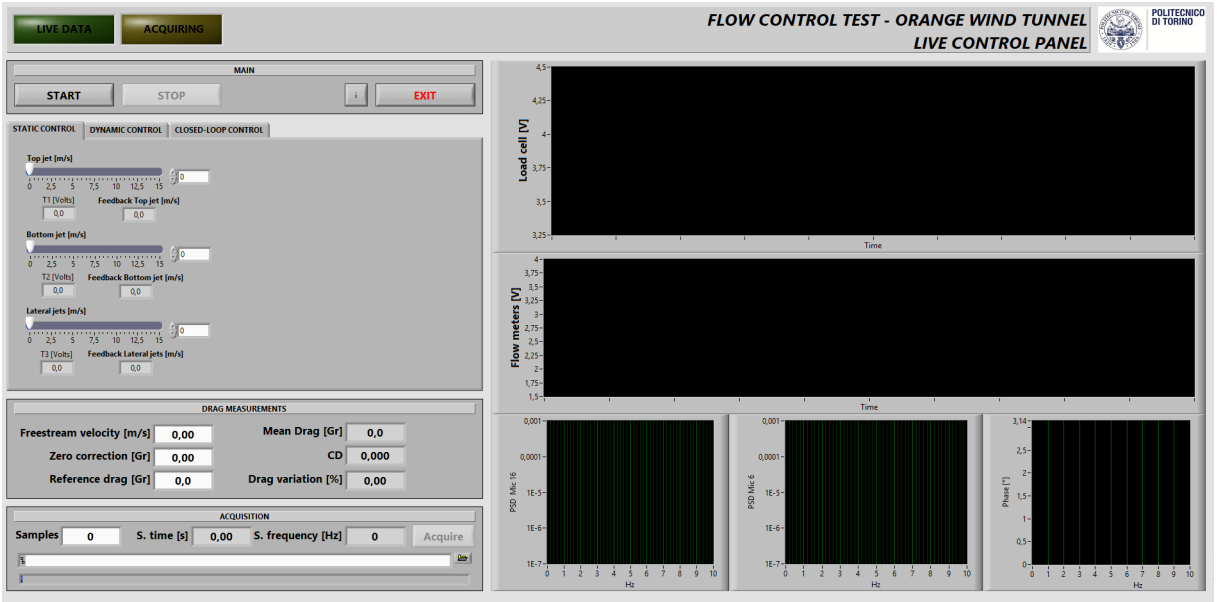

Figure 9.8: Live control panel.

References

[1] E Achenbach. The effects of surface roughness and tunnel blockage on the flow past spheres. *Journal of Fluids Mechanics*, 65:113–125, 1974. doi: 10.1017/S0022112074001285.

[2] E Achenbach. Vortex shedding from spheres. *Journal of Fluids Mechanics*, 62: 209 – 221, 1974. doi: 10.1017/S0022112074000644.

[3] S R Ahmed, G Ramm, and G Faltin. Some salient features of the time-averaged ground vehicle wake. *SAE International*, 93:473–503, 1984. doi: 10.4271/840300.

[4] N Ahuja, S Lertrattanapanich, and N K Bose. Properties determining choice of mother wavelet. *IEE Proc.-Vis. Image Signal Process*, 152:659 – 664, 2005. doi: 10.1049/ip-vis:20045034.

[5] A A Alam, A Gattami, K H Johansson, and C J Tomlin. Establishing safety for heavy duty vehicle platooning. a game theoretical approach. *IFAC Proceedings Volumes*, 44:3818–3823, 2011. doi: 10.3182/20110828-6-IT-1002.02071.

[6] A A Alam, J Mårtensson, and K H Johansson. Look-ahead cruise control for heavy duty vehicle platooning. *16th International IEEE Conference on Intelligent Transportation Systems (ITSC 2013)*, The Hague, Netherlands. 6-9 Oct 2013. doi: 10.1109/ITSC.2013.6728351.

[7] A Alamaan, A O Ashraf, and A Waqar. Passive drag reduction of square back road vehicles. *Journal of Wind Engineering and Industrial Aerodynamics*, 134: 30–43, 2014. doi: 10.1016/j.jweia.2014.08.006.

[8] T Astarita. Analysis of interpolation schemes for image deformation methods in piv: Effect of noise on the accuracy and spatial resolution. *Experiments in Fluids*, 40:977–987, 2006. doi: 10.1007/s00348-006-0139-4.

[9] T Astarita. Analysis of weighting windows for image deformation methods in piv. *Experiments in Fluids*, 43:859–872, 2007. doi: 10.1007/s00348-007-0314-2.

[10] T Astarita. Analysis of velocity interpolation schemes for imagedeformation methods in piv. *Experiments in Fluids*, 45:257–266, 2008. doi: 10.1007/s00348-008-0475-7.

[11] S R Balkanyi, L P Bernal, B Khalighi, and V Sumantran. Dynamics of manipulated bluff body wakes. *Fluids 2000 Conference and Exhibit*, Denver,CO,U.S.A. 19-22 June, 2000. doi: 10.2514/6.2000-2556.

[12] C Barbi, D P Favier, C A Maresca, and D P Telionis. Vortex shedding and lock-on of a circular cylinder in oscillatory flow. *Journal of Fluid Mechanics*, 170:527–544, 1986. doi: 10.1017/S0022112086001003.

[13] D Barros, J Borée, B R Noack, and A Spohn. Resonances in the forced turbulent wake past a 3d blunt body. *Physics of Fluids*, 28, 2016. doi: 10.1063/1.4953176.

[14] D Barros, J Borée, B R Noack, Andreas Spohn, and T Ruiz. Bluff body drag manipulation using pulsed jets and coanda effect. *Journal of Fluid Mechanics*, 805:422 – 459, 2016. doi: 10.1017/jfm.2016.508.

[15] D Bastine, B Witha, M Wächter, and J Peinke. Towards a simplified dynamic wake model using pod analysis. *Energies 2015*, 8:895 – 920, 2015. doi: 10.3390/en8020895.

[16] P W Bearman. On vortex shedding from a circular cylinder in the critical reynolds regime. *Journal of Fluid Mechanics*, 37:577–585, 1969. doi: 10.1017/S0022112069000735.

[17] P W Bearman. Bluff body flows applicable to vehicle aerodynamics. *Journal of Fluids Engineering*, 102:265–274, 1980. doi: 10.1115/1.3240679.

[18] H Berg and H Tijdeman. Theoretical and experimental results for the dynamic response of pressure measuring systems. *Nationaal Lucht - En Ruimtevaartlaboratorio Rium*, F328, 1965.

[19] C Bergenhem, E Hedin, and D Skarin. Vehicle-to-vehicle communication for a platooning system. *Procedia - Social and Behavioral Sciences*, 48:1222–1233, 2012. doi: 10.1016/j.sbspro.2012.06.1098.

[20] G Berkooz, P Holmes, and J L Lumley. The proper orthogonal decomposition in the analysis of turbulent flows. *Annual Review of Fluid Mechanics*, 25:539 – 575, 1993. doi: 10.1146/annurev.fl.25.010193.002543.

[21] A Berndtsson, W T Eckert, and E Mercker. The effect of groundplane boundary layer control on automotve testing in a wind tunnel. *SAE Technical Papers*, 880248:62 – 78, 1988. doi: 10.4271/880248.

[22] G Bonnavion and O Cadot. Unstable wake dynamics of rectangular flat-backed bluff bodies with inclination and ground proximity. *Journal of Fluid Mechanics*, 854:196–232, 2018. doi: 10.1017/jfm.2018.630.

[23] G Bonnavion and O Cadot. Boat-tail effects on the global wake dynamics of a flat-backed body with rectangular section. *Journal of Fluids and Structures*, Not published yet, 2019.

[24] G Bonnavion, O Cadot, V Herbert, S Parpais, R Vigneron, and J Délerye. Asymmetry and global instability of real minivans' wake. *Journal of Wind Engineering and Industrial Aerodynamics*, 184:77–89, 2019. doi: 10.1016/j.jweia.2018.11.006.

[25] W Bower and V Kibens. An overview of active flow control applications at the boeing company. *2nd AIAA Flow control conference*, Session: FC-17, Portland, Oregon. 28 June - 01 July, 2004. doi: 10.2514/6.2004-2624.

[26] R D Brackston, J M García de la Cruz, A Wynn, G Rigas, and J F Morrison. Stochastic modelling and feedback control of bi-stability in a turbulent bluff body wake. *Journal of Fluid Mechanics*, 802:726–749, 2016. doi: 10.1017/jfm.2016.495.

[27] R D Brackston, A Wynn, and J F Morrison. Modelling and feedback control of vortex shedding for drag reduction of a turbulent bluff body wake. *International Journal of Heat and Fluid Flow*, 71:127 – 136, 2018. doi: 10.1016/j.ijheatfluidflow.2018.03.015.

[28] J R Calvert. Some experiments on the flow past a sphere. *The Aeronautical Journal*, 76:248–250, 1972. doi: 10.1017/S0001924000042913.

[29] R Camussi and G Guj. Orthonormal wavelet decomposition of turbulent flows: intermittency and coherent structures. *Journal of Fluid Mechanics*, 348:177 – 199, 1997. doi: 10.1017/S0022112097006551.

[30] A C Canale, H A Navarro, J R Saraiva, N B Vastas, and J E D'Elboux. Fuel consumption of road commercial vehicles in the driving schedule. *SAE International*, 973053, 1997. doi: 10.4271/973053.

[31] A Capone and G P Romano. Investigation on the effect of horizontal and vertical deflectors on thenear-wake of a square-back car model. *Journal of Wind Engineering and Industrial Aerodynamics*, pages 57–64, 2019. doi: 10.1016/j.jweia.2018.12.011.

[32] L N Cattafesta and M Sheplak. Actuators for active flow control. *Annual Review of Fluid Mechanics*, 43:247 – 272, 2011. doi: 10.1146/annurev-fluid-122109-160634.

[33] J J Cerutti. Automotive aerodynamic drag control. *MsC Thesis*, Politecnico di Torino. Italy, 2014.

[34] J J Cerutti, C Sardu, G Cafiero, and G Iuso. Wake control of a square back road vehicle using continuous jets. *SAE International Journal of Commercial Vehicles*, 2019. doi: JCV-2019-0034.

[35] JJ Cerutti, C Sardu, and G Iuso. Drag reduction of squared-back body using continuous jets differently positioned on the rear base. *5th International Conference on Experimental Fluid Mechanics ICEFM 2018*, Munich, Germany, July 2-4. 2018.

[36] H Choi, J Lee, and H Park. Aerodynamics of heavy vehicles. *Annual revision of Fluid Mechanics*, 46:441 – 468, 2013. doi: 10.1146/annurev-fluid-011212-140616.

[37] A Clamen and W H Gauvin. Effects of turbulence on the drag coefficients of spheres in a supercritical flow reǵime. *American Institute of Chemical Engineers Journal*, 15:184–189, 1967. doi: 10.1002/aic.690150211.

[38] H Coandă. Perfectionnementaux propulseurs. *Patent (France)*, 796.843 /15.01.1935, 1932.

[39] A Cogotti. Ground effect simulation for full-scale cars in the pininfarina wind tunnel. *SAE International*, N 950996, 1995. doi: 10.4271/950996.

[40] J A Dahan, A S Morgans, and S Lardeau. Feedback control form-drag reduction on a bluff body with a blunt trailing edge. *Journal of Fluid Mechanics*, 704:360 – 387, 2012. doi: 10.1017/jfm.2012.246.

[41] L Dalla Longa, A S Morgans, and J A Dahan. Reducing the pressure drag of a d-shaped bluff body using linear feedback control. *Theoretical and Computational Fluid Dynamics*, 31:567–577, 2017. doi: 10.1007/s00162-017-0420-6.

[42] L Dalla Longa, O Evstafyeva, and A S Morgans. Simulations of the bi-modal wake past three-dimensional blunt bluff bodies. *Journal of Fluid Mechanics*, 866: 791–809, 2019. doi: 10.1017/jfm.2019.92.

[43] Ingrid Daubechies. Ten lectures on wavelets. *CBMS-NSF Regional Conference Series in Applied Mathematics*, pages xix + 350, 1990. doi: 10.1137/1.9781611970104.

[44] A Davila, E Aramburu, and A Freixas. Making the best of aerodynamics: platoons. *SAE Technical Papers*, 2013-01-0767, 2013. doi: 10.4271/2013-01-0767.

[45] E G Duell and A R George. Experimental study of a ground vehicle body unsteady near wake. *SAE International*, 1999. doi: 10.4271/1999-01-0812.

[46] R J Englar. Advanced aerodynamic devices to improve the performance, economics, handling and safety of heavy vehicles. *SAE International*, N 2001-01-2072, 2001. doi: 10.4271/2001-01-2072.

[47] EU-2019/1242. Setting co2 emission performance standards for new heavy-duty vehicles and amending regulations (ec) no 595/2009 and (eu) 2018/956 of the european parliament and of the council and council directive 96/53/ec. *Official Journal of the European Union*, 192:202 – 240, 2019.

[48] EU-2019/631. Setting co2 emission performance standards for new passenger cars and for new light commercial vehicles, and repealing regulations (ec) no 443/2009 and (eu) no 510/2011. *Official Journal of the European Union*, 111:13 – 53, 2019.

[49] A Evrard, O Cadot, V Herbert, D Ricot, R Vignerond, and J Délery. Fluid force and symmetry breaking modes of a 3d bluff body. *Journal of Fluids and Structures*, 61:99 – 114, 2016. doi: 10.1016/j.jfluidstructs.2015.12.001.

[50] O Evstafyeva, A S Morgans, and L Dalla Longa. Simulation and feedback control of the ahmed body flow exhibiting symmetry breaking behaviour. *Journal of Fluid Mechanics*, 817, 2017. doi: 10.1017/jfm.2017.118.

[51] B Fago, H Lindner, and O Mahrenholtz. The effect of ground simulation on the flow around vehicles in wind tunnel testing. *Journal of Wind Engineering and Industrial Aerodynamics*, 38:47 – 57, 1991. doi: 10.1016/0167-6105(91)90026-S.

[52] M Farge. Wavelet transform and their applications to turbulence. *Annual Review of Fluid Mechanics*, 24:395 – 458, 1992. doi: 10.1146/annurev.fl.24.010192.002143.

[53] C A J Fletcher and G D H Stewart. Bus drag reduction by the trapped vortex concept for a single bus and two buses in tandem. *Journal of Wind Engineering and Industrial Aerodynamics*, 24:143 – 168, 1984. doi: 10.1016/0167-6105(86)90004-8.

[54] D W Gage and J B Pletta. Ground vehicle convoying. *Proceedings, Mobile Robots II*, 0852, 1987. doi: 10.1117/12.968264.

[55] O Gehring and H Fritz. Practical results of a longitudinal control concept for truck platooning with vehicle to vehicle communication. *IEEE Conference on Intelligent Transportation Systems*, Boston, Massachusetts. USA. 1997.

[56] D Geropp and H-J Odenthal. Drag reduction of motor vehicles by coanda effect. *Experiments in fluids*, 28:74 – 85, 2000. doi: 10.1007/s003480050010.

[57] P Gilliéron and A Kourta. Aerodynamic drag reduction by vertical splitter plates. *Experiments in Fluids*, 48:1–16, 2010. doi: 10.1007/s00348-009-0705-7.

[58] M Grandemange, M Gohlke, and O Cadot. Turbulent wake past a three-dimensional blunt body. part 1. global modes and bi-stability. *Journal of Fluid Mechanics*, 722:51–84, 2013. doi: 10.1017/jfm.2013.83.

[59] M Grandemange, M Gohlke, and O Cadot. Bi-stability in the turbulent wake past parallel bodies with various aspect ratios and wall effects. *Physics of Fluids*, 25:5103–, 2013. doi: 10.1063/1.4820372.

[60] D Greenblatt. Unsteady low-speed wind tunnels. *AIAA journal*, 54:1817 – 1830, 2016. doi: 10.2514/1.J054590.

[61] W Hamiga, Wand Ciesielka. Numerical modeling of airflow over column of vehicles using ansys® package. *E3S Web of Conferences*, 46, 2018. doi: 10.1051/e3sconf/20184600025.

[62] M Hasaan, D Badlani, and M Nazarinia. On the effect of boat-tails on a simplifyed heavy vehicle geometry under crosswinds. *Journal of Wind Engineering & Industrial Aerodynamics*, 183:172–186, 2018. doi: 10.1016/j.jweia.2018.10.013.

[63] W H Hucho and G Sovran. Aerodynamics of road vehicles. *Annual Review of Fluid Mechanics*, 25:485–537, 1993. doi: 10.1146/annurev.fl.25.010193.002413.

[64] W H Hucho, L J Janssen, and G Schwartz. The wind tunnel's ground plane boundary layer - its interference with the flow underneath cars. *SAE International*, 84:380–389, 1975. doi: 10.4271/750066.

[65] Wolf-Heinrich Hucho. *Aerodynamics of road vehicles.* Butterworth-Heinemann, 1987.

[66] J C R Hunt, C J Abell, J A Peterka, and H Woo. Kinematical studies of the flows around free or surface-mounted obstacles; applying topology to flow visualization. *Journal of Fluid Mechanics*, 86:179–200, 1978. doi: 10.1017/S0022112078001068.

[67] R Hwang and C Yao. Numerical study of vortex shedding from a square cylinder with ground effect. *Journal of Fluids Engineering*, 119, 1997. doi: 10.1115/1.2819274.

[68] I Idel'chik and E Fried. *Handbook of hydraulic resistance*. 1986.

[69] J Katz. *Race car aerodynamics: designing for speed*. Bentley publishers, 1995.

[70] B Khalighi, S Zhang, C Koromilas, S R Balkanyi, L P Bernal, G Iaccarino, and P Moin. Experimental and computational study of unsteady wake flow behind a bluff body with a drag reduction device. *SAE Transactions*, 110:1209–1222, 2001. doi: www.jstor.org/stable/44730974.

[71] T Kim, B Lee, D Lee, J Hwang, and D Lee. A study on vortex shedding around a bluff body near the ground. *SAE Technical Papers*, 2003-01-0652, 2003. doi: 10.4271/2003-01-0652.

[72] E M Laws and J L Livesey. Flow through screens. *Annual Review of Fluid Mechanics*, 10:247–266, 1978. doi: 10.1146/annurev.fl.10.010178.001335.

[73] G M Le Good and K P Garry. On the use of reference models in automotive aerodynamics. *SAE Technical Papers*, 2004-01-1308, 2004. doi: 10.4271/2004-01-1308.

[74] T L D Lee and A Yamamoto. Wavelet analysis: theory and application. *Hewlett Packard journal*, 45:44–44, 1994.

[75] A W Leissa. *Vibration of plates*. NASA, 1969.

[76] B Levy and P Brancher. Topology and dynamics of the a-pillar vortex. *Physics of Fluids*, 25, 2013. doi: 10.1063/1.4792710.

[77] R P Littlewood and M A Passmore. Aerodynamic drag reduction of a simplified squareback vehicle using steady blowing. *Experiments in Fluids*, 53:519–529, 2012. doi: 10.1007/s00348-012-1306-4.

[78] J M Lucas, O Cadot, V Herbert, S Parpais, and J Délery. A numerical investigation of the asymmetric wake mode of a squareback ahmed body - effect of base cavity. *Journal of Fluid Mechanics*, 831:675–697, 2017. doi: https://doi.org/10.1017/jfm.2017.654.

[79] D E Manosalvas-Kjono, T D Economon, C Othmer, and A Jameson. Computations of active flow control for heavy vehicle drag reduction. *35th AIAA Applied Aerodynamics Conference*, Denver, Colorado, 5-9 June. 2017. doi: 10.2514/6.2017-3567.

[80] J McNally, E Fernandez, G Robertson, R Kumar, K Taira, F Alvi, Y Yamaguchi, and K Murayama. Drag reduction on a flat-back ground vehicle with active flow control. *Journal of Wind Engineering and Industrial Aerodynamics*, 145:292 – 303, 2015. doi: 10.1016/j.jweia.2015.03.006.

[81] J McNally, N Mazellier, F Alvi, and A Kourta. Control of salient flow features in the wake of a 25° ahmed model using microjets. *Experiments in Fluids*, 60:1 – 17, 2018. doi: 10.1007/s00348-018-2645-6.

[82] M Michaelian and F Browand. Field experiments demonstrate fuel savings for close-following. *UC Berkeley Research Reports*, 2000. doi: https://escholarship.org/uc/item/6j03g652.

[83] G Minelli, M. Tokarev, J Zhang, T Liu, V. Chernoray, B Basara, and S Krajnović. Active aerodynamic control of a separated flow. *Not yet published*, 2019. doi: Notyetpublished.

[84] T Morel and M Bohn. Flow over two circular disks in tandem. *Journal of Fluids Engineering*, 102:104 – 111, 1980. doi: 10.1115/1.3240599.

[85] K Ogata. *Modern control engineering*. Pearson, 1970.

[86] R M Pagliarella, S Watkins, and A Tempia. Aerodynamic performance of vehicles in platoons: the influence of backlight angles. *SAE International*, 2007-04-16, 2007. doi: 10.4271/2007-01-1547.

[87] M Pastoor, L Henning, B R Noack, R King, and G Tadmor. Feedback shear layer control for bluff body drag reduction. *Journal of Fluid Mechanics*, 608: 161–196, 2008. doi: 10.1017/S0022112008002073.

[88] J C Paul and J G LaFond. Analysis and design of automobile forebodies using potential flow theory and a boundary layer separation criterion. *SAE International*, 1969. doi: 10.4271/830999.

[89] G Pavia, M Passmore, and C Sardu. Evolution of the bi-stable wake of a square-back automotive shape. *Experiments in Fluids*, 59, 2017. doi: 10.1007/s00348-017-2473-0.

[90] G Pavia, M Passmore, and M Varney. Low frequency wake dynamics for a square-back vehicle with side trailing edge tapers. *Journal of Wind Engineering & Industrial Aerodynamics*, 184:417–435, 2019. doi: 10.1016/j.jweia.2018.12.009.

[91] A K Perry, G Pavia, and M Passmore. Influence of short rear end tapers on the wake of a simplified square-back vehicle wake topology and rear drag. *Experiment in fluids*, pages 57 – 169, 2016. doi: 10.1007/s00348-016-2260-3.

[92] A N Rao, G Minelli, J Zhang, B Basara, and S Krajnović. Investigation of the near-wake flow topology of a simplified heavy vehicle. *Journal of Wind Engineering and Industrial Aerodynamics*, 183:243–272, 2018. doi: 10.1016/j.jweia.2018.09.019.

[93] R Raul and P S Bernard. A numerical investigation of the turbulent flow field generated by a stationary cube. *Journal of Fluids Engineering*, 113:216 222, 1991. doi: 10.1115/1.2909483.

[94] I Rodríguez, O Lehmkuhl, J Chiva, R Borrell, and A Oliva. On the flow past a circular cylinder from critical to super-critical reynolds numbers: Wake topology and vortex shedding. *International Journal of Heat and Fluid Flow*, 55:91 – 103, 2015. doi: 10.1016/j.ijheatfluidflow.2015.05.009.

[95] G F Romberg, F Chianese, and R G Lajoie. Aerodynamic of race cars in drafting and passing situations. *SAE Technical Papers*, 710213, 1971. doi: 10.4271/710213.

[96] F W Roos and W W Willmarth. Some experimental results on sphere and disk drag. *AIAA Journal*, 9:285 – 291, 1971. doi: 10.2514/3.6164.

[97] A Roshko. On the drag and shedding frequency of two-dimensional bluff bodies. *NACA Report*, 1954. doi: ID:19930083869.

[98] M Rouméas, P Gilliéron, and A Kourta. Analysis and control of the near-wake flow over a square-back geometry. *COmputer & Fluids*, 38:60–70, 2009. doi: 10.1016/j.compfluid.2008.01.009.

[99] M Rouméas, P Gilliééron, and A Kourta. Drag reduction by flow separation control on a car after body. *International Journal for Numerical Methods in Fluids*, 60:1222 – 1240, 2009. doi: 10.1002/fld.1930.

[100] K Salari and J Ortega. Experimental investigation of the aerodynamic benefits of truck platooning. *SAE International*, 2018-01-0732, 2018. doi: 10.4271/2018-01-0732.

[101] A Sandrine, J McNally, F Alvi, and A Kourta. Separation flow control on a generic ground vehicle using steady microjet arrays. *Experiments in fluids*, 51: 1177–1187, 2011.

[102] C Sardu. Active flow control around simplified 3d bluff bodies. *PhD Thesis*, Politecnico di Torino. Italy, 2016.

[103] C Sardu, D Lasagna, and G Iuso. Noise filtering for wall-pressure fluctuations in measurements around a cylinder with laminar and turbulent flow separation. *Journal of Fluids Engineering*, 138, 2016. doi: 10.1115/1.4032034.

[104] C Sardu, S Sedda, and G Iuso. Drag reduction on a simplifyed 3d bluff body. *European Drag Reduction and Flow Control Meeting – EDRFCM 2015*, Cambridge, UK, March 23–26. 2015.

[105] H J Schmidt, R Woszidlo, C N Nayeri, and C O Paschereit. The effect of flow control on the wake dynamics of a rectangular bluff body in ground proximity. *Experiments in Fluids*, 59, 2018. doi: 10.1007/s00348-018-2560-x.

[106] S Shadmani, S M Mousavi Nainiyan, and R Ghasemiasl. Experimental study of flow control over an ahmed body using plasma actuator. *Mechanics and Mechanical Engineering*, 22:239 – 251, 2018.

[107] G Sovran, , and M S Bonn. Formulae for the tractive-energy requirements of vehicles driving the epa schedules. *SAE International*, 810184, 1981. doi: 10.4271/810184.

[108] H Summala. Brake reaction times and driver behavior analysis. *Transportation Human Factors*, 2:217–226, 2000. doi: 10.1207/STHF0203_2.

[109] S Szepessy and P W Bearman. Aspect ratio and end plate effects on vortex shedding from a circular cylinder. *Journal of Fluid Mechanics*, 234:191–217, 1992. doi: 10.1017/S0022112092000752.

[110] S Taneda. Experimental investigation of the wake behind a sphere at low reynolds numbers. *Journal of the Physical Society of Japan*, 11:1104 – 1108, 1956. doi: 10.1143/JPSJ.11.1104.

[111] S Taneda. Visual observations of the flow past a sphere at reynolds numbers between 10^4 and 10^6. *Journal of Fluids Mechanics*, 85:187–192, 1978. doi: 10.1017/S0022112078000580.

[112] C Torrence and G P Compo. A practical guide to wavelet analysis. *Bulletin of the American Meteorological Society*, 79:61 – 78, 1998. doi: 10.1175/1520-0477(1998)079<0061:APGTWA>2.0.CO;2.

[113] L Tsuei and Ö Savas. A wind tunnel investigation of the transient aerodynamic effects on a four-car platoon during passing maneuvers. *SAE Technical Papers*, 2000-01-0875, 2000. doi: 10.4271/2000-01-0875.

[114] G M R Van Raemdonck and M J L van Tooren. Time-averaged phenomenological investigation of a wake behind a bluff body. *BBAA VI International Colloquium on: Bluff Bodies Aerodynamics & Applications*, Milano, Italy. 20 to 24 July, 2008.

[115] P Vegendla, T Sofu, R Saha, M M Kumar, and L-K Hwang. Investigation of aerodynamic influence on truck platooning. *SAE International*, 2015-01-2895, 2015. doi: 0.4271/2015-01-2895.

[116] J Venning, D Lo Jacono, D Burton, M Thompson, and J Sheridan. The effect of aspect ratio on the wake of the ahmed body. *Experiments in Fluids*, page 56:126, 2015. doi: 10.1007/s00348-015-1996-5.

[117] R Volpe, P Devinant, and A Kourta. Experimental characterization of the unsteady natural wake of the full-scale square back ahmed body flow bi-stability and spectral analysis. *Experiments in Fluids*, page 56:99, 2015. doi: 10.1007/s00348-015-1972-0.

[118] E Wassen and F Thiele. Drag reduction for a generic car model using steady blowing. *4th Flow Control Conference*, Seattle, Washington. 23 - 26 June 2008. doi: 10.2514/6.2008-3771.

[119] M Watanabe, M Harita, and E Hayashi. The effect of body shape in wind noise. *Society of Automotive Engineers*, 1978. doi: 10.4271/780266.

[120] S Watkins and G Vino. The effect of vehicle spacing on the aerodynamics of a representative car shape. *Journal of Wind Engineering and Industrial Aerodynamics*, 96:1232–1239, 2008. doi: 10.1016/j.jweia.2007.06.042.

[121] B Wieneke. Improvements for volume self-calibration. *Measurement Science and Technology*, 2018. doi: 10.1088/1361-6501/aacd45.

[122] R Wille and H Fernholtz. Report on the first european mechanics colloquium, on the coanda effect. *Journal of Fluid Mechanics*, 23(4):801 – 819, 1965.

[123] J Williams, J Barlow, and R Ranzenbach. Experimental study of cd variation with aspect ratio. *SAE Technical Papers*, 1999-01-0649, 1999. doi: 10.4271/1999-01-0649.

[124] C H K Williamson. Defining an universal ans continuous strouhal-reynolds number relationship for the laminar vortex shedding of a circular cylinder. *The Physics of Fluids*, 31, 1988. doi: 10.1063/1.866978.

[125] K Yu, Q Liang, J Yang, and Y Guo. Model predictive control for hybrid electric vehicle platooning using route information. *Proceedings of the Institution of Mechanical Engineers, Part D: Journal of Automobile Engineering*, 230:1273–1285, 2015. doi: 10.1177/0954407015606314.

[126] M Zabat, S Frascaroli, and F K Browand. Drag measurements on 2, 3 and 4 car platoons. *SAE Technical Papers*, 940421, 1994. doi: 10.4271/940421.

[127] B F Zhang, K Liu, Y Zhou, S To, and J Y Tu. Active drag reduction of a high-drag ahmed body based on steady blowing. *Journal of Fluid Mechanics*, 856:351 – 396, 2018. doi: 10.1017/jfm.2018.703.

[128] Y Zheng, S Fujimoto, and A Rinoshika. Combining wavelet transform and pod to analyze wake flow. *Journal of Visualization*, 19:193 – 210, 2016. doi: 10.1007/s12650-015-0318-6.